The Lærdal-Gjende Fault: A detailed structural and thermochronological study

A thesis presented for Master of Science in Geodynamics

by
Ester Cobles Pérez

Supervised by
Dr. Anna Ksienzyk, Prof. Joachim Jacobs and Prof. Håkon Fossen.

Department of Earth Science
University of Bergen
2015

This page is intentionally left blank

Acknowledgements

I would like to thank the Bergen Tectonics and Thermochronology research group of University of Bergen for giving me the opportunity to form part of it. I thank my supervisors, Dr. Anna Ksienzyk, Prof. Joachim Jacobs and Prof. Håkon Fossen. I thank Dr. Anna K. Ksienzyk for introducing me to the fission track analysis and provide constructive feedback to my task. I wish to thank Prof. Håkon Fossen and Prof. Joachim Jacobs for their contributions to my structural results. I am very grateful to Dr. Friederike U. Bauer for helping me along the fission track process and for correcting with great care some of the chapters of this thesis.

I wish to thank to Tereza Konopaskova and Irina Dumitru for teaching me step by step all the laboratory procedures for mineral separation and for epoxy grain mount preparation. I also wish to thank Prof. Wojciech Nemec for his help with the statistical analysis. I am very grateful for all the ”cataclastic chatting” with Claudio Salazar Mora.

My many thanks to my former colleague Henrik Stokke and his family, who generously hosted me in their cabin in Lærdal and kept me good company during my field trips.

I would like to mention some of my colleagues from UiB: Birgitte Opås, Rosa Polanco Ferrer and Ben Couvin, who always had something interesting to share. I would like to mention as well some special people that I had the chance to meet in Svalex 2013: Gabriela Labastidas, Paola Masiu and Diana Valverde for cheering every moment we spend together. I would also like to mention to my family and friends in Spain, to whom I missed deeply during my stay in Norway, and to my welcoming, new Norwegian family for their support and encouragement.

My most special thanks to Roger Navelsaker, my partner in life, for helping me with the formatting of this thesis in LaTeX, constructing small inventions to optimize the field work and being my personal field assistant. Thanks for being always supporting and loving in the hardest moments. I dedicate this work to you.

Bergen, 1 June 2015

Ester Cobles Pérez

This page is intentionally left blank

Abstract

The development of the Caledonian orogen to a passive margin leaded to the present-day Norwegian landscape. The most recent denudation history in Mesozoic and Cenozoic times holds the key to the morphotectonic development of southern Norway. The purpose of this study is to asses the influence of the Lærdal-Gjende fault over the local exhumation pattern of the study area. The second part of the study encompasses a detailed structural analysis of the fault-rocks exposed in the Lærdalsøyri outcrop.

Low-temperature thermochronology has become more popular among geologists over the last decades. Apatite fission track analysis (AFT) was performed for 10 of samples from the footwall and the hanging wall blocks of the Lærdal-Gjende fault. AFT ages from Permian to Middle Cretaceous times were revealed by AFT analysis using the external detector method. Most of the samples were collected from the footwall block and gave scattered AFT ages ranging from Middle Cretaceous to Early Jurassic. An trend of increasing AFT age towards the Lærdal-Gjende fault was discovered for the hanging wall. In opposite, a decreasing AFT age trend towards the fault was revealed for the footwall block. The local exhumation pattern corresponds to the 'footwall uplift model' proposed by Andersen et al. (1999).

The thermal modeling was performed for 4 samples of the footwall block and suggest two accelerated cooling events from Late Carboniferous to Early Jurassic times and in Neogene times. In regional basis, the time-Temperature paths obtained can be linked to the rifting episodes of the North Sea and North Atlantic Ocean. The Hardangerfjord Shear Zone extends from the North Sea (SW) into mainland Norway (NE) and it is hard-linked to the Lærdal-Gjende fault in onshore. The post-Caledonian rifting episodes provoked the reactivation in different occasions of both the Hardangerfjord Shear Zone and the Lærdal-Gjende fault. Cooling rate estimates of <1,5 [from Late Carboniferous to Early Jurassic times are significantly slower to cooling rates reported for coastal samples. This shows the importance of rift flank uplift during Mesozoic rifting in coastal areas. The Paleogene rapid cooling, however, is attributed to thermal disturbances derived from the opening of the North Atlantic Ocean.

The Lærdalsøyri outcrop yields a wide span of fault rock types. The cataclasites of the hanging wall block show signs of ductile deformation overprint in upper amphibolite metamorphic conditions. That is interpreted to be the consequence of extensional displacement, that juxtaposed the cataclasites onto the mylonitic package from the footwall. That process represented an increase in temperature conditions. The exhumation of the hanging wall is evidenced by the retrometamorphism into greenschist facies. The thick package of medium to low-grade mylonites from the footwall block are associated to top-to-NW displacement of the Lærdal-Gjende fault during Devonian times. The fault core show different generations of fault gouges linked to Mesozoic brittle reactivation of the fault.

Table of Contents

This page is intentionally left blank

1 Introduction

The mountain range that rises in Norway represents a fundamental problem in geological terms. The Scandinavian mountains are the legacy of the past, when 420 million years ago, an Himalayan-size mountain range stood approximately where Norway is now. This mountain belt, the Caledonian orogen, was dismantled by gravitational and tectonic forces, causing a dramatic decrease in relief. Eventually, after a long post-Caledonian history of extension, Norway became a passive margin. The morphology of passive margins is typically described as a smooth transition from sea to continent, including wide coastal plains. The Norwegian and other passive margins around the world are, nonetheless, characterized by their scarped and elevated terrains along the coast. In the Norwegian western coast, fjords and other geomorphological glacial features dominate the landscape. Abrupt cliffs, scarce sand beaches and high mountains are not what is generally expected according to the depicted passive margin model, even though these are common features for many of them. For this reason, geologists are trying to decipher why this occurs and what Norway and other passive margins with similar characteristics have in common.

The present study is a piece of the puzzle to understand how the post-Caledonian events and processes have shaped the present-day landscape of southern Norway. The high topography that characterizes the southern region of Norway is the product of a complex tectonic history difficult to unravel. Post-Caledonian events are not entirely understood, to a large degree due to the lack of post-Devonian sedimentary onshore record.

Devonian denudation and Permo - Triassic rifting are rather well documented by fission track data and other thermochronological methods (e.g. Dunlap & Fossen, 1998; Ksienzyk et al., 2014; Rohrman et al., 1995). Upper Mesozoic and Cenozoic exhumation cycles seem to be affected by several interacting factors that need to be addressed carefully. Numerous geologists have addressed this problem through stratigraphic, seismic, paleomagnetic and thermochronological methods. Two contrasting hypothesis emerged from various regional studies using fission track data, and have gained special attention during the last decades. The conventional model is also known as the “peneplanation and uplift” model (presented in (Rohrman et al., 1995). This postulates that the present-day elevation of southern Norway was created by active tectonic uplift in Cenozoic times after Mesozoic peneplanation. The newer model is known as the ICE (Isostasy - Climate - Erosion) hypothesis and came from the hand of Nielsen et al. (2009). The ICE hypothesis, on the contrary, sustains that peneplanation never took place and that present day elevation derives from Caledonian ancient topography.

Recent studies using paleomagnetic and thermochronological methods suggested that tectonic component influenced in topographic configuration (e.g. (Eide et al., 1997; Redfield et al.,

2004). According to some authors, the Lærdal-Gjende Fault System (LGFS) could have played an important role in topographic control in the central region of southern Norway (e.g. Andersen et al., 1999; Ksienzyk et al., 2014). Thus, in this region, repeated fault activity has potentially caused footwall exhumation and rejuvenation of the topography since Devonian times. The most recent reactivation events produced non-cohesive brittle fault-rocks exceptionally exposed in Lærdalsøyri (near to Lærdal).

The present study is part of the Earth System Modelling (ESM) project. It aims to investigate the relations between external and internal geodynamic processes in space and time, as well as the control mechanisms of topography reduction or formation in rift zones and passive margins. The Thermochronology group at University of Bergen focuses in the development of reactivated orogens that have grown into continental passive margins. In this line of investigation, the post-Caledonian exhumation history is studied through low-temperature thermochronology methods. The apatite fission track dating technique has been applied to samples collected from both the hanging and footwall blocks of the Lærdal-Gjende fault as part of this project. The present contribution also includes a structural analysis of the fault-rock products present in Lærdalsøyri.

1.1 Objectives

Along Sognefjord, significant geological features like the Lærdal-Gjende fault are exposed and can be easily studied. The Lærdal-Gjende fault can be traced continuously along 180 km from Aurlandsfjorden to Gudbrandsdalen (Lutro & Tveten, 1996). The field work of the present study has been conducted in one of its most spectacular exposures, located at Lærdalsøyri. Previous structural, paleomagnetic and isotopic analysis have been made at the Lærdalsøyri outcrop, whereas low-temperature thermochronology methods have not been applied in much extend before.

The purpose of the present study is to constrain the exhumation history of the Lærdal-Gjende fault and to identify the associated fault-rocks present at Lærdalsøyri outcrop. Specially, I aim to provide detailed structural and petrographic descriptions of the fault-rocks at meso and microscopic scale. The results may cover in greater detail than prior studies the structural aspects observed at Lærdalsøyri outcrop and give new insights into the development of large fault zones. The fission track results intend to exhumation pattern of the Lærdal-Gjende fault, as well as to determine which role has taken in the topographic development of the Caledonian hinterland (inner southern Norway). Other fault systems in the west coast of Norway were proven to show significant offsets across crustal blocks. Whether that is a particular characteristic for the west of Norway or a spread phenomenon throughout southern Norway remains unanswered. With the present study, I will contribute to that research.

Specific goals pursued within this thesis are listed below:

1. To constrain the cooling histories of footwall and hanging wall blocks of the Lærdal-Gjende fault and identify periods of accelerated cooling.
2. To document the different generations of fault-rocks and overprinting structures observed in the Lærdalsøyri outcrop, including the footwall mylonites and the brittle fault-rocks of the hangingwall.
3. To bind structural and thermochronological data together.
4. To establish the displacement along the Lærdal-Gjende fault and its relation with footwall unroofing in the Lærdal basement window.
5. To appraise the consistency between the results obtained in this thesis and the models of Norwegian landscape evolution (ICE hypothesis, "peneplanation and uplift" and "crustal taper" models).

Summarizing, the main purpose is to shed some light on the debate concerning the landscape development of central southern Norway.

1.2 Location of the study area

The Lærdal-Gjende fault crops out cutting the Lærdalsfjord from SW to NE. The study area is located at the southern side of the Lærdalsfjord (Fig. 1.1). The main outcrop (Fig. 1.2) is located at the eastern opening of the Raudbergstunnel, following the old road to Aurdaland from the ferry quay at Revnes (Fig. 1.1c). The topography of the southern flank of the fjord arm elevates up to 1600 meters from sea-level. The petrographical and fault-rocks descriptions are focused on this outcrop. The location of the samples collected from both the hanging and the footwall blocks is depicted in Fig. 6.1 and further information is provided in Chapter 6.

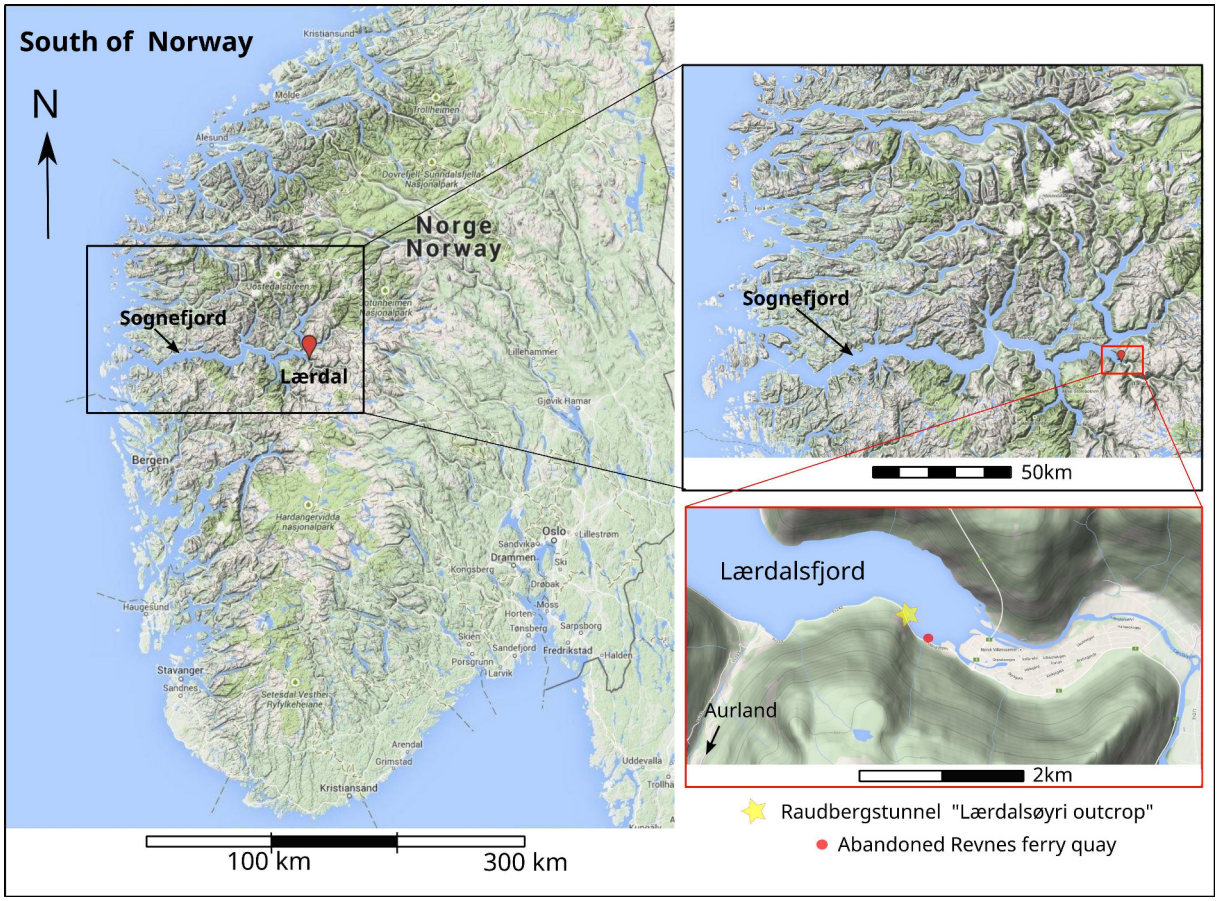

Fig. 1.1: Location in Norway of Lærdal (a), Sognefjord (b) and the detail of Lærdalsøyri and Lærdalsfjorden arm of Sognefjord. The star indicates the main outcrop next to the Raudbergstunnelen.

Fig. 1.2: Exposure of the Lærdal-Gjende fault in the "Lærdalsøyri outcrop" at the opening of the Raudbergtunnel. This spot is pin pointed in figure 1. In the picture is possible to appreciate the fault gouges, hangingwall and footwall cataclasite and the current fault plane.

2 Geological evolution of southern Norway

2.1 Precambrian history

Rodinia is believed to be one of the major supercontinents on geological history of Earth before Pangea, the name Rodinia was given in the 1990 (Torsvik, 2003) and means "the Motherland". Rodinia supercontinent was formed around 1300 to 1000 myr, evidenced in different parts of the world by mountain belts of this age with similar characteristics. The break up of Rodinia was progressive rather than simultaneous. The first break up occurred 700 mya, when the Australia - East Antartica rifted off Laurentia. Whereas, Laurentia and Baltica rifted apart in later times around 600 to 550 Ma together with Amazonia (Torsvik, 2003). The break up between Baltica and Laurentia constituted to the formation of Iapetus Ocean, also known as the Proto-Atlantic. The closing of this ocean started around 50 myr later with the Caledonian cycle and eventually both continents (Baltica and Laurentia) collided forming the Caledonian mountain belts.

The Baltic Shield (or Fennoscandian Shield) in southern Norway is product of successive accretions, magmatism and collision among continents. The Gothian orogeny (750 to 1500 mya) caused major crustal accretion and metamorphism from north to south forming most of the Baltic Shield. The Svenconorwegian orogeny (1,14 to 0,90 Ga) was not caracterized by the amount of accretion, although it overprinted Gothian granites and gneisses (Gaál & Gorbatschev, 1987). The Baltic Shield forms the Scandes foreland; some parts of southern Norway, Sweden and Finland, and Kola peninsula (Russia). The later, exhibit rocks of Archean age. The Baltic Shield is the basement of the Caledonian orogeny and has been deformed during the Caledonian (locally) and Svenconorwegian orogenies.

2.2 Insight to the Caledonian Orogeny

The Caledonian orogeny started by the collision between the continents Baltica and Laurentia, or Norway-Greenland and North America respectively during Silurian times (420 Ma) (Fig. 2.1). The collision between the two continents was leaded by the closure of the Iapetus Ocean.

The Iapetus Ocean's closure began with the subducction of the oceanic crust in Ordovician times (480 Ma) (Torsvik & Cocks, 2014). The subduction of Laurentia's slab under the Iapetus ocean-floor caused the formation of an early volcanic island arc in Laurentia's oceanic floor. Simultaneously, the island arc in the Baltic side collided with Baltica's continental margin. This

very first collision formed the eclogites from the Seve Nappes ca. 470 mya. Laurentia's continental margin collided with the early volcanic arc (ca. 440 Ma) and this was thrusted onto Laurentia's land. By this time, Iapetus ocean-floor subducted underneath Laurentia's oceanic crust, leading to the formation of a new row of volcanic islands and the generation of a back-arc basin behind them. The back-arc basin between Laurentia and the new row of volcanic islands evolved up to the generation of new ocean floor. The sea floor-spreading in the back-arc basin continued concurrently to the closure of the Iapetus Ocean. However, the sea floor-spreading could not counteract the tectonic compression and the complete closure of the ocean and collision between Baltica and Laurentia occurred approximately 420 to 410 mya, forming eclogite-bearing rocks in the Western Gneiss Region (Griffin et al., 1985). The Western Gneiss Region corresponds to the west Baltic Shield that reached the deepest parts of the upper mantle during subduction. This continent-continent collision is also known as the Scandian phase of contraction of the Caledonian orogeny. Therefore, the Scandian contraction prompted SE-directed transport of the tectonostratigraphic units or nappes (Andersen, 1998).

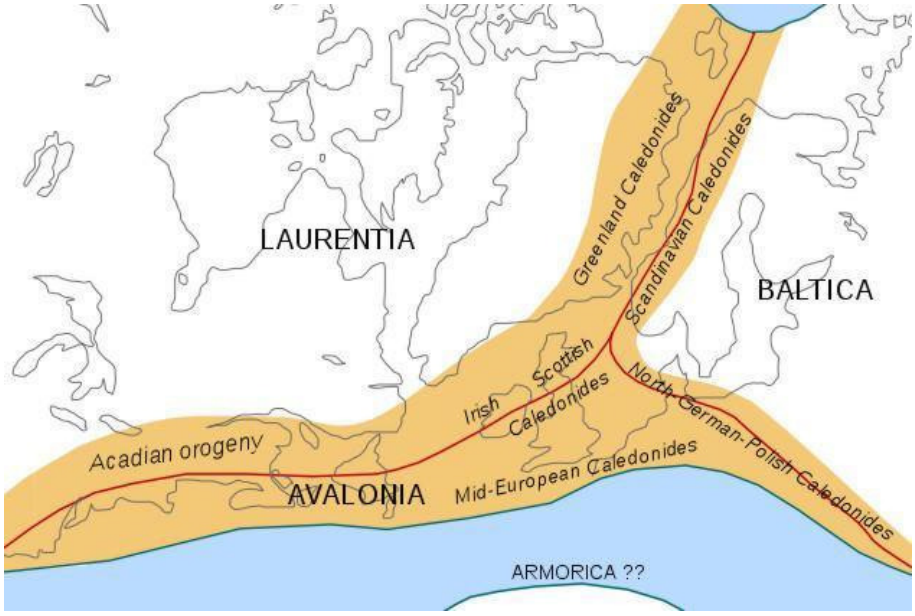

Fig. 2.1: Situation of the involved plates in the Caledonian orogeny by the time of the continent-continent collision passed (Silurian- Early Devonian times). Fig. extracted from Wikepedia, author: Woudloper.

The Caledonian tectonostratigraphic setting was configured during this complex oceanic closure process (Fig. 2.2). The compressional regime caused the thrusting of Iapetus oceanic crust, island arcs, Balticas terrain and Precambrian basement sheets, which piled up onto each other. The Proterozoic basement or Baltic Shield is considered autochthonous and not affected by the Caledonian orogeny, except for the uppermost portions of the basement (Fossen & Hurich, 2005). The sediments overlying the Baltic Shield date from Ordovician and Proterozoic times and became the phyllites and michaschists that acted as décollement levels during the orogeny. The structure of the Caledonian orogenic wedge (thrust nappes) can be divided into four main groups: Lower, Middle, Upper and Uppermost Allochton nappe series. The Lower Allochthon

correspond to detached sheets from the Baltic Shield that may have experience transport in order of tens of kilometers, whereas the Middle Allochton nappes have been transported hundreds kilometers distance and are composed by continental rock facies of Proterozoic age from Baltica's margin. Onto them, the Upper and Uppermost Allochton nappes were placed on top of the pile stack and correspond to units with the larger amount displacement. These two last nappes encompasses oceanic (island-arc complexes) and continental rocks from Laurentia prior to the closure of Iapetus, and ophilites from Ordovician-Silurian age. They can be referred also as exotic terranes when referring to ophiolites or island arc rocks.

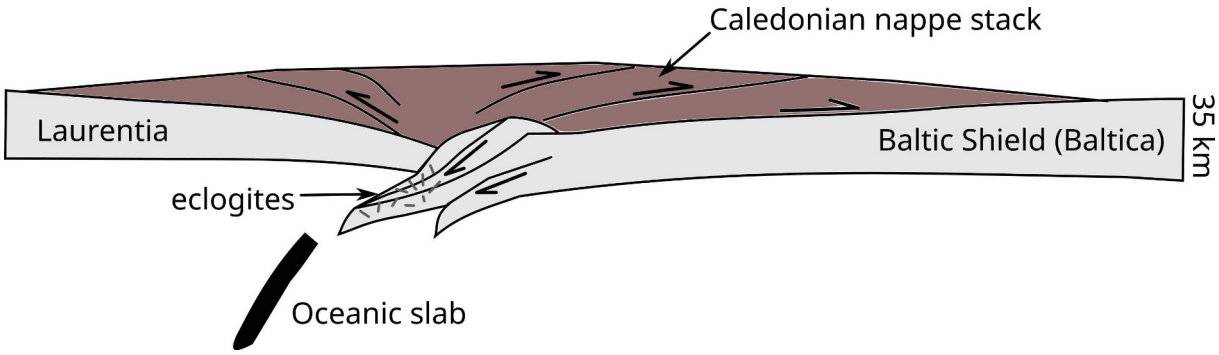

Fig. 2.2: Schematic cross-section across Baltica and Laurentia at the time of collision. Modified from Fossen (1992).

Eclogites are found in the west coast of Norway, which evidences that granulite facies conditions occurred during the Caledonian orogeny (Fig. 2.2). The metamorphosed basement in the onshore west coast is also referred as to Western Gneiss Region (WGR) and dips towards the NW. Contrary to hinterland basement, foreland basement remains undeformed and flat (Fossen & Rykkelid, 1992).

2.3 Extensional tectonics post-Caledonian orogeny in southern Norway

The denudation of Norwegian Caledonides was a long term multi-phase process that started in the Devonian and continued during Mesozoic and Cenozoic times. Paleozoic and early Early Mesozoic denudation stages are well documented through structural evidences and thermochronological analysis. On the other hand, late Late Mesozoic and Cenozoic denudation processes are still under review owing to constrains of thermochronological methods and the lack of onshore sedimentary record. In spite of the denudation, some authors consider that the topography of Caledonian hinterland remained positive along the Paleozoic and the Mesozoic, yet to be discussed.

2.3.1 Devonian extension and crustal collapse

The Devonian extension and orogenic collapse occurred right after the formation of the Caledonides and was one of the most important processes of denudation. The Devonian extension

was initially documented through stratigraphic methods (basin sedimentary record) in southwestern Norway and later on, geologists focused more in structural-kinematic imprints over the Caledonian orogeny (Fossen & Rykkelid, 1992). The Devonian extension is divided in three stages: Mode I, Mode II and Mode III.

2.3.1.1 Mode I of Extension

The Mode I of extension corresponds to the reversal of the shear sense along the basal thrust zone in middle Early Devonian times (Fig. 2.3), just after the decrease of convergence rate due to the delamination of the orogenic subduction slab (Rohrman et al., 1995). Change in convergence rate and delamination of the lower plate are both valid hypothesis that suits with the sudden change from convergence to extension of the Caledonides. Mode I extension is also referred to as "the backsliding". Fossen & Dunlap (1998) postulated that rapid change between contractional and extensional should have occurred between 408 and 402 Ma. The same authors together with Chauvet & Dallmeyer (1992) and Beck et al. (1995) obtained ages of 402 to 394 Ma for onshore eastern rocks. These authors related this age interval to Mode I deformation, which match high temperature conditions. Nonetheless, the Caledonian thrusting could have taken place contemporaneously to the gravity driven collapse in hinterland (Andersen et al., 1999; Fossen & Dunlap, 1998) within the time interval from 415 to 408 Ma.

Mode I of post-orogenic extension dates of approx. 400 Ma simultaneous to hinterland exhumation of the décollement zone (Dunlap & Fossen, 1998). During this early stage of extension, the orogenic nappe pile backslided towards hinterland (top-to-the-WNW). This was probably triggered by the exhumation of the hinterland décollement, which would have rotated the inclination to NW of the basal thrust allowing the reactivation of the basal décollement (Fossen & Hurich, 2005). The decompression took place by non-rotational vertical shortening at eclogite to amphibolite-facies conditions (Andersen, 1998). Evidences of continental eduction are found within the Caledonian basal thrust (or décollement zone). The Caledonian décollement zone exposes northwest verging folds of millimeter- to kilometer-scale that overprint the SE-directed compression structures. Mylonitic fabrics overprint ESE-directed structures in exposed areas of the décollement (Fossen & Hurich, 2005; Fossen & Rykkelid, 1992). These structures have been documented by some authors, such as Fossen (1992, 1993) and Fossen & Dunlap (1999) among others, although the pioneers were Kvale (1960), who first documented NW-directed structures. S−C fabrics, shear bands, asymmetric boudins, cleavages and asymmetric folds verging northwest overprinting compression top-to-the-ESE directed structures have been reported from hinterland to foreland (Fossen, 1992, 1993). Fossen & Holst (1995) estimated that the vertical thinning decreases towards the foreland and range from 9 to 35 km. Eduction, thus, is evidenced by top-to-the-WNW kinematic indicators in low-angle extensional shear zone that during the orogen acted as the basal thrust zone. The backslide displacement has been appraised to be 30 to 20 km through the offset of basement-cover contact in Ofoten shear zone (Fossen & Rykkelid, 1992).

2.3.1.2 Mode II of Extension

The Mode II of extension was the result of continued extension affecting basement and orogenic wedge (Fossen, 1992). This denudation phase corresponds to the beginning of the crustal collapse (Fossen & Hurich, 2005) provoked by the loss of crustal lateral support caused by the reversal of shear. In consequence, major counter-clockwise directed shear zones developed after and meanwhile the extensional reactivation of the basal thrust décollement. The denudation provoked by the rapid uplift of eclogite-bearing rocks of the Western Gneiss Region triggered the formation of greenschist facies rocks in the orogenic wedge. Most of the rocks from the Baltic Shield, nevertheless, remained almost constantly in the same crustal level, preventing from radical metamorphic changes in the upper plate (Fossen & Rykkelid, 1992). The dating in western Norwegian rocks of the late Mode II is constrained between 402 to 394 Ma through K-feldspar thermochronology. The temperatures in western Norway during Mode II denudation was higher than in the eastern part of Norway (Fossen & Dallmeyer, 1998; Fossen & Dunlap, 1998).

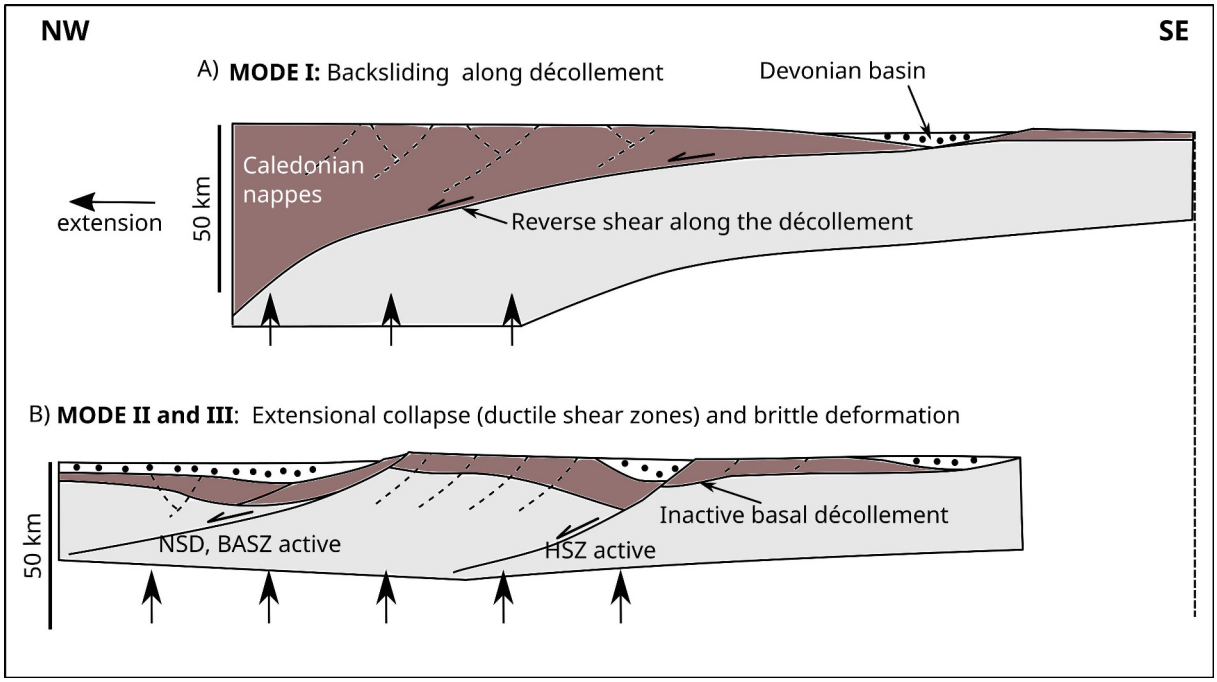

Fig. 2.3: Modes I and II of Devonian extension. A) Mode I: Backslidding of the Caledonian nappes along the phyllitic décollement levels (Early Devonian). NW directed transport. B) Mode II and III: NW dipping ductile shear zones develop (Mode II), followed by brittle normal sense faults affecting the cooled crust (Mode III). NSD: Nordfjord-Sogn Detachment; BASZ: Bergen Arcs Shear Zone; HSZ: Hardangerfjord Shear Zone. Modified after Dunlap & Fossen (1998).

As mentioned above, thick shear zones were developed in relation to the décollement exhumation in hinterland (Fossen & Hurich, 2005). Andersen (1998) associated the large-scale extensional shear zones to the rotational deformation occurred after decompression and cooling from amphibolite to greenschist facies conditions. Mode II deformation suits with a pure shear strain model, rather than simple shear strain model applied for Mode I extension (Fossen & Hurich, 2005). In the western and central southern Norway, W-NW dipping extensional shear

zones were formed across the orogenic nappes and rooted in Caledonian basement (Fossen & Hurich, 2005; Fossen & Rykkelid, 1992). The basal décollement separating basement from orogenic wedge was tilted with SE inclination (Fossen & Hurich, 2005). Subsequently, the backsliding of allochthonous nappes faded out. The ductile fabrics included WNW verging folds, S−C structures (shear bands) and large offsets with higher dipping angle than Mode I basal thrust detachment reactivation. The shear zones formation implicated (para)autochthonous units of the basement (Fossen & Rykkelid, 1992). The largest décollemnent zone is the Nordfjord-Sogn detachment zone (NSDZ). The NSDZ has 5 kilometer thick mylonitic fabrics that represent 100 to 50 km displacement based on the shear strain excess for mylonites formation as reported by Fossen & Hurich (2005). Fossen & Hurich (2005) also speculated a displacement of 50 km if the mylonites were reworked from Caledonian times. Otherwise, fresh extensional mylonites would have implied 100 km displacement (Norton, 1986). The NSDZ separates hanging-wall allochthonous lithologies from eclogite-bearing WGR basement (Norton, 1986). The continued deformation along the NSDZ after the backsliding provoked brittle deformation in the décollement zone overprinting the ductile fabrics (Fossen & Rykkelid, 1992). Devonian basins developed owing to the prolonged brittle deformation during Middle Devonian. Gabrielsen et al. (2010) mentioned the eastward migration of the topographic maximum provoked by the collapse of the footwall of master faults, whose activity was centered in Nordfjord detachment zone. The maximum topographic relief was not delimited to the suture. Instead, it had moved eastwards, away from the coast, according to Gabrielsen et al. (2010).

The Hardangerfjord Shear Zone cuts through the easternmost transect of the Baltic Shield and extends up to southern central Norway. This shear zone forms the Faultensgraben zone synformal-monoclinal structure that separate the orogenic wedge from the Western Gneiss Region. The offset has been calculated to be 2 kilometers or more by Fossen (1992). The HSZ is a major shear fault splay from the Nordfjord-Sogn detachment. On other locations, the displacement varies, like documented by Fossen & Rykkelid (1992) who estimated hundreds of meters displacement along the Ofoten region, the Rombak window.

2.3.1.3 Mode III of Extension

The Mode III of extension is characterized by high angle faults formation with more brittle elements than ductile in late Early Devonian to early Middle Devonian times (Fig. 2.3).

Brittle-ductile cohesive fault rocks exist within faults from this period and show same stretching direction NW-SE as previously and subsequent sub-vertical shortening (Fossen & Hurich, 2005). The entrance into the brittle regime was not uniform in the central southern Norway. On the contrary, Fossen & Hurich (2005) suggested that Mode II extension may had been active in the NW of southern Norway while Mode III started in the SE. Nevertheless, this progressive transition from Mode II to III throughout southern Norway was most likely fast due to the rapid

cooling. The rapid cooling of the crust was, concurrently, a consequence of the thinning of the orogenic roots and the shallowing of the crust. The uplift leaded to the generation of pure brittle faults. Some of them show listric morphology and control the subsidence of Devonian basins.

NE-SW trending brittle-ductiles faults with cohesive breccia and mylonite facies were developed. Lærdal-Gjende fault system is one of the larger developed faults within Mode III extension. According to Fossen & Hurich (2005), the Lærdal-Gjende fault is a late upper crustal expression of the HSZ that cross-cuts the central south of Norway affecting para-autochthonous basement, the Jotun Nappe Complex and other Middle Allochthon nappes.

2.3.1.4 Summary of the events from Caledonian orogeny to Late Devonian

Summarizing, the closing of Iapetus followed by delamination of eclogites at the base of the orogenic subduction slab was followed by the Devonian extensional collapse (Rohrman et al., 1995). The Caledonian nappe pile, thus, dismantled through the basal phyllitic detachments levels of the Caledonian orogen by the back-slidding of the nappes (NW directed movement). The nappes dipped down up into granulite metamorphic conditions. The large roots and dipping of the Caledonina nappes into high temperature conditions caused the loss of lateral support of the Caledonian mountain range. This was followed by a thinning of the root, which provoked the raise in thermal gradient. The high temperatures built up the conditions for ductile deformation and in concert with a continuance of extension, originated major ductile extensional shear zones NE-SW oriented with sinistral strike-slip component. The brittle deformation took over resulting from the rapid shallowing of the dissected pile. Coesite an micro-diamonds are evidences of the rapid uplift that switched from ductile to brittle regimes. Separately, intra-mountain Devonian basins were formed during the orogeny and developed big course-grain fluvial systems and alluvial and avalanche fans. The sedimentary record goes from lacustre to transition facies. The fine lacustre sediments are located in the bottom of the basins. The boundary of the basins are listric faults and steep normal faults that controlled the subsidence.

2.4 Late Devonian and Carboniferous tectonic quiescence

Dunlap & Fossen (1998) reported tectonic and thermal stability for the time interval between 380 to 330 Ma in the central southern Norway. In their study, they analyzed 7 K-felspar-bearing samples of a E-W, 250 km long traverse through the $^{40}Ar/^{39}Ar$ method. The lack of methamorphism and any other significant alteration or deformation within this time interval suggest tectonic and thermal stability. Dunlap & Fossen (1998) speculate the possible lanscape scenarios during this stable period, where mainland could have been either (1) rising up to 1 to 1,5 km high above sea level as a result of an over-thickened residual crust, or (2) deeply eroded Caledonian underthickened crust relative to mantle lithosphere. Dunlap & Fossen (1998) are inclined to the first approach in which the topography was maintained up to 300 myr (beginning of Permian times).

Nevertheless, Andersen (1998) do not concur and suggested that extensional collapse leaded to extreme crustal thinning and to exhumation of high-pressure rocks. According to Gabrielsen et al. (2010), in the late or mid Carboniferous, the elevation of the former Caledonides was reduced drastically and fault activity had already ceased in western Norway since Early Carboniferous. Therefore, Gabrielsen and co-workers suggest that surface processes controlled over the Norwegian landscape in Carboniferous times. Gabrielsen et al. (2010) suggested a relation between mature sediment basin infill and peneplanation of the orogen. Yet, in prior studies, Fossen (1992) maintained that the orogenic collapse did not completely reduced the Caledonian topography, and thus, the residual Caledonian crust was over-thickened even after the Devonian extension. In the Jotun Nappe and in the Bergen area, alkali feldspar-bearing rocks give temperatures of 200 to 350 °C from Middle Devonian until Permo-Carboniferous times (Dunlap & Fossen, 1998). This temeperature range concur with Fossen (1992) approach that Caledonian topography was not entirely destroyed after orogenic collapse. Eide et al. (1999) analyzed the transect through the Nordfjord-Sogn detachament zone by $^{40}Ar/^{39}Ar$ methods and concluded that slow cooling from 340 Ma (Early Carboniferous) occurred until the late Carboniferous to beginning of Permian, without involving any significant tectonic event since late Devonian until the Permo-Carboniferous boundary. However, Eide et al. (1999) underlined a rapid cooling episode manifested within Early Carboniferous that may possibly relate to underplating. This thermal mechanism could have provoked increased topography and accelerated denudation rates. In western Norway, Smethurst et al. (1998) and Osmundsen et al. (1998) suggested that mid-Devonian to earliest Carboniferous age large-scale folding affected the entire crust in western Norway. The folding episode may be linked to orogen-parallel sinistral transtension (Chauvet & Séranne, 1994).

2.5 Late Carboniferous and Permo-Triassic North Sea rifting

The break up of the supercontinent Pangea after tectonic quiescence and relatively thermal stability continued until Triassic times with the North Sea rifting. According to Gabrielsen et al. (2010), the rifting episode arrived to the northern North Sea during Permian times, whereas the main E-W stretching began actually during Carboniferous times and extended up to the Triassic for southern and central North Sea, evidenced by widespread volcanism in NW Europe. The extension continued after thermal subsidence throughout Permian times, causing large half-graben systems, followed by thermal relaxation (Gabrielsen et al., 1990). In onshore southern Norway, large faults striking N-S were also formed during the Permian and rotated after the thermal relaxation period (Gabrielsen et al., 2010). Great erosion from the hanging-walls is implied as the elastic response of these crustal blocks must have been of large-scale. The faults formed by the Permo-Triassic boundary acted along with the Nordfjord-Sogn detachment zone, Lærdal-Gjende fault system and Hardangerfjord Shear Zone. Fault activity followed by footwall uplift in mainland Norway may have caused greater reliefs in Late Permian compared to Carboniferous times, involving a eastward migration of the topographic maximum (Gabrielsen et al., 2010).

Dunlap & Fossen (1998) interpreted diachronous but uniform exhumation with maximum temperatures up to 200 to 300 °C (starting in eastern Norway) during the Permian (300 to 250 Ma) across the 250 km long, E-W transect of Norway. They linked the Permo-Carboniferous exhumation to the Oslo Graben, North Sea rifting, lowering of the base level and increase in rate of erosional downcutting (0,15 mm/yr.). Therefore, the onset of North Sea rifting is predicted to be earlier in Permo-Carboniferous by Dunlap & Fossen (1998) in contradiction with other authors (e.g. (Rohrman et al., 1995)), whose estimates date from Permo-Triassic or Triassic times for offshore sediments coming from Norwegian mainland. The vast accommodation space needed to host the thick deposits in the North Sea may have, thus, appeared with the onset of rifting in Permo-Carboniferous times. The Permo - Carboniferous exhumation, evidenced by the K-feldspar bearing rocks across the E-W transect of onshore Norway, indicates the erosion of 3 ± 1 km of southern Norwegian crust assuming 20 °C/km and a total of 80 °C of cooling (Dunlap & Fossen, 1998). The erosion was accommodated by isostatic rebound so that the Norwegian crust was still above sea level. Dunlap & Fossen (1998) concluded that present aerially exposed crust dropped to apatite fission track temperatures after 250 Ma (Early Triassic).

2.6 Early and Late Jurassic North Atlantic rifting

Early Jurassic times(180 to 200 myr) are linked to the beginning of the domal uplift in onshore Norway, which affected strongly to southern central Norway according to fission track and $^{U-Th}/_{He}$) analysis (Rohrman et al., 1995). In Triassic and Jurassic times, the Caledonian basement was exposed on the surface, previously cooled from 220 °C in Permian times (Dunlap & Fossen, 1998). The North Atlantic rifting occurred around Early to Late Jurassic times. The rifting affected all northwestern Europe creating a triple rift system that included southern Norway and the British Isles (Doré et al., 1999). Gabrielsen et al. (2010) and other authors (Eide et al., 1997; Ksienzyk, 2012; Torsvik et al., 1992) linked onshore fault reactivation during the Late Jurassic to rift shoulder uplift. Supporting Gabrielsen et al. (2010), Ksienzyk et al. (2014) reported higher cooling rates in coastal samples than inland samples throughout Jurassic and Cretaceous times, which suggests rift flank uplift occurred within western Norway controlled mainly by fault activity.

The maximum subsidence of the North Sea was not reached in the latest Jurassic (Gabrielsen et al., 2010). The northern North Sea extension was oriented NW-SE and produced NE-SW striking faults, which interfered with relict structures from the Permo-Triassic (or Permo-Carboniferous) E-W rifting (Ter Voorde et al., 1997). Clastic sedimentary record and progradating clinoforms from major feeder systems, namely today as Nordfjord, Sognefjord and Hardangerfjord, indicate that western Norway rejuvenated its topography as consequence of the uplift. The topography of the late Jurassic was formed by up-rotated crest of fault blocks parallel to the graben axis (Gabrielsen et al., 2010). These crests were generating a relief that was eroded in most cases, as in Skagerrak area where the Triassic- Late Jurassic sequence is missing under the mid-Cretaceous

deposits (Gabrielsen et al., 2010). This evidences that at some point they were emerged as consequence of uplift in Late Jurassic.

The complicated onshore exhumation history appraised from thermochronologic analysis seems to represent shoulder or rift flank uplift derived from the North Atlantic rifting. Fossen et al. (1997) reported Jurassic immature sediments in the Bergen Arcs area supporting the hypothesis that a rapid cooling episode near shore occurred due to Jurassic fault activity (Eide et al., 1997; Gabrielsen et al., 2010; Ksienzyk, 2012; Torsvik et al., 1992). The Jurassic rifting episode had more localized mainly on the rift branches of the Viking Graben in the north and central graben and the Moray Firth Basin in the south (Doré et al., 1999).

2.7 Cretaceous and Cenozoic tectonism

The Cretaceous - Jurassic transition brought the maximum extension followed by thermal cooling. The thermal cooling triggered rapid subsidence, evidenced by the stratigraphic record, which indicates a water depth of about 500m in Early Cretaceous. During the Early Cretaceous, thus, the crest of rotated blocks were submerged again (Gabrielsen et al., 2010).

By the end of the Cretaceous, peneplanation was taking place and the "paleic surfaces" were originated according to Rohrman et al. (1995). The AFT modelling made by Rohrman et al. and co-workers (1995) suggest a slow cooling (geothermal gradients dropped from 30 to 20 °C/km). Thus, they linked peneplanation to this stable period.

A tectono-thermal uplift of southern central Norway was initiated during Paleocene to Eocene times. Its origin is associated to the Paleogene Icelandic plume, which was triggered after the North Atlantic oceanic opening (Gabrielsen et al., 2010). The tectono-thermal uplift, according to the estimates of Gabrielsen et al. (2010), increased the gradient (0,2°) of the eastern flank of south Norway. Previously, subsidence in the northern North Sea was taking place and was being fed from the Scottish highlands, East Shetland platform and Norwegian mainland until its leveling and shallowing in Eocene times (Gabrielsen et al., 2010). In the Late Eocene to Late Miocene, the shallowing of the North Sea increased with the global sea-level fall and the tectono-thermal effects whose origins are mentioned before (Gabrielsen et al., 2010).

The Neogene uplift is not easily recognized through thermochronological methods, although its effects are somehow evidenced. The mechanism or trigger is still not fully understood, however many authors maintain that is due to tectonic processes combined with post-glacial effects. Rohrman et al. (1995) does not link the Neogene uplift (30 Ma, as suggested by AFT modeling) to post-glacial effects. These authors suggest that Neogene uplift is a continuation of the Oligocene uplift, which implies that is tectonically-driven. Stratigraphic features probe the occurrence of the Neogene uplift by diverse reasons: (1) the tilting of the Upper Pliocene and older sequences

away from mainland, (2) Pleistocene sediments are lying flat above the Plio-Pleistonce unconformity, (3) the central North Sea has less angular unconformity than close to mainland and (4) basins adjacent to uplifted terrains record accelerated subsidence (Gabrielsen et al., 2010).

2.8 Recent tectonism in Southwestern Norway

Earthquakes in Southern and Western Norway have not ceased since the Cenozoic. NORSAR independent research foundation records indicate intraplate seismic activity mainly along the western side of Norway and in the Norwegian shelf (Fig. 2.4). NORSAR remarks that the primary source of present seismicity is not ensued to deglaciation, but it rather attends to contemporary geologic processes. Some authors have referred to this seismic activity as local (compressional and extensional) adjustments resulting from the North Atlantic mid-ocean ridge spreading (Hicks et al., 2000). Onshore normal fault reactivation and offshore reverse strike-slip reactivation indicate an overall stress field oriented WNW-ESE, according to Hicks et al. (2000). The same author also mentions that added stresses from postglacial rebound and lithospheric loading and unloading are provoking fault reactivation and thus, neotectonic seismicity. Helle et al. (2007), in their study of the shoreline displacement in Hardangjerfjorden, concluded that major shifts in height of the Younger Dryas shore levels are seen across faults of Devonian and Permo-Triassic origin. The same authors hypothesized that differential uplift rates in the hanging- and foot-walls may have resulted in postglacial displacements (2 to 4 m). This adds up with anomalous uplift rates registers acquired by levelling measurements along the same fault zones (Helle et al., 2007). Nonetheless, Helle et al. (2007) rather than to assert that these uplift rates are caused by a tectonic process, leave it open to discussion.

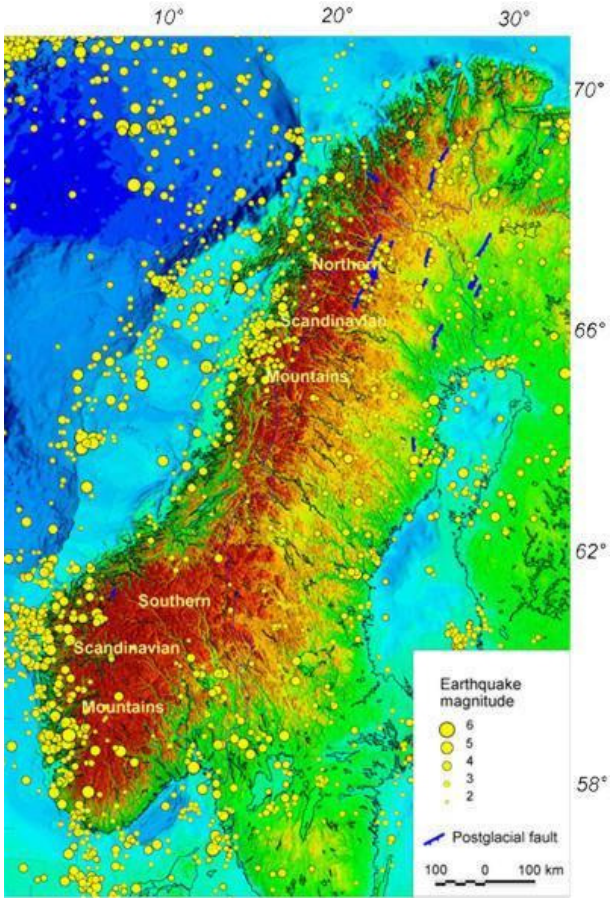

Fig. 2.4: Current seismicity map of different magnitude earthquakes in Norway. The Earthquake magnitude is indicated by the radius of the yellow circles. The maximum magnitude depicted is 6 in the Richter scale. Hipocenter depths are unknown. Maximum magnitude earthquakes occurrence is located along the Norwegian continental shelf. Major earthquakes events take place periodically around each 20 years. Image extracted from NORSAR independent research foundation.

2.9 Geological framework of the Lærdal-Gjende Fault

The Lærdal-Gjende fault is a major crustal lineament of brittle nature that runs through the central part of southern Norway (Caledonian foreland) (Fig. 2.5). It extends approximately from Rondane (northeast) to the southwest as the Hardangerfjord Shear Zone (HSZ). The Hardangerfjord Shear Zone represents kilometer-scale ductile deformation and it is rooted in the Fennoscandian basement. The Lærdal-Gjende fault (LGF) may have played a significant role in the exhumation pattern of central Norway. This is suggested by a complex history of Mesozoic and Cenozoic brittle reactivation.

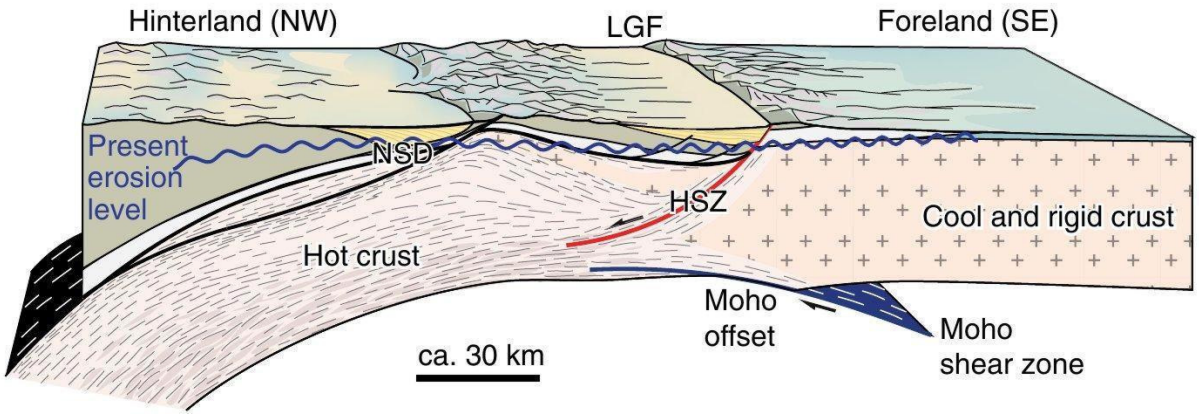

Fig. 2.5: Schematic structural setting in Devonian times showing the Hardangerfjord Shear Zone (HSZ) and the Lærdal-Gjende Fault (LGF). The Nordfjord-Sogn detachment (NSD) is a major crustal lineament located northwest of the Lærdal-Gjende Fault. The HSZ is rooted in Baltic Shield basement. Displacement along HSZ resulted in a vast fault zone of mylonites. Hinterland and foreland Caledonian sections are depicted in the sketch. The cool and rigid crust to the southeast is the (para-) autochthonous Baltic Shield. Whereas, the Fennoscandian basement in western Norway was metamorphosed during the Caledonian orogen, also referred as to the Western Gneiss Region. The western side of the WGR bears eclogites and coesite mineral preserved from the subduction. Fig. extracted from Fossen et al. (1994a).

2.9.1 Lithology and fault-rocks presents in the Lærdal-Gjende fault

The Lærdal-Gjende fault is spectacularly exposed in the study area at Lærdalsøyri. The contrast in hardness between the cataclasites of the hanging wall and the rocks of the footwall produces a steep escarpment. The Lærdal-Gjende fault is a low-angle (25 to 45°), northwest dipping fault that represents NW-directed down-throw movement (Milnes & Koestler, 1985; present study). The Lærdal-Gjende fault cross-cuts para-autochthonous basement, Proterozoic cover and allochthonous Caledonian nappes. At Lærdalsøyri, the migamtitic gneisses from the basement of the footwall are juxtaposed onto the Jotun nappe (hanging wall).

- **Fault-rocks in the Lærdal-Gjende fault**

Northeast of Lærdal, Andersen et al. (1999) collected field observations at the Årdalsvatn outcrop (Årdal). Andersen et al. and co-workers reported epidote veined proto-cataclasites to cataclasites with varying thicknesses in the Lærdal-Gjende fault. The cataclasis intensity in that location has a wide spectrum of deformation making possible to recognize undeformed syenitic

to monzonitic gneisses fault protoliths in the footwall. Felsic dykes intrude the gneisses in the Årdalsvatn outcrop. Fe-oxide staining in preserved alkali feldspar from igneous protoliths are reported within the mylonites at that location. In the hanging wall, Andersen et al. (1999) documented epidote- veined, green felspar (amazonite var. of microcline)-rich breccias to ultracataclasites above the current discrete fault plane. Brecciation in the hanging wall is still seen tens of meters above the discrete fault plane.

In the Lærdalsøyri outcrop, ca. 100 to 200 m of cataclastic rock sequences are in display affecting the Jotun nappe orthogneisses and the footwall extensional mylonites with less intensity (Lutro & Tveten, 1996; Milnes & Koestler, 1985). The cohesive breccias and cataclasites were reported to be reconsolidated with sencodary epidote and sericite (Milnes & Koestler, 1985). Both hanging wall and footwall blocks display a collection of joints and irregular fractures affecting intensely and un-deformed country rocks at all scales (Milnes & Koestler, 1985). Locally, the fractures are filled or partially filled with epidote mineral growth. Mylonites, ultramylonites and mylonitic gneisses are found within the thick mylonitic rock package (Andersen et al., 1999; present study). Post-Caledonian extensional mylonites and cohesive brittle fault rocks are cut by a 1-2 meters of incohesive fault gouge and breccia evidencing the multi-phase deformation (Andersen et al., 1999; present study). Fossen & Dallmeyer (1998) documented cohesive epidote-bearing cataclasites, cohesive microbreccia and epidote-filled structure in Lærdal.

- **Lithologies in the footwall and hanging wall blocks of the Lærdal-Gjende fault**

The area of study comprises Precambrian crystalline rocks in both fault blocks. The hanging wall rocks are from the Jotun Nappe, a Middle Allochthon Caledonian nappe. The footwall block represents a Parautochthon unit of Baltic Shield basement. In the study area, migmatitic gneisses from the basement are locally affected by mylonitization and by overprinting brittle deformation. The hanging wall rocks consist on massive and layered igneous basic rocks from the upper thrust nappe of the Jotun nappe complex: anorthosites and mangerites Fig. 2.6. The rocks from the hanging wall show signs of methamorphism into amphibolite to granulite conditions.

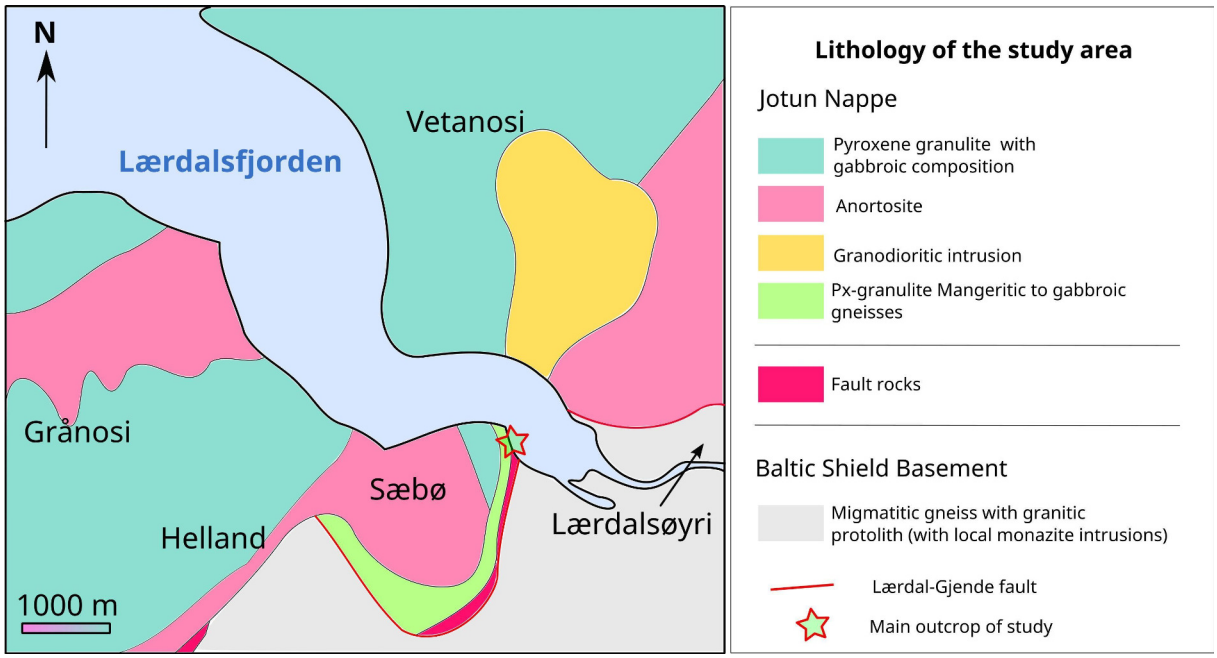

Fig. 2.6: Synthetic geological map of Lærdalsfjorden modified from the NGU 1:50000 online geological map. The Baltic Shield basement is located at the SE of the map and does not has major lithological changes. The rest of the colors, except for the fault rocks, correspond to different lithologies of the Jotun Nappe.

The Jotun Nappe/Complex corresponds to the Middle Allochthon of the Caledonian nappes. Priem et al. (1968) described it as a crystalline Precambrian nappe. The over-thrusting of this unit did not cause significant deformation according to Milnes & Koestler (1985). These authors suggested that the Jotun Complex corresponds to a 'far-traveled thrust sheet placed onto the margin of the Baltic Shield' composed by an old igneous-metamorphic complex. The Jotun nappe was part of a layered igneous complex formed by syenites, gabbros and ultramafic rocks that was metamorphosed into an "homogeneous pyroxene-granulite terrain". Pyroxene and syenitic gneisses, amphibolites and metagabbros cut by pegmatitic veins are currently forming the Jotun nappe. Anorthosites are also very prominent at some levels of the Jotun nappe.

Precambrian crystalline basement is exposed in the Lærdal and Fillefjell-Beito erosional windows, which are located at the southeast side of the Faltungsgraben (Fig. 2.7). Milnes & Koestler (1985) studied in detail the lithologies outcropping in the Fillefjell-Beito window, the smallest of the two. The basement lithologies at Fillefjell-Beito window are affected by high-grade metamorphism. Precambrian granitic gneisses, migmatitic gneisses, amphibolites, quartzites and hornblende- and garnet-schist crop out within it. The lithology present in the basement of the Lærdal window is comprised by mica-schists and migmatitic gneisses (Andersen et al., 1999). The basement present in Lærdal is heterogeneously deformed making possible to observe undeformed rocks. Along with the Fennoscandian basement there are cover deposits associated with strong deformation by thrusting and extension. The Valdres sparagmite and the Fortun phyllites are some of these strongly modified deposits (Milnes et al., 1997).

2.9.2 Structural framework

As mentioned previously, the Lærdal-Gjende fault (LGF) is the brittle continuation of the Hardangerfjord Shear Zone (HSZ) (Fig. 2.6). The latter is one of the major ductile extensional structures produced in Devonian times (Fossen & Hurich, 2005). The Hardangerfjord Shear Zone is typically described a to be the result of Mode II of extension (Milnes et al., 1997). The HSZ and the LGF are described as distinct faults with different width, length and depth of formation (Fossen & Hurich, 2005). The Lærdal-Gjende fault is connected by a hard-link to the Hardangerfjord Shear Zone, which dies out between Aurland and the Hardangerfjord (Fossen & Hurich, 2005). The ductile extensional lineament lays (i.e. The Hardangerfjord Shear Zone) in the transition from thick to thin-skinned Caledonian deformation and is parallel to the Caledonian orogenic belt (Fossen & Hurich, 2005).

The Hardangerfjord Shear Zone has a width 5 km thick of mylonitic fault-rocks and its throw estimates are 5 km. There are some mechanical problems regarding its thickness (width of the shear zone). That is the reason why some authors suggest that the HSZ was accommodated in a pre-existing Proterozoic shear zones or faults from the Svenconorwegian orogeny sitting on Svenconorwegian basement. The changes in trend and segmetation of the fault along the Sognefjord transect supports that hypothesis (Fossen & Hurich, 2005). Fossen & Rykkelid (1992) suggested that the HSZ occurred during the transition between Mode I and Mode II of extension. Kilometer to meter-scaled folding is very prominent in the hanging wall block of the HSZ next to the fault, which also suggest double shear during the formation of the HSZ (Fossen & Rykkelid, 1992). The formation of the HSZ should have been, thus, during Mode II or prior, when the Caledonian nappe pile was still backsliding.

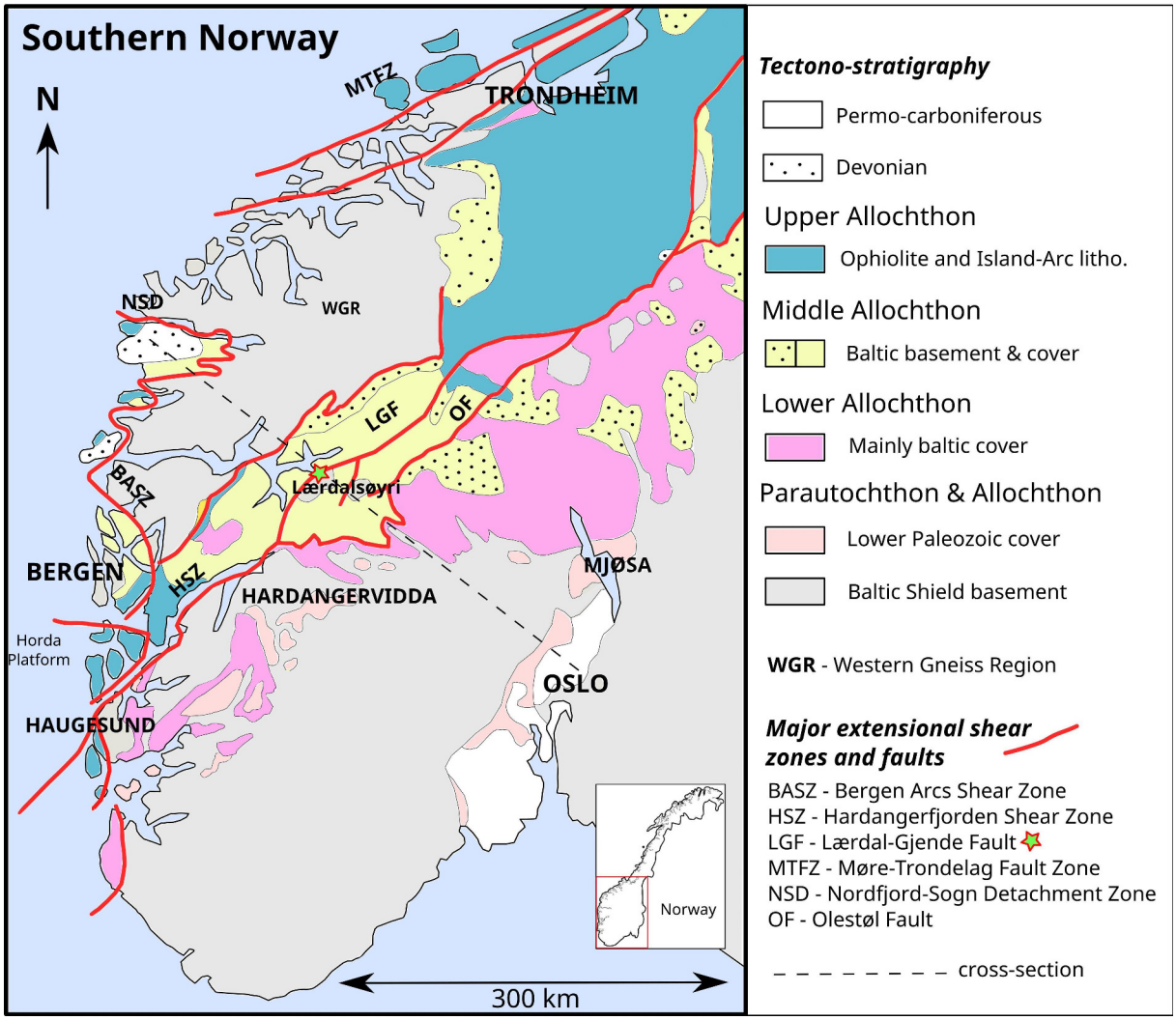

Fig. 2.7: Structural map showing the major extensional lineaments across southern Norway and the simplified tectono-stratigraphy displaying the Caledonian nappes and Fennoscandian basement. At the northwest of the map, the Fennoscandian basement is metamorphosed and contain eclogites (Western Gneiss Region) whereas, the southeastern segment is composed mainly by (para-)autochthon Baltic Shield. Lærdalsøyri, the main outcrop where the present study has been conducted, is marked on the map with a star. At this location the Fennoscandian basement is exposed in the Lærdal window (see cross-section in Fig. 2.2). Fig. based on Andersen et al. (1999), Fossen & Hurich (2005), and Ksienzyk et al. (2014).

The Hardangerfjord Shear Zone is characterized by folding and faulting overprinted by top-to-the-NW kinematic structures (Andersen, 1998). Consistent down-to-NW ductile fabrics such as microfolds, asymmetric boudins and S-C structures, have been reported from the décollement zone and the allochthonous units (Fossen et al., 1994b). S-C foliation exhibit an overprinting between Mode I and Mode II displacement structures in some locations (Fossen & Hurich, 2005). The formation of the HSZ produced many simultaneous NE-SW trending brittle faults as a response to deformation in shallower crustal levels.

The Lærdal-Gjende Fault System (LGFS) consists of a linked strand of faults trending NE-SW that form several relay ramp structures (Andersen et al., 1999). The LGFS is well developed in the Aurland-Årdal-Tyin area (Battey & McRitchie, 1973). The Lærdal-Gjende fault (LGF)

is one of the subsidiary faults that are comprehended within the Lærdal-Gjende Fault System (LGFS). Lutro & Tveten (1996) traced the fault strike for 180 km from Aulandsfjorden to Gudbrandsdalen in a continuos lineament. The Lærdal-Gjende fault has a significant throw characterized by down-to-the-west normal displacement. The vertical displacement accounts for 8 km. The easternmost boundary of the LGFS is limited by the Olestøl fault, which has relatively less throw than the Lærdal-Gjende fault (Andersen et al., 1999). Andersen (1998) and Gathe & Andersen (1996) concur that the wide span of fault-rocks observed in the LGF formed after several reactivation events.

The Lærdal Gjende Fault is characterized by a thick package of cohesive cataclastic rocks (previously described) affecting mainly the hanging wall block. These are cut by more recent incohesive fault rocks. In the footwall block, a package of mylonites ca. 200 meters thick exhibit consistent top-to-NW kinematic indicators (Milnes & Koestler, 1985).

The cohesive cataclasites of the Lærdal-Gjende fault formed at 10 km depth according to Fossen & Hurich (2005). The kinematic indicators are consistent with down-to-NW displacement, corresponding to the strain field of Devonian times, rather than with the Permian strain field (E-W). These facts and other thermochronological studies suggest that the cataclasites of the Lærdal-Gjende fault are product of Mode II Devonian extension. Milnes et al. (1997) also considered that the Lærdal-Gjende fault formed during Mode II of Devonian extension. The structural study carried out by Andersen et al. (1999) provided field observations that suggested sinistral strike-slip movement overprinting top-to-NW structures. The described structures were mainly fault-plane striations which were attributed to Permian reactivation (E-W stress field). The last reactivation episode of the LGF produced incohesive fault gouges which cross-cut the pre-existing ductile to semi-ductile fault-rocks.

The LGFS is separating the Baltic Shield basement from para-authochtonous, lower and middle allochtonous tectonostratigraphic units. As mentioned before, the migmatitic gneisses from the basement are exposed in erosional windows in the southeastern flank of the Faltungsgraben.

The Lærdal-Gjende fault is the youngest major structure within the 'Faltungsgraben' juxtaposing the Jotun nappe on the Baltic basement (Fig. 2.8). The structure referred as to "Faltungsgraben" forms a regional NE-trending synformal depression in central Norway. Goldschmidt (1912) was the first to define this large-scale synformal post-orogenic structure that transects the nappe stack in southern Norway. The eastern flank of the Faultungsgraben is where the Lærdal-Gjende fault transects the Jotun Nappe Complex and Lower Paleozoic cover. In both western and eastern flanks of the super-structure, top-to-NW(WNW) fabrics have been reported. Among these fabrics, there are consistent NW verging folds and top-to-NW (and to-W) kinematic indicators within semi-brittle and ductile fault zones (Andersen, 1998). Andersen (1998) pointed out

the overprinting character of the NW-directed structures over thrusting top-to-SE structures in several locations within the Faltungsgraben. The core of Faltungsgraben presents normal-sense, NE-SW trending faults of semi-ductile to brittle nature originated as a result of the Mode II of extension (Andersen, 1998).

Large-scale extensional faulting is related to footwall uplift (Jackson & McKenzie, 1983). Andersen et al. (1999) suggested footwall uplift along ductile Devonian shear zones as the main cause for the exhumation of Fennoscandian basement. The same reason can also be accounted for the existence of the different fault rocks generations in the LGFS, specifically the incohesive brittle fault rocks found in the Lærdal-Gjende and the Olestøl faults cores. Thus, the Lærdal-Gjende Fault System seem to be an important key in the development of basement culmination distribution and structural windows in south Norway.

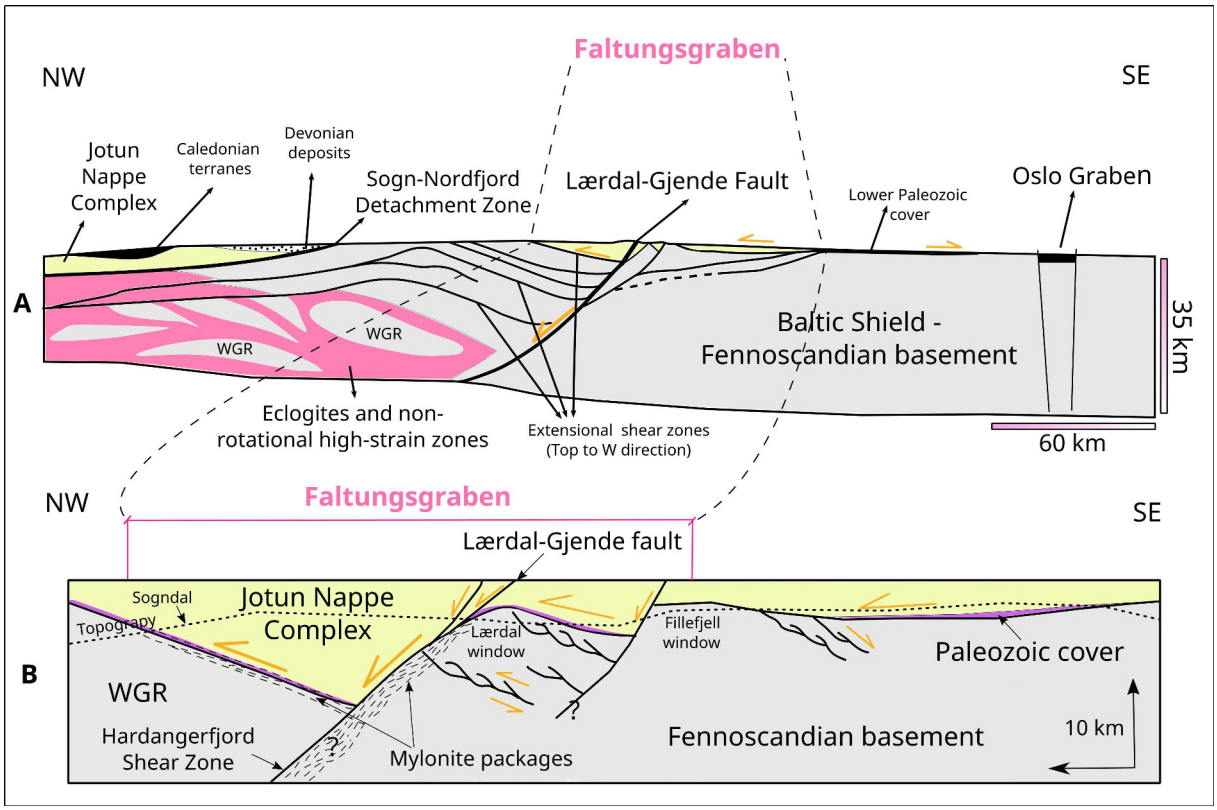

Fig. 2.8: The lower Paleozoic cover of the Fennoscandian basement is also defined as Valdres sparagmite with strong Caledonian overprinting (Milnes et al., 1997). A) Cross-section from Fig. 2.1. B) Detail of the Faltungsgraben synformal structure from the larger cross-section. Figs. Modified from Andersen (1998).

2.9.3 Thermochronological studies of the Lærdal-Gjende fault and other faults in Norway

The study of post-Caledonian brittle faults is important for determining the tectonic evolution of the Norwegian continental margin. For that reason, there are a handful of thermochronological and paleomagnetic analysis dedicated to western faults. The Lærdal-Gjende Fault System,

running in central southern Norway, is now acquiring more attention among geologists. The Lærdal-Gjende fault is the result of various reactivation periods throughout Mesozoic and Cenozoic times. Evidence for Mesozoic and Paleogene reactivation of the Lærdal-Gjende fault was recently reported by Ksienzyk (2012). Late reactivation movements are evidenced by an array of unconsolidated breccias and gouges along the discrete fault plane. Other faults along western Norway show a ceasing of activity in Cenozoic times.

The time of formation of the Lærdal-Gjende fault is resolved by thermochronological studies. $^{U}/_{Pb}$ dating of titanite from basement rocks in the west of Bergen (BASZ) gave an age of 396 Ma. Similar ages were found for $^{Rb}/_{Sr}$ isochrons on epidote and hydrothermally altered alkali-feldspar (Larsen et al., 2003), and also on mineral fractures of the LGFS (Schärer, 1980). The ages obtained in those studies range from 363-371 Ma to 367 Ma, respectively. Ksienzyk et al. (2014) tested two samples from the fault gouges of the Lærdal-Gjende fault through $^{K}/_{Ar}$ illite dating method. The $^{K}/_{Ar}$ illite results suggested multiple periods of fault reactivation in Early Carboniferous, Permian, late Triassic to early Jurassic and late Cretaceous to early Paleogene. $^{40}Ar/^{39}Ar$ dating for breccias within the Nordfjord-Sogn detachment zone in Atløy were tested by Eide et al. (1997). The ages obtained for those correspond to Permo-Triassic (260 to 248 Ma) and Late Jurassic to Early Cretaceous periods of fault activity. Permian and Late Jurassic to Early Cretaceous fault reactivation ages were also confirmed by paleomagnetic methods for the NSDZ and the LDFS (Andersen et al., 1999; Torsvik et al., 1992). Andersen et al. (1999) presented a collection of data for the breccias of the Lærdal-Gjende fault and the Olestøl fault (eastern boundary fault of the LGFS). Andersen et al. and co-workers suggested that southern central Norway was equally affected by the Mesozoic rifting episodes as the western side of Norway. Færseth Færseth and co-workers (1996) linked the fault activity of the Lærdal-Gjende Fault System to the reactivation of offshore and onshore segments of the Hardangerfjorden Shear Zone caused by Permo-Triassic and Jurassic rifting. In northern Norway, fault gouges from Troms and Vesterålen regions were analyzed through $^{K}/_{Ar}$ illite method (Davids et al., 2013). The collected samples dated from Carboniferous to Permian for the region of Troms. The Vesterålen region indicated fault activity from Carboniferous until Cretaceous times.

Late Jurassic fault activity in southwestern Norway was confirmed by Fossen et al. (1997), who discovered Jurassic sediments trapped in a fault zone near Bergen. The fault zone was disrupted by late brittle faults indicating that fault activity occurred at least until Late Jurassic times in this region.

Summarizing, the dismantlement of central Pangea produced numerous fault zones with signs of brecciation in western and central Norway. The inner parts of mainland Norway have not received as much attention as coastal areas due to the distance to the rifting axis. Nonetheless, there are proofs that southern inner Norway has also been influenced by the rifting events whatsoever. Jurassic breccias were found through paleomagnetic methods in Møre-Trøndelag Fault

Zone (southwestern Norway) and also within the Lærdal-Gjende Fault System (southern inner Norway). Thermochronological studies show several reactivation episodes within the LGFS. Andersen et al. (1999) linked them to Permo-Triassic and late Jurassic rifting events. Furthermore, offshore segments of HSZ show signs of reactivation during Permo-Triassic and Jurassic times, which might be connected to the fault activity in the LGFS in mainland Norway (Færseth, 1996). There are enough evidences to believe that fault activity affected first to western Norway and continued after in eastern regions (Caledonian foreland). Based on previous analysis of the Lærdal-Gjende fault, fission track reactivation ages are anticipated to date from the Triassic-Jurassic boundary and late Cretaceous - early Paleogene times. Incohesive fault-rocks of the Lærdal-Gjende fault exhibited at Lærdalsøyri are due to the most recent reactivation event(s) that remains undetermined.

This page is intentionally left blank

3 Thermochronological studies in southern Norway: Fission track and other dating methods

Uplift in different regions of Norway (including Shetland and Faroe islands) and Greenland caught the attention of many thermochronologists. The elevated topography of these regions is not what is predicted for neither of the passive margins of the North Atlantic Ocean. The trigger mechanisms behind these series of uplifts remain uncertain. The lack of onshore sedimentary record after Devonian time is complicating the labor of establishing the post-Caledonian history in detail. Thermochronology is used as a tool to quantify the vertical movements occurred throughout Norway after the orogenic collapse and to help constraining the timing of post-Caledonian extensional episodes. Fission track analysis in Norway have been most commonly done with apatite rather than zircon and titanite (Hendriks et al., 2007). In this master thesis, I will focus in the Lærdal-Gjende fault, located in the central southern region of Norway.

The first studies using fission track dating methods were carried out by Andriessen & Bos (1986) at Eidfjord and Hardangerjøkulen. Despite of the limited working area, Andriessen & Bos (1986) could interpret an initial fast uplift and cooling (100 m/Ma) occurred after Devonian times, followed by a slow cooling episode (20 m/Ma) after late Carboniferous to early Permian. They recognized an increase in age with elevation from 110 Ma at sea-level to 166 Ma above 1500 m height. Andriessen & Bos (1986) estimated 13 km of crustal removal after the Caledonian orogeny and 8 km after Late Carboniferous.

Two of the most extensive and representative studies for the southern Scandes were made by Leighton (2007) and Rohrman et al. (1995). Rohrman et al. (1995) was the first most extensive fission track study covering southern Norway. Their apatite fission track data-set showed a domal distribution of ages, where the oldest ages were displayed along the coastline and on high topographic levels inland, whereas younger ages were located at sea-level within inland fjords. Twos phases of accelerated cooling were inferred from this extensive study: the first one occurring in the Jurassic (coinciding with North Sea rifting and progradation of deltas with mainland Norway source) and the second being of post-Cretaceous origin. The Triassic - Jurassic uplift is interpreted to have migrated from east to west. Rohrman et al. (1995) states that the post-Cretaceus cooling event is the responsible for the domal pattern distribution of age.

The radial age pattern has been noticed by numerous authors. Gabrielsen et al. (2005) refers to it either as a Mesozoic domal feature broken by faults or as shoulder uplift. Nevertheless, they discussed shoulder uplift to be less conceivable. The paper of Gabrielsen et al. (2005) summarizes the vertical movements of southwestern Fennoscandia and speculate on the possible

triggering mechanisms. As in relation to the Lærdal-Gjende Fault system and related regional structures, they mention that those could had been reactivated during Mesozoic times due to thermal changes, which provoked simultaneously the domal uplift. Whereas, Gabrielsen et al. (2005) do not provide an explanation for the Neogene uplift but admit that a tectonic component should have enhanced it.

More recent extensive studies were carried out by Leighton (2007), who obtained similar results to Rohrman et al. (1995) in terms of general trends (Henriks, 2007). Leighton, however, found large offsets in adjacent fault blocks in southern and central Norway confirming that tectonic activity occurred in Mesozoic and Cenozoic times. This observation was also done previously by Redfield et al. (2004) within the Møre-Trøndelag Fault Complex (MTFC). The fission track and $^{U-Th}/_{He}$ analysis reported ages from Permian to Early Cretaceous and Early Cretaceous to Oligocene. Leighton observed that structural architecture impacts directly on the fission track ages and crustal block cooling history, albeit he discerned a positive correlation between elevation and age of the samples. The youngest ages reported date from 110 to 130 Ma at the sea-level (southern Norway), and the oldest ones date from 200 Ma at high elevations (2000 m). Leighton (2007) interpreted two rapid cooling events through inverse thermal modeling. The first one from Jurassic to Paleogene, affecting the southern region of Norway with cooling rates of 1 to 5 °C/Ma and the second rapid cooling event in Neogene times. The first cooling event is constrained to Triassic time and followed by slow-cooling until late Cenozoic, whereas the latter-most Cenozoic uplift is hardly constrained. Triassic uplift can be correlated with preserved deposits of central Europe and the North Sea, whose source was the Scandinavian highlands. Leighton (2007) also implied that the differential cooling histories between basement and Caledonian nappes is caused by fault reactivation within Mesozoic and Cenozoic times. He proposed that Møre basin extension had much influence on onshore reactivation and therefore in development of onshore topography, in accordance with the crustal taper hypothesis. This relation was established through Digital Elevation Model (DEM) analysis, which showed that the topography was greatly influenced by underlying structure (Leighton, 2007). He speculated that the reactivation mechanisms acting nowadays may be the same than for the Mesozoic fault reactivation. Henriks (2007), nonetheless, proposes that the main mechanism controlling Fennoscandinavian cooling has been the multi-stage North Atlantic rifting during the Tertiary.

As mentioned previously, Redfield et al. (2004) already observed significant offset among major crustal faults within the MTFC. The Møre-Trøndelag fault complex (MTFC) presents an aging trend from east to west, where the innermost crustal blocks were active during Cretaceous and Tertiary times. They divided the data into 4 crustal blocks and found out that the outermost region (Smøla) showed 150 Ma since the last exhumation signature, whereas the innermost crustal block (Sundalsøra) gave ages of only 25 to 45 Ma. Redfield et al. (2004, 2005) registered top-to-the west normal displacement along the faults that comprehend the boundaries for the

MTFC. Redfield et al. (2004) suggested reactivation of the Lærdal-Gjende fault system (LGFS) during late Paleozoic, Mesozoic and late Cenozoic times, as well as for the MTFC. Andersen et al. (1999) also reported that activity may have taken place within the LGFS around mid to late Permian and Late Jurassic. Record of onshore extension in Permo-Triassic and late Jurassic to Early Cretaceous times is evidenced by paleomagnetic and $^{40}Ar/^{39}Ar$ methods (e.g. Eide et al., 1999; Torsvik et al., 1992). Redfield et al. (2004) suggested a prolonged fault activity through Mesozoic to Cenozoic in central Norway as a product of the Norwegian Sea extension. Redfield et al. (2005) refers to the present-day topography, incised valleys, incised lineament, geohazards, present-day seismicity, etc. as result of continental-scale lithospheric flexure governing isostatic processes that reactivate the structural architecture inherited from Caledonian and post-Caledonian times (orogeny and rifting times).

Ksienzyk (2012) analyzed onshore faults in SW Norway through different low-temperature thermochronological methods and obtained a major concentration of ages from 294 to 160 Ma. Early to Middle Jurassic ages (200 to 160 Ma) dominate the Bergen region, although other coastal samples presented Permo-Triassic ages. $^{U-Th}/_{He}$ gave a large age gap compared to AFT ages. Ksienzyk (2012) and Ksienzyk et al. (2014) reported $^{U-Th}/_{He}$ ages ranging from 276 to 86 Ma, with a majority of samples dating from early to middle Cretaceous. The thermal history modeling show two rapid cooling phases in (1) from Permian to Early Jurassic times (2 to 3 °C/Ma) corresponding to Permo-Triassic rifting of the North Sea and (2) in the Neogene with rates of 1 to 2 °C/Ma. The second cooling event was inferred to start in Jurassic times and continued throughout the Cenozoic times. Ksienzyk (2012) also noticed differential thermal histories across faults. Inland samples presented higher temperatures than coastal samples, which was interpreted to be caused by higher post-Jurassic inland erosion (Ksienzyk et al., 2014). Ksienzyk et al. (2014) suggest that coastal samples have undergone reburial during Cretaceous times and have experienced higher cooling rates due to rift flank uplift, whereas the inland samples cooled slower throughout Jurassic and Cretaceous and were exhumated at later time than coastal samples. Therefore, the rifting did not affect equally to the coast and inland Norway. The Lærdal-Gjende fault gouges were analyzed through $^{K}/_{Ar}$ illite dating method and provided reactivation ages of early Carboniferous, Permian, late Triassic to early Jurassic and Cretaceous to early Paleogene times (Ksienzyk, 2012). Ksienzyk et al. (2014) concluded that age distribution is tectonically controlled by fault reactivation in Cretaceous and Cenozoic times, erosion and uplift processes.

Andersen et al. (1999), Eide et al. (1997), and Torsvik et al. (1992) also documented evidences of post-Caledonian onshore faulting with palemagnetic and $^{K}/_{Ar}$ dating methods in the Lærdal-Gjende Fault System and the Nordjord-Sogn Detachment Zone (in Ksienzyk et al., 2014).

Concluding; there are two major episodes of rapid cooling: the first is constrained to Mesozoic times and the second is poorly limited to the Cenozoic. Tertiary and Mesozoic uplifts are

accepted and acknowledged within the thermochronologist community by authors such as Andersen et al. (1999), Eide et al. (1999), Eide et al. (1997), Fossen & Dunlap (1998), Riis (1996), Torske (1972), Torsvik et al. (1992), and Torsvik et al. (1997). A strong tectonic signal is linked to these two episodes affecting major crustal blocks throughout southern Norway and the west coast. In consequence, it is undeniable that a tectonic component should be considered for the Cenozoic uplift and that neither southern or northern Norway are not acting as a singular crustal block.

Several thermochronologists have attempted to provide an explanation to the processes involved the vertical movements of post-Caledonian history that contributed to the formation of the present-day topography of Norway. In spite of the vast pile of literature dedicated to it, this chapter intends only to give an insight to the extensive research in relation with thermochronological studies of Norway.

3.1 Models of Norwegian landscape evolution

Over the last decade, various views for explaining the Norwegian landscape evolution arose from regional studies conducted through thermochronological methods. The discussion continues nowadays. The oldest model, regarded sometimes as the "peneplanation and uplift" model, came out first in the 1889 by the hand of Davis. This model suggests that peneplanation of the Caledonian continental crust occured in Mesozoic times, followed by active tectonic uplift in Cenozoic times. In this model, the cause of the present high topography in southern Norway is attributed to tectonic driven uplift. This approach was discussed by Nielsen et al. (2009), who argued that the elevated profile of western Scandinavia is the remnant of the ancient Caledonian topography. Nielsen et al. (2009) proposed that neither peneplanation nor Cenozoic active tectonic uplift took place. The latter hypothesis is also known as the ICE (Isostasy - Climate - Erosion) hypothesis and has been the target of discussion among many geologists because it is not entirely consistent with thermochronological data. The ICE hypothesis however, is based in the well-known elastic flexural crustal behavior. Many other authors have contributed to the discussion with new suggestions, as for example Osmundsen & Redfield (2011), who remarked the long-lasting influence of rift geometry in the topography of a passive margins. This last approach, referred by the authors as the "crustal-taper", would be explained in further extend. Many thermochronologists are in no favor of any of them since the post-Caledonian history of Norway seem to be rather a complex sum of processes, than to respond just to one single model.

3.1.1 The peneplanation and uplift model

The "peneplanation and uplift" model is the first hypothesis suggested for explaining the elevated western Scandinavian topography. The model upholds peneplanation occurred as a result

for/of the destruction and erosion of the Caledonian relief. According to this model, the erosive, residual, flattish, peneplanized surfaces were eventually uplifted during Cenozoic times, although the triggering mechanism is yet unknown. The Davisian model portrays the present-day topography of Norway as the end member of peneplanation and uplift. Nevertheless, practically only Lister & Davis (1989) considered it as the resulting end member. On the contrary, most of geologists accept peneplanation and uplift under the premise that current western Scandinavian landscape has been modified by glacial and (in minor degree) periglacial processes, and admit that exhumation due to unloading should be considered. An important remark is that the peneplanation model is reasoned under the assumption that extensional post-collisional events thinned successfully the orogenic crust down.

The existence of a peneplanation event is based on the interpretation of paleic surfaces described as undulating upland plateaus (Gjessing, 1967). The paleic surfaces are interpreted as to be graded to sea-level after erosion of orogenic crust, caused by the total destruction of topography driven by extensional processes. There are several authors such as Doré (1992), Riis (1995), and Torske (1972) that tried to constrain an age for the formation of theses surfaces. In spite of the focus of many in this topic, there is still a lack of consensus regarding their formation time.

The "peneplanation and uplift" model is defended by Rohrman et al. (1995) who proposed active Cenozoic uplift as the cause for the high elevation in regions from western and northern Norway, east Greenland, Svalbard and the Barents Sea. The uplifted regions seen across the Atlantic share the same domal age pattern distributions, reason why Rohrman et al. (1995) believe that the uplifts were originated by the same regional tectonic trigger. Theyconcluded that the most recent uplift occurred in Neogene times in the south of Norway. The onset was estimated to be 30 Ma through AFT dating and track length distributions. They noticed the occurrence of young ages at sea-level in inland fjords (around 100 Myr), whereas old ages increase radially to higher peaks and coastal areas (Fig. 3.1). The oldest AFT ages date from 220 Ma (Triassic times) in eastern Norway and along the west coast, whereas exhumation seem to have occurred at later Jurassic times in southwestern Norway (160 Ma ago). The domal age distribution (young ages inland and old ages in coastal areas and eastern Norway) corresponds to the topographic profile in Norway (Fig. 3.1). The domal age distribution pattern in Norway is portrayed as consequence to Neogene (Pliocene) uplift, which probably started in the Late Oligocenea and was overprinted afterwards by Plio-Pleistocene glaciations (Rohrman et al., 1995). Thus, they assumed that no exhumation took place due to glacial erosion neither in Tertiary or Quarternary icehouse periods. Rather than that, Rohrman et al. (1995) suggested 1,5 to 2,5 km exhumation dating from Oligocene, prior to glaciations, and initiated as a combination of mantle convection and intraplate stresses. AFT ages date from Triassic (southern coast) and Jurassic times (high elevated terrains and western coast) in the lower part of the dome pattern. The estimates of exhumation rate for Triassic and Jurassic times were very high corresponding to the geothermal

gradients of 30 °C/km. Lower elevated terrains present mainly Early Cretaceous ages. Old ages in the shoreline are in accordance with the radial uplift, whose focus was in the southern central Norway, leaving older ages in the shoreline and the eastern side as proposed by Rohrman et al. (1995).

Rohrman et al. (1995) exposed two-phased exhumation discovered through fission track modeling for southern Norway. Rohrman et al. (1995) concluded that sublithospheric thermal erosion caused by convective inestabilities by the arrival of the icelandic plume around 30 Myr ago could have been the onset trigger of the uplift (mechanisms suggested in Buck (1986) and Fleitout & Yuen (1984). The accelaration in cooling around 5 Myr ago is believed to happen as a result of intraplate stress fluctuations (compressional effects). These two uplift mechanisms and the unloading response to Plio-Pleistocene glaciations may explain or partially explain the total amount of exhumation estimates of 1 to 1,5 km producing the domal age distribution pattern.

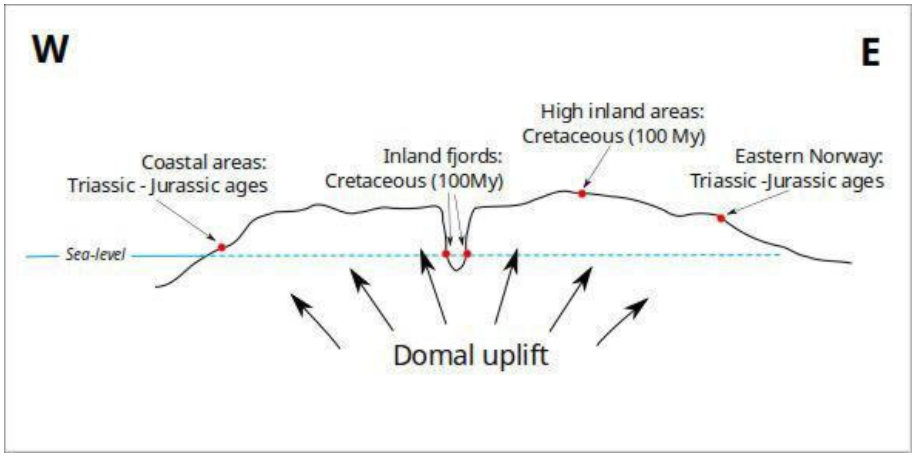

Fig. 3.1: Synthetic East - West southern Norway profile showing the age pattern collected by Rohrman et al. (1995). The domal distribution pattern is inferred through isochrone distribution: old ages gather around coastal and eastern areas, whereas young isochrones are focused on central Norway. Fjords present young ages at sea-level, which arise some problems to the domal hypothesis.

Nielsen et al. (2009) and Rohrman et al. (1995) are in agreement regarding the climate-erosion and sediment deposition relationship during Cenozoic, although the first believes that Oligocene active tectonic uplift indeed happened and relates it to the thick Oligocene sedimentary record (mouth bars and km-scaled fans) found in the North Sea.

Different kind of evidences that may support the peneplanation and uplift model have been presented by many authors. Diatoms dating from Late Paleocene were found in Sweden at 300 m above sea-level (Fenner, 1988), which indicates the sea had extended up to Sweden and that the Cenozoic uplift postdate from Late Paleocene. Dahl & Nesje (1994) suggested that glaciations predated the uplift and concluded that climate control over exhumation was no relevant.

3.1.2 The ICE (Isostasy-Climate-Erosion) hypothesis

The ICE hypothesis is the antagonistic theory to the Davisian model or "peneplanation and uplift" model. Nielsen et al. (2009) proposed no peneplanation occurred and claimed no tectonic uplift, but instead suggested a long-term exhumation affecting differently to western and eastern Norway. One of the most important premises of the ICE hypothesis is that the present-day Norwegian topography is the remnant of the ancient Caledonian highlands, whose thick roots partially survived throughout the extensional post-Caledonian history until the present day. Nielsen et al. (2009) were not the pioneers in promoting Cenozoic uplift as isostatic glacial rebound, in fact this is an old concept proposed by other geologists such as Riis & Fjeldskaar (1992) or Rohrman et al. (1995), the latter one supporter of the "peneplanation and uplift" model. However, the ICE hypothesis as it is known was developed and shaped in first place by Nielsen et al. (2009).

According to Nielsen et al. (2009), the observed large negative values of the Bouguer anomaly across the west-east profile of Norway are caused by the placement of orogenic residual crust beneath western Scandivian highlands. As suggested in the ICE hypothesis, this residual crust acts as a buoyant agent and consequently provides crustal support to the western Scandinavia, which is linked in great extend to the high topography seen nowadays in Norway. The existence of Caledonian orogenic crustal root is considered to be the consequence of the lack of success of topography-destroying-processes (orogenic collapse and rifting). Current topography is therefore the remnant of the ancient highlands 400 My ago. This statement involves continued erosion affecting throughout all the post-Caledonian history. Under this perspective, a peneplanation event is dismissed since it is not suitable neither with the actual Bouguer anomaly values present from the coast to inland profile nor with the long-term erosion assumption.

The apatite fission track data (MLT and AFT ages) collected by Nielsen et al. (2009) revealed different exhumation histories across the west-east profile. Large amounts of exhumation were inferred in coastal areas, whereas inland experienced more steady and slow exhumation rates. AFT ages distribution shows older ages in the coast than inland, contrary as it is expected. Furthermore, AFT ages modeling curves reflect a slow exhumation rate after late Paleozoic to early Mesozoic. Nevertheless, many of the samples with ages older than 100 My, present signs of MLT reduction marking a long duration in the PAZ. The old ages are thereby preserved due to the occurrence of a cooling event that placed them on the present-day surface (Nielsen et al., 2009). The glacial erosion effect (enhanced by periglacial processes) may have been the cause for the most recent cooling event. They also linked the frequent switch between Cenozoic icehouse-greenhouse cycles with sediment oscillations in the North Sea. Large clastic deposits from the Eocene-Oligocene boundary are correlated generally with active Cenozoic tectonic uplift, however the ICE hypothesis attributes this lithological change to a well-known sea-level and temperature drop at that time. On the other hand, Steer et al. (2012) attested that glacial

and periglacial erosion agents affecting western Scandinavia could have not produced enough sedimentary material as observed for the Plio-Pleistocene sedimentary record, which may imply that active tectonics could have occurred and persisted even after Oligocene times. Nielsen et al., 2009 acknowledged recent fault tectonics in the Møre-Trøndelag fault zone and Lofoten-Vesterålen area documented by other AFT analysis. This is explained in the ICE-hypothesis as lateral post-glacial rebound adjustments. Thus, fault movements as well as Cenozoic uplift are considered differential isostatic adjustments as response to erosional unloading, discarding any active tectonic uplift during Cenozoic times. The flat surfaces and low-relieve characteristics in highlands previously interpreted by other geologists as "paleic surfaces" (graded to sea-level in late Paleozoic to early Mesozoic) are explained as to be originated by glacial and periglacial landscape-shaping processes occurred mainly during Neogene time. Hence, peneplanation does not account for flattened surfaces in highlands anymore.

Low vitrinite reflectance values and the presence of coal wood-fiber structures in the Bjorøy fm. of Jurassic age (Oxfordian age) indicate low maturity of this sedimentary formation located at west Bergen (Fossen et al., 1997), as well as stable sea-level position of this formation during Mesozoic times. Thereby, it implies that the hinge zone has been held at the approximate same position through Mesozoic times as required for the ICE hypothesis to be coherent. In the ICE hypothesis, coastal sediment overburial is attributed to the sea-level fall and consequent erosion, and effective Quaternary glacial erosion.

Summarizing, the ICE hypothesis attributes the high present-day topographic elevation of Norway as to be the remnant of Caledonian highlands. The Neogene/Cenozoic uplift is therefore the isostatic response to unloading controlled by climate, rather than caused by active tectonic uplift. Isostatically controlled feeding of the crustal material by buoyant root affects inland Norway, but not coastal areas. That explains the cease in exhumation along the Norwegian coast. Thus, peneplanation and uplift are not required as a resource to explain either some geomorphological features in highlands or inland exhumation.

3.1.3 Crustal taper

The "crustal taper related-to-topography model" is one of the possible ways to explain the Norwegian landscape. This hypothesis was extensively developed by the hand of Osmundsen & Redfield (2011). They made a review of offshore and onshore Norwegian margin data and other passive margins in the globe with elevated escarpments facing seawards. The mechanisms of how the scarped passive margins can be continued or rejuvenated after millions of years after the rifting stopped, are not entirely known. In their paper, Osmundsen & Redfield (2011) explained that the topography of passive margins is dependent on the taper break location (the first highly thinned crust in the distal margin).

The offshore Norwegian margin possesses a diverse range of structural scenarios from north to south. The crustal taper is more significant in some areas, as for example the Møre basin, whose necking geometry is due to detachment faults dated from Late Jurassic to Early Cretaceous. The thickness of the thinned crust in the Norwegian margin corresponds the magnitude of displacement of Jurassic and Cretaceous faults. Osmundsen & Redfield (2011) also proposed that the necking position was influenced by the interference of faults from Jurassic and Cretaceous, position of distal crustal minimum thickness, and the location of post-rotational "sag" basins. Cenozoic and Mesozoic offshore sediments required of a large material source from Norwegian mainland (uplifted terrains). Onshore (mainland Norway) Cenozoic uplift was inferred through the Molo formation (a prograding delta), distinguished from the Plio-Pleistocene sedimentary wedge related to the Neogene glaciacions. The onshore Norwegian margin present more asymmetric and higher relief in the continental side (inboard) of the most sharply tapered segments of the passive margin (Osmundsen & Redfield, 2011). AFT minimum ages of 110 Ma occur in this scarped regions, as well as in Møre and Lofoten-Vesterålen areas. AFT ages throughout the MTFC do not follow an uniform pattern owing to post-Cretaceous period climate changes and multi-phase normal-sense fault reactivation. These characteristics are common in most passive margins as for example the Brazilian margin. Based on onshore topography data and 40 published depth converted cross-sections from offshore and the Norwegian passive margin, Osmundsen & Redfield (2011) observed a relationship between apparent taper length and escarpment elevation, as well as a link between distance from taper break and escarpment elevation. These authors identified a relationship between crustal thinning (syn-rift process) and escarpment evolution (post-rift process). Other factors tested by the same authors; such as age of the break-up, magmatism and climate seem to be irrelevant in this hypothesis. The lateral variations in crustal thinning and taper break are most likely controlled by large detachment faults as the rifting advances, as suggested by Osmundsen & Redfield (2011). Fault activity may migrate towards hinterland (or inboard) during post-rift, on the contrary to what happens during rifting. This may be due to a transient state of low crustal strength from weakened faulted crust during the rifting that becomes stronger after rifting and thermal relaxation.

In conclusion, Osmundsen & Redfield (2011) claim that highland escarpments are a consequence of the crustal behavior during and after rifting. They proposed that passive margins escarpments along the coast are linked to the crustal thinning gradient and therefore the topography of passive margins should no longer be considered as a product of break-up age, magmatism, climate or mantle convection. Thus, they link the high irregular and sharp topography to the location of taper break and apparent taper length. Concerning the fault activity in southern Norway, this hypothesis does not provide with any explanation for the vertical movements along faults that are further away from the coastline in hinterland areas. However, since crustal thinning gradients control the thermal subsidence (Osmundsen & Redfield, 2011), footwall uplift followed by erosion and renewed uplift may explain the reactivation of onshore larger faults and

terrain rejuvenation.

This page is intentionally left blank

4 Fault-rocks review

This chapter intends to be a relatively short review of fault-rocks classification, kinematic indicators and fault zone architecture. A general consensus has not been conveyed for classifying fault-rock types yet, principally because the terminology may result problematic to apply (Schmid & Handy, 1991; Snoke et al., 1998) and because some terms have been misused in different fields of geology (Killick, 2003). This issue has been discussed over the years by several authors (e.g. Killick, 2003; Rutter, 1986; Sibson, 1977; Snoke et al., 1998). Nevertheless, there is a broadly accepted conceptual model of the characteristics of the diverse fault-rock products depending upon crustal depth formation, based on Sibson (1977) (Fig. 4.1). Sibson (1977) is known for compiling different fault-rock characteristics into a general classification, among others. Many other geologists before him focused on giving detailed descriptions and trying to classify the different fault-rock products. In this chapter, some of the most popular terms and discussions around these will be introduced.

Sibson (1977) suggested that cataclastic processes occur within the first 10 to 15 km of the crust in the elasto-frictional regime assuming a quartzo-fedspathic crust. In the quasi-plastic regime, at greater depth than 10 to 15 km, mylonitic fault-rocks are produced instead. Killick (2003) commented that rock composition, strain rate and the presence or absence of fluid can alter the depths at which mylonites and cataclasites occur. Deformation mechanisms in the elastico-frictional regime involve brittle fracture and frictional sliding, leading to dilatancy except for initially porous rocks (Rutter et al., 2001). The strength of brittle faults increases with depth (by increasing effective pressure), based on Byerlee's law principle. As a note, Byeerle's law can be shortly summarized as the relation in which the shear stress required to make two crustal blocks slide, decreases as the normal stress increases. Frictional deformation mechanisms occurring in the upper crust are neither thermal or strain-related processes, which excludes among others the lithological composition factor. Cataclastic frictional processes are conditioned by effective pressure and pore pressure of the crustal material (Sibson, 1994). The transition between brittle and ductile regimes coincides with the strength maximum in the lithosphere (Sibson, 1977). Deeper crustal deformation mechanisms are different from those of the upper crust. Mylonitic fault-rocks are produced under the ductile regime and their deformation is dominated by viscous flow deformation mechanisms. Temperature conditions and strain rate are, therefore, the responsible factors determining the deformation of these rocks. Non-frictional, thermically dependent mechanisms act to produce crystal plasticity, dynamic recrystallization, and dislocation and diffusion creep, the latter acting principally once the grain-size is reduced (Fossen, 2010; Rutter et al., 2001; Sibson, 1977; Tullis & Yund, 1977). Deep shear zones are able to transport aqueous and melt fluids within weaker fault zones, which may be related to a certain factor of dilatancy also present in the deeper crust (Bruhn et al., 2000).

It is important to remark that both brittle and ductile deformation may occur within low grade, poly-phase mylonites (Schmid & Handy, 1991). Therefore, brittle deformation is not exclusively localized in the upper crust. Cataclastic flow at a microscopic scale may seem ductile deformation if the cracks remain distributed (Snoke et al., 1998), which leads to confusion if genetic criteria is applied to the terminology. A further detailed discussion of deformation mechanisms is beyond the scope of this summary. If the reader seeks out for more information about deformation mechanisms, definitions and genetic aspects of fault-rocks, I would recommend looking into the work of Schmid & Handy (1991).

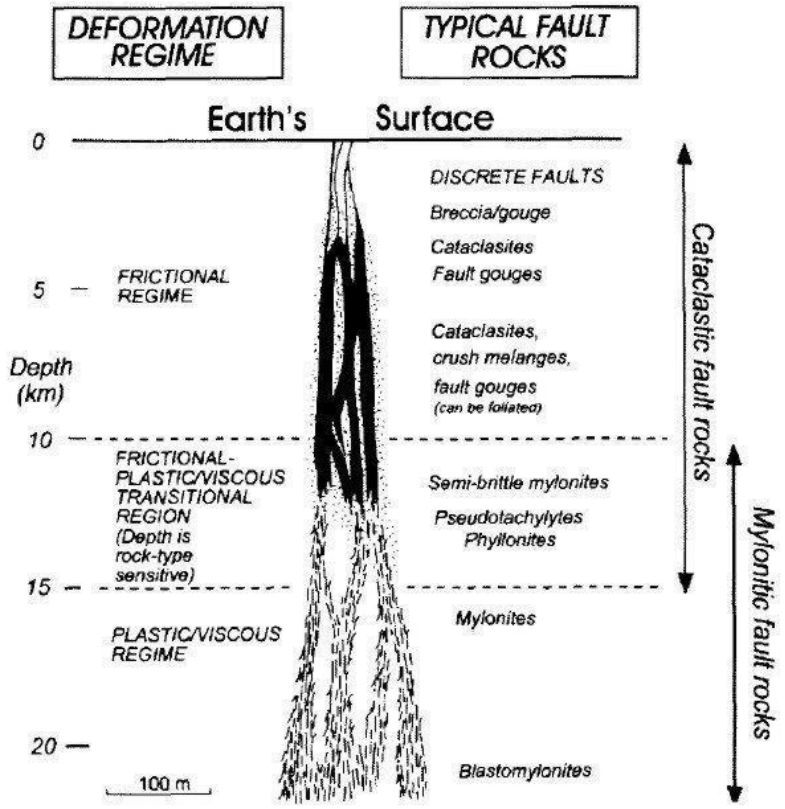

Fig. 4.1: Accepted conceptual model for fault-rock formation associated with crustal depth based on sibson1977fault. Cataclastic fault rocks are produced at the surface and down toa depth of 15 km. Transition into mylonitic fault rock production occurs at 10 km depth. Mylonites are found from 10 km depth down to >20 km depth. Cataclastic fault rocks are formed at brittle-frictional regime, whereas mylonitic fault rocks are produced under ductile regime and viscous flow processes dominate as deformation mechanisms. Figure extracted from Rutter et al. (2001).

The reactivation of faults is highly conditioned by the fault zone geometry and crustal (or rheological) history. Major faults found in the continental crust persist during longer periods of time thanks to the continental crustal resistance to subduction (Rutter et al., 2001). Thus, major large faults, rooted in the middle to lower crust, would probably have various fault-rock types corresponding to changes in P, T and fluid conditions along with displacement and/or exhumation (Snoke et al., 1998). Thereby, deep faults crossing various crustal levels at different depths may contain a range of fault-rocks according to the regime where they were generated.

This observation may help to unravel the deformation history of series of faults with a complex deformation history, as noted by Snoke et al. (1998) and Killick (2003). Brittle over ductile deformation is easy to recognize. On the contrary, ductile deformation overprinting a brittle deformation event results more difficult to assess. This is because high temperature events (such as grain growth, recrystallization or other superpositions) may overprint completely the pre-existing structures and erase the brittle signature (Snoke et al., 1998). Overprinting relations can only be observed clearly under a petrographic microscope. In normal-sense fault zones, the footwall block would present mylonites juxtaposed on top of brittle fault-rocks (e.g. kakirites and cataclasites) of the hangingwall block. On the contrary, in reverse-sense fault zones, ductile deformation structures (in mylonites) of the hanging-wall would be juxtaposed above the brittle rocks of the footwall block (Fig. 4.2) (Snoke et al., 1998).

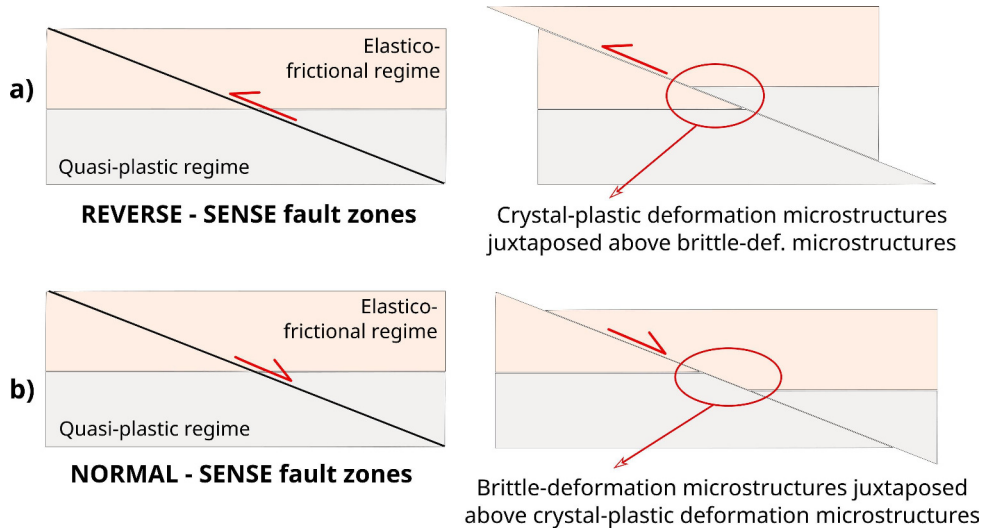

Fig. 4.2: Different scenarios of fault-rock juxtaposition according to the nature of the fault, based on Butler & Coward (1984). (a) Juxtaposition of ductile fault-rocks of the hanging-wall above footwall brittle fault-rocks. (b) Juxtaposition of brittle fault-rocks of the hanging-wall above footwall ductile fault-rocks.

4.1 Fault-rocks classification

The term ‘fault’ is applied to shear fractures and shear zones with longitudes of at least some meters. Regularly, the term ‘shear fracture’ applies to centimeter-scaled or smaller features (Twiss & Moores, 1992). The term ‘microfault’ is applied when the structure may only be recognizable under microscope. There are different styles of faulting that can be discerned at meso-scale. The faulting can occur in a discrete, single shear fracture plane (Fig. 4.3a) or form a fault zone (Fig. 4.3b). Ductile shear zones are among the faulting styles (Fig. 4.3b) and form when the displacement does not affect the rock cohesion at outcrop scale. The fault-related rocks, sometimes called tectonites, are the product of intense deformation within fault planes, fault zones and shear zones.

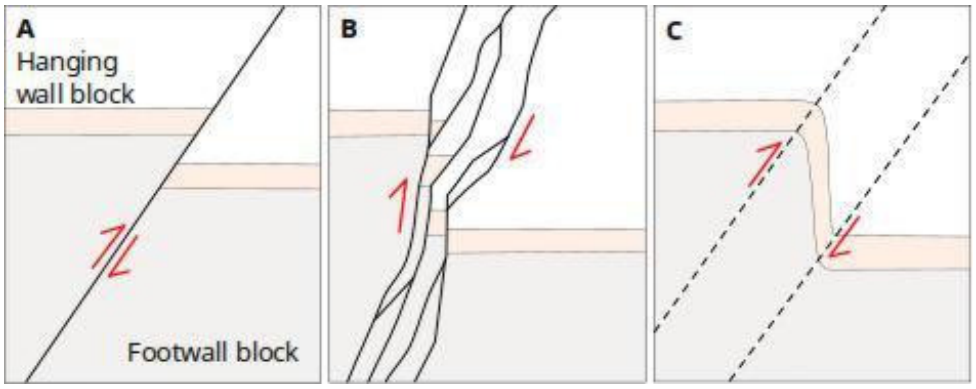

Fig. 4.3: Different styles of faulting at meso-scale based on Twiss & Moores (1992): a) Fault: single shear fracture, b) Fault zone: Strand of shear fractures, c) Ductile shear zone.

Each tectonite possesses different fabrics and textures according to the formation conditions and the rate of strain that they have been subjected to (Twiss & Moores, 1992). Fault-rock classification has been discussed over the last decades. Sibson (1977) proposed the first and more acknowledged general textural fault-rock classification. Many other classifications are based in Sibson's work. Twiss & Moores (1992), for example, classified fault-rocks according to their texture, the clasts grain-size and the percentage of matrix (Table 4.1). Sibson (1977) also provided matrix percentage for cohesive fault-rocks. Due to much controversy establishing accurate genetic and petrographic terms Snoke et al. (1998) proposed a classification based on macroscopic features, leaving aside any genetic criteria into the fault-rock terminology. In this thesis, the applied fault-rock terminology is the one presented in the textbook of Twiss & Moores (1992) (Table 4.1). For problematic samples, additional terminology suggested by other authors is provided. In the present manuscript some terms that are currently in use for describing fault-rock products will be introduced. Short remarks about the discussion of some terms is also included.

Table 4.1: Fault-Rock Terminology

Catalastic rocks					
Fabric	Texture	Name		Clast size	Matrix
Generally no preffered orientations	Cataclastic: sharp, angular,fragments	Breccia series	Megabreccia	>0,5 m	<30 %
			Breccia	1-500 mm	<30 %
			Microbreccia	<1 mm	<30 %
		Gouge		<1 mm	<30 %
		Cataclasite		Generally ⩽~10 mm	>30 %
		Pseudotachylite			Glass, or grain size ⩽1 µm
Mylonitic rocks					
Fabric	Texture	Name		Matrix grain size	Matrix
Foliated and lineated	Metamorphic: interlocking grain boundaries, sutured to polygonal	Mylonitic gneiss		>50 µm	
		Mylonite series	Protomylonite	<50 µm	<50 %
			Mylonite	<50 µm	50-90 %
			Ultramylonite	<10 µm	>90 %

Fault-Rock Terminology suggested by Twiss & Moores (1992) and based on Press & Siever (1986).

The fault-rocks that form in the upper crust, under the brittle regime, are cataclastic rocks.

These fault-rocks present signs of comminution and fragmentation due to cataclastic deformation mechanisms. The clasts, or fragments, are fractured, sharp and angular. Generally these rocks do not display any internal foliation or linear structure. However, some cataclasites from the San Andreas fault display micro-scale foliation (Chester et al., 1985). Chester et al. & coworkers observed that foliation of fault gouges (at shallow crustal depths) was due to compositional banding when polymineralic rocks were involved, and to frictional iding, rigid-rotation of grain fragments and fracture mechamisms. Sometimes, cataclastic rocks may be grounded to powder rock. This occurs in the first kilometers below the surface (1 to 4 km depth). Incohesive fault-rocks can appear up to 10 km depth. Cataclastic cohesive rocks occur in the range between 10 to 15 km depth and do not present any internal structure at meso-scale. In textbook of Twiss & Moores (1992) the sub-divisions within cataclastic rocks are presented in four categories from brittle to semi-brittle behaviour: (1) breccias series, (2) gouges, (3) cataclasite series and (4) pseudotachylites. The breccia series are incohesive fault-rocks that can be sub-divided into different groups according to the size of the clasts. Whereas in megabreccias and breccias the clasts are usually rock fragments, the clasts in microbreccias are mineral grain fragments (Twiss & Moores, 1992). Fault gouges are incohesive rocks with smaller clast size than breccias and can even be grounded to powder rock. The breccias series can be hardened during or after deformation. Cataclasites form under higher pressure and temperature conditions than the previously mentioned. Cataclasites are cohesive and their matrix portion ranges from 30 to 100 %. They may be narrow (millimeters) to kilometer wide within the fault zone depending on displacement. Thicker cataclasites are associated to small grain-size and represent large fault displacement.

Pseudotachylites were first described by Shand (1916) as irregular veins with variable thickness, shape and orientation. Evidence of melting (spherulitic and microlitic textures in Fig. 4.4) can be found in the dark groundmass, which is generally glassy material with similar chemical composition to the country rock. Spherulitic and microlitic textures are found in volcanic rocks with less than 95 % of amorphous or recrytallized glass (Bard, 1986).

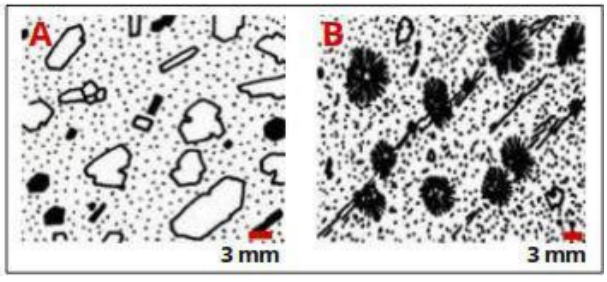

Fig. 4.4: A) Microlitic texture: includes phenocrystals, phenoclasts and microlites in amorphous groundmass. If the phenocrystals are large is called 'porphyroidal'. Microlites are mineral species of larger form than crystallites (embryonic crystals in glass). B) Spherulitic texture occur in microlitic rocks. This is characterized by radial recrystallized spherules from glass or acicular microcrystals produced by rapid cooling. Figures extracted from Bard (1986).

Pseudotachylite is a problematic term that involves a certain genetic criteria. In Twiss & Moores (1992) pseudotachylites are defined as massive rocks with dark veins of glass or cryp-

tocrystalline material. It is very common to find either glass or devitrified glass cementing fractured rock, in which the matrix crystals do not exceed 1 µm in diameter. Twiss & Moores (1992) attributed their formation to frictional heating during earthquakes at <10 to 15 km depth. The fractures of the wall rock will be filled with melted rock, forming veins of pseudotachylite. Other authors (e.g. Maddock, 1983) stated that pseudotachylites are formed due to fluidized ultracataclasis processes. The formation of these kind of fault-rocks has been also attributed to impactogens[1] (Reimold, 1995) in (Killick, 2003). Pseudotachylites have commonly been classified together with the mylonitic rock series because the dark groundmass presents signs of recrystallization and may show internal structures (Spry, 1969). Sibson (1977) and Wise et al. and co-workers (1984), nonetheless, classified them into the cataclastic rocks group (Fig. 4.5). Some of their characteristics may indicate that pseudotachylites are formed due to great strain and low recrystallization rate. Some geologists acknowledged signs of comminution and flow banding (rather than internal crystal orientation fabrics). Furthermore, recrystallization of the matrix does not represent a continuous deformation event but it is rather due to post-tectonic thermal cooling (Killick, 2003).

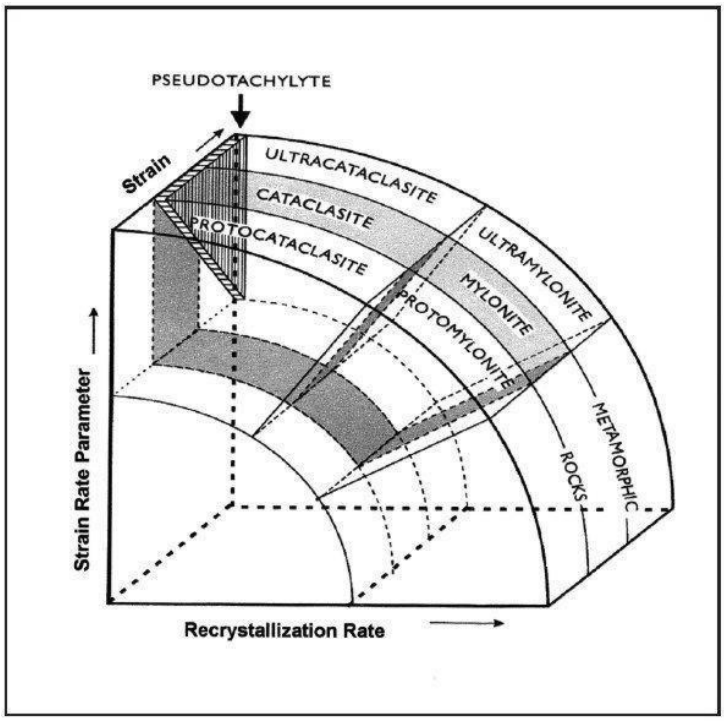

Fig. 4.5: Conceptual graph for fault-terminology based on wise1984fault. The fault-rocks types are classified according to strain rate, recrystallization rate and finite strain. The psedotachylites position involves medium to high strain and no recrystallization.

Mylonitic rock series occur under the quasi-plastic (semi-brittle to ductile) regime and deform mainly by crystal-plastic processes. Mylonitic rocks contain a very a high matrix-portion

[1] Impactogen: is a term first introduced by Burke et al. (1978) and used to designate those rifts that strike at high angles to collision-type orogenic belts (Dewey & Bird, 1970). The origin of these rifts is attributed to the strain generated within the fore- or hinterland of the orogen by the collision process. (Online Springer dictionary).

but porphyroclasts may be present. Cataclastic flow deformation processes may also take place, as previously mentioned, although it is not common. The grain-reduction is achieved through crystal-plastic deformation processes and dynamic recrystallization (Fossen, 2010). The depth of formation can range from 10 to 20 km at temperatures from 250 to 450 °C. Recrystallization is usually responsible for rock hardening, and grain boundaries may display triple junctions (of 120°) and highly sutured grains (Twiss & Moores, 1992). Generally, internal foliation is found within the shear zone forming C−S and C−C$'$-structures or simply displaying shear bands. Wise et al. (1984) defined mylonitic rocks as coherent rocks that experienced grain-size reduction of the country rock to less than 50 µm diameter. Mylonitic rocks involve recrystallization and should exhibit at least microscopic foliation. In addition, Wise and co-workers mentioned that porphyroblasts might be present in the matrix.

Mylonites are classified according to the matrix portion (Schmid & Handy, 1991; Scholz, 1990; Sibson, 1977). From increasing to lower matrix portion, are: ultramylonites, mylonites and protomylonites. In the Mylonites Atlas of Trouw et al. (2010), the given classification of the mylonites goes from low-, medium- to high-grade based on the grain-size, type and recrystallization rate.

Mylonitic gneisses are portrayed as high metamorphic degree rocks by Hanmer & McEachern (1992). Killick (2003) resolves that the term mylonitic gneiss should be applied for mylonites with advanced annealing and signs of metasomatism. Trouw et al. (2010) refer to these rocks as striped gneiss. In the textbook of Twiss & Moores (1992), mylonitic gneisses are classified by the size of the clasts, which should be >50 µm diameter.

The term phyllonite is also in use by some geologists. These fault-rocks are ultramylonites and/or mylonites rich in mica derived from schists (Trouw et al., 2010). The term is generally used just to indicate mylonites with high mica content.

The term blastomylonite refers to mylonites with blastos (or large grains) grown during mylonitization (Fossen, 2010). The clastomylonites also exhibit large grains, in this case clasts inherited from the original rock (Fossen, 2010). Some of the first authors to refer to blastomylonites were Bell & Etheridge (1973). The term was later used by Hobbs et al. (1976) referring to a very fine-grained rock produced under the ductile deformation regime. These rocks are different from the rest of the mylonitic rock series because they present pronounced grain growth due to recrystallization of the matrix. Spry (1969) pointed out that these rocks may be difficult to recognize due to the advanced recrystallization. As well as in metamorphic rocks, the porphyroblasts in blastomylonites have also grown during metamorphism (Killick, 2003). In the Mylonites Atlas by Trouw et al. (2010), a definition for blastomylonites is provided in terms of general use. Blastomylonites are portrayed as “mylonites with static recrystallization of part of

the fabric after deformation ceased". Trouw et al. (2010) chose to neglect this term from their suggested classification because of the difficulty to discern between dynamic and static recrystallization.

Mylonites are classified based on the visible structures. The foliations that may contain a mylonitic rock are S-surfaces (or mylonitic fabrics) and C-surfaces (shear bands). With advanced deformation, the S-foliation can be completely wiped out by C-surfaces. Lister & Snoke (1984) suggested two types of S−C mylonites based on the discernible fabrics: (1) Type I, with visible, continuous S-surfaces and (2) Type II, with domination of mesoscopic C-surfaces. The terminology used in this thesis would discern between C−S and C−C' foliations and S/C fabrics (see Section 4.2.2) but would not refer as to the classification proposed by Lister & Snoke (1984).

4.2 Kinematic indicators

Kinematic indicators are structural elements, structures or fabrics within fault rocks or in fault planes that are used to determine the direction and sense of the fault-slip or shear sense. In some cases, kinematic indicators help to identify the nature of faults: reverse, normal or strike-slip. The magnitude of displacement however is not possible to obtain in most of the cases. In this section, some shear-sense indicators and fault lineations that can be seen in the field and under the microscope will be briefly introduced. In the textbook "Microtectonics" by Passchier & Trouw (2005), the classification of microstructures and processes is provided in great detail.

4.2.1 Lineation in fault surfaces

Slickensides are defined as smooth, polished surfaces produced by shearing on the fault plane or gouges (Twiss & Moores, 1992). These surfaces might exhibit strongly oriented lineations, also called slickenlines, slickenside lineations or striations. The lineations found in slikensides are slickenfibers, ridges and grooves, and mineral strikes.

- **Slickenfibers or mineral fibers:**

Slickenfibers are a set of single crystal mineral fibers that grow parallel to the direction of displacement. The mineral fibers grow concomitantly to the displacement and are usually oriented at low angle respect to the fault blocks. The length of the fibers marks the finite displacement during the time of growth. The imaginary vector coming out from the point of attachment indicates the relative movement of the opposite fault block (Fig. 4.6).

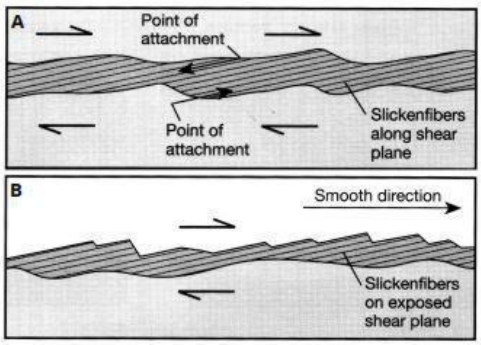

Fig. 4.6: Slickenfibers within the fault fracture oriented parallel to the relative displacement between fault blocks. A) Initial scenario depicting the fibers formation. The vectors defined from the point of attachment inward the fault fracture mark the relative displacement of the opposite fault block. B) Slickenfiners exposed by removal of the missing fault block. The smooth direction is portrayed by a "downstairs" shape of the slickenfibers that indicates the shear sense of the missing block. Fig. Extracted from Twiss & Moores (1992).

- **Ridges and Grooves:**

These are lineaments caused by "scratching and gouging of the fault surface, accumulation of gouge behind hard protrusions, from growth of slickenfibers, or by irregularities in the surface of the fault itself (i.e. Fault mullions)" (Twiss & Moores, 1992). They mark direction of the fault slip.

- **Mineral streaks:**

Mineral streaks are stripes on the fault surface caused by the shearing out of minerals within the gouge during fault displacement. Mineral streaks mark the slip direction of the fault.

4.2.2 Shear-sense indicators in mylonites (non-coaxial deformation).

The deformation within mylonites is attributed to simple shear. The shear sense may be recognizable by the different structures generated during deformation (Fig. 4.7). The next section introduces some of these structures. If the reader wishes to deepen into coaxial deformation structures (e.g. Boudinage), I recommend the structural geology textbook written by Fossen (2010).

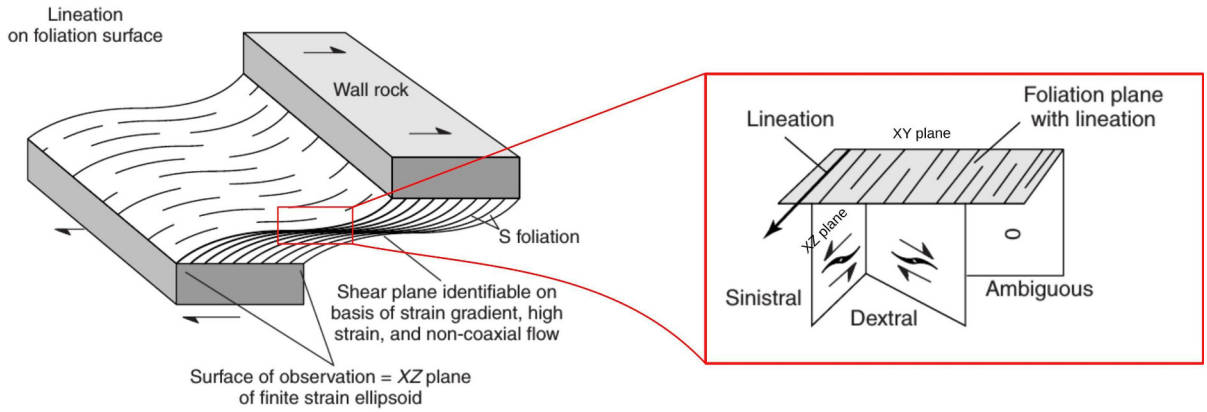

Fig. 4.7: Ductile shear zone elements and enlargement view of elements within the the shear plane of highest strain. Zoomed in foliation plane (XY plane) different views of shear indicators that can lead to confusion depending on the observation plane. The correct observation surface should be parallel to the XZ plane of finite strain ellipsoid. Figures extracted from Fossen (2010).

- **Grain-tail complexes in Mylonites:**

A gran-tail complex (also known as winged object) is formed by a porphyroclast that in most of the cases has reduced its diameter due to shearing and has asymmetric tails surrounding it. The tails (or wings) form by syntectonic recrystallization of the porphyroclast mantle and are composed by fine grains of recrystallized porphyroclast mineral material.

Earlier stages of grain-tail complexes start out as mantled porphyroclasts. During this early stage, it is not possible to identify the sense of shear in mantled porphyroclasts. Although, mantled porphyroclasts may give the shear direction. Porphyroclasts embedded in a fine-grained ductile matrix cause a deflection of the external foliation (Se). There are two main types of flow patterns that the matrix can adopt: eye-shaped (Fig. 4.8) and bow-tie shaped flow patterns (Figs. 4.8 and 4.9) (Passchier et al., 1993). These two flow patterns can derive in a set of grain-tail complexes. When the mantle of the porphyroclast is slightly or significantly larger than the separatrix, two types of grain-tail complexes indicating the sense of shear may develop: δ-type (delta) and σ-type (sigma) (Figs. 4.8 and 4.9). Sigma-type objects can either be isolated in a mylonitic matrix or be included in a developing C−S fabrics. In the latter situation the C-surfaces tend to enclose the larger porphyroclasts. There are also winged objects ϕ-type but these cannot be used as shear indicators.

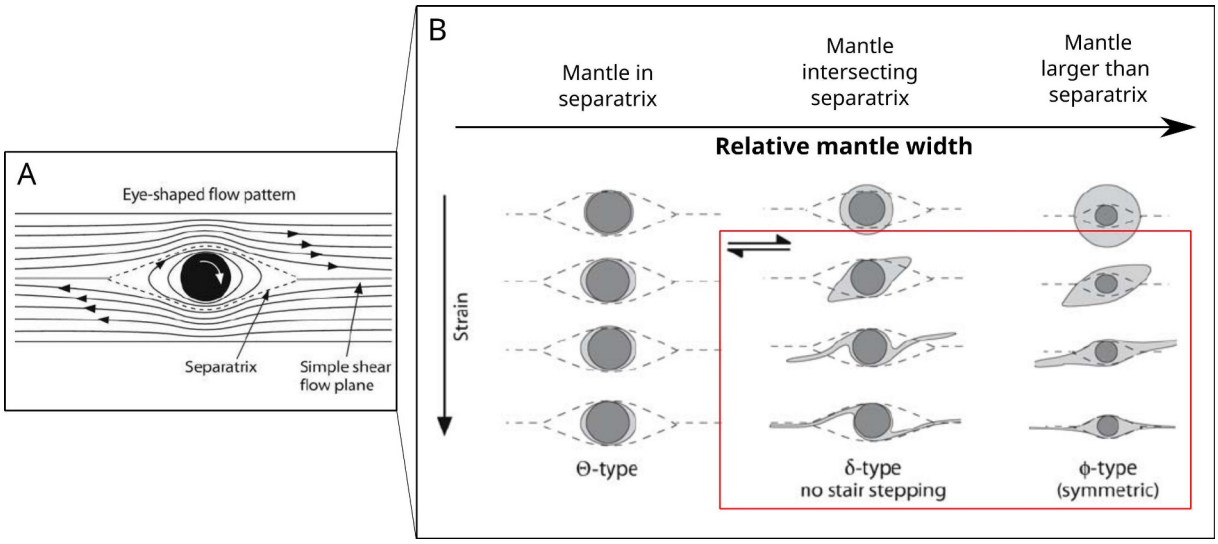

Fig. 4.8: A) Eye-shaped flow perturbation pattern. The separatrix is defined as the boundary between the far field displacement paths and the elliptical paths (Passchier et al., 1993). B) Grain-tailed complexes developed from eye-shaped flow patterns for an idealized spherical clast. The red box encompasses the grain-tail complexes delta and phi types used as shear sense indicators. ϕ-type wings get symmetric with high strain, therefore are indicative of high strain but shear sense becomes indistinguishable. δ-type tails (or wings) mark the rotation of the shear with strain and the early stages of formation present a sigma-type morphology. Figs. extrated from Passchier & Trouw (2005).

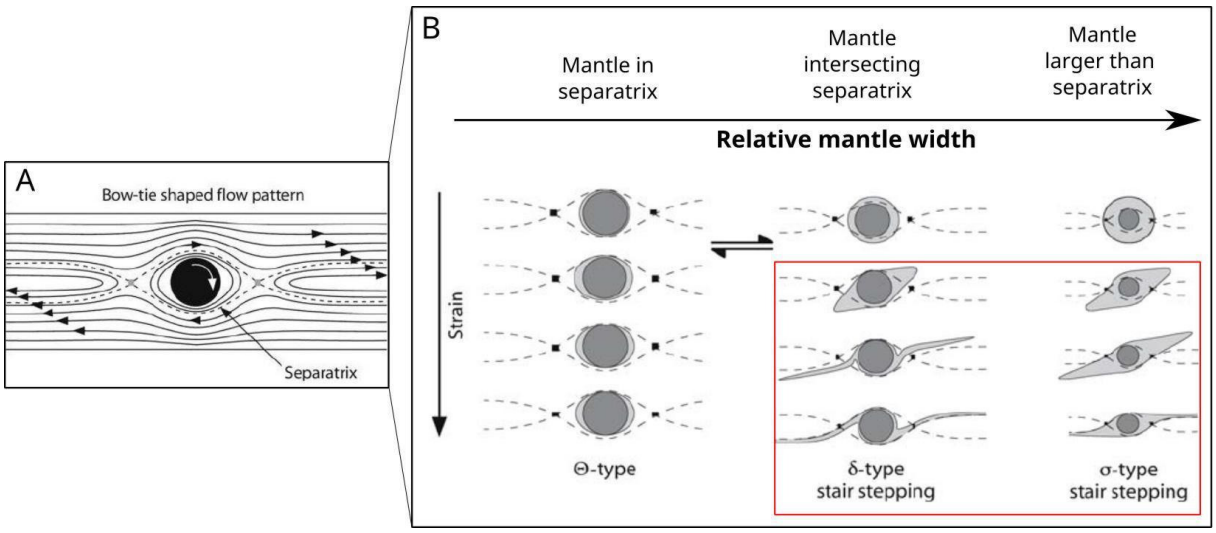

Fig. 4.9: A) Bow-tie shape flow perturbation pattern. The separatrix is defined as the boundary between the far field displacement paths and the elliptical paths (Passchier et al., 1993). B) Grain-tailed complexes developed from bow-tie shape flow patterns for an idealized spherical clast. The red box encompasses the grain-tail complexes δ- (delta) and σ- (sigma) types used as shear sense indicators. σ-type tails (or wings) are formed by syntectonic recrystallization of the porphyroclast and are clear shear sense indicators. If the porphyroclast was initially elongated and recrystallizes syntectonically, the separatrix will form complex objects as deformation advances. Figs. extrated from Passchier & Trouw (2005).

- **Fractured porphyroclasts Rotation**

Porphyroclasts may be fractured and rotated during the shearing of the matrix (Fig. 4.10). The rotation sense of the fragments of the fractured grain can be evidenced by the slip direction of the microfaults. The direction of slip that the microfaults acquire will be dictated by the angle of the fractures respect to the shear direction(Fig. 4.10A, B).

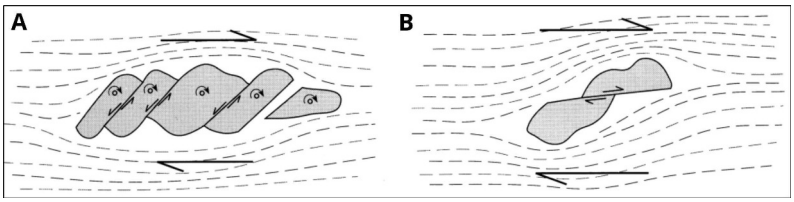

Fig. 4.10: Fractured porphyroclasts. The slip direction of the microfaults across the grain depends upon the angle between the fractures and the direction of shear. A) Domino fractured porphyroclast. Domino systems occur when the fractured grain forms a high-angle with the shear sense. The microfaults will acquire antithetic displacement direction. In this case, it is important to rely on the rotation direction of the fragments within the porphyroclast as shear sense indicator. B) Low-angle microfaults that slide synthetically to the bulk shear sense. In this case the shear sense can be extrapolated by the microfault movement. Figure extracted from Twiss & Moores (1992).

- **Porphyroblasts structures in mylonites**

Porphyroblast inclusion trails can be good shear-sense indicators. Porphyroblasts rotate as rigid bodies syntectonically to deformation of the matrix. As they rotate and grow, they may include adjacent minerals from the matrix. The inclusion trails exhibit the sense of rotation and thus, the sense of shear can be inferred (Fig. 4.11). Nevertheless, these structures are not recommended to be used as main shear indicators since there is much controversy about how well these are oriented in the S-fabrics direction. Furthermore, the rotation needs to be large to ensure the correct interpretation of the shear sense.

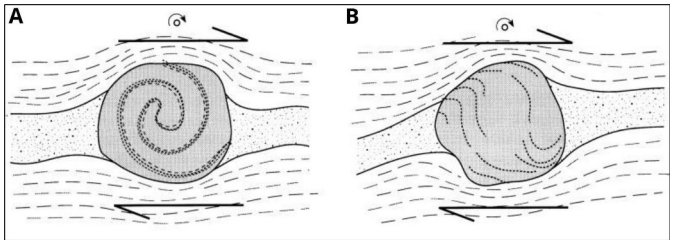

Fig. 4.11: Inclusion trails of matrix minerals into the porphyroblast. A) Spiralled inclusion trail. Thse kind of inclusion trails are typical for large amounts of rotation, and therefore are reliable shear-sense indicators. Nevertheless is recommendable not to use this criteria by itself, but as a support for interpretation of the shear sense. B) Non-matured inclusion trail. Small amount of rotation is not good enough shear sense indicator. Figs. extrated from Twiss & Moores (1992).

Based on the same principle, intertectonic and syntectonic porphyroblasts can be good shear indicators. Since porphyroblasts act like rigid bodies in a deforming mylonitic matrix, they rotate generating geometric relations between S_i (internal foliation) and the S_e (external foliation). Intertectonic porphyroblasts grow over a secundary foliation but the surrounding matrix is affected by a later deformation phase. Syntectonic porphyroblasts are formed by a single deformation phase.

- **Sheath folds**

These folds are caused due to great ductile deformation by simple and pure shear and flattering among other mechanisms (Reber et al., 2013). Sheath folds are generally “tube-shaped”,

meso-scale conical folds and are associated to high heterogeneous strain. Sheath folds formation involve rotation of the fold hinge (bent up to 180°). In field geology are used as bulk strain indicators and can also indicate sense of shear within mylonitic fault zones (Fig. 4.12).

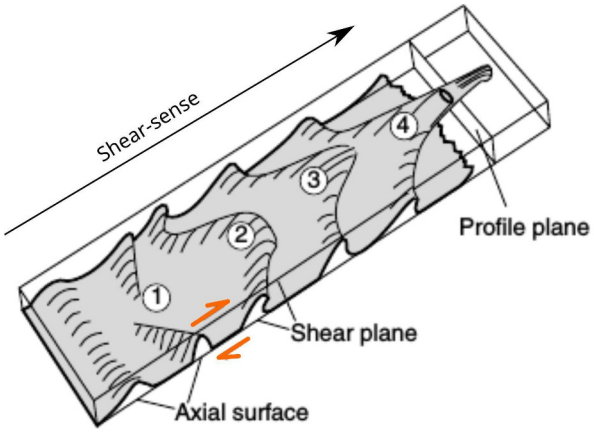

Fig. 4.12: Sheath folds are initially formed by the deformation of double plunging folds due to shear. From 1 to 4: Successive stages of a sheath fold development with accumulated shear strain, being 1 the scenario that has been subjected to less shear strain, and 4 a complete developed sheath fold. At higher shear strain (4), the fold hinge is totally folded (almost 180°) producing a "tube-shape" fold. Fig. extrated from Fossen (2010).

- **Mica-fish structures**

The mica-fish originates when a mica porphyroclast is fractured and the fragment of mica is peeled off from its original place. The mica fish is tilted against the sense of shear (following C-surfaces) with a high or a low angle (up to 30°). Mineral fish structures are deformed bodies that have a strong preferred orientation of mineral fish following the C-foliation (Passchier & Trouw, 2005). Mineral fish may form by the drag along zones of concentrated shear, although there are distinct formation mechanisms for each of the groups. Mineral fish may have different shapes and they can be used as shear sense indicators (Fig. 4.13).

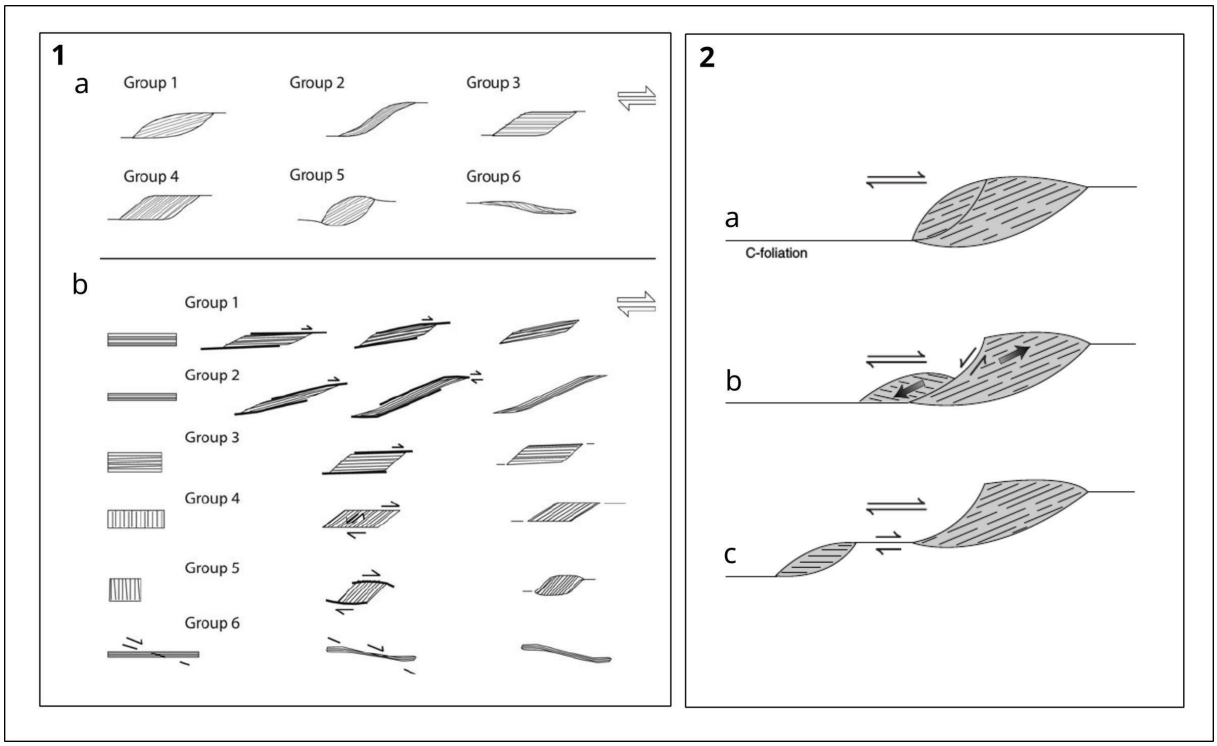

Fig. 4.13: 1a) Mineral fish groups according to the different shape in a dextral-shear context. 1b) The mineral fish groups development with dextral-shear from an initial position of the "to be" deformed mica clast. Figs. 1a & 1b in Passchier & Trouw (2005). 2) Successive development of mica-fish along C-surfaces from 'a' to 'c' by antithetic listric fractures in relation to the bulk shear sense. Figs. 2a, 2b, 2c extrated from Fossen (2010).

- **Fold transposition and fold hooks**

Fold asymmetry can be an asset for identifying the sense of shear. Fold transposition is the product of continued shearing, provoking reorientation of the short limbs of the affected folds parallel to the foliation (Fossen, 2010) (Fig. 4.14). Fold hooks commonly occur during metamorphism and shearing of layers with contrasted competence. In the case where shortening occurred parallel to the competent layers, the pre-existing fold limbs will rotate and thin down. In some cases, limbs would detach from the hinges generating fold hooks. As a result, the foliation and the bedding may be totally parallel (Fossen, 2010). Sometimes it may be difficult to recognize fold transposition.

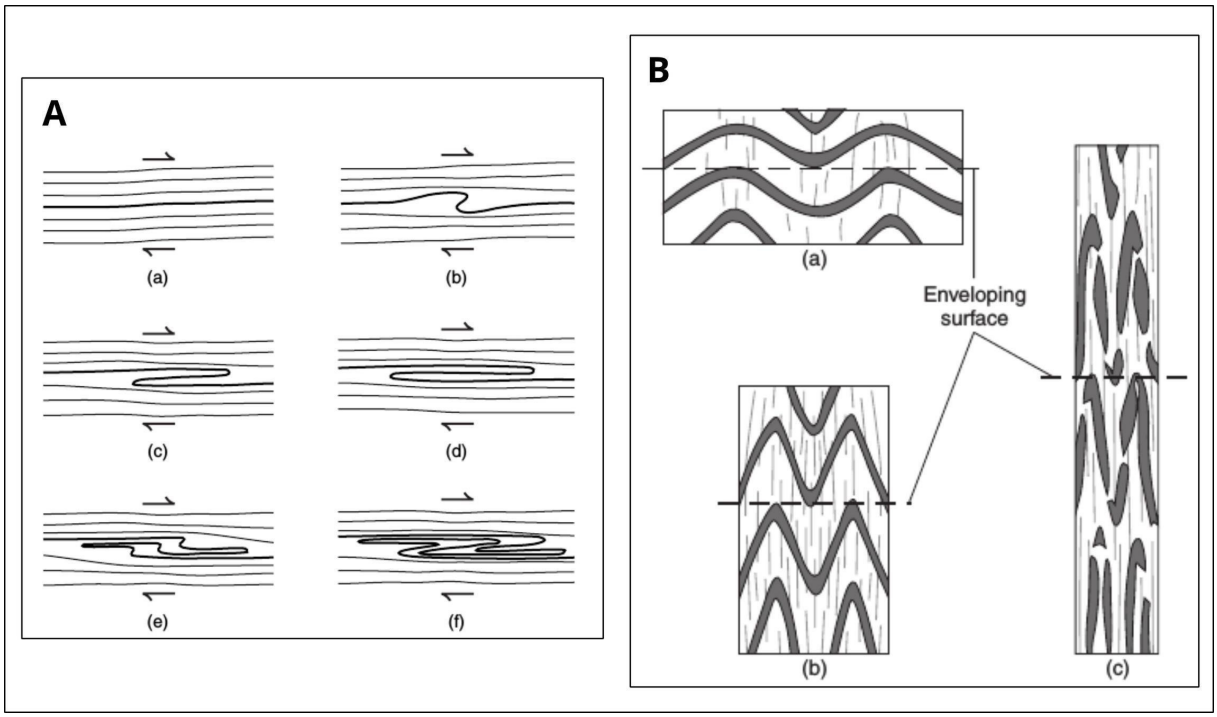

Fig. 4.14: A) Fold transposition in successive sheared layers from (a) to (f) produced by layer-parallel shear transport (non-coaxial deformation). B) Shortening parallel to the competent layers producing continuous fold transposition from (a) to (c) by coaxial deformation. In (c), limb attenuation and boudinage ended up producing disrupted folds (also fold hooks). Isoclinal folds recognition help to identify the fold transposition in the field. Figs. extracted from Fossen (2010).

- **Sigmoids**

Sigmoids are sheared bodies with internal deformation formed without a rigid central clast (Fig. 4.15) (Passchier & Trouw (2005)). The formation of sigmoids may be due to several reasons: complete recrystallization of the core of a σ-type object, inhomogeneous flow at the edges of the sigmoid, recrystallized deformed rectangular bodies or separation of asymmetric boudins or boudinage (Passchier & Trouw, 2005).

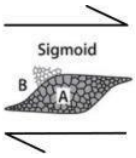

Fig. 4.15: Sigmoid indicating clockwise sense of shear formed by a polycrystalline grain of mineral A surrounded by matrix of composition B.

- **C–S and C–C' Foliations and S–C fabrics**

There are three kinds of foliations encountered within shear zones. (1) S-foliation is subparallel or oblique to the shear boundaries that follow the axis of the finite strain ellipsoid. Grains tend to elongate following the S-foliation. S-foliation is also referred as to mylonitic foliation/fabrics (Fossen, 2010). (2) C-foliation is parallel to the shear boundary and is also referred as to shear bands. C-surfaces form the main anisotropy within the shear zone. (3) C'-foliation is oblique to the shear zone boundary and its generation follows the apparition of the C-foliation,

displacing the latter. C'-foliations are discrete shear bands that appear with the accumulation of shear strain (Fossen, 2010).

S/C fabrics occur in medium-grade shear zones where the microlith is not as rigid as in well developed foliations (like in C–C'-structures). In S/C fabrics the C-foliation does not dominate as much as in other structures. C–S foliation (C-type cleavage) is part of the S/C fabrics. C-type cleavage (or C–S structures) is formed by C-surfaces transecting S-surfaces. The C-surfaces are rather straight and continuous. C-surfaces mark the bulk shear sense (not the XY plane of finite strain). The C–C'-structures (C'-type) are formed by short and wavy new shear bands (C'-surfaces) transecting the prior C-surfaces. The C'-foliations are synthetic to the sense of shear and are therefore good kinematic indicators (Fossen, 2010). This late foliation is usually anastomosing (Passchier & Trouw, 2005). See Fig. 4.16 for pictures and sketches of the three structures.

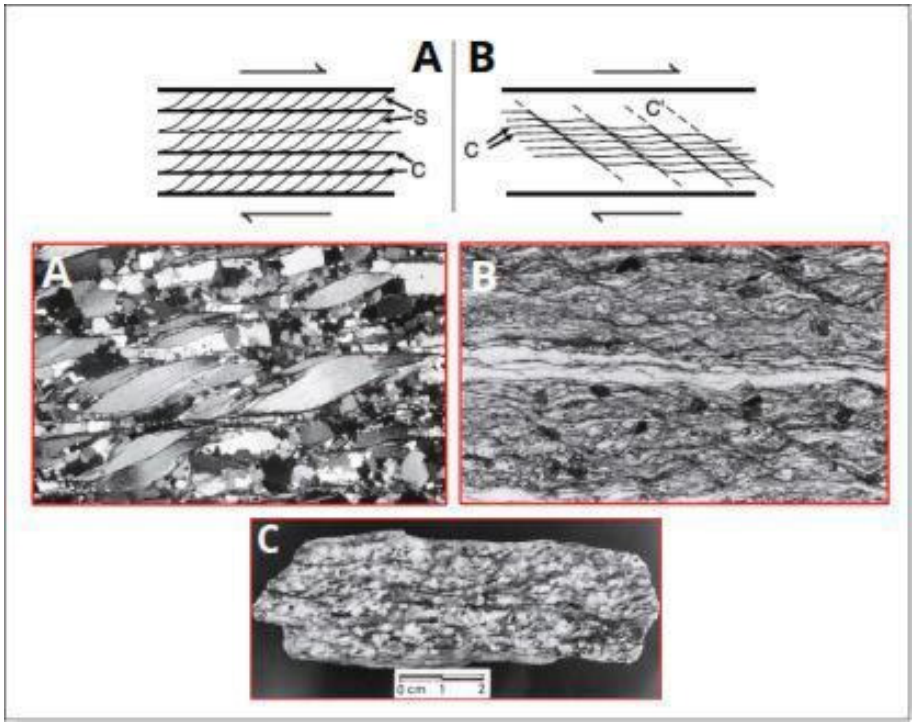

Fig. 4.16: Foliation fabrics with C-surfaces, S-surfaces and C'-surfaces. A)C–S structures sketch showing dextral shear sense (Fossen, 2010), and beneath a microphotograph 4 mm wide of a mylonite quarsite with mica-fish from Passchier & Trouw (2005). B) C–C'-structures sketch showing dextral shear sense (Fossen, 2010) and beneath a microphotograph 3,5 mm wide of a micaschist from Passchier & Trouw (2005). C) S/C fabrics in a granite hand-specimen from Passchier & Trouw (2005).

4.3 Architecture of fault zones

The generation of a fault starts with the formation of the process zone. This zone is characterized for being a zone of distributed cracking, where fractures will end up linking with each other after accumulation of strain and eventually will result in a new fault "plane" (Twiss & Moores, 1992). In the elastico-frictional regime, the process zone prior to the fault formation

thickens as the movement continues. The first fractures will accumulate more deformation, and therefore greater displacement. Once the fault plane is formed, it will continue growing from the tips outwards (Fossen, 2010). The fault zone, or portion of rock affected by faulting, might not be symmetrical at both sides of the fault. Generally, fracture density will decrease away from the fault in both the hanging and the foot-walls (Mitra & Ismat, 2001). Within the fault zone, fracturing and fragment rolling and sliding is very common and leads to brecciation and intense defomation producing cataclastic fault-rocks.

When a fault originates, the surrounding protolith rock is affected according to the distance to the fault plane. Therefore the fault zone can be divided into at least two categories: the damage or transition zone and the fault core. The outer contact between the undeformed wall rock and the damage zone (Caine et al., 1996) or transition zone (Yonkee, 1992) presents inhomogeneous deformation comprised by minor faults and breccias that do not involve large fault-parallel displacement (Mitra & Ismat, 2001). This boundary is usually irregular and should be analyzed at meso- and microscopic-scale (Mitra & Ismat, 2001). The contact between the damage zone and the zone of more intense deformation (fault core) is the closest to the fault plane. Mitra & Ismat (2001) referred to this zone as to the fault-related deformation zone (FRDZ).

Mitra & Ismat (2001) remarked that many detailed studies of fault zone models gathered the same kind of field observations. They concluded that distribution patterns of deformation are not uniform. Either at microscopic or at meso-scales, the maximum deformation usually appears in clusters in between undeformed pods of rocks (Mitra & Ismat, 2001). The textural evolution and distribution of deformation is governed by lithological and environmental factors (Rutter et al., 2001). The lithological controls are the structure and scale of fracture network, intensity of strain, and retrograde metamorphism, as well as protolith composition. The environmental factors are crustal depth (P, T conditions), fluid influx, and kinematic boundary conditions (imposed strain history and strain rate).

Fault zones vary in thickness depending on the displacement that the fault has undergone, generating thicker fault zones with greater displacements. The fault zone generally displays internal zonation corresponding to the deformation degree, e.g. from cataclasites or ultracataclasites to breccias towards the undeformed wall rock (Mitra & Ismat, 2001). The gouges are found in the core of the fault. Gouges are very fine-grain fragmented material with penetrative foliation also called ultracatacaclasites (Mitra, 1984). The ultracataclasites may either have fault-normal shortening due to pressure-solution mechanisms, or fault-normal extension by vein growth (Mitra & Ismat, 2001). Fine-grained cataclasites without penetrative foliation are found with an increasing distance from the core. In both sub-zones an anastomosing pattern alternating less-deformed and intensely deformed rocks can be recognized, which is observable also at microscopic-scale. At microscopic scale, a high density of microcracks can be a good indicator of the fault proximity.

In ultracataclasites, however, the microcracks might decrease in density due to their difficulty nucleating in reduced grain size. Microcracks could occur at elastico-frictional or quasi-plastic regimes.

The movement history may alter the fault zone architecture in diverse ways. The internal fault core zonation may be offset by later faults, fractured or might serve to accommodate new faulting episodes. Reiterated movement can increase the thickness of the fault zone when the fault core grain size is reduced because of strain hardening (Mitra, 1994). Instead, if the core experiences pressure-solution mechanisms, e.g. by differential mineral composition, softening will occur and only a thin part of the fault zone will be affected and deformed. If this is the case, the fault zone will not increase in thickness even with continued displacement along the fault (Mitra, 1994). Reiterated fault movement may result, thus, in either weakened or strengthened fault zones, which are type 2 and 1 respectively, defined by Means (1984) and Mitra (1984). Type 2 zone would be reactivated within the fault zone. Whereas, a strengthened fault zone (type 1) will promote reactivation between the fault zone and wall rock surface due to the contrast of competence. In the latter case, the recognition of secondary structures will be more difficult if the fault reactivation occurred parallel to the original fault orientation. In case of oblique reactivation, complex overprinting patterns will occur.

Reactivation usually occurs at a similar orientation as the relict fault-plane. That may be due to the weakening of the rocks compared to the fresh surrounding protolith (Rutter et al., 2001). Rutter et al. (2001) suggested that weakened fault zones may be due to the formation of fragmentary products leading to a loss of cohesion and an increase of porosity in fault rocks. This also may allow the fluid-rock interaction, weakening and increase of volume of the fault zone. Furthermore, foliation and chemical differentiation within the sheared rocks may lead to the formation of low competence clay bands within the fault zone (Rutter et al., 2001).

Architectural deformation patterns caused by superimposed deformation episodes may be acknowledged at a microscopic scale by morphological differences in microcrack populations related to different deformation events and cross-cutting relations. These criteria should be applied only within the FRDZ (fault-related deformation zone) (Mitra & Ismat, 2001). Microcrack distribution patterns for faults with multi-deformation histories may look the same as single-deformation patterns found across the area from the fault zone to the damage zone. Successive generations of microcracks may be identified by fracture characteristics and preservation modes (Mitra & Ismat, 2001).

Within mylonites, thick shear zones may comprehend the whole range of mylonitic rocks from mylonitic gneisses to ultramylonites (Twiss & Moores, 1992). Mylonitic rocks would systematically exhibit wider shear zones than faults formed at the upper crust (under the brittle regime). The thickness may range from 1 to hundreds of meters according to displacement.

This page is intentionally left blank

5 Apatite Fission Track (AFT) Methodology

The fission track method has consolidated as an important tool among thermochronological methods capable to provide significant thermal information. Fission track analysis is applied in a wide spectrum of geological problems such as thermal history modeling, as for in this thesis. The apatite fission track method provides information about the most recent exhumation history of rocks. The following chapter presents an overview of the key aspects to the fission track method and fundamental concepts.

5.1 Method Background

Uranium fission tracks were noticed much before their applications were discovered in the early 1960's. The earliest study reporting the existence of nuclear tracks came by the hand of Baumhauer (1894), who described them as anomalous figures in apatite crystals. After the invention of the transmission electron microscope (TEM), the nuclear tracks were better documented by Silk & Barnes (1959) and Young (1958). Chemical etching was a common practice in the 1950's to reveal crystal defects. It was not until the shared efforts of P. Buford Price, Robert M. Walker and Robert L. Fleischer that nuclear tracks were understood. In 1963, these three physicists developed a non-destructive method to date damage track-bearing solids. Etching the track-bearing solid is needed in order to count the fission tracks under a regular microscope. In the 1980's, many contributions about this recently developed method were made after an International Workshop in Pisa (Wagner & Haute, 1992).

Fission track is nowadays used to determine the long-term continental denudation, structural evolution of orogenic belts, sedimentary provenance and thermal history modeling. The application of fission track thermochronology to orogen and passive margin geological scenarios began around the 1980's (Gleadow et al., 1986).

5.2 Fission track formation

Damage or fission tracks are linear trails of disrupted atoms (Gallagher & Johnson, 1998) produced after the spontaneous fission of a ^{238}U atom. The spontaneous fission is a type of radioactive decay and occurs to very heavy nuclides of atomic number larger or equal to 90 (Wagner & Haute, 1992). The fission of other heavy isotopes (e.g. ^{235}U and ^{232}Th) is less likely to happen due to their long fission-half-lives, and thus fission tracks are presumably generated almost exclusively by ^{238}U isotopes (Wagner & Haute, 1992). The fission process involves the generation of two daughter nuclei from a heavy nuclide, in this case a ^{238}U isotope. The two daughters are new nuclides of similar atomic mass. The splitting of the parent involves the ejection of the two

daughters in opposite directions at very high speed, leaving a narrow linear damage track in the U-bearing crystal lattice.

The track-forming mechanisms in different solids are still matter of discussion and many contributors have added new insights to the topic. A broadly accepted model for explaining the track-forming mechanism was postulated by Fleischer et al. (1975), known as the 'ion spike explosion'. Fleischer et al. (1975) considered the specific ionization (which is the number of ions formed per unit of distance along the pathway of the moving particle) as criterion for the track-forming process (**Wagner & Van den Haute (1998)**). According to the 'ion spike explosion' model, the track formation occurs in three steps (Fig. 5.1) (Fleischer et al., 1975). The first step involves a charged particle product of the spontaneous fission of an uranium isotope and the atoms of the lattice affected along the particles trajectory. The positively, charged particle travels ionizing the atoms from the lattice, taking electrons from these to balance out its charge. The second step or reaction, is when the ionized atoms from the lattice repel each other for being positively charged (Coulomb respulsion) forming a series of vacancies in the crystalline lattice and filling interstitial spaces. Finally, what enables the observation of the fission track in transmission electron microscope (TEM) is the elastic relaxation of the stressed lattice. The damage trail will be broader than the particle itself after the elastic relaxation. The ion spike explosion model does not predict the track-formation according to, for instance, the crystallography of the solid (Gallagher & Johnson, 1998). Thereby, ion spike explosion model should be regarded as a simplification of the track-formation process.

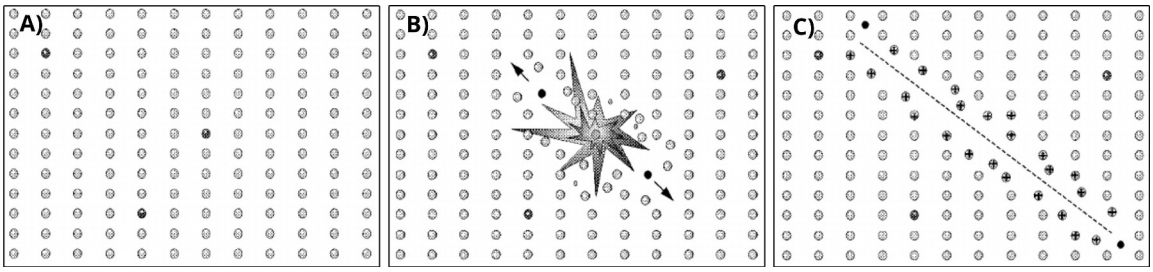

Fig. 5.1: 'Ion spike explosion' model in three steps described by Fleischer et al. (1975). A) Crystal lattice including some ^{238}U radioactive isotopes. The unstable isotopes are depicted in black. B) The second step of track-formation correspond to the spontaneous fission of one of the ^{238}U isotope. The daughter nuclei travel along a linear trajectory trapping electrons from the atoms of the solid lattice. C) The ionized atoms from the solid lattice are repelled from each other creating an interstitial space where the daughter nuclei passed through. The elastic relaxation causes permanent damage to the crystal lattice making feasible its observation under TEM.

The charged particle traveling at high speed through the solid will interact with the constituents of solid medium (**Wagner & Van den Haute (1998)**). The interaction of the particles with the constituents of the solid will decelerate them (the daughters from the spontaneous fission). The range, or distance traveled by the particle, will depend upon the needed stopping power to stop the particle that is creating the track. There are two types of stopping processes according to the energy of the particle (**Wagner & Van den Haute (1998)**). If the particle is moving

at high velocity and thereby, is charged with high energy, the electronic collisions or electronic stopping power will predominate as stopping process. The electronic collision process occurs when the velocity of the particle is such that the electrons are expelled off from the orbits to the crystal lattice. At lower energetic level, the nuclear collisions (or nuclear stopping power) take over as the main stopping process. This process involves the collisions of the particle with lattice atoms of the solid as main stopping process.

5.3 Track revelation

Revelation or visualization techniques have been developed in order to reveal latent fission tracks. Latent fission tracks, i.e. unetched fission tracks, are only possible to visualize under transmission electron microscope (TEM). The first workers to observe latent fission tracks under the TEM were Price & Walker (1962) and Silk & Barnes (1959). The etching techniques were developed successfully by the cited authors among others. Etching involves the attack to the detector (solid bearing fission tracks) with a chemical reagent. The attack with the etchant should be able to reveal the superficial fission tracks present in the detector. According to Fleischer et al. (1975), the etching is a suitable revelation technique due to the higher susceptibility to dissolution along the damage trail, which has low inter-atomic binding energy in its core in comparison to the non-affected apatite lattice.

The etching for apatite is typically made with a solution of 20 % diluted hydrofluoric acid (HF) at a temperature between 20 to 30 °C (Wagner & Haute, 1992). The dilution of the acid prolongs the etching time, so the results are easier to reproduce with the same boundary conditions (**Wagner & Van den Haute (1998)**). Dipping the apatites for 10 s into the diluted solution of HF acid is enough to enlarge the track marks up to an optimal point.

Track density is subjected to a number of parameters. Among them, the etching time is the most important factor. The etching process can be divided in three parts: (1) a first an initial phase with no track density, (2) a second phase called the underetching phase, when track density increase rapidly (rapid revelation of tracks), (3) and the final phase of slow increase in track density (Wagner & Haute, 1992). The optimal etching moment for track visualization is between the end of second and the beginning of the third phase (Gleadow & Lovering, 1977). Track density decreases together with the mean track length of annealed apatites for tracks oriented perpendicularly or at high angle of the crystallographic c-axis (Green et al., 1986). For that reason, it is advisable to discriminate those sections that not parallel to the c-axis of the apatite during the counting (external detector method).

The shape and orientation of the surface openings may depend upon the etchand, the crystallographic orientation of the mineral and the mineral itself. Those factors influence in etching

rate and etching efficiency. The etching efficiency in the apatite varies in the different crystallographic faces due to the anisotropic character of the mineral (Fleischer et al., 1975). In general, the etching rate is larger in the tip of the track deriving into a needle-like features in the internal surface (Wagner & Haute, 1992).

5.4 Track annealing

As introduced in the previous section, fission tracks have the capability to anneal or heal. The annealing of fission tracks was discovered in the first stages of development of the fission track dating method. (Fleischer & Price, 1964; Naeser, 1967) obtained younger ages by the fission track dating method than by $^{K}/_{Ar}$ and $^{Rb}/_{Sr}$ methods. Annealing takes place at different temperatures in different minerals. That occurs because each mineral has a different closure temperatures in which below it the tracks are preserved. Thus, above the closure temperature, a fission track would begin to anneal, which involves the shortening of tracks. The lengths of confined fission tracks are an asset for thermal history analysis (e.g.Gleadow et al., 1986).

5.4.1 Annealing in apatites

Annealing is the process of thermal fading of a fission track in which the damage trail in the crystal lattice is healed. It is an irreversible process that is affected by a number of factors (Gallagher & Johnson, 1998). The mechanisms behind fission track annealing are still poorly comprehended, yet it is known to be the consequence of thermal diffusion (Gallagher & Johnson, 1998).

The fission track stability varies for each mineral and it also depends on the cooling rate (Wagner & Haute, 1992). Thus, a given mineral (e.g. Apatite) may exhibit different track stability depending on the exhumation history of the rock. Apatite annealing properties should be considered carefully during the thermal modelling due to the great number of factors influencing the annealing behavior of fission tracks.

Annealing behavior in apatites is related to the apatite solubility, which can be assessed through Dpar measurements. Dpar refers to the mean maximum etch pit diameter oriented parallel to the crystallographic c-axis (Donelick et al., 2005). The chemical composition of the mineral influences the Dpar value, probably related to the solubility of the mineral phase (Donelick et al., 2005). It is demonstrated that grains with lower Dpar's are less resistant to annealing than grains with greater Dpar values (Carlson, 1990). Apatite mineral anisotropy seems also to control the annealing behavior of fission tracks within the grain. The fission tracks located in the basal plane of the apatite anneal quicker than the ones oriented parallel to the c-axis (Green & Durrani, 1977).

Fission track stability is linked to the closure temperature in which the fission tracks are preserved. As mentioned before, the closure temperature for apatite is estimated to be around 120 °C based on borehole studies and experimental analysis (e.g. Gleadow & Duddy, 1981; Naeser & Forbes, 1976). The closure temperature concept is usually an oversimplication, since annealing can occur in a range of 60 °C in most minerals (Gallagher & Johnson, 1998). That temperature range was referred as to the partial annealing zone (PAZ) by Wagner & Wuthrich (1979). The partial annealing zone temperature range for Durango apatites goes from ~60 °C to ~110 °C (Laslett et al., 1987). Empirical results obtained by several authors show that Cl-apatites are generally more resistant to annealing than F-apatites (e.g. Gleadow & Duddy, 1981; Green et al., 1986). On the contrary, Young et al. (1969) found that Durango Cl-apatites were easier to anneal than F-apatites. Barbarand et al. (1996) adverted that additionally to compositional changes, lattice structure and crystallographic imperfections may be equally important for annealing rate. Therefore, fission track susceptibility to annealing at different temperature conditions should be regarded as a sum of many factors. Nevertheless, temperature is the parameter of maximum significance responsible for annealing (Fleischer et al., 1965). Currently there is limited quantitative knowledge to develop a standard annealing algorithm encompassing all the parameters affecting annealing rate. The annealing algorithm used for modeling should be carefully chosen.

5.4.2 Apatite fission track system

Apatites usually include unstable isotopes of uranium and thorium in the crystal lattice, which makes apatites suitable candidates for fission track studies. Donelick et al. and co-workers (2005) described the apparition of apatite in smaller sizes than 300 µm. The tracks in apatite are preserved below 120 °C (closing temperature). The closing temperature of the apatite was established through diverse borehole studies and laboratory experiments (e.g Gleadow & Duddy, 1981 for the borehole of the Otway Basin). Above that temperature, the tracks begin to fade and they may obliterate completely (see next Section 5.4.1). The track stability has been demonstrated to be sensitive to the Cl^-/F^- ratio content within apatites (e.g. Gleadow & Duddy, 1981). Cl-rich apatites are more resistant to annealing, which may lead to misinterpretations of the age and may cause difficulties in thermal modeling. On the contrary, fluoroapatites (F-rich) are less resistant to annealing.

5.4.3 Track types

As mentioned previously, confined tracks are used as a diagnostic tool for thermal modeling. The confined tracks are non-truncated etched tracks that remain within the crystal (Fig. 5.2). Truncated tracks displayed in the polished surface are called semi-tracks. Semi-tracks are not commonly used to calculate track length distributions due to the errors involved in length projection (Gleadow et al., 1986). In confined tracks, the etchant should reach them through the crystal cleavage or through semi-tracks (Bhandari et al., 1971). There are two main types of

confined fission tracks according to Bhandari et al., 1971: 1) the tracks in tracks (TINT) and 2) the tracks in cleavage or cracks (TINCLE). The TINT refers to confined tracks that are connected to the surface by other semi-tracks of the polished crystal (Fig. 5.2). The TINCLE type of tracks become etched due to the natural cleavage conduits or cracks within the crystal, through where the etchant is transported to the confined track (Fig. 5.2). Donelick et al. (2005) also noticed confined tracks that are linked to the surface through a fluid inclusion or defect. This type of tracks are named 'tracks in defect' (TINDEF).

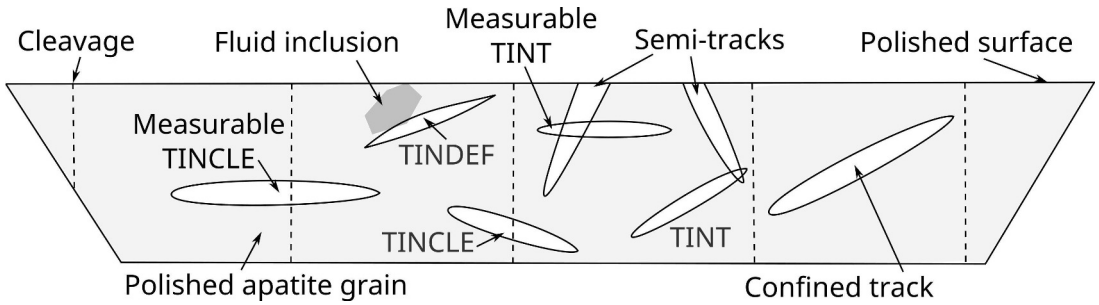

Fig. 5.2: Types of confined tracks according to the classification of Bhandari et al. (1971) and Donelick et al. (2005). Semi-tracks are also depicted in this illustration. The semi-tracks are the ones intersected by the polished surface. Whereas, the confined tracks remain within the crystal, and are reached by the etchant through different paths (TINT, TINCLE and TINDEF).

5.4.4 Track length distribution

The track length of fission track is a powerful tool for thermal modeling. Track length measurements account for the etchable length of the latent fission track (Wagner & Haute, 1992). The lengths of the tracks are subjected to the thermal conditions that the host rock undergo after the formation of the track. Tracks are formed at any moment of the thermal history and therefore, different generations of tracks can be determined in each crystal. Each track in a crystal could have been generated at different ages and have undergone distinct fractions of the host rock history. The recognition of the distinct generations of tracks allows to reconstruct the thermal and exhumation history of the rock.

Gleadow et al. and co-workers (1986) recognized and classified four main track lengths distributions according to distinct thermal histories (Fig. 5.3). The first distribution is typical for rocks that have undergone rapid cooling. The second recognized type is characteristic for rocks that have had a slow and steady cooling along the partial annealing zone (PAZ). The third distribution type corresponds to rocks that have been subjected to two differentiated episodes of elevated temperature. Finally, the fourth recognized distribution type is characteristic for complex histories with several track generations.

The first cooling type is characterized by a symmetrical, narrow, uni-modal track length distribution (Gleadow et al., 1986). The mean track length (MTL) range between 14 to 13,5 µm.

This track length distribution is constituted by just one singular episode of rapid cooling followed by thermal quiescence. Volcanic rocks are maximum representative of this type (Fig. 5.3a).

The second type of distribution represents slow cooling through the partial annealing zone (PAZ). Gleadow et al. (1986) suggested this type to be the characteristic cooling of crystalline basements, assuming no thermal disturbances during exhumation. This distribution of track lengths is characteristically negatively skewed (Gleadow et al., 1986). The MTL is smaller than the previous group and its range goes from 12,5 to 13,5 µm (Fig. 5.3b).

A bimodal distribution of track lengths was also well documented by Gleadow et al. (1986). This third type comprehend two well differentiated peaks of MTL and can be regarded as a variety of the 'mixed' distribution type (Fig. 5.3c). The thermal history of this distribution involves an episode of elevated temperature conditions after the first initial cooling. The tracks with shorter lengths represent the oldest tracks which underwent partial annealing during the thermal disturbance. The thermal event can be quantified by the MTL of the shorter track generation.

The fourth and last recognized distribution corresponds to the 'mixed' type. This distribution is characterized by a wide unimodal peak of MTL with a large standard deviation. It implies a complex thermal history of the host rocks difficult to decode (Fig. 5.3d).

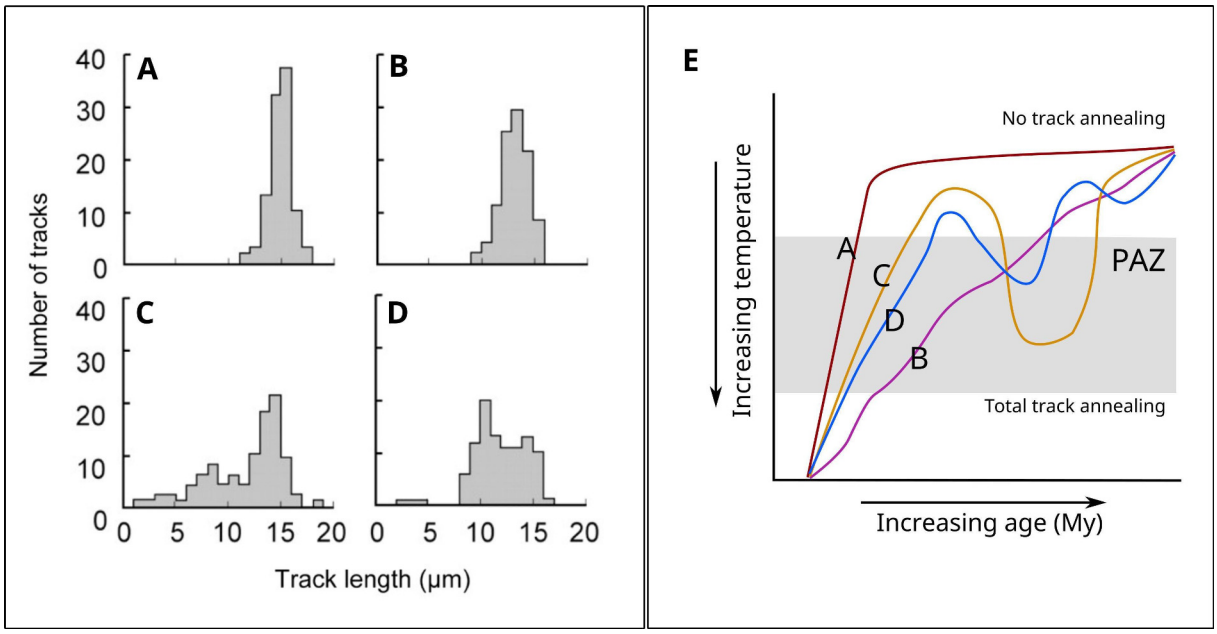

Fig. 5.3: Cooling styles distribution types after Gleadow et al. (1986). A) Inferred rapid cooling and subsequent thermal stability. B) Slow cooling through the PAZ. C) Bimodal distribution caused by a thermal disturbance. Two well differentiated cooling episodes are inferred. D) Mixed unimodal distribution. A broad peak of MTL caused by a complex thermal history or insufficient thermal disturbance regarding time or/and temperature. E) Paths of the different distribution scenarios through the PAZ.

One of the observations made by Gleadow and co-workers was that spontaneous tracks are generally shorter than induced tracks. Furthermore, induced tracks in apatite usually comprehend a length between 15,8 to 16,6 µm (Gleadow et al., 1986). Spontaneous tracks in apatites are usually not older than 500 Ma even for long-term exhumed basement rocks.

5.5 Age calculation

The fission track analysis is most commonly carried out with apatite, zircon or titanite (sphene). These three minerals usually contain an optimal amount of ^{238}U for generating fission tracks in terms of million years, whose concentration ranges from ~1 to 1000 ppm (Gallagher & Johnson, 1998). The basis of the fission track dating method falls into the assumption that almost exclusively all the natural fission tracks in Earth are generated by the spontaneous fission of an ^{238}U isotope (Wagner & Haute, 1992). ^{238}U fission tracks are generated at a constant rate through time (Gallagher & Johnson, 1998).

5.5.1 External detector method

There are two ways of proceeding with fission track analysis: (1) the grain-population methods and (2) the grain-by-grain methods (Wagner & Haute, 1992). Within the grain-by-grain methods there are three types: the external detector, re-etching and repolish techniques. On the other hand, laser ablation (LA-ICP-MS) provides accurate values of ^{238}U concentrations and it is quicker than the conventional methods, although it is destructive method (Hasebe et al., 2004). The external detector zeta calibration method is preferred by numerous thermochronologists because of all its advantages, among them that it is non-destructive nature. It has been recommended by the Internation Union of Geological Sciencies Working Group (Gallagher & Johnson, 1998). Along with other advantages, it brings the possibility to date each grain individually (Gallagher & Johnson, 1998; Wagner & Haute, 1992). Therefore, the distribution of uranium is not assumed to be uniform as for other techniques.

The external detector method involving zeta calibration is used in the present study. In order to determine the age of a sample is necessary to determine the ^{238}U content. In the external detector method, the means to obtain that and other values is establishing the density of spontaneous and induced fission tracks for a specific area (Durrani & Bull, 1987). The external detector method is based in the principle stated by Steiger & Jäger (1977) that the $^{238}U/^{235}U$ ratio is constant in nature. The spontaneous or natural fission tracks, as mentioned previously, are formed exclusively by ^{238}U; whereas induced tracks are generated only by ^{235}U isotopes. The fission of a ^{235}U isotope is achieved through the thermal neutron irradiation, whereas neither ^{238}U nor ^{232}Th atoms produce fission tracks under these circumstances (Donelick et al., 2005; Gallagher & Johnson, 1998). Therefore, the induced fission tracks are directly related to the ^{235}U content and the natural fission tracks are strictly associated to ^{238}U isotopes.

The external detector method requires the revelation of latent fission tracks in apatite crystals (Wagner & Haute, 1992). The etching will be made on the polished grain mount containing the embedded apatites (Fig. 5.4.B). Afterwards, the detector will be attached on top of the polished surface of the grain mount (Fig. 5.4.C). The detector is a thin muscovite with no uranium content.

The detector foil should be in strict clean conditions in order to avoid any interference and bias of results (Durrani & Bull, 1987). The grain mounts with the attached detector will be introduced in the irradiation beam tube together with different standards (e.g. Durango sandstones and Fish Canyon tuff) as a control. After the thermal neutron irradiation, induced fission tracks from ^{235}U will be generated in the crystal (Fig. 5.4.D). Some induced fission tracks would have cross-cut the polished grain and the detector. Finally, the detector would be etched with the purpose of enlarging the induced fission tracks in the mica (Fig. 5.4.E). As the final step, the sandwich will be dismantled and grain mount and mica will be placed in the same plate to proceed with the counting (Fig. 5.4.G).

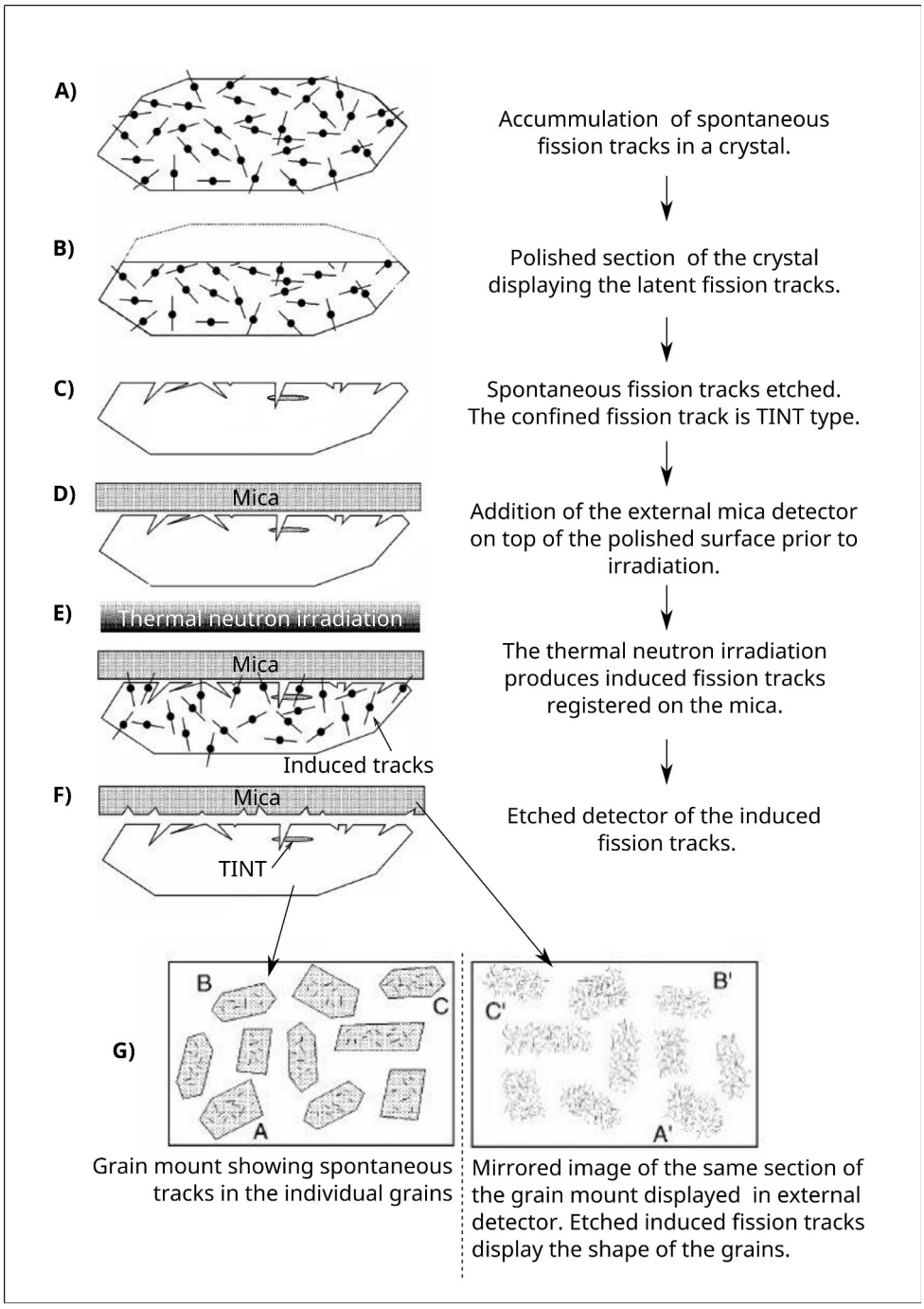

Fig. 5.4: The external detector method step by step, after Hurford & Carter (1991) and modified from Gallagher & Johnson (1998). A) Polished grain of apatite in the grain mount. B) Etching of the grain mount to enlarge the spontaneous fission tracks. C) Attachment of the detector onto the polished grain mount (muscovite crystal without U). D) Induced fission tracks after thermal neutron irradiation. E) Etching of the mica detector to enlarge the induced fission tracks. G) Product ready for counting: grain mount to the left and mica to the right. This will be further explained in the next chapter.

5.5.2 Calculation of the age of the samples

The fission track method is based on the equation of constant radioactive decay of a parent to a stable daughter (Wagner & Haute, 1992). The radioactive decay is a random process. The rate of decay is proportional to the number of parent atoms (N) remaining at a given time (Eq. 5.1).

$$-\frac{\partial N}{\partial t} = \lambda \cdot N \tag{5.1}$$

Where:

λ : decay-constant
N : number of nuclei from the radioactive isotope present

At initial conditions ($t = t_0$) non of the parent atoms have produced any daughter ($N = N_0$) (Eq. 5.2). The mathematical expression for initial conditions (Eq. 5.2) can be found by the integration of the first equation (Eq. 5.1).

$$N_0 = N \cdot e^{\lambda \cdot t} \tag{5.2}$$

Where:

N_0 : initial parent nuclides

The initial number of parents can not be measured directly, but can be expressed as function of the daughter nuclides (D) or the remaining parent isotopes at a given moment (Eq. 5.3).

$$D = N_0 - N \tag{5.3}$$

The substitution of N_0 in Eq. 5.3 (between Eqs. 5.2 and 5.3) gives the mathematical expression for the number of daughter nuclides in function of time (Eq. 5.4).

$$D = N \cdot e^{\lambda \cdot t} - N \tag{5.4}$$

For this purpose, the variable that we wish to solve is time (Eq. 5.5). In the Eq. 5.5, the number of daughter nuclides is already known (D), which is the revealed tracks produced by the decay of ^{238}U.

$$t = \frac{1}{\lambda} \log\left(\frac{D}{N} + 1\right) \tag{5.5}$$

After the basics presented above, the fission track age equation gets slightly more complicated. The spontaneous fission of ^{238}U atoms occur simultaneously to the α-decay. The total decay constant is, therefore, given by the addition of both spontaneous and α-decays ($\lambda_d = \lambda_f + \lambda_\alpha$).

For the ^{238}U atom, the proportion of spontaneous decays occurs at a fixed ratio to the total number of decays $\left(\frac{\lambda_f}{\lambda_d}\right)$. The total number of spontaneous decays is expressed as function of time and remaining parents (Eq. 5.6).

$$N_s = \left(\frac{\lambda_f}{\lambda_d}\right) \cdot {}^{238}N \cdot \left(e^{\lambda_d \cdot t} - 1\right) \tag{5.6}$$

Where:

N_s : number of spontaneous fission tracks
^{238}N : number of remaining ^{238}U

The induced tracks are used in order to measure the remaining uranium in the sample. The induced tracks are achieved through the thermal neutron irradiation in a nuclear reactor, that provokes the artificial fission of the ^{235}U atoms. The equation expressing the number of induced fission events is as follows (Eq. 5.7):

$$N_i = {}^{235}N \cdot \sigma \cdot \phi \tag{5.7}$$

Where:

ϕ : the neutron fluence $\left({}^{neutrons}/_{cm^2}\right)$
^{235}N : number of remaining ^{238}U
σ : represents the cross-section, that is the probability for an atom of ^{235}U to absorb a thermal neutron.

The $^{235}U/^{238}U$ ratio (I) is constant in nature, for what it is possible to replace by the ^{235}N of the past equation by $I \cdot {}^{238}N$ (Eq. 5.8).

$$N_i = {}^{238}N \cdot I \cdot \sigma \cdot \phi \tag{5.8}$$

Where:

I : $\left({}^{235}U/^{238}U\right) = 7.2527 \cdot 10^{-3}$
N_i : induced fission events

The fission track equation (Eq. 5.9) is obtained by the substitution of N_i into the Eq. 5.6:

$$t = \frac{1}{\lambda_\alpha} \cdot \log\left[\left(\frac{\lambda_\alpha}{\lambda_f}\right)\left(\frac{N_s}{N_i}\right) \cdot I \cdot \phi \cdot \sigma + 1\right] \tag{5.9}$$

The densities of induced and spontaneous tracks can be measured through the microscope. The track density is the number of observed tracks per a certain area. The measured densities will depend upon the type and duration of the etching process and of the observation conditions (Eqs. 5.10a and 5.10b).

$$\rho_s = g_s \cdot N_s \cdot R_s \cdot \mu_s \cdot f(t)_s \cdot q_s \tag{5.10a}$$

$$\rho_i = g_i \cdot N_i \cdot R_i \cdot \mu_i \cdot f(t)_i \cdot q_i \tag{5.10b}$$

Where:

- $\rho_{s,i}$: spontaneous and induced track densities (number of tracks/unit area).
- $g_{s,i}$: the geometric factor refers to the initial geometry of the of the pre-etched sample surface.
- $R_{s,i}$: the average length of a track after the etching process (nearly identical)
- $\mu_{s,i}$: the etching efficiency factor (depending upon the used technique)
- $f(t)_{s,i}$: the etch time factor (depending upon the used technique)
- $q_{s,i}$: the observation factor (depending upon the used technique)

The practical age equation (Eq. 5.13) is obtained if the spatial track densities are substituted by the observed planar track densities. Where, the factor G is the initial geometry ratio of the counted surfaces (Eq. 5.11). The factor Q is the personal bias of the analyst or observer, considered as a procedure factor (Eq. 5.12) (Wagner & Haute, 1992).

$$G = \frac{g_i}{g_s} \tag{5.11}$$

$$Q = \mu_i \cdot f(t) \cdot \frac{q_i}{\mu_s} \cdot f(t) \cdot q_s \tag{5.12}$$

$$t = \frac{1}{\lambda_\alpha} \log\left[\left(\frac{\lambda_\alpha}{\lambda_f}\right)\left(\frac{\rho_s}{\rho_i}\right) \cdot Q \cdot G \cdot I \cdot \phi \cdot \sigma + 1\right] \tag{5.13}$$

5.5.3 Age standard approach: Zeta calibration

This approach is one of the two developed for fission track analysis. The absolute approach lays the foundation on the fission decay-constant (λ_f) and the neutron flux (ϕ). These two parameters are poorly constrained, which makes the age calculation less reliable. The method used in this thesis involves the zeta-calibration of age standards, which was promoted in first place by Fleischer & Hart (1972) and Fleischer et al. (1975). Hurford & Green (1982) and Hurford & Green (1983) developed it further and recommended it as the preferred fission track method. The zeta calibration procedure requires the use of geological standard samples of known age to avoid the use of physical constants.

The principles for this method lay on the factors Z and Q (the latter was introduced previously, Eq. 5.11). The ζ-value (Eq. 5.14) is derived from the analysis of standards of known age that are irradiated together with samples of unknown age (same ϕ). All the samples of unknown age and the age standards are analyzed with the same procedure (same Q). The age of the samples is achieved through a comparative study of the track densities obtained for the age standards and the samples of unknown age (Eq. 5.15). For computing the ζ- value the expression used is as follows:

$$\zeta = \frac{\left(e^{\lambda_d t_{std}} - 1\right)}{\lambda_d \left(\frac{\rho_s}{\rho_i}\right)_{std} \cdot g \cdot \rho_d} \tag{5.14}$$

Where:

t_{std} : age of the standard
$(\rho_s/\rho_i)_{std}$: ratio of spontaneous to induced fission tracks counted on the standard
ρ_d : is the track density in a dosimeter (a glass of known uranium concentration)
λ_d : α decay constant of ^{238}U

The age equation with this variable replaced will be the following:

$$t = \left(\frac{1}{\lambda_d}\right) \ln\left(1 + \lambda_d \cdot \zeta \cdot g \cdot \rho_d \cdot \left(\frac{\rho_s}{\rho_i}\right)\right) \tag{5.15}$$

Where:

t : age
λ_d : α decay constant of ^{238}U
ρ_d : is the track density in a dosimeter (a glass of known uranium concentration)

The ζ-calibration method is an accurate way of proceeding with the fission track analysis because, in addition to the reasons mentioned before, it balances the analyst bias during the counting process.

5.5.4 Chi-square (χ^2) test

In order to do a good sampling for statistical analysis is necessary to pick more than 10 grains within one sample (Wagner & Haute, 1992). Regularly, 20 to 30 grains are counted for each sample. The counted areas of each grain do not need to be the same (Wagner & Haute, 1992). However, the area counted in one grain for spontaneous fission tracks should be the exact same as for the induced fission tracks area (Galbraith, 1984; Galbraith & Laslett, 1985).

For each grain the analyst will obtain a ratio between N_s/N_i, which will be a good estimation to the ρ_s/ρ_i ratio. The variation in ρ_s/ρ_i ratio follows a Poissonian statistical distribution, although experimental results suggest that in some cases there are more variables involved. In general, the uranium content for each grain should not affect the ρ_s/ρ_i ratio, since the ratio is individual for each grain. The ρ_s/ρ_i ratio should be very similar for each grain in a crystalline sample.

Variations in the ρ_s/ρ_i ratio among different grains of the same sample may represent a problem for age calculation and could have geological significance. Poisson statistical analysis may fail to predict these variations. The Chi-square (χ^2) was developed by Galbraith (1981) to assess whether the variations among ρ_s/ρ_i ratio of the grains in one sample are significantly large or, on the contrary, fall into the Poissonian distribution. In other words, the chi-square test is applied to calculate the dispersion of ages in a single grain. The Chi-square test formula is as it follows (Eq. 5.16):

$$\chi^2 = \frac{1}{(N_s \cdot N_i)} \sum_{j=1}^{n} \frac{(N_{sj} \cdot N_i - N_{ij} \cdot N_s)^2}{(N_{sj} + N_{ij})} \tag{5.16}$$

Where:

N_s : number of spontaneous fission tracks
N_i : number of induced fission tracks
N : total number of grains
N_{sj} : number of spontaneous and induced tracks in grain j.
N_{ij} : number of induced and induced tracks in grain j.

When the χ^2-test fails for one sample, there are less than 5 probabilities of finding the same χ^2 value and it means that the ρ_s/ρ_i ratio is not homogeneous for that sample. In general, crystalline samples should pass the Chi-square test, whereas sedimentary samples from different provenance fail the test.

The radial plots for each sample display the age dispersion for each grain of the sample (y) against precision (x) (Galbraith, 1988, 1990). The radial plot is a good visual support that also displays the convenient age scale and the central age.

5.5.5 Error age calculation

The precision of fission track age, or error in age calculation, is determined by the neutron fluence (ϕ) and the ρ_s/ρ_i ratio ($= R$). The relative errors on ϕ and R are expressed as s_R/R and s_ϕ/ϕ respectively in the relative error age (s_t/t) formula (Eq. 5.17).

$$\frac{s_t}{t} = K\sqrt{\left(\frac{S_R}{R}\right)^2 + \left(\frac{S_\phi}{\phi}\right)^2} \tag{5.17}$$

Where $K \approx 1$ for samples with ages <600 Ma and the s_R/R (or relative error of spontaneous to induced fission tracks) is given by conventional Poisson statistics when using a grain-by-grain procedure, as in this case. The relative error of the track density ratio (R) is expressed as follows (Eq. 5.18):

$$\frac{S_R}{R} = \sqrt{\frac{1}{N_s} + \frac{1}{N_i}} \tag{5.18}$$

Where:

N_i : total number of induced fission tracks
N_s : total number of spontaneous fission tracks

This page is intentionally left blank

6 Sampling strategy and structural data acquisition

The samples used for AFT dating were collected for this thesis during the fall of 2013. Some thin sections and hand-specimens were provided by my supervisor Dr. A. Ksienzyk.

6.1 Sampling strategy for the horizontal profile across the Lærdal-Gjende fault

The sampling for the apatite fission track dating was carried out in November 2013. Approximately 5kg or more of rock were collected for each of the 15 samples. The rock was extracted by hammer and chisel from the outcrop into pieces of various centimeters long. The rest of the crushing was carried out at university by hammering up to optimal size in order to introduce the rock fragments in the fine-crushing machine.

The sampled lithologies were diverse and some of them did not present high quality apatite. The sampled rocks belong principally to the Jotun-Valdres complex. Some rocks from the Valdres formation were also sampled (Fig. 6.1). The Valdres formation is composed by younger rocks than in the Jotun nappe which correspond to lower Paleozoic cover of the Baltic Shield basement. These rocks appear typically highly deformed. They behaved as lubricant between thrust sheet and para-auchtocton migmatitic gneisses in the area of study. The Jotun nappe rocks encompass gneisses from different protoliths deformed at granulite and amphibolite metamorphic conditions. Aside of the sampled rocks from the Jotun nappe unit, the other rock samples were collected from the para-auchtocton unit, which are exposed in the Lærdal and Fillefjell erosional windows (Fig. 6.2). Cataclasites and mylonites were also included for apatite fission track dating (Fig. 6.2). In general, mica-rich rocks are expected to have a favorable apatite quality and content. Mafic rocks rich in Ti_3^+ usually contain relatively high content of apatite.

As mentioned before, the samples were collected from the hanging and the footwall blocks of the Lærdal-Gjende faul. The adopted strategy was to sample the different lithologies along the roads going from the Vinedalen locality up to Øvre Årdal. The roads taken were E16, Rv5, Rv53 and Fv243 (Fig. 6.1). The objective was to sample close and far away from the Lærdal-Gjende fault in both fault blocks. The main purpose is to detect the uplift of the hanging and the footwall blocks, as well as the influence span of the fault in the study area. The sample EC-13 belongs to the Fillefjell window, which is affected by another superficial fault rooted within the para-auchtocton gneisses, parallel to the Lærdal-Gjende fault. That may create some complications to determine the span of influence of the Lærdal-Gjende fault. On the other hand, this brings a good opportunity to observe the uplift pattern across distinct crustal blocks within the LGFS.

6.2 Structural data acquisition: fieldwork and thin sections

The main focus of the fieldwork at Lærdalsøyri outcrop was to asses the degree of deformation along 100 m of cataclasite. The cataclasite was analyzed through the transect of the Raudbergestunnelen, which is oriented SE-NW almost perpendicularly to the observation plane corresponding to the Lærdal-Gjende fault. The mylonites of the footwall were also documented together with the fault gouges. The mylonites have an apparent dip of 35° at the Lærdalsøyri outcrop. Less deformed wallrock from the para-auchtocton migmatitic gneisses was studied with the purpose of providing some petrographic and structural descriptions.

For the elaboration of this thesis, a total of 18 thin sections were made across the fault zone. 5 more samples of fault rocks provided by my supervisors are also included in this study. The thin sections were extracted from the 250 m of footwall mylonites and from the first 100 m of the hanging wall cataclasites. The samples were cut perpendicular to transport plane in the XZ plane of observation, which is NW-SE oriented. The fault dips between 30 and 55°.

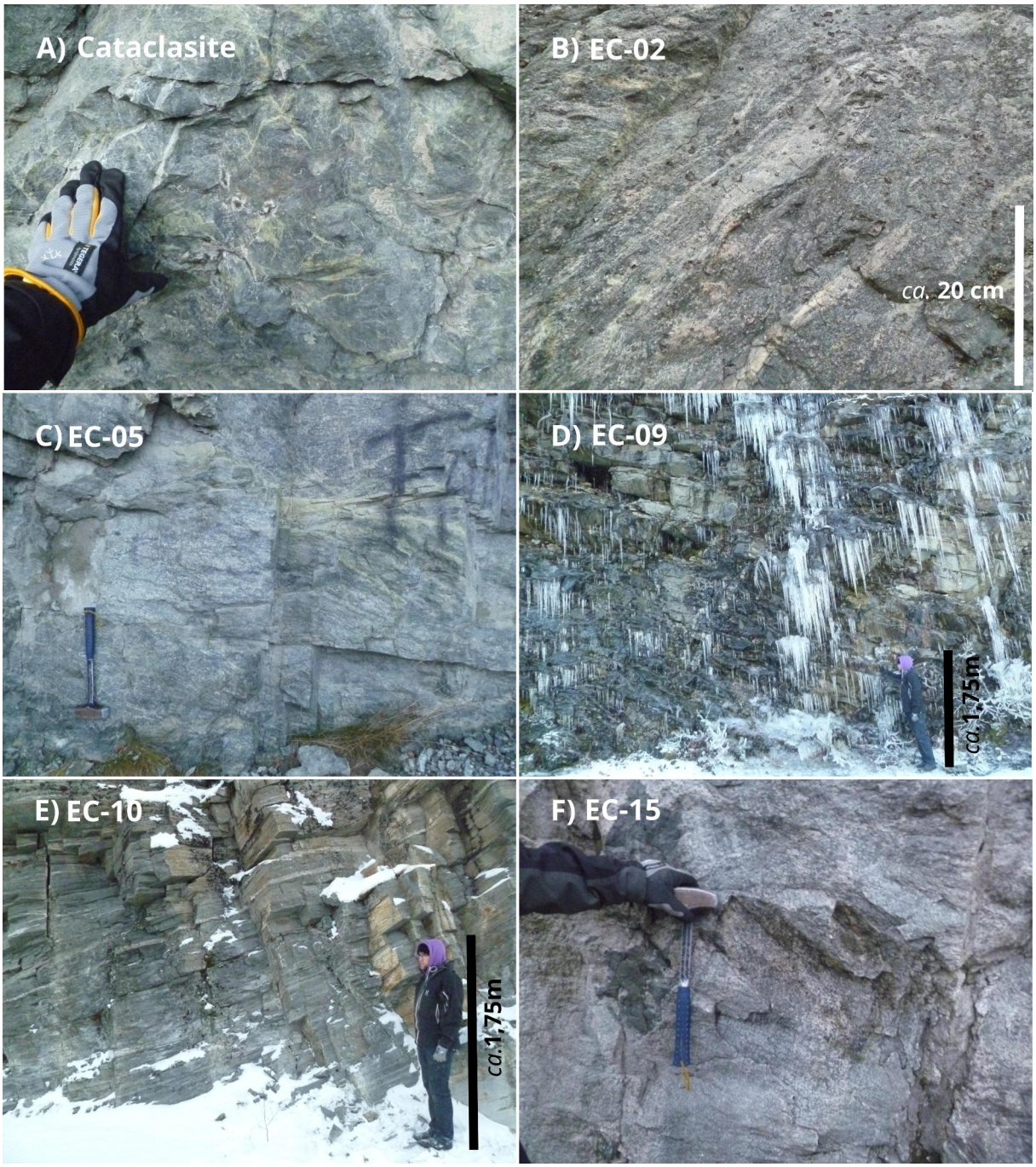

Fig. 6.1: Selection of outcrops where the samples were taking from. A) Picture of the cataclasite from the hanging wall of the Lærdal-Gjende fault in the Lærdalsøyri outcrop, B) Outcrop where the sample EC-02 was collected. The rock lithology is difficult to classify in the field because of the alteration degree. It is possible to appreciate green veins cross-cutting the rocks, most likely filled with epidote. The felsic component is abundant (plagioclase) and the mafic component can be pyroxene. The rock type is officially classified as part of an anorthosite complex. C) Sample EC-05 corresponds to mylonites overprinted by brittle deformation, D) Sample EC-09 is part of the anorthose complex of the Jotun nappe cut by dykes. Field assistant as scale. E) Sample EC-10 corresponds to a well foliated meta-arkose from the Valdres formation. Field assistant as scale. F) Sample EC-15 is part of the Fennoscandian basement, 1 km away from the fault. It is a migmatitic gneiss with granitic to monzogranitic protolith.

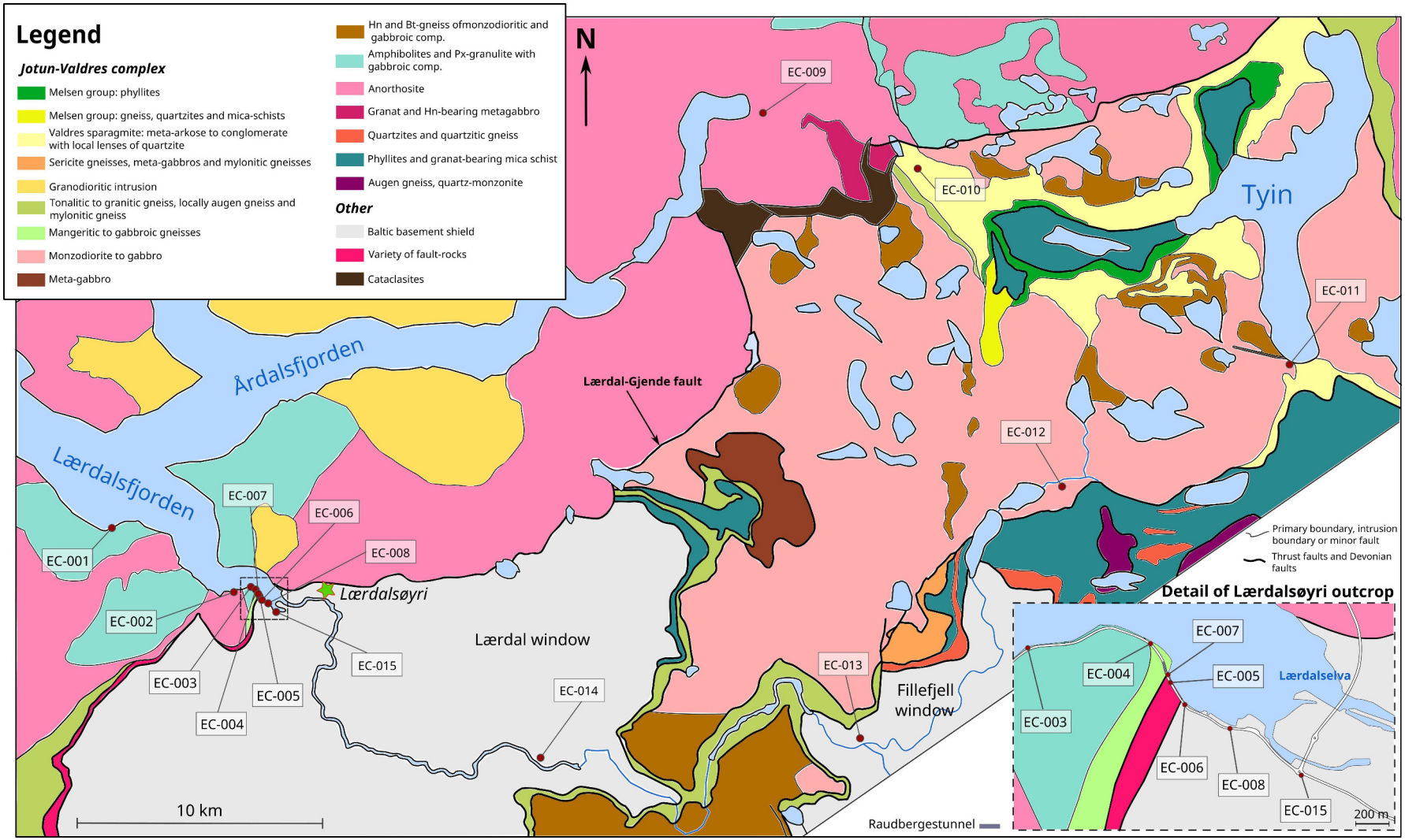

Fig. 6.2: Sampling locations for apatite fission track dating in both blocks of the Lærdal-Gjende fault. A detail of the Lærdalsøyri outcrop is attached in the right corner.

This page is intentionally left blank

7 Analytic procedure for Apatite Fission Track thermochronology

Apatite fission track analysis is used in the present study to constrain the thermal history of the latest deformation events of the Lærdal-Gjende fault. The sample set used for the analysis encompasses 10 samples of rock from few meters to some kilometers away from the Lærdaløyri outcrop. In order to carry out the fission track analysis is necessary to separate the apatite content and prepare grain mounts for irradiation. The present chapter explains all the steps followed to elaborate this apatite fission track analysis using the External Detector Method (EDM). A workflow diagram for all the followed analytic steps is also included in this chapter (Fig. 7.2).

7.1 Mineral separation

Each sample collected in the field was reduced to pieces of few centimeters in situ. In order to get the apatite content of each sample, the rocks needed to be crushed up to sand size with the Pulverisette 300 disc-mill. The product obtained after using the disc mill was sieved and the <315 µm fraction was used on the Holman Wilfley table. The settings for the Holman Wilfley table were adjusted according to speed, angle and vibration. The Wilfley table separates minerals according to their density (i.e. lighter and denser than $\geqslant$2,8 g/cm^3). Within the heavy fraction, heavy minerals such as apatite, zircons, monazites, magnetites, pyrites among other are expected to be encountered. Therefore, the heavy fraction obtained by the Wilfley table was selected for further heavy liquids separation in order to collect the apatite fraction (3,10 to 3,20 g/cm^3). The first heavy liquid separation procedure was performed with a sodium polytungstate solution (SPT), whose density is close to 2,87 g/cm^3 (Tagami et al., 1988). Both lighter and heavier resulting portions were dried at a 60 °C in a dry oven for hours. The heavier remaining fraction bearing the apatite was selected for magnetic separation. The magnetic separation was performed with a Frantz magnetic separator. Strongly ferromagnetic minerals, such as magnetite and hematite, were separated manually by a regular magnet. In order to separate correctly magnetic from non-magnetic minerals, the Frantz separator was run more than 3 times varying on the sample. The first runs' settings were made at 0,3 A with an inclination of ca. 15°. The further runs were made at 1,2 A with an inclination of ca. 15°. The non-magnetic fraction was introduced into diiodomethan (DIM) liquid, whose density is 3,33 g/cm^3 (Tagami et al., 1988). After some minutes in the DIM liquid, the heavier minerals were separated from the lighter. In this case, the heavier fraction was not used The lighter portion carrying, mainly, but not exclusively apatite was dried at 60 °C in a dry oven. The grain mount process started once the apatite portion was totally dried.

7.2 Grain mount preparation

For the preparation of the grain mounts that will be send to irradiation it is necessary to select the best apatite crystals within each sample. A first sieving of the samples was made for the samples with more amount of apatite in order to separate crystals smaller than 100µm. After collecting both fractions with <100 µm and >100 µm, the latter fraction is used for the grain mount (Fig. 7.2). Some of the samples were very poor in apatite and all the grains were directly embedded without sieving (EC-07, EC-02, EC-03 and EC-12). The interior of the apatite crystals was exposed by grinding manually.[The interior of the apatite crystals was exposed by grinding.] Subsequently, the polishing of the grain mounts was done with a Struers polisher machine (6 and 3 µm diamond paste) (Fig. 7.2). The last polishing was made with 0,05 µm Al2O3 powder. The grain mounts were finished after cutting them in small rectangles of approx. $1 \times 1{,}3$ cm.

7.3 Etching of latent fission tracks

The revelation of latent tracks was performed with 5 mol/dm^3 nitric acid (HNO_3) for 20 s at 20 ± 1 °C. Immediately after the 20 s under the etchant, the samples were submerged into water to eliminate the rests of the reagent. The etched samples rested at a moderate high temperature around 40 °C in order to evaporate the residual etchant.

7.4 Packing and irradiation

After revealing the latent fission tracks of the grain mounts, these were covered with a muscovite detector so that there was no air between detector and grain mount. The binding of detector and grain mount involved the wrapping of these two with regular tape. Finally, the thermal neutron irradiation was carried out at the Garching Forschungsreaktor FRM II at the Technical University of Munich. The neutron flux (ϕ) applied was 1×1016 neutrons/cm^2. The dosimeter glasses with uranium concentration of 15 ppm (IRMM-540R) were located on top, middle and bottom of the irradiation tube. The mica detector of the IRMM-540R glasses is used to establish the track density in the dosimeter.

The samples sent to irradiation were 10 out of 15 (EC-02, EC-03, EC-05, EC-06, EC-08, EC-09, EC-12, EC-13, EC-14, EC-15). The sample EC-07 was polished and etched, nevertheless the apatite content was very low and consequently, EC-07 was discarded.

7.5 Etching of induced fission tracks

After the cooling of the irradiated samples for months, five pinholes were made in each mica-mount pair to reference the sample in the glass slide for counting (Fig. 7.2). The etching of the induced tracks in the detector was performed with 40 % hydrofluoric acid (HF) for 20 min at room temperature. Due to the corrosive power of the HF, the samples were left on running water

overnight. Once the detectors were dry, it was possible to proceed with the glass slide mounting. The mica detector is placed to the right of the glass slide mirroring the grain mount, which is located to the left. An additional copper-grid crosshair was also added in each glass slide as a reference.

7.6 External detector method: Analytic procedure

The fission track analysis of the 11 samples was conducted under a 1250 × magnification with an Olympus BX51 optical microscope with transmitted and reflected light. A Kinetek (Ludl) automated stage system and the CalComp Drawing Board III digital tablet supplying the microscope enabled the counting process. Track length measurements were made with a cursor with a light-emitting diode (LED). To visualize the followed steps for the external detector method the reader is referred to the workflow diagram attached at the end of this chapter (Fig. 7.2).

7.6.1 Counting of dosimeter glasses and estimation of ρ_d

The dosimeter glasses (IRMM-540R) were counted for the irradiations NoB-002, NoB-003, NoB-014, NoB-017 and NoB-025 under 1250 × magnification for a grid of 10 × 10 squares, which represents an area of 54,76 mm^2. Those grid were counted 25 times in a 5 × 5 net guide. NoB-025 is the irradiation number containing the samples of the present study. The measurement of the dosimeter glasses is made in order to determine the track density along the irradiation can (ρ_d). The track density values are estimated through a regression line of the different counts (N_d) of dosimeter glasses according to the position they were occupying in the container.

7.6.2 Counting standards and samples. Z-calibration and age calculation

The counting technique employed for age determination and Z-calibration was applied in both standards and samples. The standards counted for Z-calibration belong to the Durango and the Fish Canyon tuff age standards. The AFT age of the samples was calculated after a control test driven with other non-related samples from past irradiations. In the standards as well as in the samples, the minimum area counted was 3 × 3 squares. Generally, the grains with larger track density were counted in smaller areas. Grains that were too fractured, too dirty or too small were neglected from the counting. Suitable grains for counting should be parallel oriented to the crystallographic c-axis of the apatite. A margin of 2 to 3° deviation of the tracks to the c-axis was tolerated. Some crystal dislocations are very similar or sometimes identical to fission tracks, therefore they migth have been involuntarily included during counting.

The pinholes and the crosshair grid (Fig. 7.1) allowed the referencing between grain mount and detector in the petrographical glass slide. The convention, as explained in the previous chapter, is to count the same exact area of the grain on the grain mount and on the detector. In order

to get reliable $^{N_s}/_{N_i}$ ratio, the alignment should be carefully adjusted. During the referencing process, the alignment was accepted only if there was <1 square off difference. In order to obtain accurate values of ρ_s and ρ_i, a total of at least 20 grains were analyzed for each sample and standard. The software FTstage developed by Dumitru (1993) was used in order to reference and saving the counted grains in the samples.

The personal Z-value was calculated with the ZETAmean program by Mark Brandon. The TrackKey software (by István Dunkl) was used in order to calculate the Z-value for each of the standards. The collected N_i, N_s and N_s obtained from counting were used to calculate the age of the grains in each sample through the same software used for Z-calibration. Usually the age picked is the central age, which is a weighted mean of the normal distribution of individual grain ages. The track densities ($\rho_{i,s,d}$) will also be used for the calculation of the chi-square value and the associated p-value. The p-value is the probability that the chi-square (χ^2) value has of being greater than the calculated χ^2.

7.6.3 Track length and Dpar measurements

Before taking the length track measurements, a calibration file was created by taking 61 measures of around 150 µm with a ruler grid under 2000 × magnification. Subsequently, Dpar measurements were taken for all the each grain of all the samples also under 2000 ×. Dpar and Dperp refers to the etch pit diameters parallel and perpendicular to the c-axis. The Dpar measurements are used for thermal modeling, whereas Dperp are not relevant for AFT analysis. The Dperp were taken in order to follow the FTStage software rutine. Five to ten Dpar and Dperp pairs of measurements were taken for each counted grain. 100 to 46 track length measurements were carried out for four samples (EC-15, EC-12, EC-08 and EC-05) under a magnification of 2000 ×. One additional sample (AS-23) from Ahmed A Al-Samarrray's master thesis were measured as representative of the hanging wall block. The measurements were taken from horizontal confined tracks within the apatite grains with the LED cursor and the digital tablet. The software used for registering the measurements was FTStage (Dumitru, 1993). The recognition of confined fission tracks under microscope is better done under reflected light (Fig. 7.1). The c-axis was marked for each grain and the deviation angle between c-axis and confined track was also recorded for each case. The track length measurements were performed in TINT and TINCLE tracks. The TINCLE type were registered in a different manner than the TINT in the FTStage software.

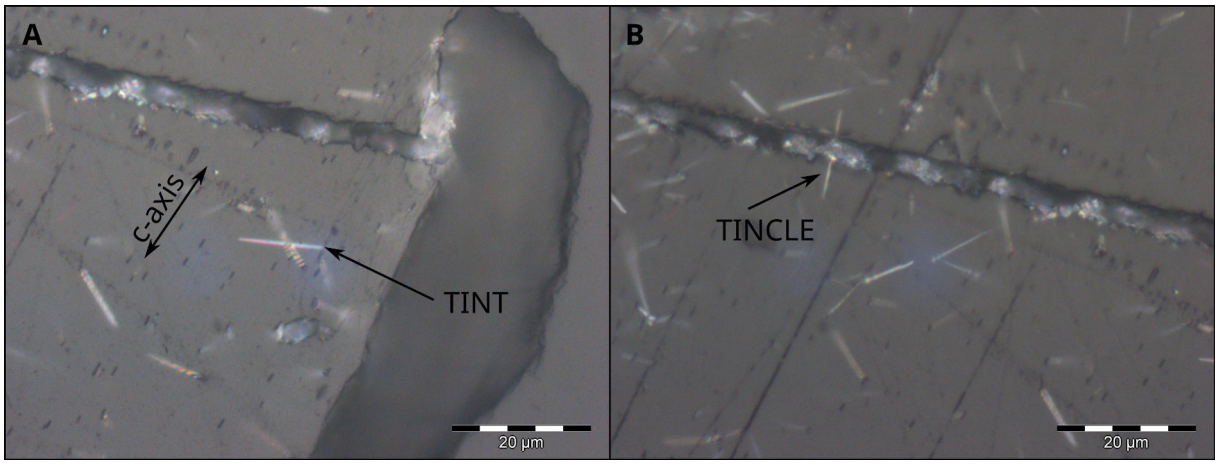

Fig. 7.1: Confined tracks in an apatite grains that belong to the sample EC-12a. A) Snapshot of an apatite grain used for counting and for track length measurements. The track pointed by the arrow is a very good example of TINT type of tracks. The c-axis is also depicted. B) Snapshot showing some confined tracks that are not completely horizontal and a TINCLE type. FTStage software is able to mark the crack orientation and width for this type of tracks.

7.7 Petrographic thin section preparation

The oriented cuts for thin section preparation were carried out with a diamond blade saw. The oriented rocks slabs were cut as rectangular pieces with a width from 0,6 to 2 cm. Further preparation and polishing was done by Irina M. Dumitru at University of Bergen. The rocks slabs were pre-polished and ground prior to gluing them onto the glass slide. The glue between glass slide and rock slab is made with a thin layer of epoxy. The rock slab would be cut down to 2 mm thick. Subsequently, the rock sample glued the glass slide was introduced into the Struers DP-U2 polisher, which thinned down the rock slab up to 35 µm thick. Further polishing was carried out manually.

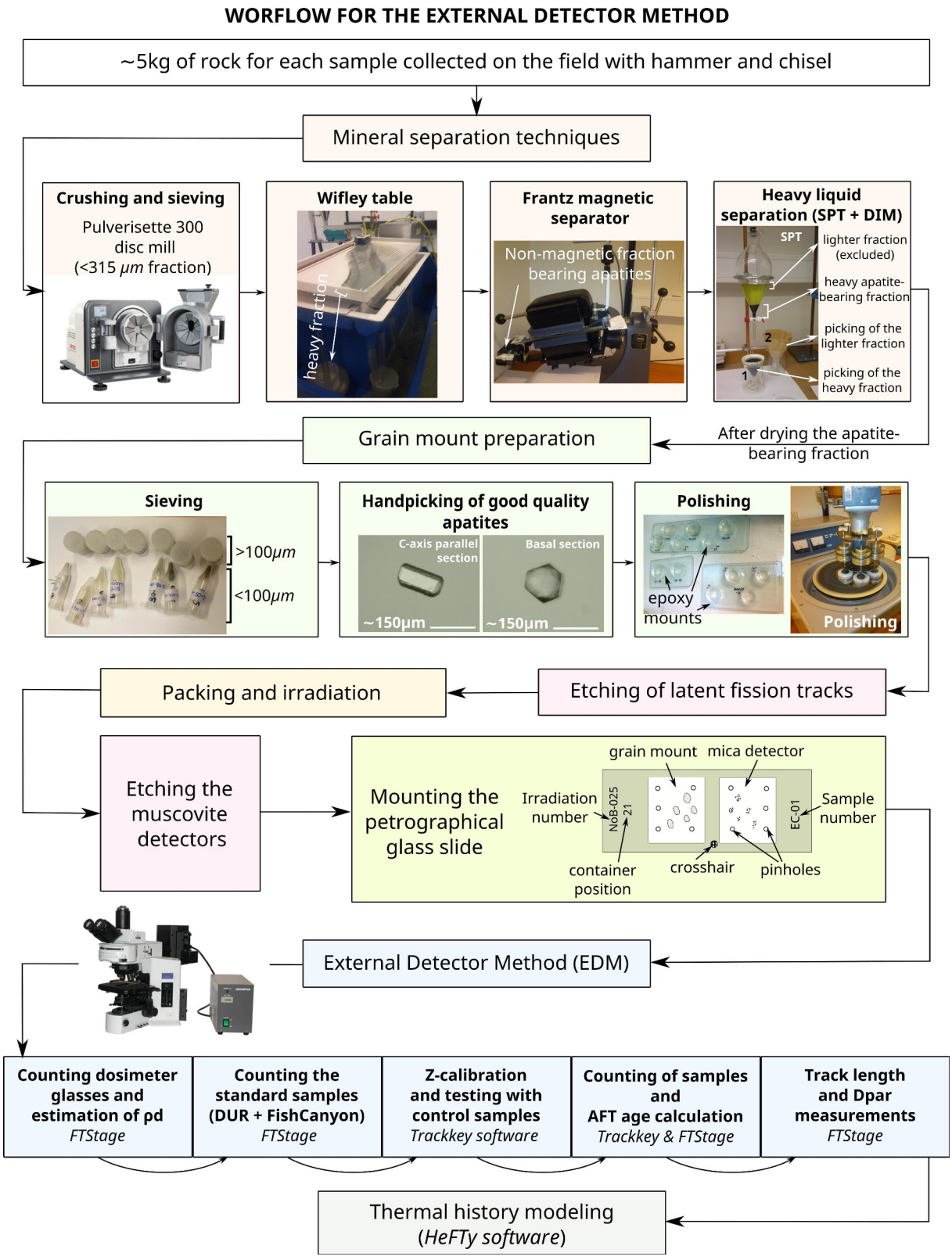

Fig. 7.2: Workflow diagram for the analytical steps followed for AFT analysis using the External Detector Method. The hand-picking process is performed by some thermochronologists, therefore it has been included in the workflow.

This page is intentionally left blank

8 Structural Results

The exposure of the Lærdal-Gjende fault in Lærdalsøyri reveals diverse fault related rocks and local brittle overprint to older deformation events. Structural observations suggest that the Lærdal-Gjende fault has been reactivated throughout post-Caledonian history. Additionally, thermochronological studies conducted on cohesive cataclasites and fault gouges of the Lærdal-Gjende fault support these observations (Section 2.9).

In Lærdalsøyri, a 250 m thick package of mylonites crops out in the footwall block of the Lærdal-Gjende fault. The mylonites are derived from quartzo-feldspatic rocks with mafic content. Cohesive cataclasites stick out in the hanging wall and create an abrupt relief. The cataclasites affect to lithologies from the Jotun nappe complex. Fault gouges and other incohesive fault-rocks form the fault core, which separates the footwall mylonites from the cataclasites of the hanging block. This latter brittle deformation overprints both the mylonites and the cataclastic rocks.

The field observations and thin sections are taken from the cohesive cataclasites of the hanging wall, along the Raudbergerstunnel, from fault gouges and from the mylonites of the footwall (Fig. 8.1). A total of 12 thin sections were described from the samples picked for this thesis. BG-129c, d, e and f are additional samples provided by Dr. Anna Ksienzyk. Some pictures with reference number (coded as samples) are included as support to some field observations.

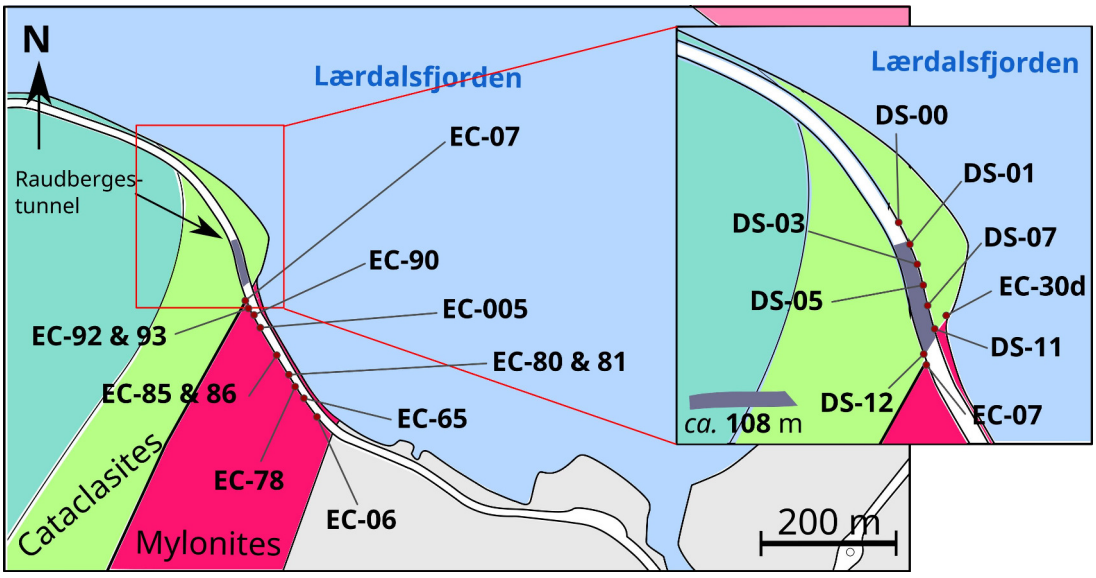

Fig. 8.1: Map with the location of the thin sections and field observations described in this chapter. A detailed map showing a close up from the Raudbergerstunnel is provided to the right of the figure.

8.1 Joints and lineations throughout the study area

A large number of measurements of joints, minor faults, lineations and mylonitic foliation were taken from different lithological units of the study area (Appendix A).

The stereographical nets for each region are presented in Fig. 8.2. The para-autochthonous basement (migmatites in Fig. 8.2) show a random pattern of joints that goes in all directions. In despite of that, the migmatitic gneisses from the basement show a conjugate set of joints with very penetrative character in the field. The most frequent population plotted on the sterographic net trends NNE-SSW and dips steeply to NW. Some of the joints have had relative minor displacement, evidenced by well-developed slickenfibers. The slickenfibers suggest normal sense of shear. Most of them are located in very steep joints and have very steep pitch. The measurements from the migmatitic gneisses were taken from all the area depicted in light gray in Fig. 8.2.

The mylonite package (called as "Mylonites" in Fig. 8.2) presents two very distinctive populations of joints and foliations. The joints and foliations follow a trend ENE-WSW and dip ca. 40° to NW. Some lineations indicate displacement to WNW (pink dots). The second population of joints is oriented almost N-S and dips around 80° to NW. The sample EC-05 belongs to the mylonite package as well, but the measurements taken at that location do not show the same two main populations seen in the stereographical net called "Mylonites".

EC-07 represents the fault core. Many population of joints with more penetrative character than in the wall rocks (mylonites and cataclasites) are observed within the fault gouges. There are two main population of joints that could be inferred from the stereopgraphical net: (1) the first, trending almost N-S dipping 70°; and (2) the second, trending ENE-WSW as seen in the mylonites but dipping steeper (approx. 60°). Similar results are obtained from the measurements taken from the cataclasites (pointed with an arrow to outside the Raudbergerstunnel in Fig. 8.2). The cataclasites, however, show a third population that trends NE-SW and dips steeply to SE. Lineations in minor faults show displacement directed to NWW.

In the Raudbergerstunnel (detail in Fig. 8.2), the measurements are shown in an individual stereographic net for each of 18 meters (DS-01 and DS-02, DS-03 and DS-04, etc.). In the stereographic plots two main joint populations can be inferred: (1) trending ENE-WSW dipping NW and (2) another trending NNW-SSE and dipping very steeply. A third population vaguely depicted in the stereographical plots, also trends ENE-WSW and dips to SE. This last population is the conjugate set of the first described population of joints. These results are similar to the ones obtained for the measurements from the cataclasites outside the tunnel. Joints with NNW-SSE orientation occur frequently along the tunnel. The joint population that trends ENE-WSW manifests more pervasively towards the fault core.

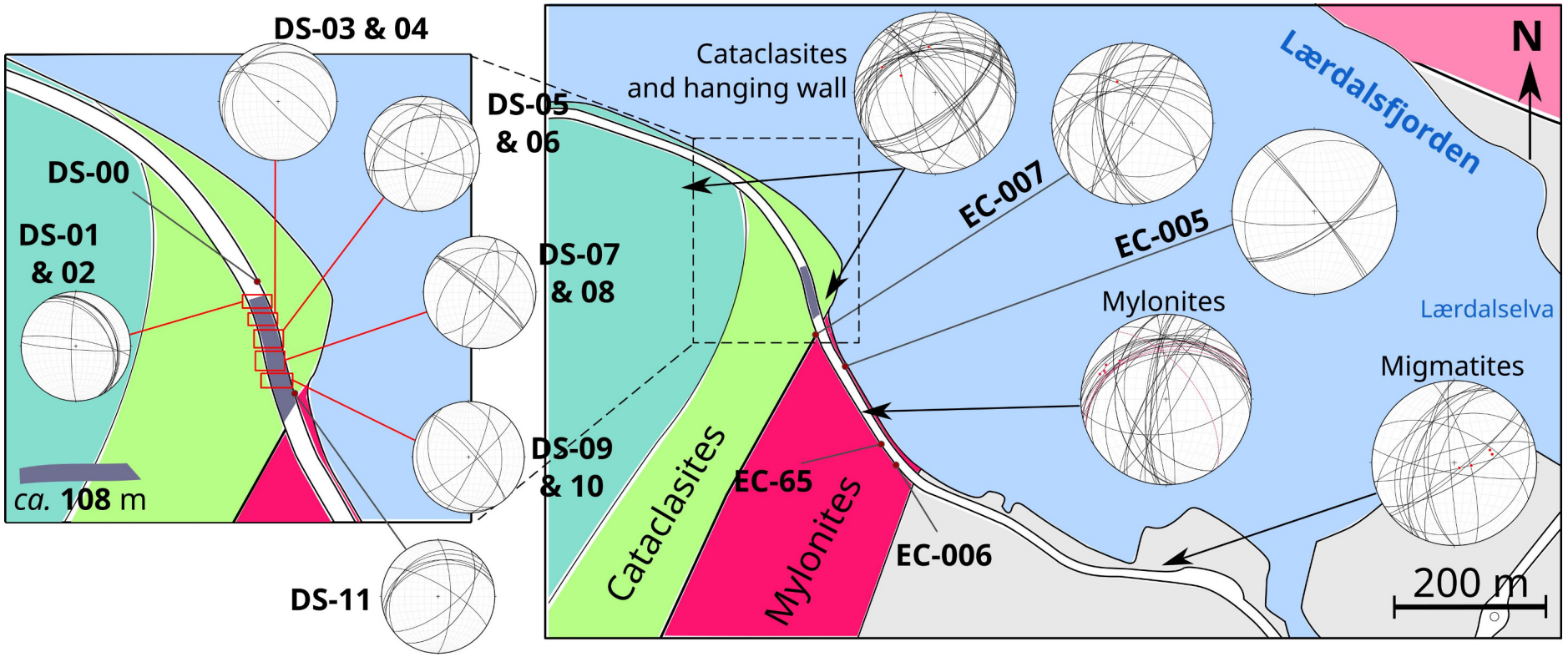

Fig. 8.2: Schematic map of the locations were the structural measurements (joints, foliations and lineations) were taken. Each stereographical net represents an area, pointed by an arrow or a marker (for more specific locations). All the measurements in black adjusted to a great circle are joints. The dashed pink lines represent the foliation of the mylonites. The dots in the stereonets are lineations. A detailed map along the Raudbergerstunnel is provided to the left of the figure. The stereographical net of the migmatites refers to the whole area depicted in gray color, which corresponds to the Baltic basement.

8.2 Footwall fault-rocks: mylonites

Mylonitic rocks give information about the intensity of deformation in the shear zone and about the metamorphic conditions during and after mylonitization (T, P and presence and composition of fluids). The formation of mylonites is dependent upon these factors and the composition of the parent rock (Trouw et al., 2010). The prefixes 'proto-' and 'ultra-' are used to indicate low and high intensity of deformation respectively (Section 4.1). For referring to temperature conditions is common to use either 'high-', 'medium-' or 'low-grade' mylonites.

8.2.1 Field observation

In the Lærdaløyri outcrop, a package of mylonites 200 to 250 meters is cut by the current fault plane, which consists mainly of fault gouges. The mylonites are derived from a parent rock with quartz, felspar and other mafic minerals. At meso-scale, the matrix portion forms 90 to 98 % of the rock and the porphyroclast sizes are millimetric. The porphyroclasts present on the rock are clustered in leucrocratic bands exclusively and have diameters of 1 to 5 mm. According to the classification given by Twiss & Moores (1992), these rocks should be referred as ultramylonites. Some localities may have less than 90 % of matrix, whose rock should be classified as mylonite; although the variations are not obvious and not relevant for interpretation purposes. The mylonitic foliation (C-foliation) is well developed throughout the whole mylonitic package. The mylonitic foliation is easily recognizable due to the alternating compositional banding of leucrocratic bands of <1cm thick with the mafic-rich mineral portion of very fine grain size. The felsic bands and layers have usually coarse grain size and show signs of recrystallization in dynamic conditions. The mylonites and ultramylonites of the footwall show very few kinematic indicators due to the reduced grain size. Some coarse recrystallized felspar porphyroclasts of few millimiters diameter can be recognized in the field, although they are not frequently observed.

The felsic sigmoidal bodies of few centimeters long are present and indicate top-to-NW shear. Asymmetric isoclinal folds are frequently seen in leucocratic bands and are consistent with top-to-NW normal-sense of shear (Fig. 8.3.A). Some Z-shaped folds are found in leucocratic layers or bands that have several transposed folds (Fig. 8.3.C). In spite transposed folds are not the best kinematic indicators in mylonitic rocks, the presence of consistent S-like fold geometry within the mylonites may be taken as indicative of the shear sense. S-C fabric can be locally spotted (Fig. 8.3.B) indicating dextral-sense of shear in the observation plane, which corresponds to a movement of the fault directed to NW. Boudinage of felspatic bands is sometimes present within the outcrop (Fig. 8.3.F). Controversial porphyroclast-tailed complexes are found ca. 100 m away from the fault (Fig. 8.3.C). The delta tail part of the complex seems to indicate top-to-NW shear, whereas the sigma part seems to indicate top-to-SE shear.

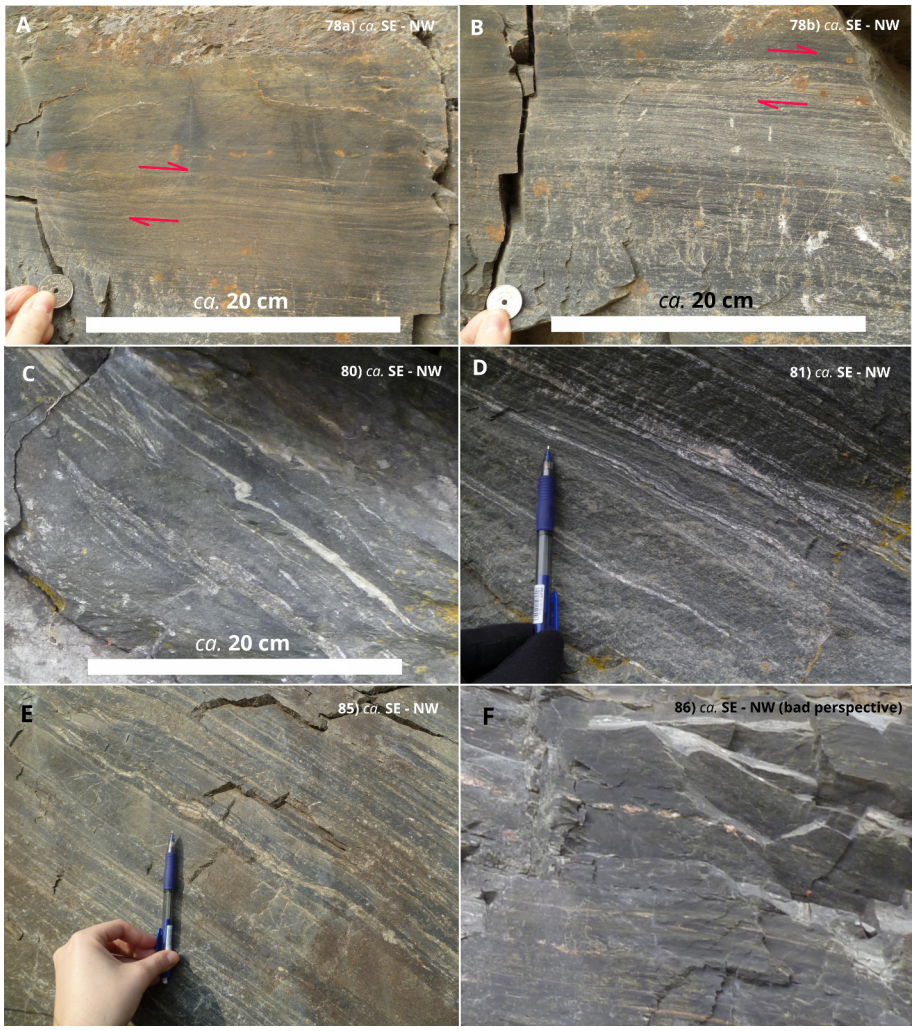

Fig. 8.3: Field observations of the mylonites. The numbers to the upper right corner of the pictures correspond to the sample number (e.g: 80 for EC-80). The locations are found in Fig. 8.1.A) The leucocratic band within the ultramylonite show asymmetric isometric folds consistent with top-to-NW shear movement (dextral shear in the observation plane). B) S-C foliations indicating top-to-NW shear movement of the mylonites. C) Complex tailed-object with sigma and delta component. The sigma component (left side) is indicating top-to-SE shear sense, whereas the delta component (right side) shows top-to-NW shear movement. D) Overview of the look of the mylonites at that location with a lack of porphyroclasts observable with naked eye. E) Complicated fold pattern of asymmetric isoclinal folds in leucocratic band in mylonites. A sigmodal-like shape in the leucocratic band indicating top-to-the-NW can be observed (lower right). F) Boudinage in a feldpatic band.

The mylonites 20 to 10 m away from the fault are overprinted by incipient brittle deformation. Shear bands cross the mylonitic foliation and display offsets of various centimeters (1 to 25 cm, Fig. 8.3.A and C) with top-to-NW displacement. The coloration of the rocks close to the fault is slightly different; the dark portion has distinct banding alternating dark gray and dark green (Fig. 8.4.B). Well developed planar foliation is recognizable by the coloring of the banding. The rock is very hard and the grain size is the same as previously observed. Porphyroclasts are rarely seen as well. Joints are more penetrative across these 20 meters of ultramylonites close to the fault. Veins of pale green color are abundant 3 to 2 m from the fault core, and are oriented in the same direction as the C fabrics and cross cutting them.

Fig. 8.4: Field observations of the mylonites at 5 m distance from the fault. The numbers to the upper right corner of the pictures correspond to the sample number (e.g: 90 for EC-90). The locations are found in Fig. 8.1.A) Evidences of brittle deformation in leucrocratic thick band within the mylonites. The brittle structure show normal-sense of shear. B) Wet surface of the mylonites showing straight mylonitic foliation and offsets of <1 mm on small faults. C) Evidences of brittle deformation on mylonites in a random the observation plane (E-W). Normal-sense of shear is also inferred.

8.2.2 Microscopic scale

In this subsection, 5 thin sections from mylonites will be described. The location of the samples collected for this thesis is depicted in Fig. 8.1. The samples are from 150 m away from the fault to a couple of meters away (BG129).

The parent rock of the mylonites was a quartzo-felspatic rock. The mylonitic matrix is formed by bands of recrystallized felspar and quartz, quartz ribbons and fine-grained mafic bands. Porphyroclasts of feldspar are commonly seen and form winged-objects. Some dark brown porphyroclasts appear occasionally and usually fractured. The brown porphyroclasts have high relief, very marked cleavage, low pleochroism and high birrefringence colors. Chlorite and sericite are present as alteration minerals and generally affect fine-grained portions of the matrix. Opaque bands follow the mylonitic foliation. Rutile, zircon and some monazites stick out from the matrix by their relief and birrefringence colors.

- **EC-06**
  This sample is collected from the mylonitic package, ca. 200 meters away from the fault core.

The matrix volume of the rock is around 60 to 70 %. The porphyroclasts are generally large plagioclases and alkali feldspar grains and its size range from 3 to 0,5 mm. The size of the grains of the matrix is significantly smaller than the porphyroclasts. According to this observation scale, this rock should be classified as a mesomylonite, most commonly named as mylonite (50 to 90 % of matrix).

The matrix consists of quartz and felspar grains signs of size reduction and recrystallization. The clasts in the matrix are sub-rounded to rounded and usually exhibit incompletely developed mantles. Polycrystalline recrystallizing grain in the matrix show lobate contacts between sub-grains and bulging. Small polycrystalline quartz ribbons appear very often around felspar clasts and porphyroclasts (Fig. 8.5.C). Occassionally quartz ribbons acquire sigmoidal-like shapes. Some alkali felspar porphyroclasts show incipient production of mymerkite structures on the edges of the grain (Fig. 8.5.A). Some larger porphyroclasts conserve their original crystalline habit but show evidences of rotation within the mylonitic flow. The rotation is evidenced by their position respect to the mylonitic foliation (Fig. 8.5.A & .B). Plagioclase grains are seen occasionally with flame-perthite structures (Fig. 8.5.C). Plagioclases tend to form better mantled objects and are usually better kinematic indicators. The mantles usually show signs of SGR recrystallization (Fig. 8.5.B). Bookshelf fractured porphyroclasts and low-angle fractured porphyroclasts indicate very consistently top-to-NW displacement, seen as dextral shear in Fig. 8.6.B & .C. Boudinage of fractured grains is rather common. Shear bands are locally cross-cutting large felspar grains. Shear bands are rarely observed within this sample.

Sericite and epidote commonly affect the rims of porphyroclasts and the finer recrystallized fraction of the matrix.

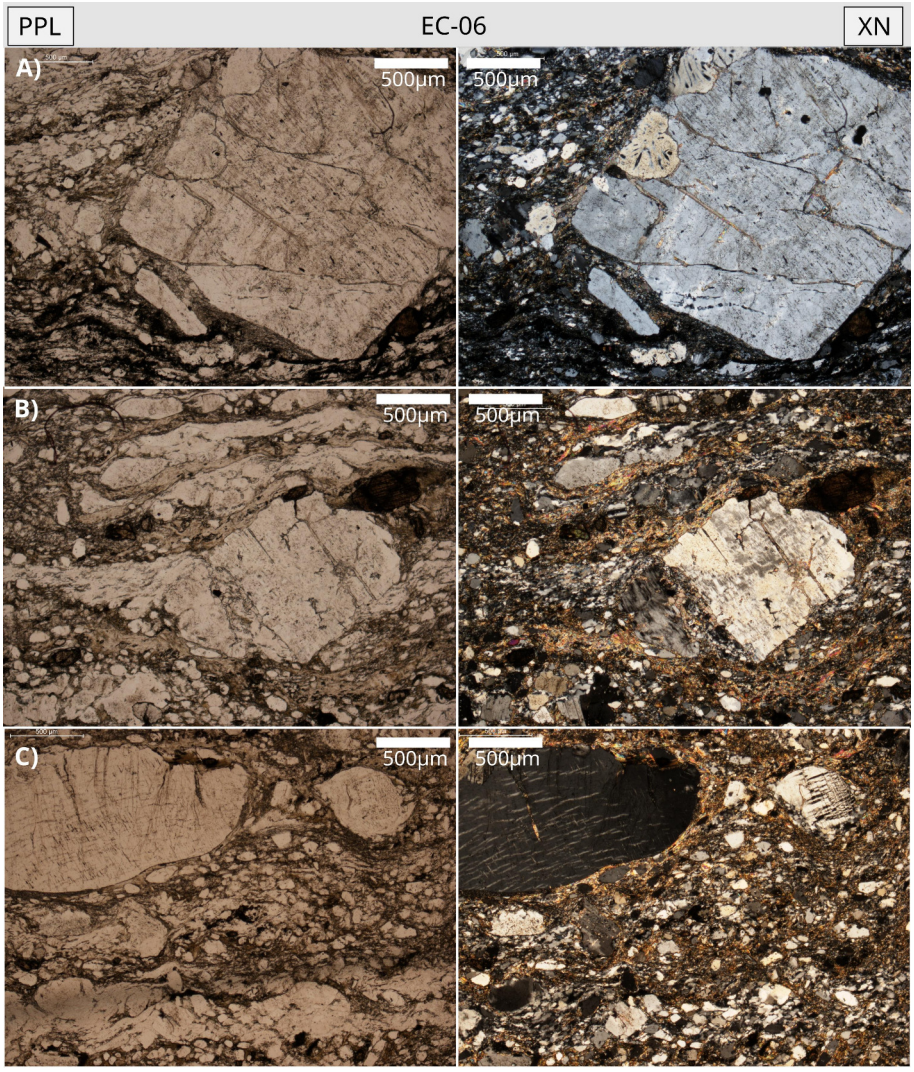

Fig. 8.5: Selected set of photomicrographs of the sample EC-06. On the left, image without analyser (PPL) and on the right, with crossed-nicols (XN). The orientation of the photomicrographs is SE-NW (i.e., SE to the left side and NW to the right side). A) Myrmekite on the edges of an alkali feldspar porphyroclast. B) Fractured mantled object with feldspar core indicating top-to-NW sense of shear. The mantle show evidences of SGR recrystallization. Quartz ribbons with wrapping the tailed object show S fabrics orientation. C) To the left of the photomicrograph: large porphyroclast of plagioclase with flame pethites with a rim of sericite. A porphyroclast of 0,5 mm diameter with deformation lamellae is located to the right of the image. None of these clasts can be used as kinematic indicators.

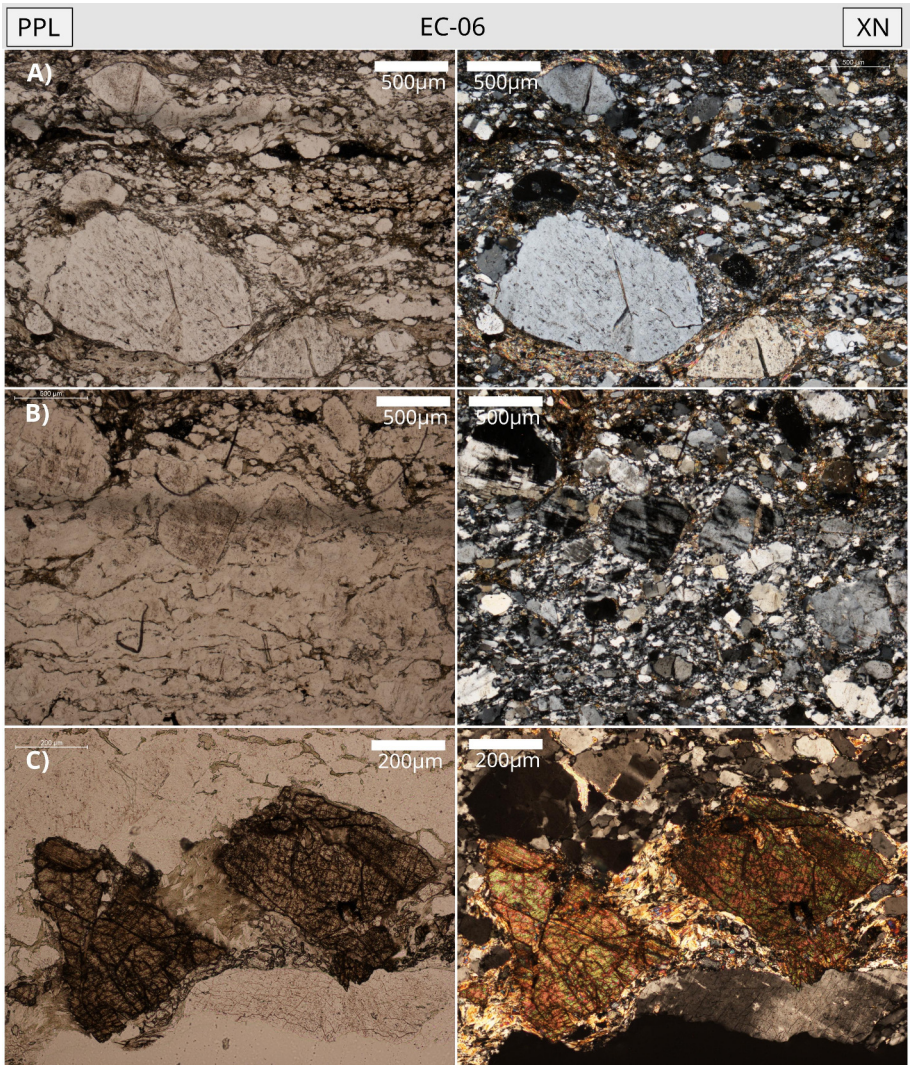

Fig. 8.6: Selected set of photomicrographs of the sample EC-06. On the left, image without analyser (PPL) and on the right, with crossed-nicols (XN). The orientation of the photomicrographs is SE-NW (i.e., SE to the left side and NW to the right side). A) Porphyroclast cross-cut by a shear band. B) Fractured porphyroclast showing a domino structure, which indicates dextral shear on the picture (top-to-NW displacement). The porphyroclast show internal deformation. C) (Pyroxene) porphyroclast fractured and boudinaged. It may represent a low-angle fractured porphyroclast displaced synthetically to the sense of shear of the fault zone (dextral shear in the picture, which corresponds top-to-NW sense of shear).

- **EC-65**

  This sample is collected from the mylonitic package, ca. 150 m away from the fault core.

EC-65 exhibits a large matrix portion of approximately 60 to 65 %. The size of the porphyroclasts ranges from 0,5 to 0,1 mm. The matrix size is considerably smaller than porphyroclasts, but ranges between 0,2 mm to <0,05 mm. According to this observation scale, this rock should be classified as a mesomylonite.

The photomicrographs of the sample EC-05 show evidences of dynamic recrystallization by subgrain boundary rotation (SGR). Lobate contacts on the edges of larger porphyroclasts are

also evidence of dynamic recrystallization (Fig. 8.7.C). Monomineralic grains of quartz had acquired sigmoidal-like shapes and form quartz ribbons. Fold transposition is exhibited by a set of S-type of folds within the thin section and indicate top-to-NW sense of shear (Fig. 8.7.D). Sigma-tailed porhyroclasts are encountered within this sample and are consistent with top-to-NW displacement (Fig. 8.7.A & .C). S-C fabrics indicating top-to-NW displacement can be discerned within the quartzo-feldspatic matrix and by the orientation of rectangular clasts parallel to the S-foliation (Fig. 8.7.C). Dextral sense of shear (corresponding to top-to-NW normal sense of shear) can be inferred from a structure that resembles to a mineral fish in Fig. 8.7.B. The mylonitic foliation is defined by the orientation of mantled porphyroclasts, compositional banding, mineral fish structures and elongation of quartz grains in the matrix.

Sericite is frequently placed on bands within the matrix and on rims surrounding porphyroclasts. Chlorite with blue and dark gray birrefringence colors is found following the mylonitic foliation and around larger clasts.

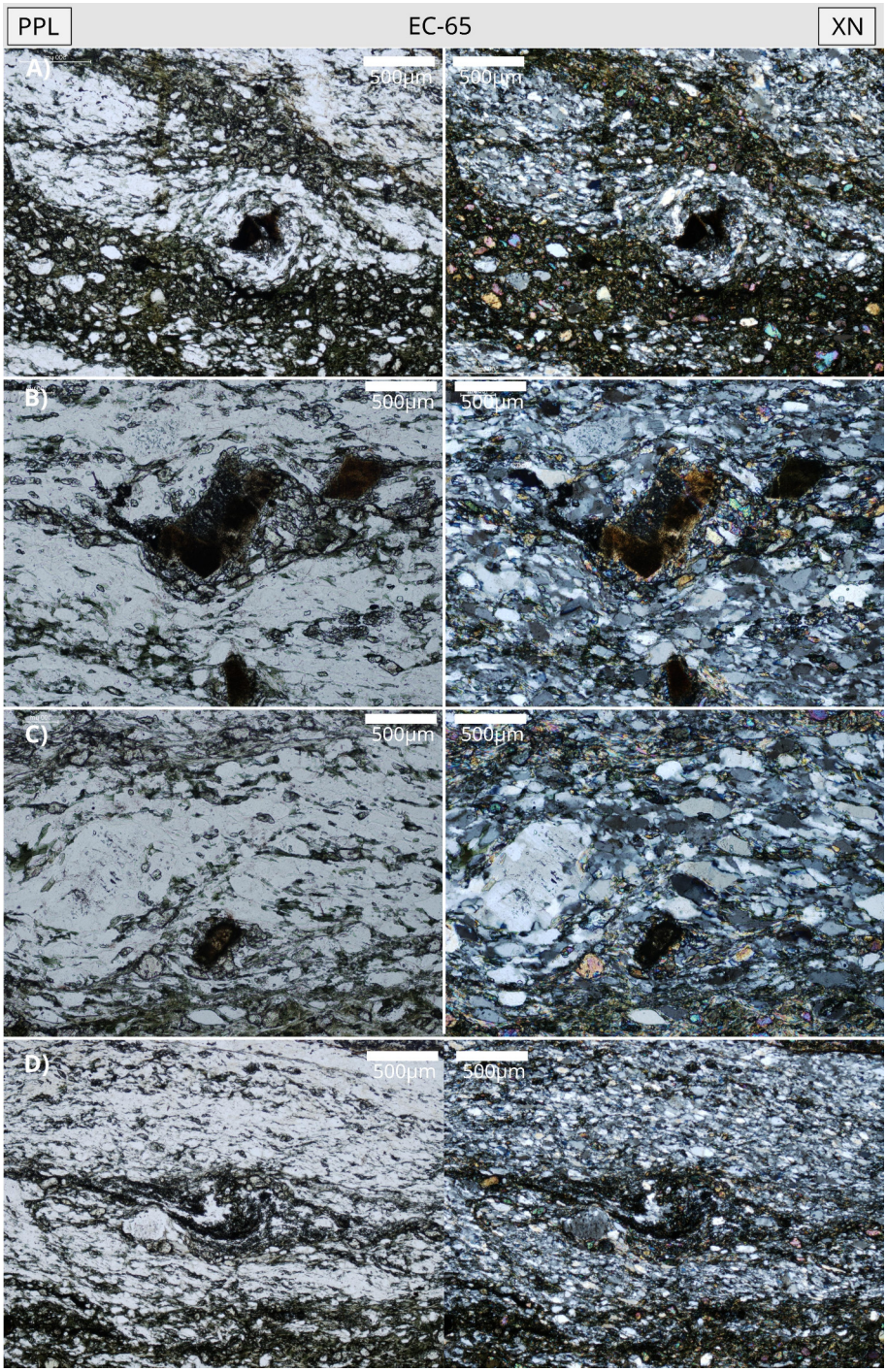

Fig. 8.7: Selected set of photomicrographs of the sample EC-65. On the left, image without analyser (PPL) and on the right, with crossed-nicols (XN). The orientation of the photomicrographs is SE-NW (i.e., SE to the left side and NW to the right side). A) Sigma-object indicating top-to-NW displacement. The mantle show SGR recrystallization syntectonic to the formation of the tailed object. B) Structure with resemblance to a mineral fish structure formed by the porphyroclast of the center and the clast of the same mineral to the right. The porphyroclast of the center of the image has a mantle structure which is partially altered by saussurite. The mantled object resembles to a sigma-object indicating top-to-NW displacement (dextral sense in the figure). C) S-C fabrics defined by a porphyroclast of felspar and a rectangular section of zircon. Both clasts are parallel oriented to the S-fabrics. The porphyroclast of felspar show lobate contacts on the edges and its mantle resembles to a sigma-type object indicating top-to-NW displacement. D) Transposed fold with S-like geometry indicating top-to-NW displacement.

- **BG-129-c**

The set of thin sections coded as BG-129 correspond to mylonites collected nearby the fault core. BG-129c, d, e and f show very similar characteristics among each other. A detailed description will be given for BG-129c and a briefer description will be made for the rest of the BG-129 collection.

The sample BG-129c exhibits a matrix portion of approximately 80 to 95 % depending on part of the thin section. The size of the porphyroclasts ranges from 0,3 mm to <0,1 mm. According to the matrix proportion this rock should be classified as a ultramylonite to mesomylonite.

The photomicrographs show a marked compositional banding alternating between cryptocrystalline bands rich in mafic content and quartzo-felspatic bands. The compositional banding mark the mylonitic foliation along with mineral fish and mantle-and-core structures. Few porphyroclasts are seen within the samples coded as BG-129. The size of porphryclasts is <0,5 mm and can be as small as 0,1 mm. Mantle-and-core porphyroclasts are relatively common but not all of them can be used as kinematic indicators. In Fig. 8.8.A, a sigma-type tailed complex mark top-to-NW sense of shear. Mineral fish occur locally within the sample and are consistent with top-to-NW sense of shear (Fig. 8.8.B). Brittle deformation overprinting the mylonites is evidenced by synthetic and antithetic microfaults with normal sense of displacement (Fig. 8.8.C). Very fine-grained quartzo-feldspatic bands sometimes display sigmoidal-like shapes. A sigmoidal body is cross cut by an antithetic microfault in Fig. 8.8.D. Evidences of recrystallization are found in the quartzo-feldspatic bands and can be inferred by the lack of porphyroclasts.

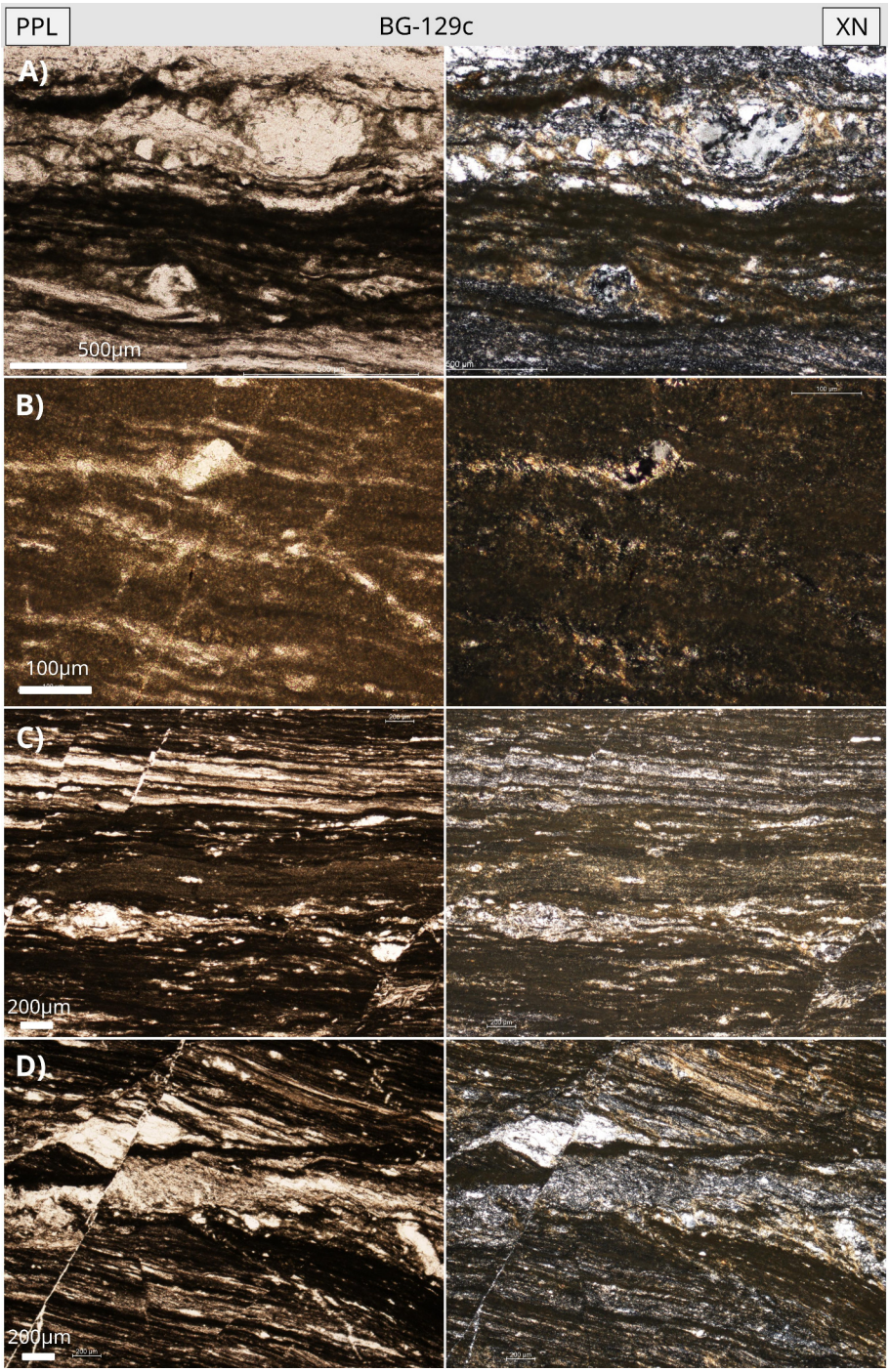

Fig. 8.8: Selected set of photomicrographs of the sample BG-129c. On the left, image without analyser (PPL) and on the right, with crossed-nicols (XN). The orientation of the photomicrographs is SE-NW (i.e., SE to the left side and NW to the right side). A) Vaguely defined sigma object indicating top-to-NW shear. Compositional banding is observed easily in this photomicrographs. B) Mineral fish of what seems plagioclase with undulous extintion. C) domino antithetic microfaults cross-cutting the mylonitic foliation. D) sigmoidal quartzo-feldspatic body faulted indicating normal sense of displacement.

- **BG-129-d,e**

In the thin sections BG-129d and e, microfaults are widespread throughout the samples overprinting the mylonites. The offsets show always normal sense of shear (Fig. 8.9.A). The lack of porphyroclasts and mantle-and-core structures make difficult to determine the sense of shear

within this thin samples. S-C fabrics are seen locally and indicate top-to-NW shear sense. Recrystallization by SGR is inferred by the reduced grain-size. In BG-129d, large plagioclase porphyroclasts (1,5 mm of diameter) show intracrystalline deformation by kinking. Dynamic recrystallization by bulging is evidenced by the lobate contacts in the edges of the porphyroclast.

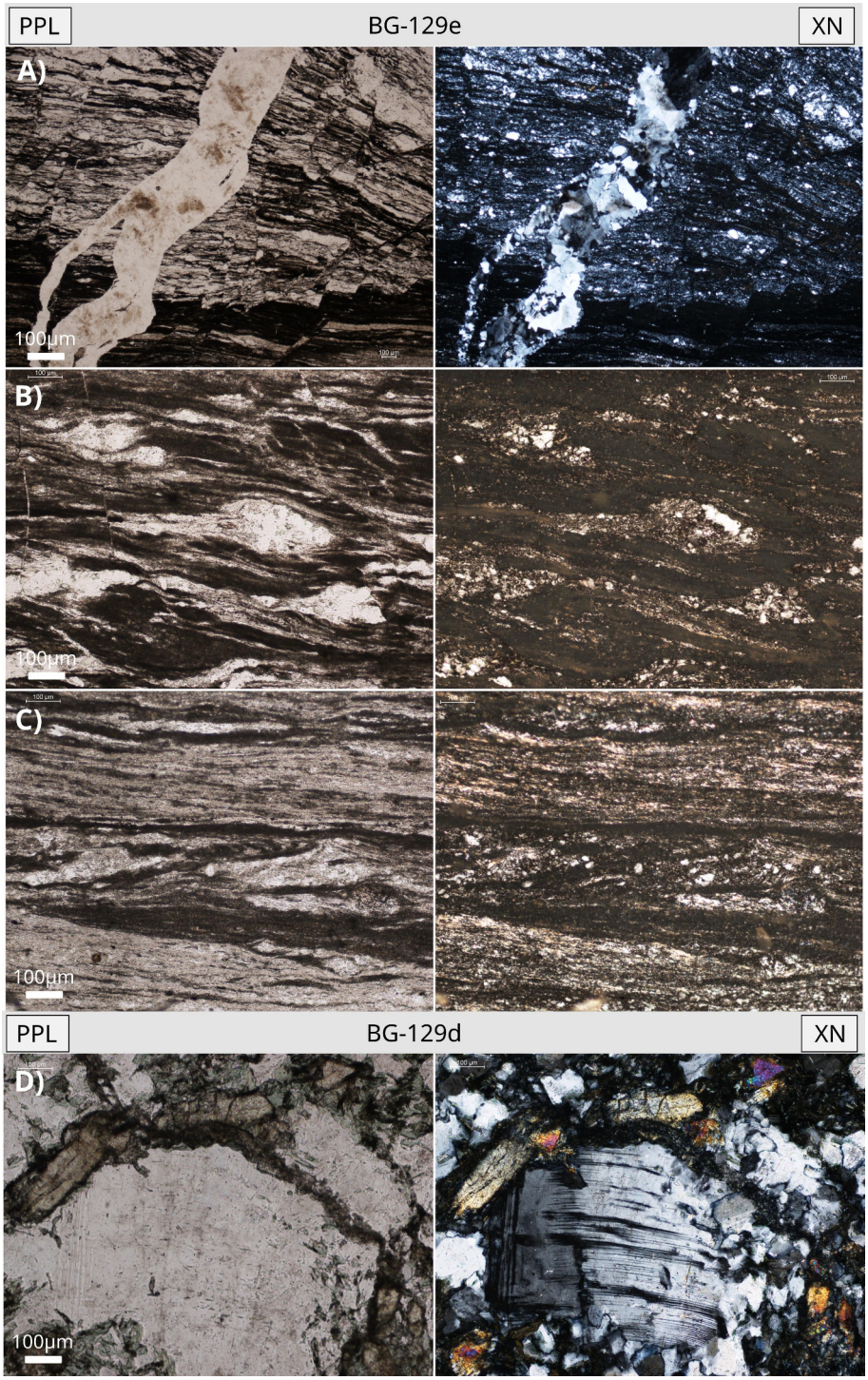

Fig. 8.9: Selected set of photomicrographs of the sample BG-129d and e. On the left, image without analyser (PPL) and on the right, with crossed-nicols (XN). The orientation of the photomicrographs is SE-NW (i.e., SE to the left side and NW to the right side). A) Quartz vein between microfaults. Microfaults displaying normal sense of displacement. B) Quartzo-feldspatic bands with incipient sigmoidal-like shape. (indicating close fd total plasticity). C) S-C fabrics indicating top-to-NW shear (dextral sense in the photomicrographs). D) Porphyroclast of plagioclase with intracrystalline deformation by kinking.

- **BG-129-f**

This thin section exhibit a larger number of porphyroclasts with mantles. Sigma-type objects show top-to-NW sense of shear (Fig. 8.10.B). S-C fabrics can be inferred from quartzo-feldspatic bands and are consistent with top-to-NW displacement, as seen in Fig. 8.10.A. Domino fracture is also consistent with this shear sense direction (Fig. 8.10.B). Undulous extinction of felspars and deformation lamellae in the plagioclase are evidences of plastic deformation of feldspar. Dynamic recrystallization by SGR mechanism is seen in the matrix by reduced grain size and on the edges of porphyroclasts (Fig. 8.10.B). Perthites are seen in some porphyroclasts of plagioclase (Fig. 8.10.C).

The matrix portion of this sample is slightly lower than seen in BG-129c, e and d. This rock may be classified as an ultramylonite alternating with mylonite bands.

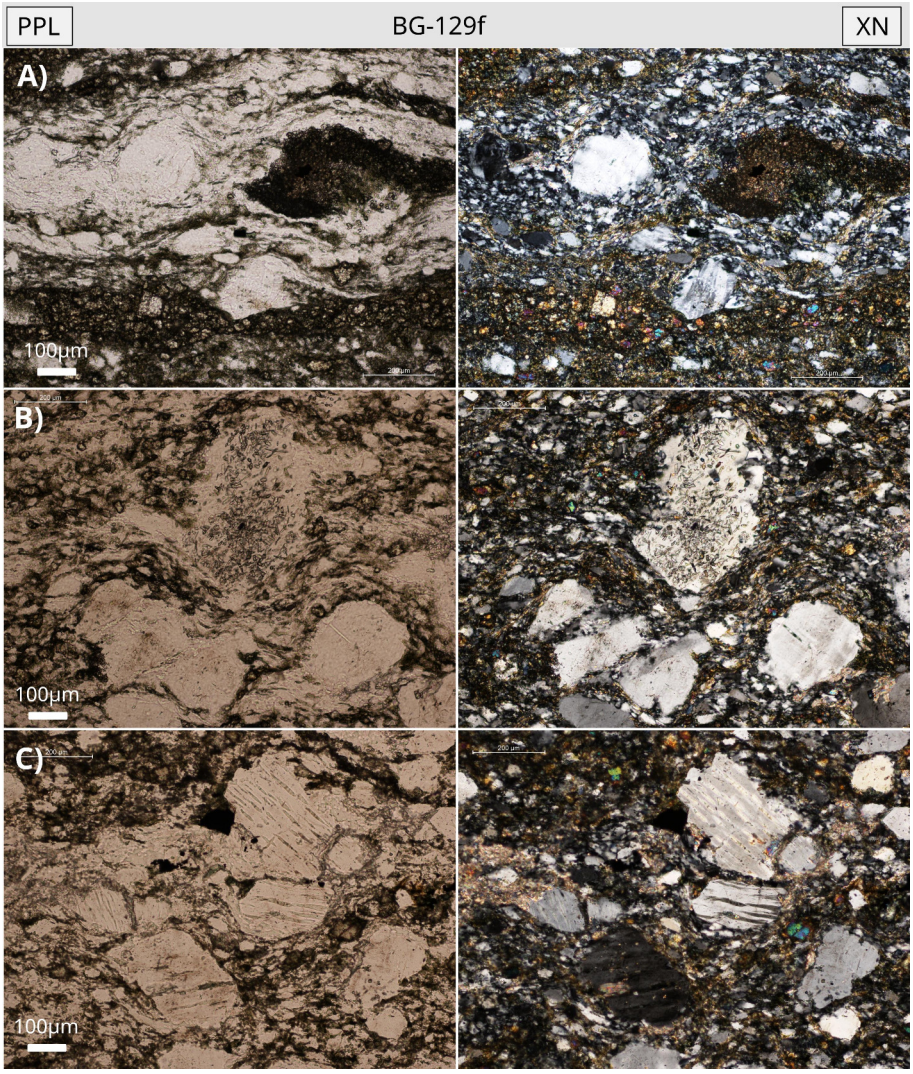

Fig. 8.10: Selected set of photomicrographs of the sample BG-129f. On the left, image without analyser (PPL) and on the right, with crossed-nicols (XN). The orientation of the photomicrographs is SE-NW (i.e., SE to the left side and NW to the right side). A) S-C fabrics inferred from the clasts of the quartzo-feldspatic band, indicating top-to-NW shear sense. B) Sigma-object indicating top-to-NW shear sense. To the lower left side of the photomicrograph, a fractured porphyroclast with antithetic fractures also show consistent top-to-NW sense of shear. C) Perthitic plagioclases porphyroclasts with angular to sub-rounded shapes.

8.3 Hanging wall fault-rocks: cataclasites

A series of field sketches and pictures together with 6 thin sections of the cataclasites along the Raudbergerstunnel were made to assess the influence of cataclasis away from the fault.

8.3.1 Some field observations

The cohesive cataclastic rocks on the hanging wall show an intricate veining pattern of increfasing density towards the fault core. There are veins with different coloration; most of them are pale green and some others are white. White veins are more frequent nearby the fault and are generally overpreinting pale green veins or parallel to them. Pale green veins may range from

<1 mm to 1 cm. These cross cut each other and diplay millimetric offsets consistent with sinistral shear. Qualitatively, the increasing veining frequency towards the fault indicates higher degree of deformation by cataclastic mechanisms.

At meso-scale, it is rather difficult to observe the characteristic features of cataclasis besides the veining. Cataclastic rocks along the tunnel usually show a banding between quartzofeldspatic and mafic bands. The banding is very folded in some locations along the Raudbergerstunel. The typical textures of cohevise cataclastic rocks, with large portion of matrix and cataclastic fragments, are better observed at the SE entrance to the Raudbergerstunnel, along the pedestrian path. Layer of cohesive fault breccias are seen along the strike slip of the fault, next to the fault core.

8.3.2 Microscopic scale

In this subsection, the thin sections made along the cataclasites will be presented with pictures and described. The thin section location is depicted in Fig. 8.1. The code for the thin sections taken from the cataclastites is 'DS-', although EC-30d is also part of the cataclastic fault rocks. The thin sections are oriented SE-NW, thus SE correspond to the left of the photomicrographs and NW correspond to the right.

Cohesive cataclasites and breccias are classified on the same basis as incohesive rocks: cataclasites are composed by <30 % of wall rock fragments, unlike breccias; which consist of >30 % of wall fragments. Cohesive cataclasites and breccias are generally produced deeper than incohesive fault rocks, and some common features are recrystallization and cementation between fragments. Epidote, quartz and chlorite are usual mineral infills found in cataclastic and extensional veins and matrix. The cataclastic flow is the responsible mechanism of deformation, which involves grain boundary sliding and pressure solution. Rock fragments are usually transected by healed cracks (visible through fluid inclusions).

- **Petrographic aspects of the cataclasites**

The rock forming minerals are K-feldspar, albite, plagioclase (anortite) and quartz. The ratio of plagioclase to alkali feldspar lays in the monzonite domain. The quartz portion to plagioclase and alkali feldspar is estimated to be <20 %. Larger preserved porphyroclasts are in some cases interpreted as titanites and undistinguished pyroxenes. The porphyroclasts are wedged and rhomb-shaped and occasionally square to rectangular. These have very high relief and high-order birefringence, which suggest the presence of clino-pyroxenes rather than orthopyroxenes. They are usually idomorphic and very fractured. The fractures are nearly orthogonal, resembling to the cleavage of pyroxenes, although the cataclasis makes their recognition more difficult. The accessory minerals that can be recognized are apatite, monazite, titanite and rutile. The rock is classified as a pyroxene-bearing quartz-monzonite to monzonite.

Secondary mineral phases, chlorite (by chloritization and fluid crystallization) and epidote, were crysallized in later events. The opaque minerals are also interpreted as secondary minerals phases and are inferred to be Fe-rich minerals, such as hematite and pyrite. Fluid alteration manifests in all thin sections through visible saussuritization of Ca-rich minerals, sericitization of alkali feldspars, and relatively large crystals of epidote and saussurite. Fe-rich chlorite is refilling veins and growing radially. The chlorite is distinguished as Chl_1 and Chl_2 in the figures. Chl_1 refers to the replacement chlorite, which has probably altered totally pre-existing biotites of the host rock. Chl_2, or chlorite 2, refers to a later chlorite phase that crystallized after deformation under greenschist metamorphic conditions. Fe-rich veins filled with fine-grained opaques are more prominent the closer the rock is to the fault.

The presence of rutile and titanite, and some relict polygonal contacts among Fd and Quartz indicates that the host rock comes from an igneous mafic protolith rich in Ti_3^+. Some relict foliation can be discerned from oriented elongated chlorite (probably originally biotite).

- **DS-00**

DS-00 is located just outside the Raudbegerstunnel, approximately 108 m away from the fault plane. This sample represents the less deformed rock along the tunnel to the old road to Aurland.

The cataclastic component in this thin section is rather difficult to observe, since no large cataclastic fragments are evidenced in the thin section photomicrographs (Figs. 8.11 and 8.12). Evidence for cataclasis is found in transgranular microcracks that can be followed from clast to clast (Fig. 8.11.C). Feldspar crystals are affected by penetrative fracturing. The microcracks link with each other from side to side of the clasts (Fig. 8.11.C & .D). Transgranular microcracks, rather than intragranular microcracks, are interpreted in basis of the crystalline nature of the host rock (Blenkinsop, 2000). The recrystallization of the matrix overprint the transgranular fracturing of initial cataclastic deformation. The matrix is formed by dynamic recrystallization of quartz and feldspar by subgrain rotation and bulging mechanisms. Quartz ribbons are not very common yet they are present. Large porphyroclasts of plagioclase are seen with inherited polysynthetic twinning. Many of these clasts have lobate boundary contacts and incipient kinking (Fig. 8.11.B). Mechanical/deformation twinning is also observed in plagioclase (Fig. 8.11.B). Large feldspars with lobate edges display perthitic exsolutions (Fig. 8.12.D). Relict C foliation can be inferred in Fig. 8.11.A by the oriented bands of chlorite. Oblique S-type foliation may also be inferred from the orientation the porphyroclast and elongation of quartz ribbons in Fig. 8.11.A.

The sample also presents clear evidences of fluid alteration by saussuritization, sericitization and chloritization. The relation between these two mineral phases is not clear in this thin section. Regardless, two different chlorite growth phases can be distinguished in this thin section (Chl_1 and Chl_2), according to the prior petrographic explanation. The Chl_1 is seen recrystallizing in the

boundaries of the porphyroclasts (Fig. 8.11.A). Replacement chlorite (Chl_1) may have recrystallized as Chl_2 after deformation at greenschist facies conditions (Fig. 8.11.B & Fig. 8.12.A). Chl_1 is easily distinguished by its pseudomorphic appearance.

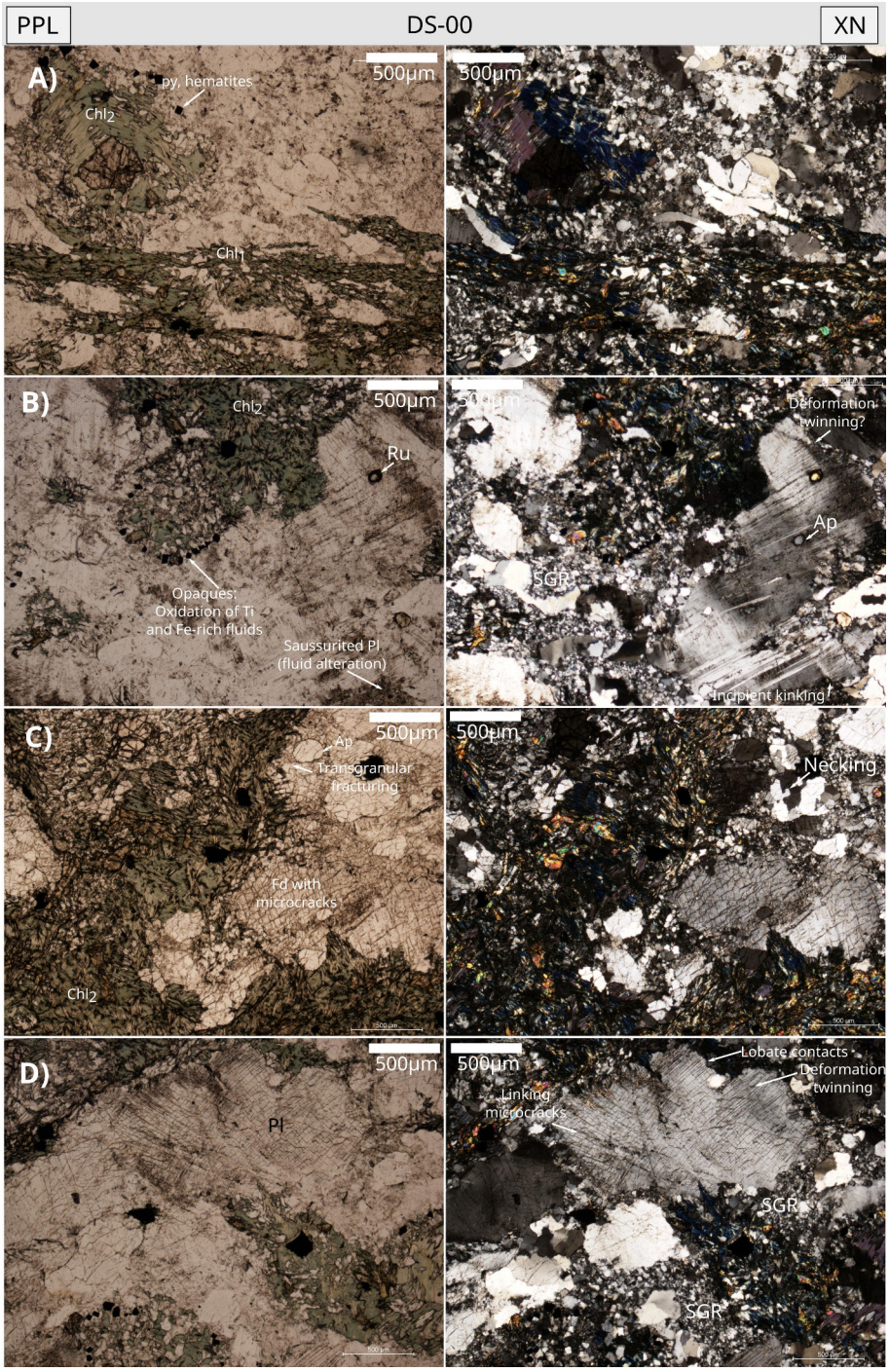

Fig. 8.11: Set of photomicrographs under transmitted light of the sample DS-00. The left picture is taken without analyser (PPL) and the right picture is taken with crossed-nicols (XN). A) Relict C and S foliations inferred from oriented chlorite (Chl_1) and elongation of quartz ribbons. B) Saussurization in Ca-plagioclase. Euhedral opaques in rims of chloritized porphyroclasts. XN: crystal-plasticity of plagioclase. C) Transgranular microcracking in feldspar into apatite grain, easily recognizable Chl_2 and XN: bulging (necking) in quartz. D) Linking of microcracks in plagioclase, deformation twinning and recrystallizing lobate contacts.

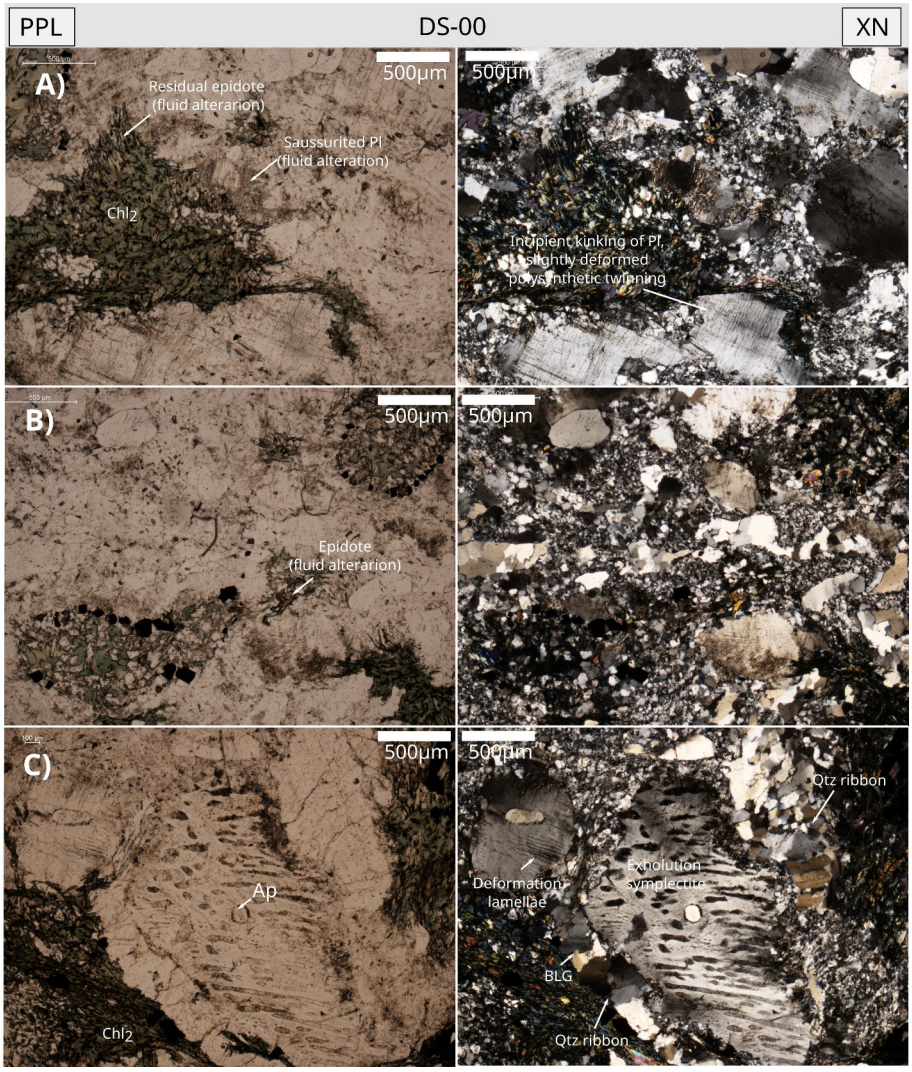

Fig. 8.12: Set of photomicrographs of the sample DS-00. On the left, image without analyser (PPL) and on the right, with crossed-nicols (XN). A) Epidote growth together with Chl_2. XN: Incipient crystal-plasticity of plagioclase. B) XN: polycrystalline quartz ribbons and developed subgrain rotation recrystallization. C) Large apatite crystal in feldspar. XN: The feldspar manifest exsolution and lobate contacts on the edges of the grain. Quartz ribbons with internal bulging are discernible.

- **DS-01**

DS-01 is collected at the entrance in the NW side of the Raudbergestunnel, around 100 meters away from the fault (Fig. 8.1).

The evidences of cataclasis are clearer in this sample than in the previous. Cataclastic fragments in the order of 10 mm to <1 mm are observed in the photomicrographs. The cataclastic fragments have polymineralic composition and have large matrix portions of recrystallized feldspar and quartz (Figs. 8.13 to 8.15). Crystal plasticity of feldspar minerals is evident by incipient kinking. Flame perthites with mutidirectional component are abundant within larger feldspars. Lobate contacts at the edge of large clasts of felspar are common. Subgrain boundary rotation (SGR) takes over as a recrystallization mechanism but bulging (BLG) is still present. Transgranular microcracks are partially healed and refilled by fluids. Some polygonal contacts of

quartz suggest static recrystallization, which may be preserved from the initial igneous texture or recrystallized after deformation. Some unrecognizable wedged porphyroclasts presumably present simplectites that have been completely replaced by chlorite (Fig. 8.13.C & Fig. 8.14.B). Porphyroclasts of monazite and pyroxene (Fig. 8.13.A) appear very fractured within cataclastic millimetric veins but they do not present evidences of shearing or rotation. Undulous extintion of some grains and deformation lamellae of quartz is present in some crystal fragments (Fig. 8.15).

Cataclastic veins filled with saussurite also contain a small portion of angular fragments. Saussuritization has affected perthitic exsolutions in feldspars. Well developed crystals of epidote are recognizable in plagioclase crystals, and are usually accompanied by secundary chlorite (Chl_2). The veining occur at many micro-scales ranging from 1mm to <50 µm. The thinnest veins present usually irregular shapes and are accommodated between fragments or locally cross-cut them (Fig. 8.15.A). The irregular amoeboid-shaped veins are very incompetent compared to the cataclastic rock. Veins are usually banded with outer thin layers of fine grain-sized opaque minerals. Opaque mineral phases occur where Chl_2 clusters as idiomorphic cubic, rhombic and elongated sections of crystals. The elongated crystals may be ilmenite, whereas the other phases can be magnetite or pyrite. Differential rheological behavior of quartz and feldspar is observed in accross veins (Fig. 8.15.C). In Fig. 8.15.C, the upper side of the photomicrograph show obvious signs of cataclasis, whereas the lower part of the photomicrograph, along the vein in the center, show sigmoidal lenses of recrystallized quartz.

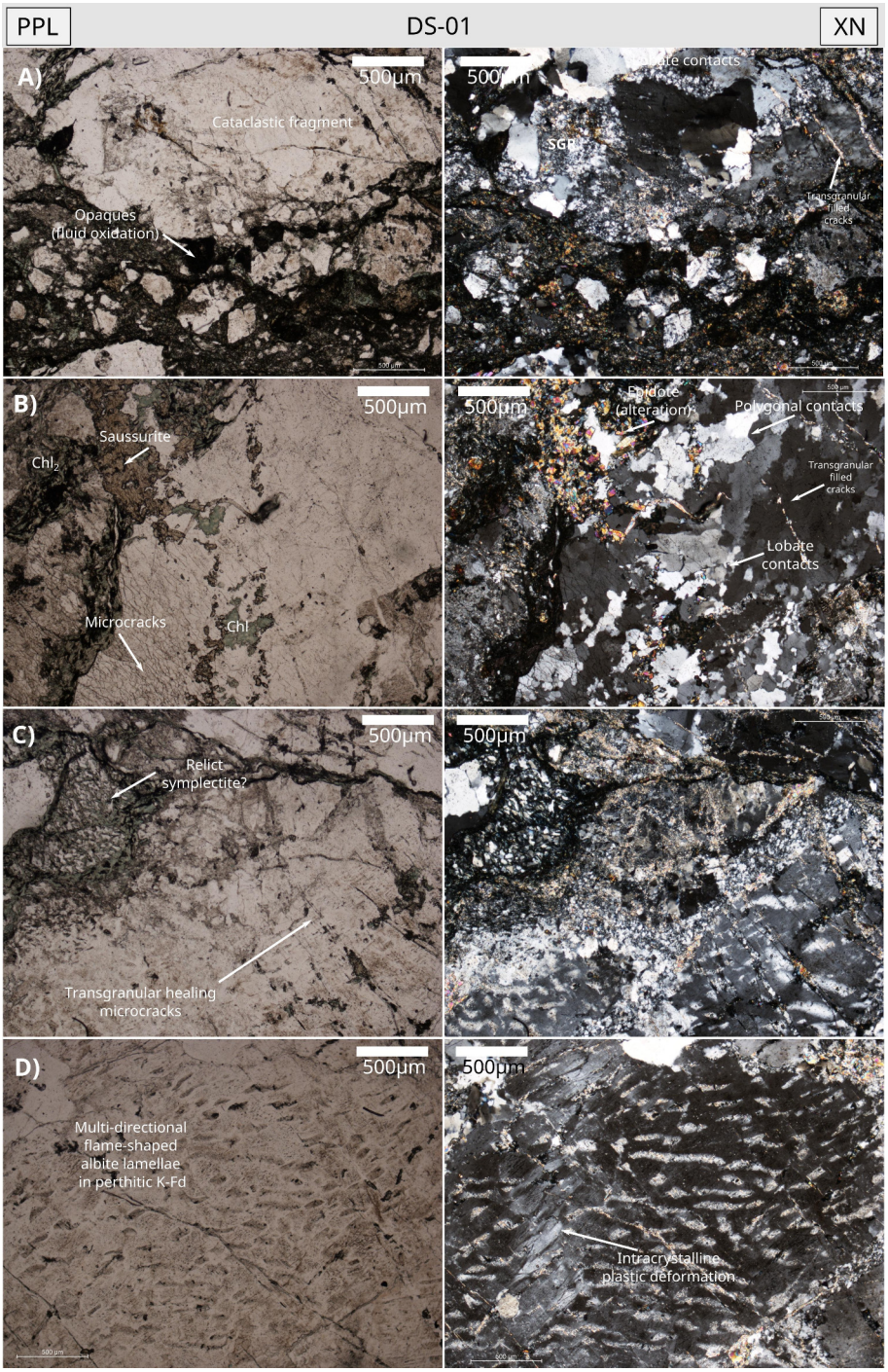

Fig. 8.13: Set of photomicrographs of the sample DS-01. On the left image without analyser (PPL) and on the right, with crossed-nicols (XN). A) Large cataclastic fragment with SGR recrystallization and larger Fd and Q clasts. B) preserved microcracks in recrystallized quartz. Fluid alteration products are easily recognizable. C) Transgranular microcracks crossing K–Fd filled with saussurite and presumably exholution simplectites replaced by chlorite. D) Multi-directional flame-shapedpresent albite lamellae in perthitic K–Fd. XN: crystal-plastic deformation.

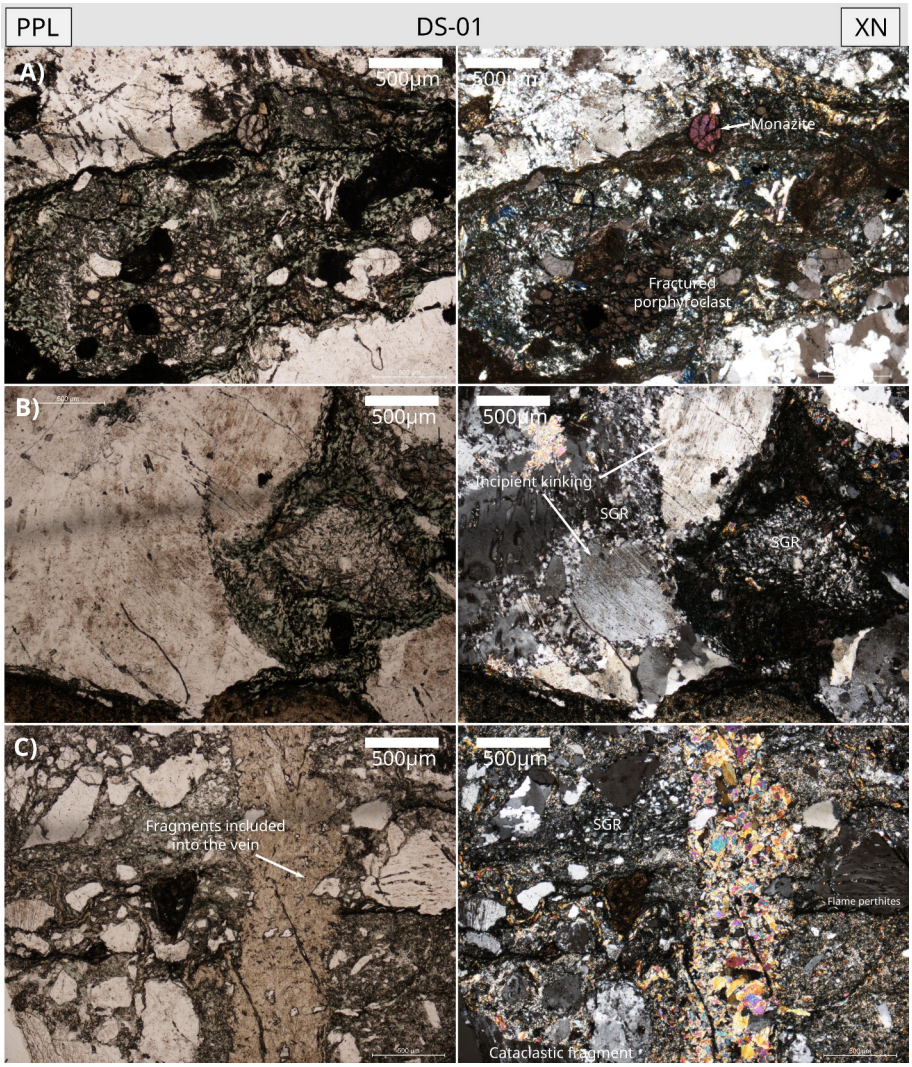

Fig. 8.14: Set of photomicrographs of the sample DS-01. On the left image without analyser (PPL) and on the right, with crossed-nicols (XN). A) Monazite (round mineral with 3rd to 4th order interference colors) and presumed pyroxene (rhombic-shaped porphyroclasts with dark interference colors at the bottom left) strongly fractured within cataclastic vein totally recrystallized with Chl_2. B) XN: Evidences of SGR and incipient kinking in plagioclase. C) Vein filled with relatively large crystals of epidote/zoisite. The vein is obliquely fractured and the fractures fade out on the walls of the vein. An angular K–Fd grain with perthites is also observable at the right side of the picture.

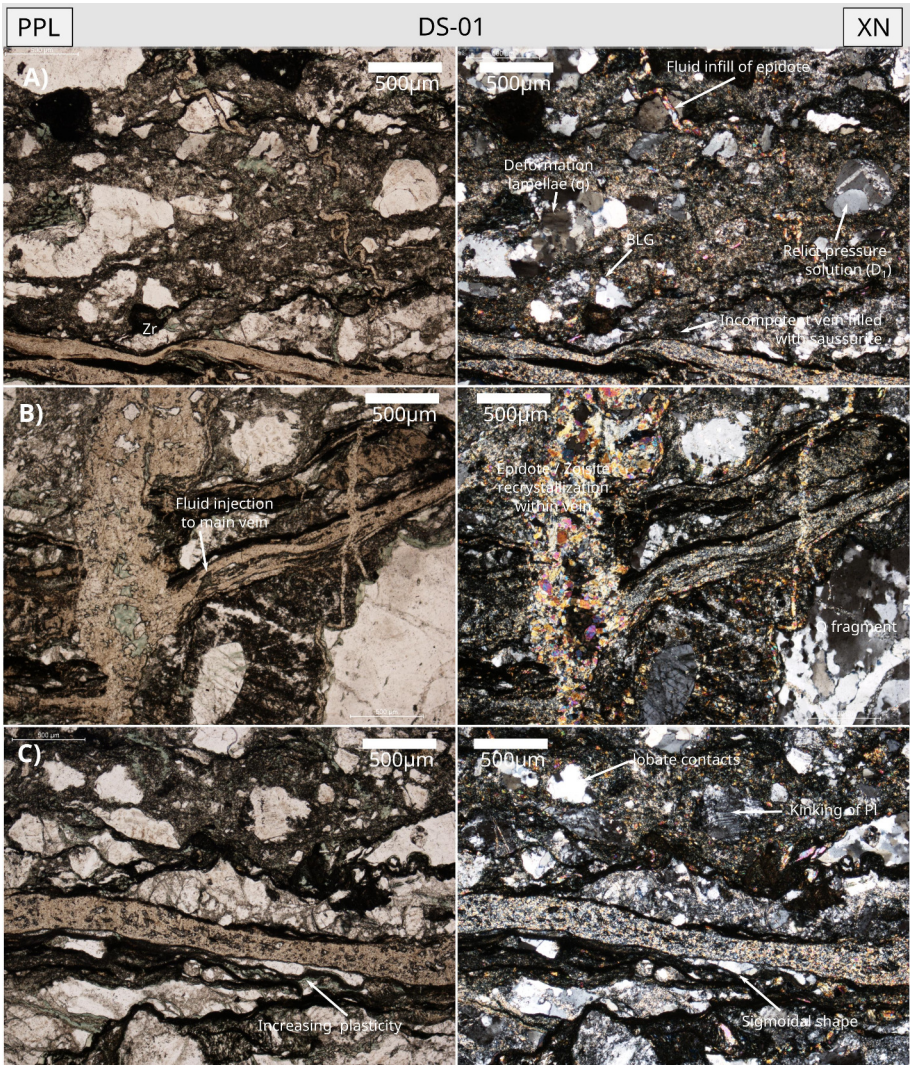

Fig. 8.15: Set of photomicrographs of the sample DS-01. On the left image without analyser (PPL) and on the right, with crossed-nicols (XN). A) Micromillimetric vein filled with epidote cutting an angular crystal with undulous extintion. XN: Evidences of deformation lamellae in quartz and BLG, corresponding with low-grade conditions. Bi-mineralic clast with presumably relict structure from initial cataclasis (D1). B) Fluid injection from subsidiary vein feeding the main vertical vein, which is filled with chlorite in the center and rims of epidote. The epidote crystals are normal to the walls of the vein. C) Differential rheological behavior in either sides of the horizontal cataclastic vein. The lower part seems more ductile-like, whereas the upper part of the photomicrograph presents obvious cataclastic deformation.

- **DS-03**

This sample is located about 82 meters away from the fault, inside the Raudbergerstunnel (Fig. 8.1).

The thin section photomicrographs show evidences of cataclasis flow affecting a highly recrystallized rock probably of mylonitic origin (Fig. 8.16). The dynamic recrystallization mechanisms most commonly observed in this rock are SGR and grain boundary migration (GBM) at smaller scale. The cataclastic fragments are larger in at this point than at the entrance of the tunnel (i.e. DS-00). No transgranular microcracking from DS-01 is evidenced from this thin section. Some cataclastic fragments are single crystals of alkali feldspar with saussurited exso-

lution lamellae. The recrystallized portion of the cataclastic fragment do not show signs of fluid alteration, which is rather affecting to the cataclastic matrix than the larger fragments.

Veininig is frequency and comonly infilled by Ca and Fe-rich fluids that has crystallized as iron rich chlorite and epidote minerals along the walls (Fig. 8.16.A & .B). The veins range from a 2 mm to <50 µm. The thicker ones contain angulous cataclastic fragments, whereas the thinner veins usually do not show cataclastic flow (Fig. 8.16.C). Epidote minerals (probably zoisite) is crystallizing orthogonally to the vein walls, which can be taken as an indicator of the paleo-stress field under the structures were produced. Secondary chlorite is refilling veins and altering matrix, although the Chl_2 is not crystallizing with radial or fibrous habit. Replacemnt chlorite (Chl_1) is observed in relict mylonitic foliation. Large quartz crystals are refilling some veins.

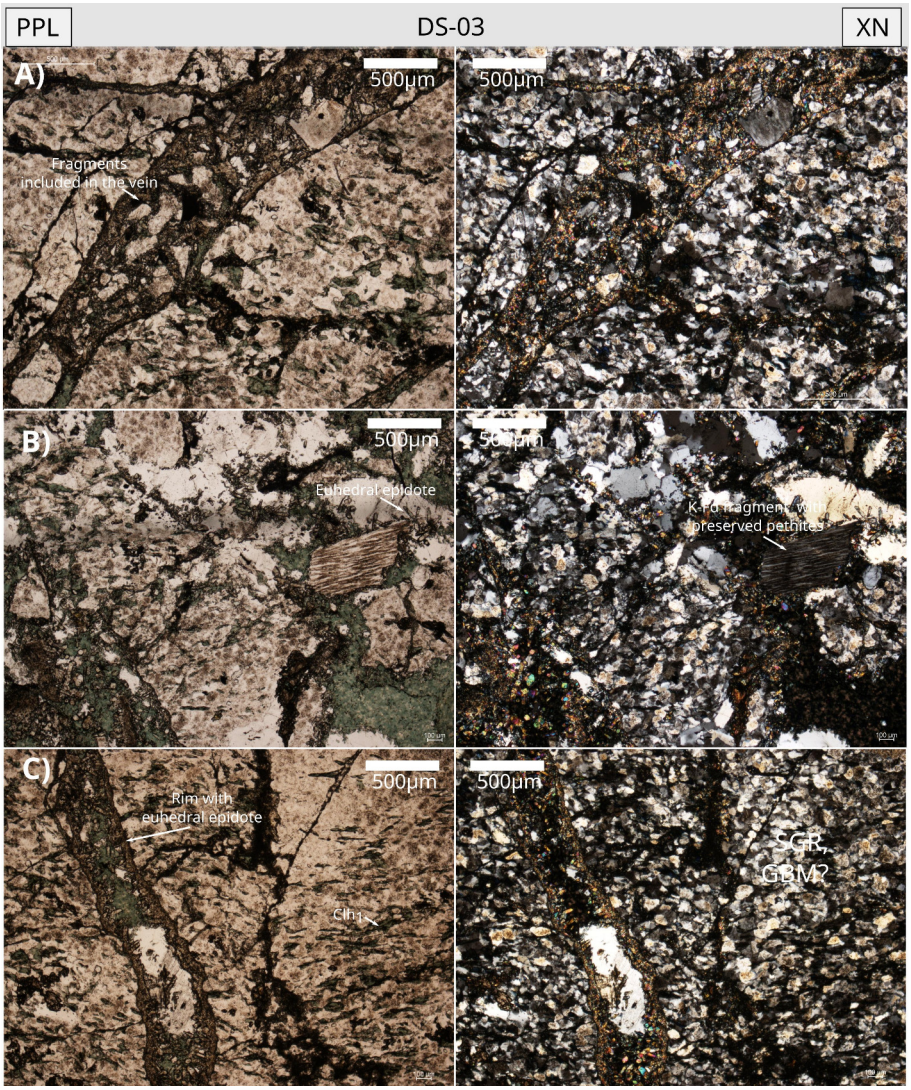

Fig. 8.16: Selected set of photomicrographs of the sample DS-03. On the left image without analyser (PPL) and on the right, with crossed-nicols (XN). A) Vein with cataclastic fragments included within it. Epidote and chlorite are also observable within veins and fractures. B) K-feldspar with altered perthites. C) Vein of irregular thickness filled with orthogonal oriented c-axis of epidote to the walls. Dynamic recrystallization by SGR and GBM has affected the previous cataclasited rock. Chl_1 is easily recognizable in relict foliation within a cataclastic fragment.

- **DS-05**

DS-05 is collected from the middle part of the tunnel approximately 60 to 50 m away from the fault.

The photomicrographs show a collection of exsolution structures strongly affected by later fluid alteration(Figs. 8.17 and 8.18). Sympletites and flame-shaped perthites in alkali feldspar are the main structures indicating exsolution. The cataclastic fragments show signs of SGR re-crystallization and crystal-platic deformation evidenced by their sigmoidal-like shape. Bulging is also present in larger polycrystalline quartz fragments. Quartz ribbons are observed around feldspar porphyroclasts. Alkali feldspar and undistinguished porphyroclasts strongly affected by exsolution of two mineral phases are locally included into a sigmoide-like shaped core-and-mantle structures (Fig. 8.18.C). Sometimes these porphyroclasts with symplectites are forming a sigmoidal-like shape themselves with not obvious mantle (Fig. 8.18.A). These porphyroclasts are locally boudinaged and recrystallized as shown in Fig. 8.18.B). Symplectites have generally preferred orientation direction (rather than vermicular un-oriented lamellae), which can be used for the estimation of the paleo-stress field.

Transgranular microcracks affect cataclastic fragments, quartz ribbons and recrystallized fragments (Fig. 8.17.C). Transgranular microcracks are overprinting recrystallization textures of cataclastic fragments,reason why it is not related to the transgranular fractures seen in DS-00 and DS-01

Chlorite of replacement have recrystallized after deformation in relict foliation (Fig. 8.17.B). Euhedral opaques are found within the cataclastic matrix but do not show preferred distributions. Saussuritazion occurs in the exsolution lamellae and fine-grained recrystallized parts. Epidote is found filling transgranular microcracks.

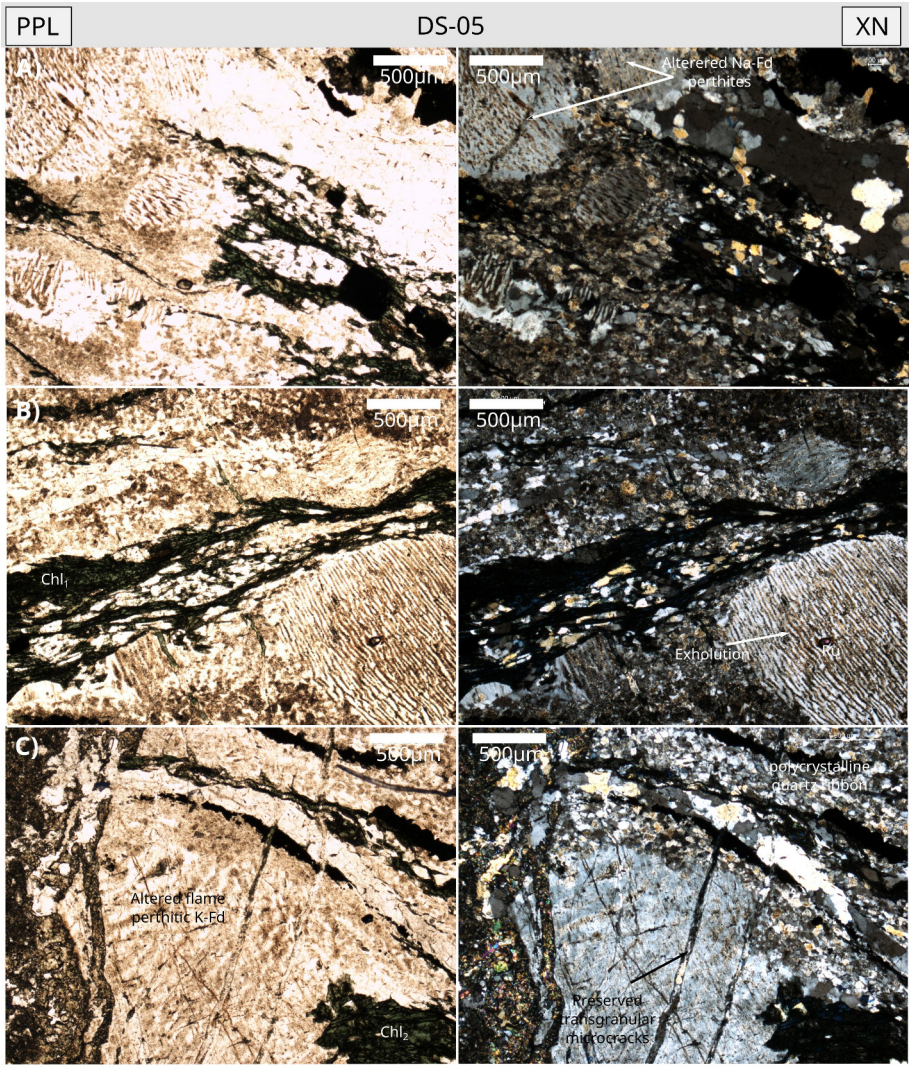

Fig. 8.17: Selected set of photomicrographs of the sample DS-05. On the left image without analyser (PPL) and on the right, with crossed-nicols (XN). A) Undistinguishable fragments of recrystallized matrix and feldspar with sympletites. B) Chl1 in relict mylonitic foliation (?). XN: Exsolution symlectites. C) Transgranular fractures different from the ones from D1. XN: Quartz ribbons around feldspar porphyroclasts.

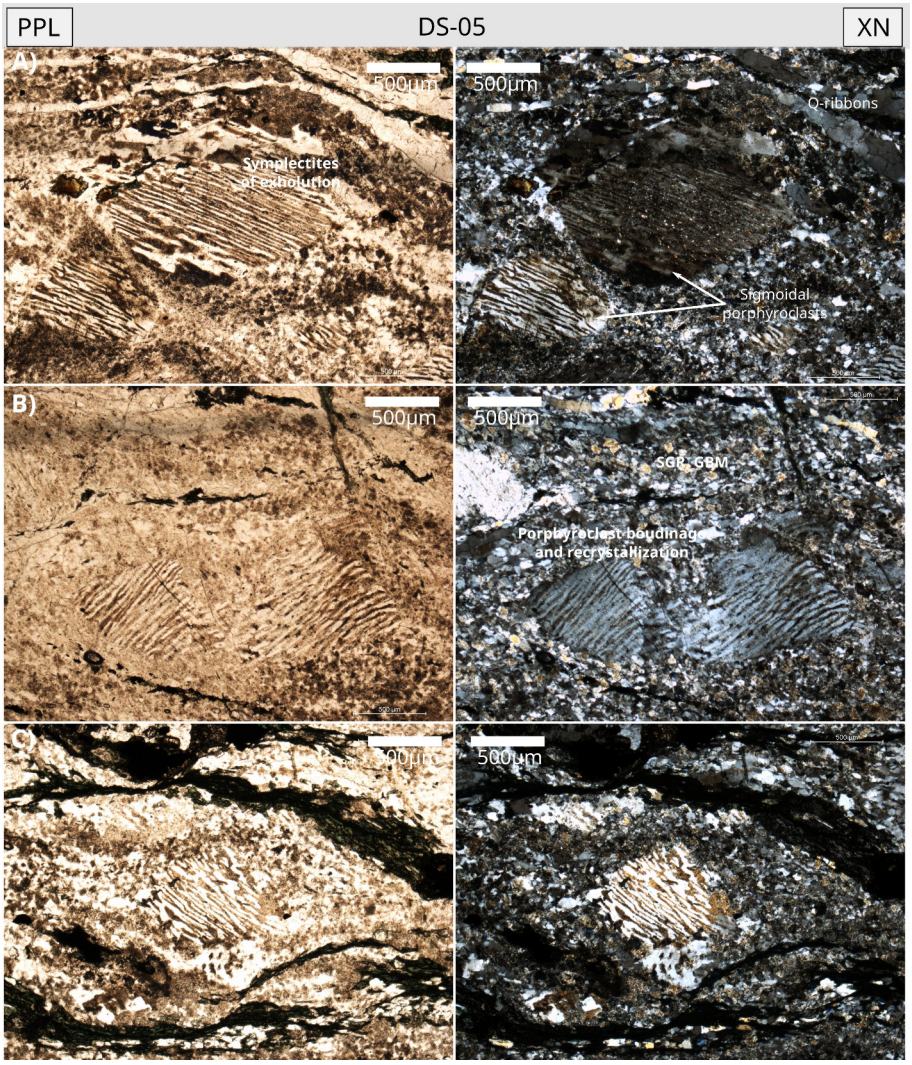

Fig. 8.18: Selected set of photomicrographs of the sample DS-05. On the left image without analyser (PPL) and on the right, with crossed-nicols (XN). A) Sigmoidal-shaped porphyroclasts wih symplectite structures following a preferred orientation. B) Boudinaged and recrystallized porphyroclasts with prior sigmoidal shape. C) Core-and-mantle structure with sigmoidal-like shape.

- **DS-07**

This sample is picked from 36 m away of the fault, from inside the Raudbergerstunnel. An easy observable feature of this sample is that veining and fracturing is more prominent than in DS-05.

Cataclastic angular fragments in this sample have from millimetric to micrometric size. Some cataclastic fragments with feldspar show recrystallization on the edges ((Fig. 8.19.B). Dynamic recrystallization occurs by BLG and SGR mechanisms (Fig. 8.19.B). Polygonal contacts between crystals of quartz and feldspar are found in larger polycrystalline fragments, which either have been preserved from a pre-existing structure or as onset of static crystallization (Fig. 8.19.B).

Fluid injection is fed through fractures to larger veins. Larger veins display internal structure evidenced by compositional changes (switch of vein infill). Dark brown to black bands or subveins are generally in the outer part of thick veins filled with saussurite (Fig. 8.19.D). The dark

veins and subvein inside thicker ones occur more frequently in this sample than seen before. Veins usually include fragments and idiomorphic crystals of opaques of secondary generation. Euhedral crystals of epidote are found in the cataclastic matrix growing in random directions. Thinner veins occasionally displace thicker veins with clasts (Fig. 8.19.C), providing time constrains in relative terms.

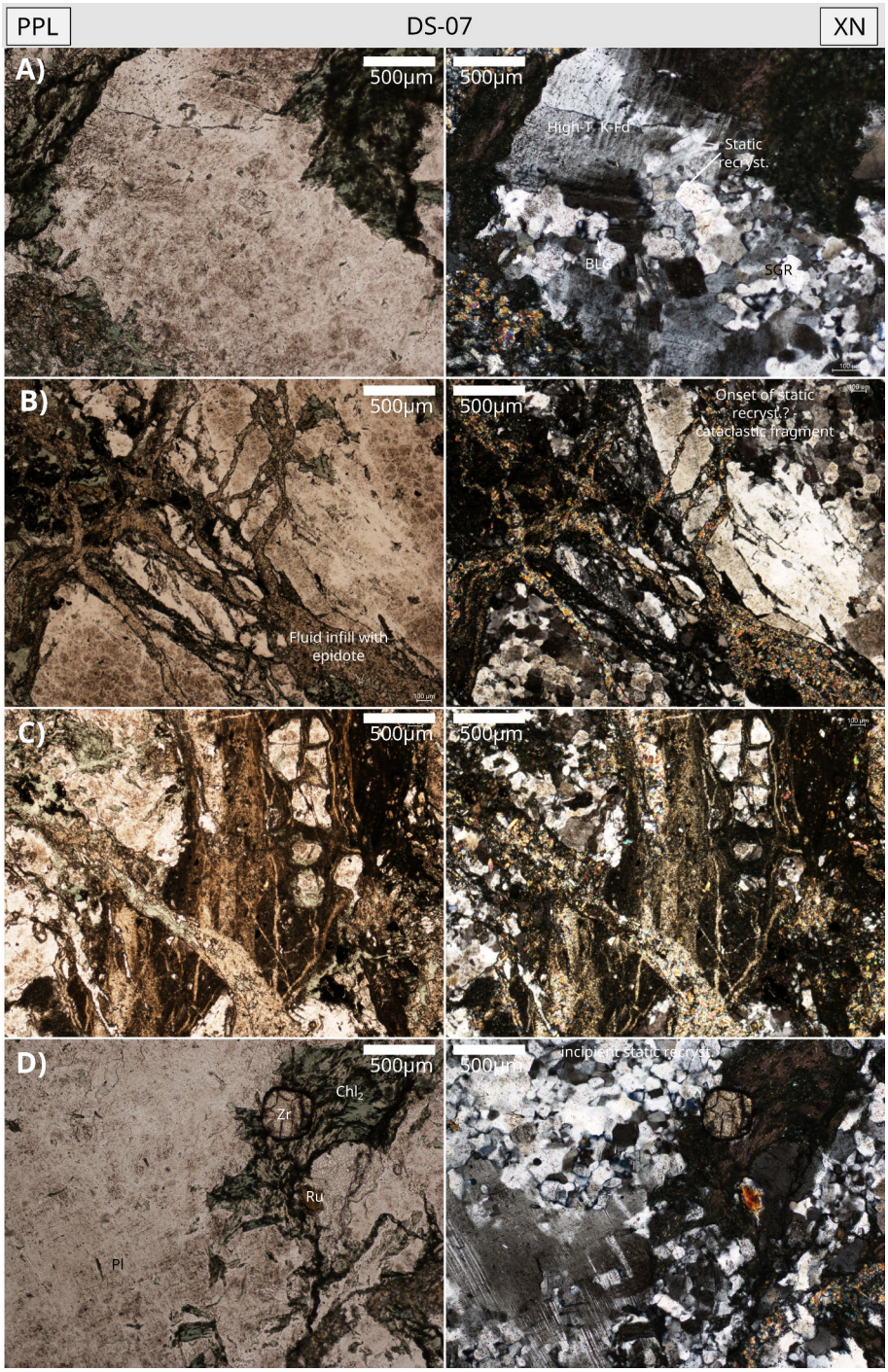

Fig. 8.19: Selected set of photomicrographs of the sample DS-07. On the left image without analyser (PPL) and on the right, with crossed-nicols (XN). A) Evidences for static recrystallization, bulging and subgrain rotation. B) Fractured polycrystalline fragment that has undergone dynamic recrystallization. Saussurite is filling veins and fractures. C) Shear displacement of a large vein caused by a thinner one. D) Bulging recrystllization along the edges of the plagioclase crystal and incipient static recrystallization. Large zircon crystal and rutile crystals are observed.

- **DS-11**

This sample belongs to cataclastic rocks from 3 m away of the fault. In thin section, however, it is difficult to appreciate its cataclastic component.

The presence of sigmoidal-like shaped polycrystalline aggregates, quartz ribbons and onset of plagioclase kinking are indicators of crystal-plastic deformation (Fig. 8.20.B). The quartz ribbons observed in this thin section are often elongated and quartz subgrains show frequently preferred orientation (Fig. 8.20.D). Dark bands of fine grain sized material may be marking a relict foliation (Fig. 8.20.B, .C & .D). S-C foliation may be discern as well from the orientation of quartz ribbons and subgrains (Fig. 8.20.B & .D). The relict S-C foliation indicates dextral sense of shear. Transgranular fractures affecting altered and unaltered matrix are filled with felsic minerals (not shown in the presented photomicrographs). Veins filled with saussurite cross-cut the dark bands of fine-grained material mentioned previously. Some veins of saussurite show dextral shearing by the displacement of other veins (Fig. 8.20.C), which could be linked to the youngest episode of transgranular fracturing.

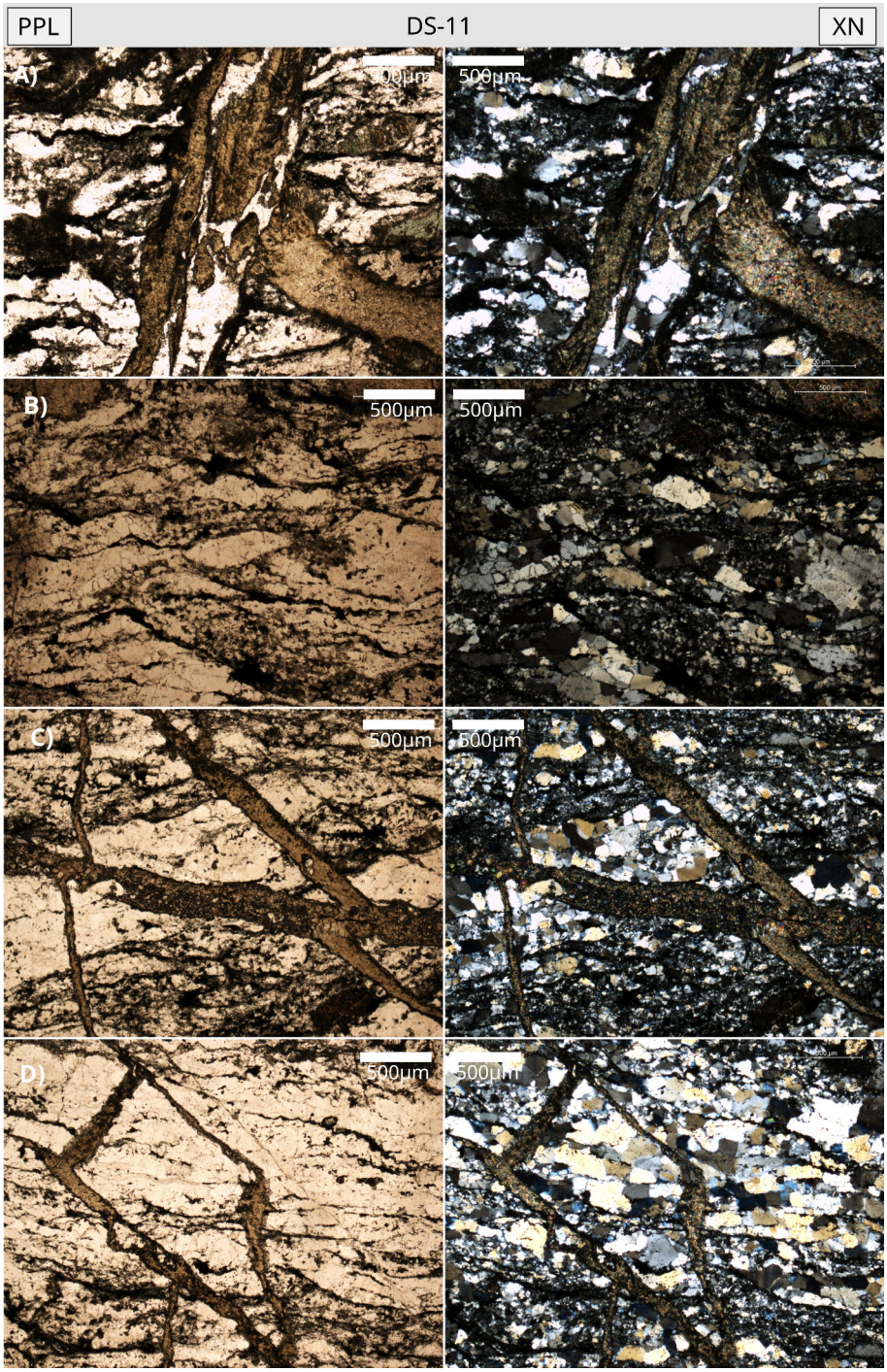

Fig. 8.20: Selected set of photomicrographs of the sample DS-11. On the left image without analyser (PPL) and on the right, with crossed-nicols (XN). A) Quartz in veins. B) Relict S-C foliation idincating dextral sense of shear (bottom lefft and center) and quartz sigmoid indication dextral sense of shear with polygonal to lobate contacts. C) Recrystallized cataclastic-mylonitic matrix cross-cut by two generations of veins. The smoothly inclined oblique vein from left to right displace in a dextral sense of shear the pre-existing veins of saussurite. D) S-C foliations cross-cut by veins with saussurite infill. Dynamic recrystallization by bulging and subgrain rotation mechanisms.

- **EC-30d**

This thin section is extracted outside the tunnel parallel to the strike of the fault. The orientation of this thin section does not correspond to the observation plane. The the observation plane of this thin section is parallel to the fault strike (NE-SW). In the photomicrographs, NE is

located to the right and SW is in the left of the photomicrographs collection.

Bulging and subgrain rotation recrystallization are recognizable in fractured cataclastic fragments and matrix. Some fragments may show grain boundary migration mechamism of recrystallization (Fig. 8.21.B). Quartz and feldspar ribbons are encountered in alternating bands of finer and coarser grain size of the matrix (Fig. 8.21.C). Polycrystalline ribbons display slight grain shape preferred orientation (Fig. 8.21.C).

Some kinematic indicators typical from mylonitic rocks such as bookshelf fractured clasts and porphyroclasts tailed complexes are encountered within the finest matrix portion (Fig. 8.21 A & .C). In the photomicrographs, the kinematic indicators portray sinistral shear and thus, indicate a counter-clockwise fault-movement component according to the NE-SW observation plane. A S-C foliation supporting the later kinematic observations may be also inferred by the arrangement of mantled porphycroclasts (Fig. 8.21.C). Shear bands affecting porphyroclasts and displacing compositional banding are frequent in this thin section.

Chlorite is present but not as frequent as observed for thin sections that are collected farther away from the fault (e.g., DS-00). Saussuritizion is present and localized in the fine-matrix portion. However, large crystals of epidote, as seen in previous samples, are not present.

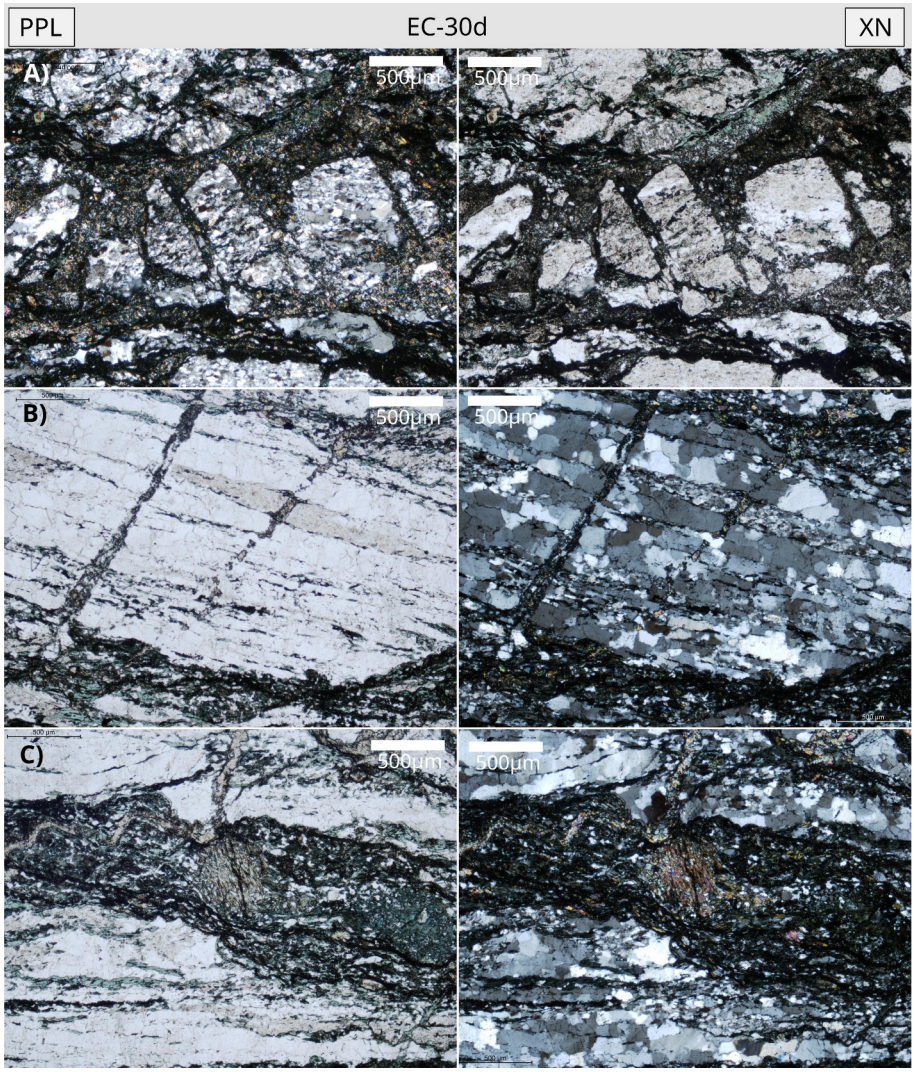

Fig. 8.21: Selected set of photomicrographs of the sample EC-30d. On the left image without analyser (PPL) and on the right, with crossed-nicols (XN). A) Bookshelf fractured clast in fine matrix portion indicating sinistral shear.B) Healing transgranular fractures and filled ones visibly cross cutting a cataclastic fragment. Subgrain rotation is recognizable within the fragment and in the matrix. C) Slight grain shape preferred orientation of ribbon subgrains. Porphyroclast tail-complex indicating sinistral shear located within the matrix portion.

8.4 Deformation at shallow levels

At Lærdalsøyri, brittle deformation and related fault rocks overprint pre-existing fault rocks formed a lower crustal levels. Descriptions for two thin sections and for field observations are provided in this section.

- **Introduction to brittle fault rocks**

Brittle fault-related rocks can be incohesive and cohesive. At shallow levels of the crust, breccias and cataclasites are incohesive. Incohesive breccias are distinguished from cataclastic non-cohesive rocks by the volume of fragments from wall rock (>30 %). Incohesive cataclastic rocks contains <30 % of wall rock fragments and have fine-grained matrix. Fault gouges occur

in very narrow fault zones and consist mainly of very fine crushed material with very few porphyroclasts implying high strain at shallow crustal levels. Clay minerals are usually found within fault gouges along with transgranular and intragranular microcracks.

Fault gouges, cataclasite and breccias typically develop an internal fabric within the fault core named as Riedel fracture geometry (in Snoke et al., 1998). The Riedel fracture geometry is useful determine the shear sense due to the geometrical relations among fractures or foliations (Fig. 8.22). The Riedel fracture geometry involves P and Y shear surfaces, reason why it is also regular to refer to it as PYR1 foliation. Y shear surfaces are parallel to the fault boundary and represent the principal shear displacement. Y-shears are the equivalent to C-fabrics in mylonites. P shear surfaces develop at different angles from the Y fabrics. P-shears can be subparallel to Y-shears or form an angle of 135° (Rutter, 1986)). Riedel 1 shears resembles to ductile shear bands form by brittle fracturing and are the equivalent to C'-fabrics in mylonites. Riedel 2 is the conjugate set to the Riedel 1 fractures (Fig. 8.22).

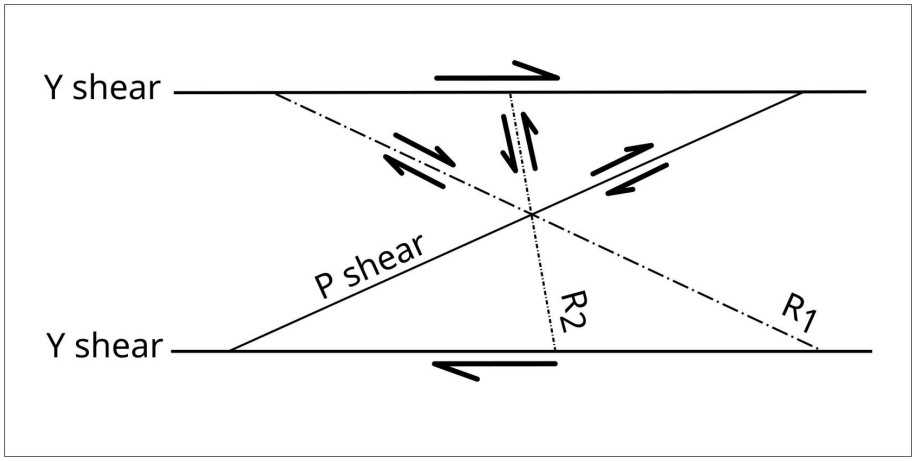

Fig. 8.22: Schematic representation of the Riedel fracture geometry in incohesive fault rocks (PYR foliations). The Y shear is equivalent to the C-fabrics of mylonites. In the picture, the Y shear are defining the fault boundary. P shear are developed as S foliations found in mylonites. The Riedel 1 (R1) are shear surfaces equivalent to C'-fabrics. The Riedel 2 (R2) are conjugated fractures to Riedel 1 but these are not always present or well developed.

The classification of incohesive rocks given by Twiss & Moores differs slightly from the one given by Sibson (1977). Sibson (1977) differences between fault breccias and gouges by the volume of visible fragments, which should larger than 30 % for breccias and less than 30 % for gouges. Twiss & Moores (1992) did not attribute any change in matrix portion between breccias and gouges (both <30 %), but they based their classification on the size of clasts. At meso-scale, it is easy to recognize breccias by the size of their clasts.

8.4.1 Field observations

In the Lærdalsøyri outcrop, brittle fault-related rocks are exposed in the fault core, which is 1,3 meters thick. The fault core consists of fault gouges and fault breccias. At meso-scale, the

fault gouges have no recognizable clasts with naked eye (<30 %). There are two kinds of fault gouges exposed at Lærdalsøyri; powder rock gouges totally incohesive (i.e. rock powder) and hardened fault gouges. The hand specimens collected from hardened fault gouges show little cohesion and are easy to break up. However, they were possible to collect because they have a degree of competence.

The coloration of the fault core is very different from the mylonites and cataclasites in the footwall and hanging wall blocks. The fault core is colored in white and distinct pale green colors. Darker gray bands mark the compositional banding between white and pale green levels.

The fault core presents internal fabrics and it is divided in two main parts (Fig. 8.23). The upper part of the fault core consists of 40 cm of fault breccias and powder rock (fault gouges). The lower part encompasses approximately 90 cm of fault gouges (Fig. 8.23.B).

In the upper part of the fault, the fault breccias are in contact with the upper fault boundary and have irregular thickness along the fault, ranging from a couple of centimeters to almost 30 cm thick (Fig. 8.23.F). The fault breccias have less than 30 % of matrix portion and the sizes of clasts range from 1 to 3 cm of diameter. The fault gouges do no exhibit any recognizable sub-internal fabric or foliation. The upper part of the fault core is well delimited from the lower part by a thin layer of brownish gouges that is parallel to the fault boundary, and it is interpreted as an Y shear surface (Fig. 8.23c).

Different levels of fault gouges can be distinguished within the lower part of the fault core: (1) powder rock gouges and (2) hardened gouges. The powder rock gouges are located along the lower fault boundary and along the P shear surfaces. The thickness of hardened and power fault gouges is irregular within the lower part of the fault core (Fig. 8.23.c). The fault gouges exhibit internal fabrics defined by diverse shear surfaces that have been interpreted as PYR1 foliation (Fig. 8.23.C & D). Riedel 1 fractures may seem like shear bands (Fig. 8.23.D). The PYR1 foliation interpreted on the field corresponds to top-to-NW directed movement of the fault during brittle reactivation (as the dextral shear represented on Fig. 8.22). A conjugate set of penetrative joints with centimetric spacing between them cross-cut the hardened fault gouges.

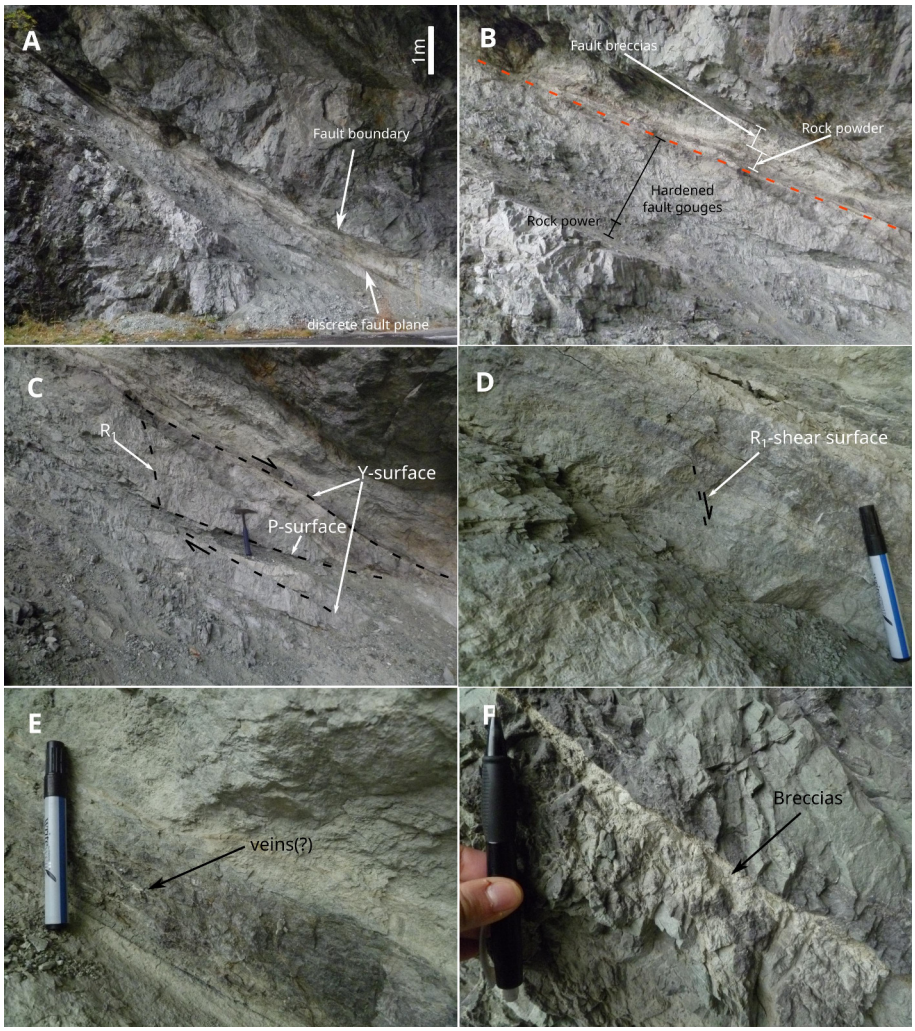

Fig. 8.23: Pictures of the Lærdal-Gjende fault at Lærdalsøyri outcrop with orientation SE - NW (i.e. SE to the left and NW to the right). A) Overview of the core of the Lærdal-Gjende fault and footwall and hanging wall blocks to the sides. B) Close up of the fault core and the two main divisions of the fault core (upper and lower part). In the picture, the dashed red line indicated the boundary between upper and lower parts. C) Interpretation of PYR1 foliations. D) Riedel1 fractures (R1) showing an offset of <1,5 cm. E) Thin white veins in the powder rocks gouges of the upper part of the fault core. F) Fault breccias along the upper fault boundary.

8.4.2 Microscopic scale

One thin section from the fault gouges will be described in the following section (Fig. 8.24) and one thin section from the cataclasites of the hanging wall will be very briefly commented (Fig. 8.25).

- **EC-07**

The photomicrographs show a rock with variable matrix portion and variable volume of clasts. The size of the clasts is related to the matrix content. At microscopic scale, it is possible to observe that the proportion between matrix and clasts is related. When the clasts are larger, the matrix portion is reduced. On the contrary, an augment in matrix portion occurs when the size of the clasts is smaller (Fig. 8.24). The photomicrographs show that fractures refilled by

quartz cross-cut clasts and matrix. No fracture preferred orientation is observed, although some antithetic microfaults with millimetric offsets are occasionally seen.

The size of the clasts range from >1 mm to 10 µm. The shape of the clasts is generally angular with exception of the smallest fragments embedded on the matrix, which may exhibit subrounded shape. There are bands with larger matrix volume around 50 to 70 %, and felsic bands with <20 % of matrix volume (Fig. 8.24.B). The felsic bands of fragmented quartz and felspar contain the widest range of clasts sizes, whereas matrix-rich bands are generally do not contain clasts larger than 200 µm. Transition zones between felsic and matrix-rich bands are observed (Fig. 8.24.B).

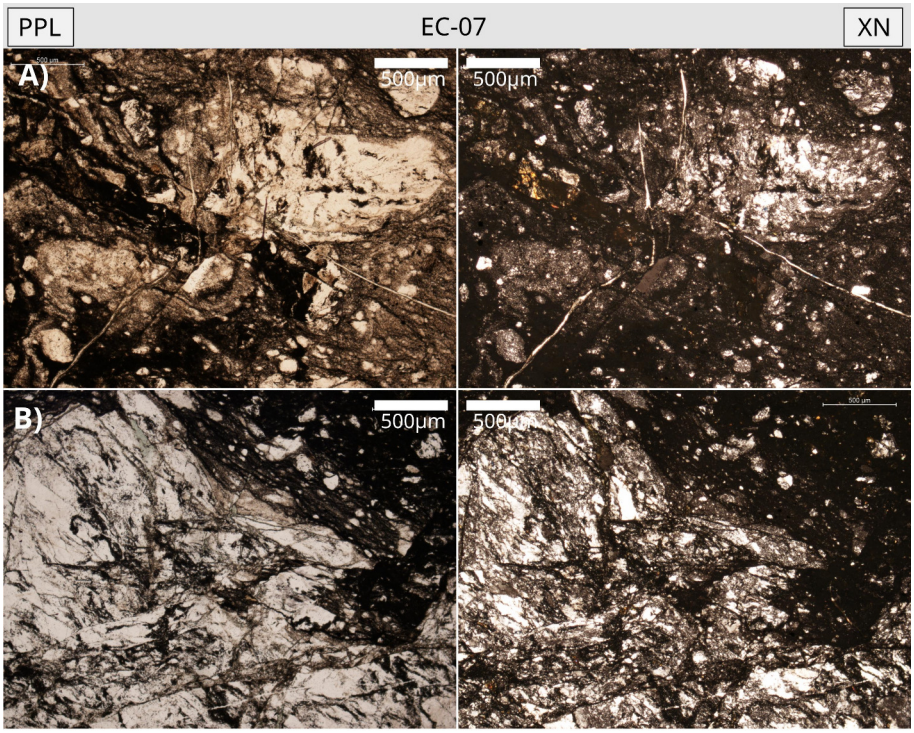

Fig. 8.24: Oriented SE-NW photomicrographs of the fault gouges from the fault core of the Lærdal-Gjende fault. A) Strongly fractured clast of >1 mm diameter. The fragments are angular to sub-rounded. The sub-rounded clasts are clustered on matrix-rich parts. B) Strongly fractured felsic band (upper left to lower right sides) and transition to matrix-rich band with few and smaller clasts.

At microscopic scale, it is more difficult to define whether a rock with cataclastic texture is a microbreccia, breccia, gouge or cataclasite based on matrix percentage. According to the classification given by Twiss & Moores (1992), cataclasites should contain more than 30 % of matrix. Cataclasites are associated to cohesive rocks, however, according to this criteria the fault gouges described previously at meso- and micros-scale should be classified as cataclastic rocks when observed at microscopic scale. As seen under the microscope, the fault gouges from the Lærdal-Gjende fault are rather heterogeneous in terms of matrix/clast sratio. This fact makes difficult the classification of this fault-related rocks. Breccias are easily discern by the size of the clasts, but not by the matrix portion.

- **DS-12**

DS-12 is taken from 1 m above the upper fault boundary in the hanging wall cataclasites. In this sample, brittle deformation structures overprint dynamic recrystallization textures and other features typical from deformation at higher crustal levels. The photomicrographs from DS-12 show fractured angular clasts of felspar and transgranular fracturing. Necking and SGR textures are cut by latter fractures. Slightly ductile deformed plagioclases are also affected by microfaulting (Fig. 8.25.B).

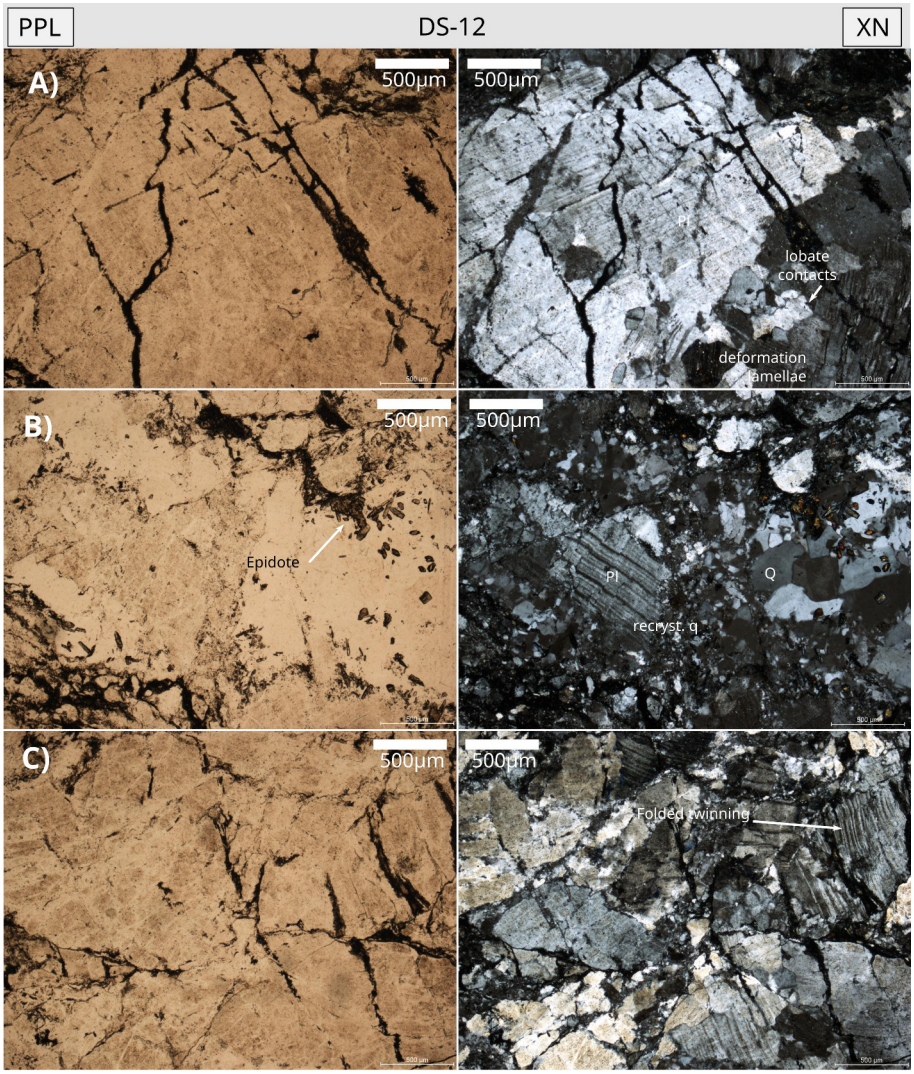

Fig. 8.25: Photomicrographs in transmitted light of the thin section DS-12. The picture to the left is taken without analyzer and the right with analyzer. A) Plagioclase with joined fractures and transgranular fractures. Lobate contacts and deformation lamellae are also observed and overprinted by transgranular fracturing. B) Microfaulted plagioclase and evidenced of static and dynamic recrystallization by bulging and SGR. Euhedral epidote crystals do not decribe any relative time relation with the brittle deformation episode. C) Folded twinning in plagioclase and transgranular fractures between clasts.

This page is intentionally left blank

9 Apatite Fission Track (AFT) results

9.1 Pre-analysis: Z-calibration and track density gradient

Ten Durango and FishCanyon age standards from four irradiations were used with the purpose of calculating the Zeta personal value (Table 9.1). Each irradiation contained at least a pair of Durango and Fish Canyon Tuff standards. The Durango and Fish Canyon tuff date from 31,4 $\pm$ 0,5 Ma (McDowell et al., 2005) and 27,9 $\pm$ 0,5 Ma (Hurford & Hammerschmidt, 1985) respectively. The weighted mean Zeta value obtained through the ZETAmean program by Mark Brandon was 241,86 $\pm$ 6,05.

Table 9.1: Durango and Fish Canyon Tuff age standards counted to obtain the personal zeta value

Irradiation	**Standard**	**Counted grains**	**Spontaneous** N_s	**Induced** N_i	**Dosimeter** N_d	**Dosimeter** $\rho_d\ (10^5)$	**Zeta** Z	**Zeta** 1σ
NoB 014	DUR	21	379	2015	33896	14,3843	232,68	13,6
	FCT	22	204	1257		14,3229	240,56	18,71
NoB 017	DUR1	20	284	2240	30433	18,50203	268,34	17,5
	DUR2	21	215	1752		18,29982	280,32	20,8
	FCT1	20	127	852		18,43462	203,45	19,73
NoB 002	DUR1	22	175	1142	27373	16,6235	256,83	21,3
	DUR2	21	150	879		16,6493	221,57	19,93
	FCT1	21	202	1424		16,5977	237,51	18,41
NoB 003	DUR	20	113	866	35651	18,65555	258,61	26,23
NoB 025	DUR	20	212	1432	28053	18,7993	236,31	17,85
Weighted mean Zeta: **241,86 $\pm$ 6,05**								

All age standards were analyzed by the external detector method. For the external detector method, a 0,5 geometrical correction factor was applied ($^{4\pi}/_{2\pi}$ geometry). $N_{s,i}$ are the total number of spontaneous and induced tracks counted per sample. N_d is the total number of induced tracks counted in the dosimeter glasses. $\rho_d\ (10^5)$ is a theoretical value for calculating the thermal neutron fluence during irradiation.

Three dosimeter glasses from the irradiation NoB-025 were counted in order to obtain the variation of the neutron fluence along the irradiation tube (Appendix B). The three glasses were located on top, middle and bottom of the irradiation can. The density gradient is necessary to proceed with the age calculation (Fig. 9.1).

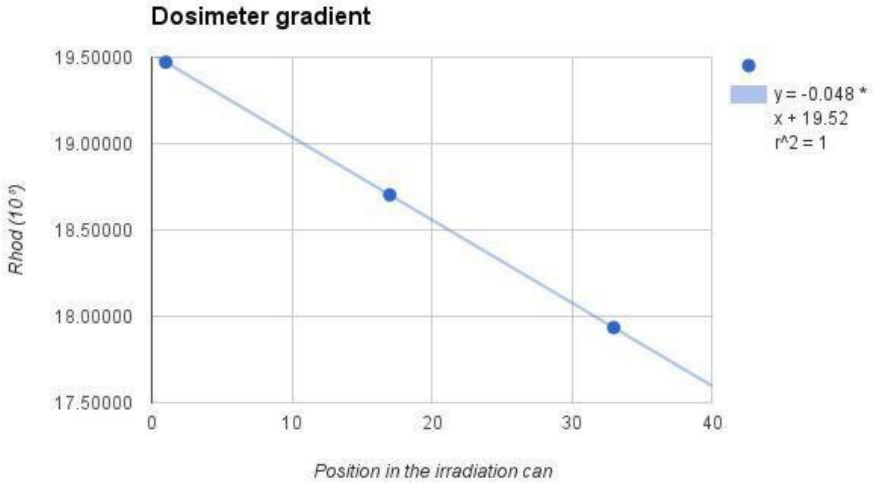

Fig. 9.1: Dosimeter gradient from the irradiation NoB-025.

9.2 Apatite quality assessment

The quality of the apatite crystals was diverse within the sample collection (Fig. 9.2). The samples EC-02 and EC-03 had regular quality and were difficult to count. The apatite crystals from EC-02 were generally very fractured and in occassions look 'dirty' and were very small. Some scratches were produced during the process of polishing. EC-03 presented few good apatites for counting, and the general look of the apatite crystals was similar to EC-02. Many of the apatite grains from these samples were strongly zoned. EC-09, from the same tectonostratigraphic unit than EC-02 and EC-03, presented less scratches and larger crystals, although practically all the grains were zoned and had low content of fission traks. The grains counted were either not zoned or slightly to moderately zoned. In average, the quality of the apatite crystals in EC-05 was good, but some of them were strongly zoned. The state of the apatite crystals from the samples EC-06 and EC-08 was similar to the crystals from EC-05. In the samples EC-06 and EC-08, some grains were slightly zoned rather than strongly zoned. Notable cracks were also present in EC-06. The apatite crystals from EC-12 'a' and 'b' were slightly zoned to zoned. The apatite crystals from EC-13 had inclusions, many dislocations, some of them looked dirty and were slightly zoned as well. EC-14 and EC-15 were easy samples to count. The apatites were occasionally zoned to slightly zoned but did not present much difficulties. The Table 9.2 provides a summary of the quality of the apatite crystals of each sample.

Table 9.2: Summary of the apatite quality in each sample.

Sample name	Apatite quality	Zoning	Inclusions	Notable Cracks
EC-02	Poor	×	×	×
EC-03	Very poor	×	×	×
EC-05	Fair	×		×
EC-06	Fair	×		×
EC-08	Fair	×		
EC-09	Moderate	×	×	×
EC-12a	Fair	×		
EC-12b	Fair	×		
EC-13	Moderate	×	×	
EC-14	Great-Fair	×		×
EC-15	Great-Fair	×		

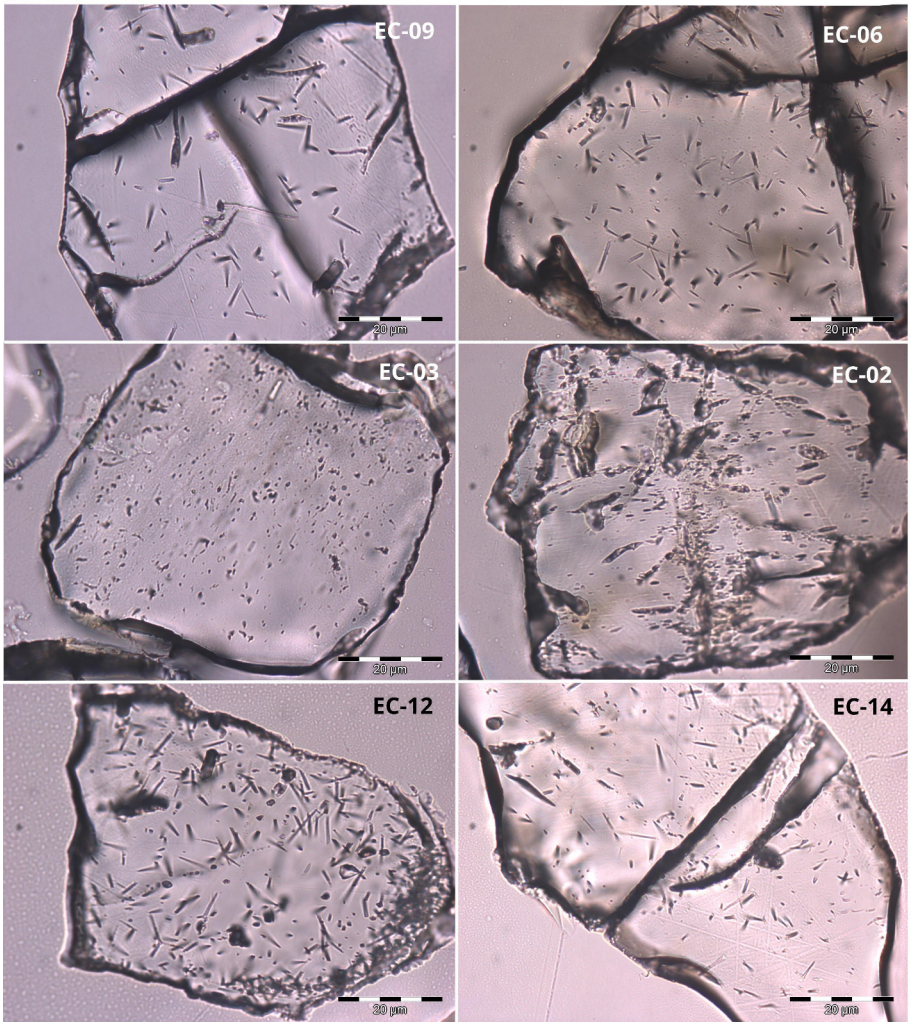

Fig. 9.2: Pictures of c-axis parallel oriented apatite crystals under transmitted light. The pictures of EC-09 and EC-06 show cracks cross-cutting the apatite. EC-09, EC-06 and EC-14 are slightly zoned. EC-12 is moderately to strongly zoned. EC-03 and EC-02 exhibit many dislocations and scratches, which made the counting process more difficult.

9.3 Ages across the Lærdal-Gjende fault

The results from apatite fission track analysis are presented in the following section. The irradiation code for the analyzed samples is NoB-025. The sample AS-23, which belongs to the irradiation NoB-019, is used for track length measurements as a representative sample from the hanging wall block. All the results produced for this thesis are listed in Table 9.3. The sample collection contain only 3 samples from the hanging-wall of the Lærdal-Gjende fault. The AFT ages coded with 'AS' in the Fig. 9.2 were included from the master thesis of (Al-Samarray, 2013) as a complement to the samples taken for this Master Thesis.

A wide span of AFT ages was obtained for the footwall and hanging wall rocks. The rocks from the footwall block gave a range of ages from Middle Cretaceous to Early Jurassic (105 ± 6 to 187 ± 18 Ma), although most of the samples date from Early Cretaceous. The samples with Early Cretaceous age cluster next to the fault. The distribution of ages on the map in the footwall suggest that age increases with distance away from the fault (Fig. 9.3). The sample EC-12 deviates from the general trend, since it is the sample that is farthest away from the fault and dates from Early Cretaceous. This sample will be discussed in Chapter 11.

The ages obtained for the 3 samples from the hanging wall were very disperse: Permian, Late Triassic and Early Jurassic. EC-02 and EC-03 date from Permian and Late Triassic, and are collected from 3 m above sea level. The samples coded with 'AS-' included in Fig. 9.3 do not display any observable relation on the map between age and distance from the fault.

The radial plots from all the samples are included in Appendix C. The radial plots display the age dispersion of the grains counted in each sample.

Table 9.3: Apatite fission track results.

Irradiation code	Sample name	Elevation (m)	Counted grains	Spontaneous		Induced		Dosimeter		AFT Age (Ma)		$P(\chi^2)$ (%)	disp.	MTL ±1σ (μm)		MTL ±1σ (μm)		SD (μm)	No. tracks for MTL	Dpar ± SD (μm)		U (ppm)
				$\rho_s\ (10^5)$	N_s	$\rho_i\ (10^5)$	N_i	$\rho_d\ (10^5)$	N_d	Central age	1σ											
NoB-025	EC-02	6	21	5,1	136	5,4	144	18,46311176	28053	211	28	32,78	0,21							2,056571429	0,33643195	3,86
	EC-03	6	14	3,665	58	2,907	46	18,415084		289	67	46,98	0,38							1,296928571	0,105122979	1,89
	EC-05	3	20	13,959	412	29,103	859	18,36705625		112	10	2,84	0,21	9,9	2,05	12,01	1,05	2,052945578	55	1,302	0,170352576	19,73
	EC-06	3	20	10,567	320	19,781	599	18,31902849		117	9	72,99	0,01							1,31635	0,14377185	14,64
	EC-08	3	20	22,597	761	47,51	1600	18,27100073		105	6	44,58	0,08	11,16	1,97	12,62	1,48	1,96850934	59	1,18385	0,226464654	33,21
	EC-09	405	23	6,069	225	7,04	261	18,22297297		187	18	89,39	0							1,20526087	0,139211486	6,13
	EC-12a	935	20	28,959	915	45,923	1451	18,17494522		137	7	47,16	0,04	11,78	1,79	13,04	1,3	1,794470725	41	0,91365	0,119844318	33,81
	EC-12b	935	21	29,558	1010	46,181	1578	18,12691746		138	7	67,04	0,01	11,92	1,92	13,25	1,4	1,92377508	60	1,221952381	0,103984362	37,37
	EC-13	495	22	16,081	730	20,464	929	18,0788897		173	11	17,99	0,13							1,264318182	0,105850922	15,33
	EC-14	169	22	8,867	488	9,994	550	18,03086194		187	18	0,26	0,29							1,269045455	0,15552292	7,09
	EC-15	3	21	31,941	955	49,467	1479	17,98283419		139	8	1,6	0,15	10,74	1,63	12,49	1,14	1,680217595	101	1,34452381	0,109778695	38,96
NoB-019	AS-23	20												11,24	1,48	12,81	1,01	1,480167091	46			

Where:

$\rho_{s,i,d}$ = track density (10×10^5 track/cm^2) for spontaneous and induced tracks, and dosimeter.

N = number of counted tracks.

$P(\chi^2)$ = probability value of the chi-square age homogeneity test, which is passed when $P(\chi^2) \geqslant 5$ (Galbraith, 1981).

SD = Standard deviation (given for the MTL values and for the Dpar values).

$4\pi/2\pi$ = geometry correction factor of 0,5 was used during age calculation.

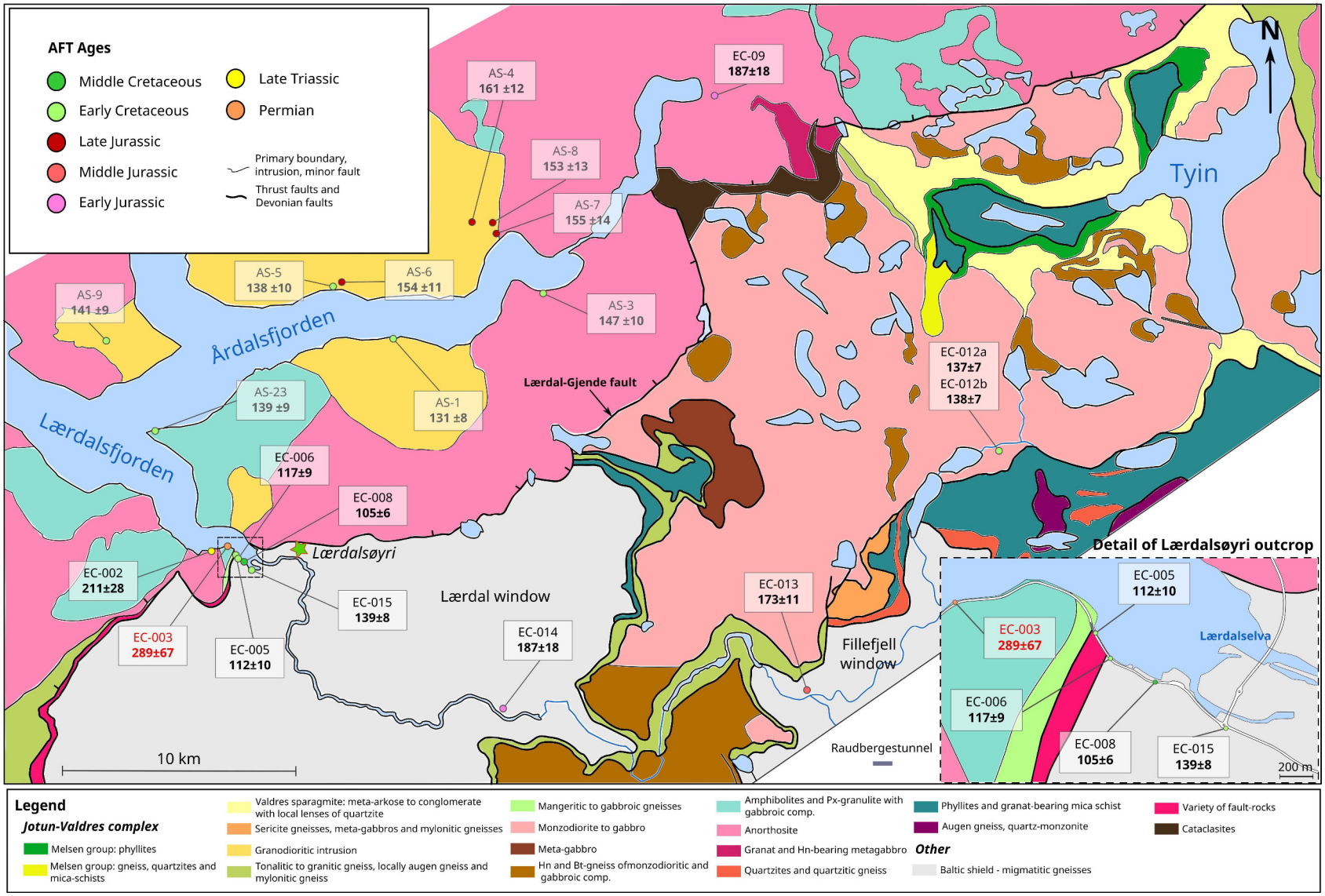

Fig. 9.3: Color coded AFT-age map of the study area. The AFT ages presented on the map are the results obtained in this thesis (EC-) and the results from (Al-Samarray, 2013) (AS-). The detailed map of the Lærdalsøyri outcrop is provided in the bottom right corner. The ages are given in Ma.

9.3.1 Distance from the fault vs. AFT age

AFT ages were plot against the distance from the fault in order to recognize if a correlation between both parameters exists. The distances are perpendicular to the SW-NE orientation of the Lærdal-Gjende fault. The AFT ages for the samples next to the fault may record the last episode of exhumation as long as it is a fault-related process. Whereas, distant samples might not be influenced by fault movements. Thus, a trend of decreasing age towards the fault might be expected for the samples of the footwall. Samples from different elevations are included in the plot. A total of 12 samples were analyzed for the hanging wall block, and consist mainly on data extracted from (Al-Samarray, 2013) (Table 9.4. The sample set of the footwall consists of 8 samples collected and analyzed for the present study (Table 9.4).

As observed in the plots, AFT ages vary as a function of the distance to the fault (Fig. 9.4).The red regression line representing the hanging wall draws a negative slope with a coefficient of determination (R^2) of 0,634. The blue regression line show a positive slope with a correlation of 0,581. Thus, the ages in the hanging wall block increase towards the fault, whereas the ages decrease towards the fault in the case of the footwall block. A statistical analysis of the data is performed and discussed on Chapter 11.

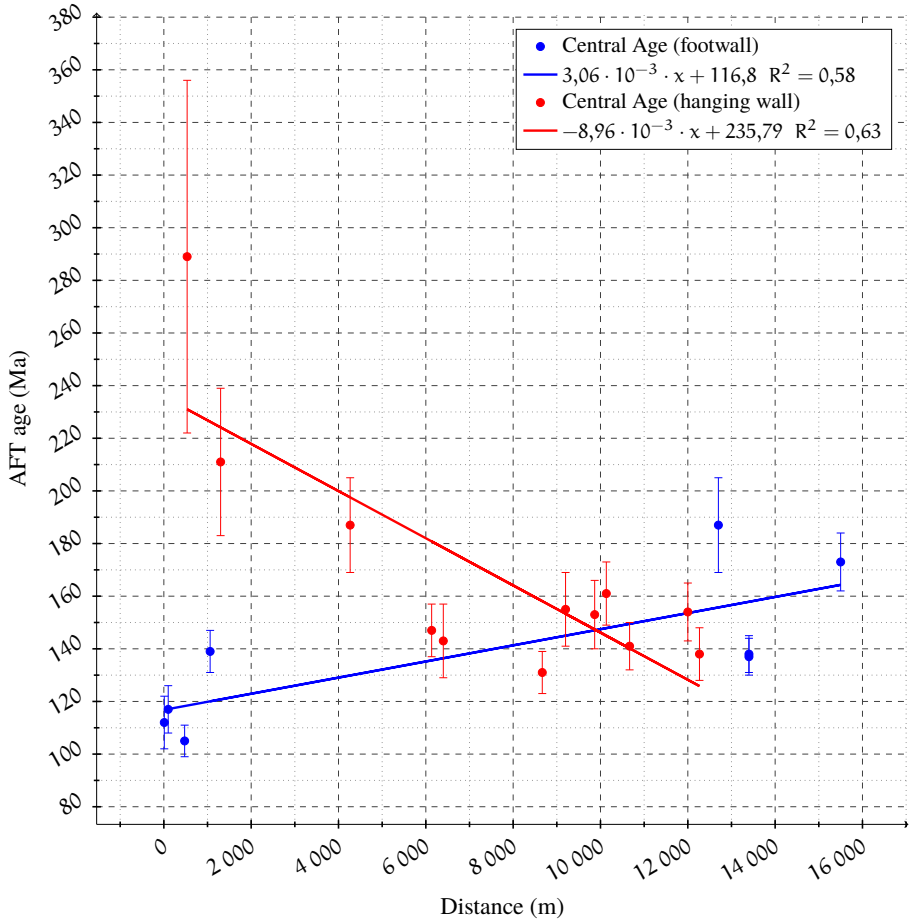

Fig. 9.4: Plot of distance away from the fault (m) against AFT age (Ma). Red dots for hanging wall, which include some results from (Al-Samarray, 2013). Blue dots for the footwall results.

Table 9.4: Sample distance to fault

Sample name	**Distance from the fault** (m)	**Central Age** (Ma)	1σ (Ma)
EC-05	10	112	10
EC-06	100	117	9
EC-08	476	105	6
EC-12a	13400	137	7
EC-12b	13400	138	7
EC-13	15500	173	11
EC-14	12700	187	18
EC-15	1060	139	8
AS-1	8666,7	131	8
AS-3	6133,3	147	10
AS-4	10133,3	161	12
AS-5	12266,7	138	10
AS-6	12000	154	11
AS-7	9200	155	14
AS-8	9866,7	153	13
AS-9	10666,7	141	9
AS-23	6400	143	14
EC-02	1300	211	28
EC-03	533,3	289	67
EC-09	4266,7	187	18

The distance of the fault for each of the samples plotted. The red-colored samples belong to the hanging-wall. The blue-colored samples belong to the footwall.

9.4 Elevation vs. AFT age

The plot of AFT age against elevation shows whether there is a relation between age and elevation (Fig. 9.5). No age-elevation correlation is observed could be observed in this case.

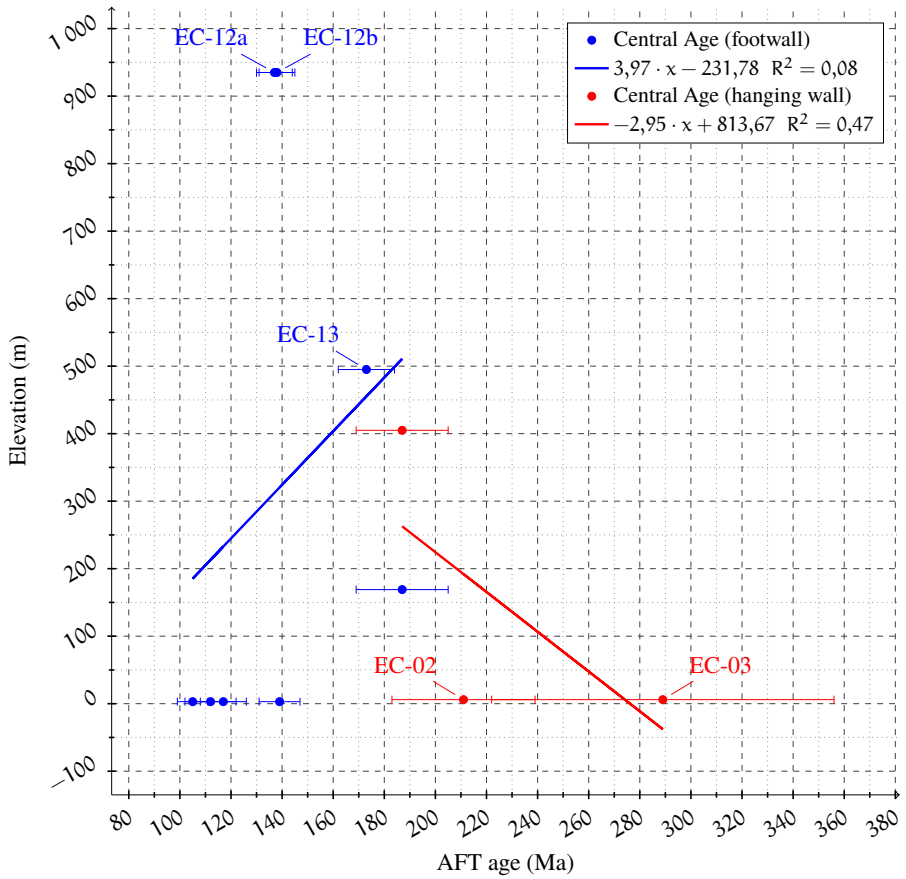

Fig. 9.5: Plot of elevation (meters) against AFT age (Ma). Red dots for hanging wall. Blue dots for the footwall samples.

9.5 Mean Track Length (MTL) vs. AFT Age

The relation between track lengths and AFT age can reveal certain aspects of the thermal history. If the rock have experienced a complex history of exhumation, it is most likely to be observed through MTL vs. AFT age plots. For the samples of this study, a slight positive correlation between MTL and AFT age is shown in the plot Fig. 9.7. Thus, a slight increase in MTL is expected in older samples. In practice, the difference is not meaninful. The MTL range from 12 to 9,9 µm. EC-08 (105 Ma) has a large MTL value(11,16 µm) in comparison to the rest of the values in the sample set.

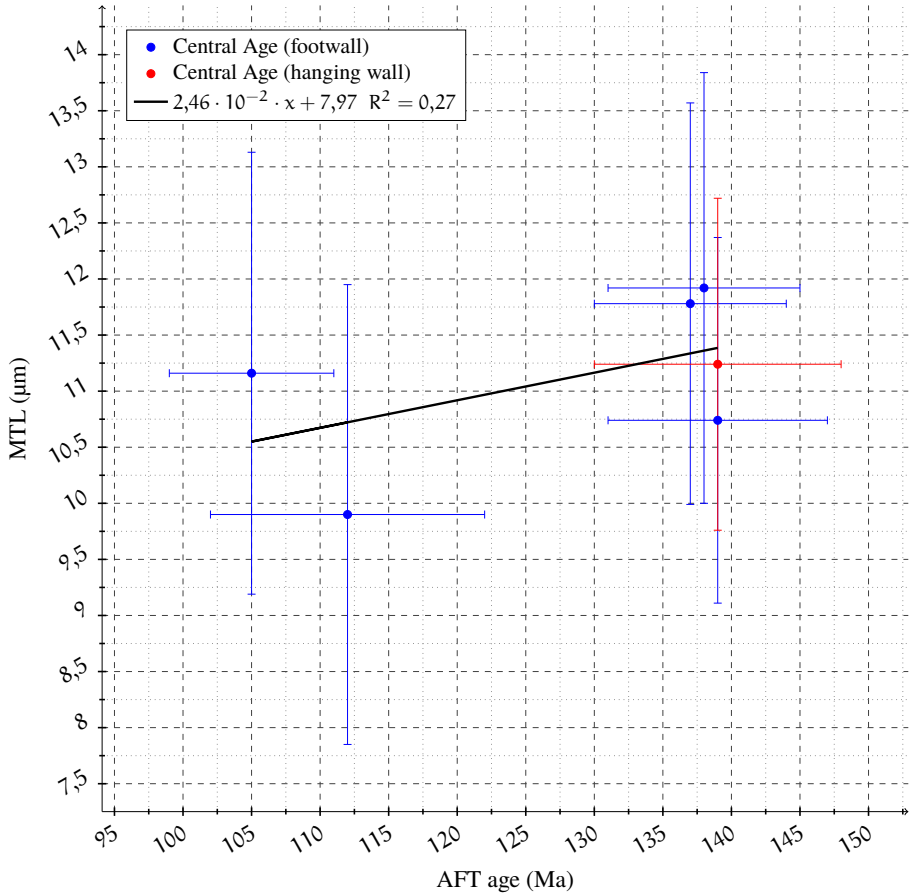

Fig. 9.6: Plot of MTL (µm) against AFT age (Ma). Red dots for hanging wall. Blue dots for the footwall samples.

9.6 Etch pit diameter (Dpar) vs. Age

Dpar values are plotted against AFT ages with the purpose of recognizing whether there is any relation between age and the apatite chemical composition. Establishing a relation between these two variables is important to identify any bias in the results and to avoid misinterpretations.

All the Dpar values (Fig. 9.7) cluster around 1 to 1,4 µm (Fig. 9.7), with exception of EC-02. EC-02 has a large Dpar (2,05 µm) compared to the mean values of the rest of the samples. EC-03 is an old sample with a large error, although its Dpar value match with the rest. The positive trend shown in the plot (Fig. 9.7) is probably caused by EC-02. Thus, with exception of EC-02, there is no reason to believe that there are chemical variations among the apatite minerals of the sample set that may affect the AFT ages.

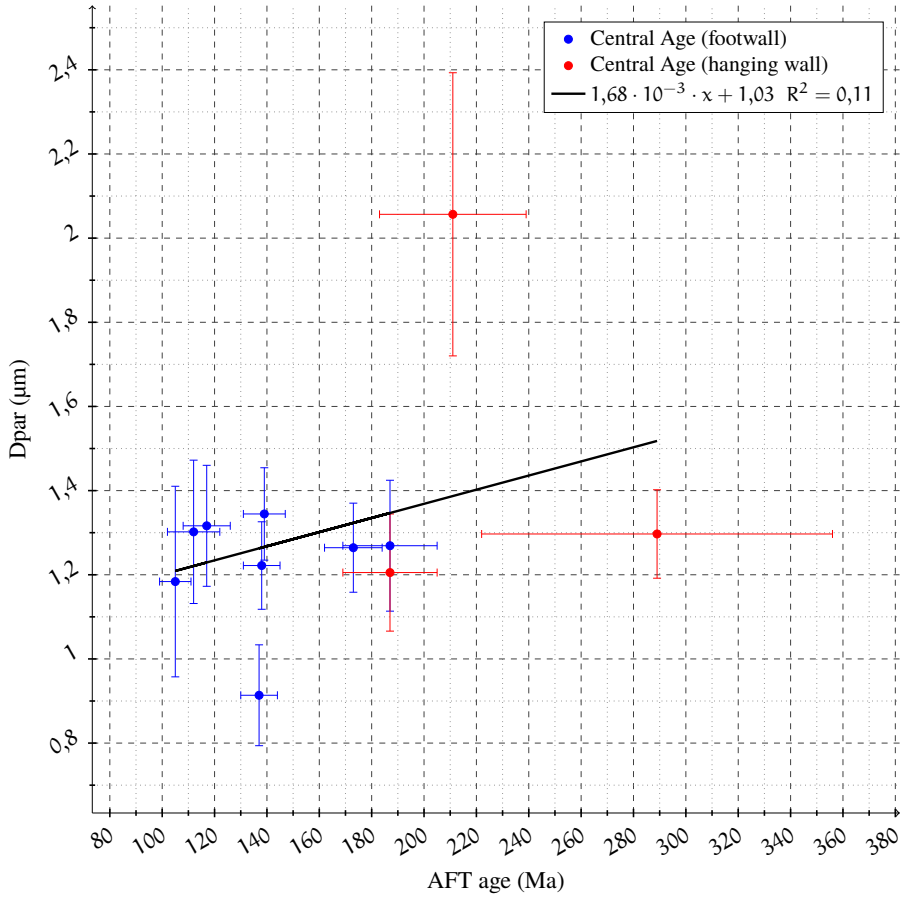

Fig. 9.7: Plot of Dpar (µm) against AFT age (Ma). Red dots for hanging wall. Blue dots for the footwall samples. The black trendline is made for all the sample collection.

10 Thermal history modelling

Modeling was performed with the software HeFTy 1.7.4 (Ketcham, 2005). The modeling software requires to import the values obtained from age calculation, track length measurements and etch pit diameters (Dpar) for all the counted grains of the sample. These parameters enable the thermal history modeling.

10.1 Thermal history modeling strategy

The samples selected for thermal modeling were EC-05, EC-08, EC-12 and EC-15, which form part of the footwall of the Lærdal-Gjende fault. The sample AS-23 from the irradiation NoB-019 was used to obtain a representative track length distribution from the hanging wall. The results for AS-23 were compared to the ones presented by Al-Samarray (2013).

Between 40 and 101 track length measurements were made for each sample in order to run the thermal modeling in the HeFTy software. The etch pit diameters (Dpar) were used as kinematic parameter (Donelick et al., 2005). For modeling, the confined track lengths were corrected by c-axis projection (Ketcham et al., 2007).

The inverse modeling was conducted under the Monte Carlo search method. For modeling, it is necessary to constrain at least the starting conditions (temperature and age) from another geological source. The thermal constraints used as a starting point were extracted from the zircon fission track study of Andriessen & Bos (1986). The zircon fission track system provides older ages than the apatite system and can be used as starting constraint for apatite fission track modeling. Andriessen & Bos (1986) obtained a zircon fission track age of 306 ± 22 Ma for rocks at Eidford, south of the study area (Hardangerfjord). The fission track ages of zircon record the last time that the rock experienced cooling through the annealing temperature, which is between 175 and 225 °C (Andriessen & Bos, 1986). Therefore, the initial constraint box was set up with time and temperature boundaries from 280 to 330 Ma at 180 to 230 °C. The end constraint was adjusted to 8 ± 5 °C as average surface temperature for Norway nowadays.

The modeled time-Temperature paths presented here were tested for a search of 1000 acceptable paths. The models were set up with episodic randomizer style since the study area is under the influence of the fault. Some samples were tested with intermediate randomizer style, but the results were worse than for episodic style in terms of fewer good and acceptable paths obtained. Thus, only the models where the episodic randomizer style was applied were picked. The weighted mean curve (blue in the model) is considered as the time-T path representative of each run.

The thermal modeling was performed with the minimum constraints (start and end conditions) in order to compare the thermal histories of the different regions. WIth the purpose of testing the peneplanation scenario suggested by many geologists (e.g. Rohrman et al., 1995), additional models were made for the samples EC-05 (10 m away from the fault) and EC-12b (several km away from the fault) (Figs. 10.7 and 10.8). Reheating after peneplanation was necessary in order to produce good models. Nevertheless, there are no geological evidences that support a reheating episode since no sediments are known from the study area. These models will be discussed in further detail in the following sections.

10.2 Thermal modeling with start and end constraints

The samples EC-05, EC-08 and EC-15 form part of the same region, close to the fault. Thus, the thermal models from these three samples will be jointly interpreted as representative of the area next to the fault. The sample EC-12 is a distant sample from the fault, approximately at 13,4 km away. AS-23 is used as a representative sample for the hanging wall and will be commented aside.

A description for each thermal model will be given in this section followed by a summary.

10.2.1 EC-05

This sample was collected from 3 meters above sea-level along with EC-08 and EC-15, and gave an AFT age of 112 ± 10 Ma, between Early to Middle Cretaceous. EC-05 belongs to the footwall mylonites, and it is collected from a couple of meters away from the fault.

The thermal model produced 115 good ones and revealed two episodes of rapid cooling and one long stable period. The beginning of the first modeled cooling event is not well limited. The end of this cooling episode is around the Early Jurassic (180 Ma). According to the weighted mean curve, the cooling rate estimates for this first cooling event are inferred to be around 1 °C/Ma. The modeled weighted mean curve indicates a relatively constant temperature between 60 and 80 °C from early Late Jurassic times (160 Ma) throughout the Cretaceous and Paleogene and until Early Miocene (17 Ma). The last episode of accelerated cooling starts in the Late Miocene (ca. 15 Ma) lasts until the present day according to the weighted mean curve. The inferred cooling rate estimates for this episode of accelerated cooling are 5 °C/Ma.

10.2.2 EC-08

This sample was collected from the migmatitic gneisses of the Baltic Shield basement at an elevation of 3 meters. For 1000 acceptable paths, the model produced 235 good paths.

EC-08 experienced two rapid cooling events and one slow cooling period. The first cooling event started before the entrance of the PAZ and prolongued up to Late Triassic (220 to 200 Ma), followed by a progressive change into a slow cooling period. A renewed period of rapid cooling started abruptly between middle Paleogene and early Neogene (30 to 20 Ma) until present times with a cooling rate 2,2 °C/Ma.

10.2.3 EC-15

This sample belongs to the migmatitic gneisses from the Baltic basement and was collected close to the mylonites from the footwall at an elevation of 3 meters above sea level.

The thermal modeling for 1000 acceptable paths produced a weighted mean curve very similar to the best fiT path. EC-15 presents a composite history of two rapid cooling events and one stable period with relatively constant temperatures (Fig. 10.2). The first accelerated cooling event is recorded before entering the PAZ (120 °C) with cooling rate estimates of 1 °C/Ma. A period of stable conditions with indiscernible cooling starts in Middle Jurassic times (170 Ma) and is maintained at a temperature between 70 to 60 °C throughout the Mesozoic and Paleogene times. The sample exists the PAZ simultaneously to the beginning of a renewed episode of rapid cooling in Neogene times (20 Ma ago). The cooling rate estimates for this last episode are 4 °C/Ma. The histogram has a slight negative skewness, reflecting a relatively long history within the PAZ.

10.2.4 EC-12a and EC-12b

EC-12 was picked from an elevation of 935 m above sea-level and are the one located farthest away from the fault. Due to the amount of zircons mixed with apatite, two apatite mounts were done out of this sample (‘a’ and ‘b’).

The modeles for EC-12a and EC-12b for a delimited search of 1000 acceptable paths produced an average of 125 good paths. The GOF for the age and the MTL are not as good as in other samples. The best fit path (in black) show approximately the same cooling history as the mean weighted curve (blue) (Fig. 10.1). It is possible to identify a rapid cooling period that begins prior to the entrance into the PAZ (at 120 °C) in the two runs of EC-12. The accelerated cooling ends Ma 185 Ma ago in both samples and is followed by a slow cooling period with estimates of 0,1 °C/Ma. The slow cooling period ends earlier in EC-12a than in EC-12b. The thermal model for EC-12a draws rather an angular line in comparison to EC-12b, whose mean curve show signs of more progressive change among cooling episodes. The exit from the PAZ in EC-12b occurs in the Late Cretaceous (75 Ma), coinciding with a switch to a faster cooling rate. Whereas according to the model of the sample EC-12a, the most recent rapid cooling starts in the Paleocene (63 Ma ago) with an approximate cooling rate of 0,7 °C/Ma.

Summarizing, for EC-12 a period of rapid cooling is identified prior to the entrance to the lower boundary of the PAZ (120 °C). This rapid cooling continues within the PAZ and progressively changes to a period of slow cooling that starts in Early Jurassic. The slow cooling is maintained until Late Cretaceous to Paleocene times. The switch to a faster cooling rate occurs around the time that the rock exists the PAZ. The accelerated cooling continues throughout the Cenozoic.

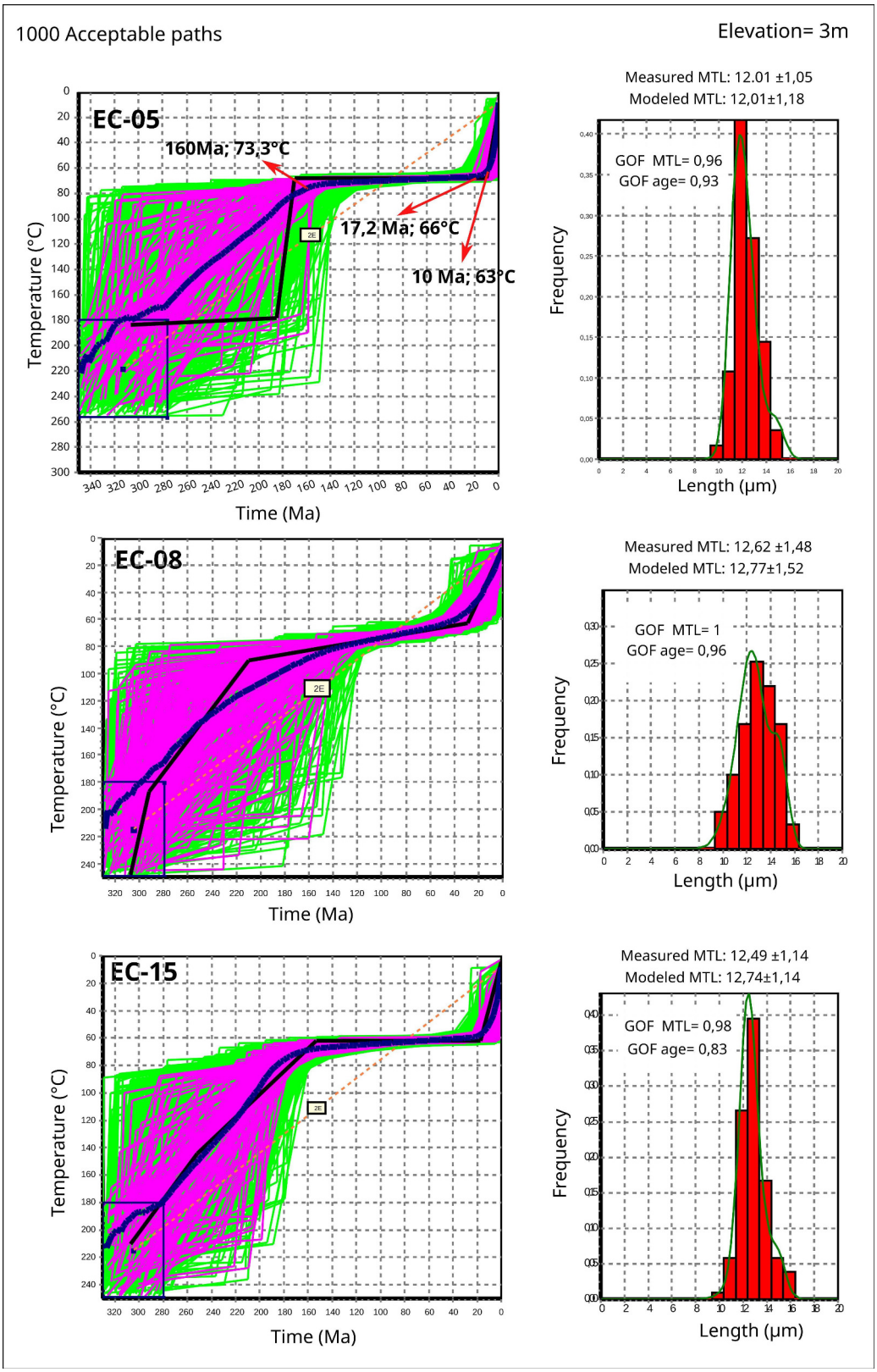

Fig. 10.1: Thermal models set up for the search of 1000 acceptable paths for the samples EC-05, EC-08 and EC-15. The three samples belong to the same region. Thus, the 3 thermal models are compared among them and interpreted as one single model. The green lines represent the acceptable paths and the purple lines represent the good paths. The black line is the best fit path, and the blue line is the weighed mean curve. The goodness-of-fit (GOF) values are given in the figure together with the mean track lengths (MTL).

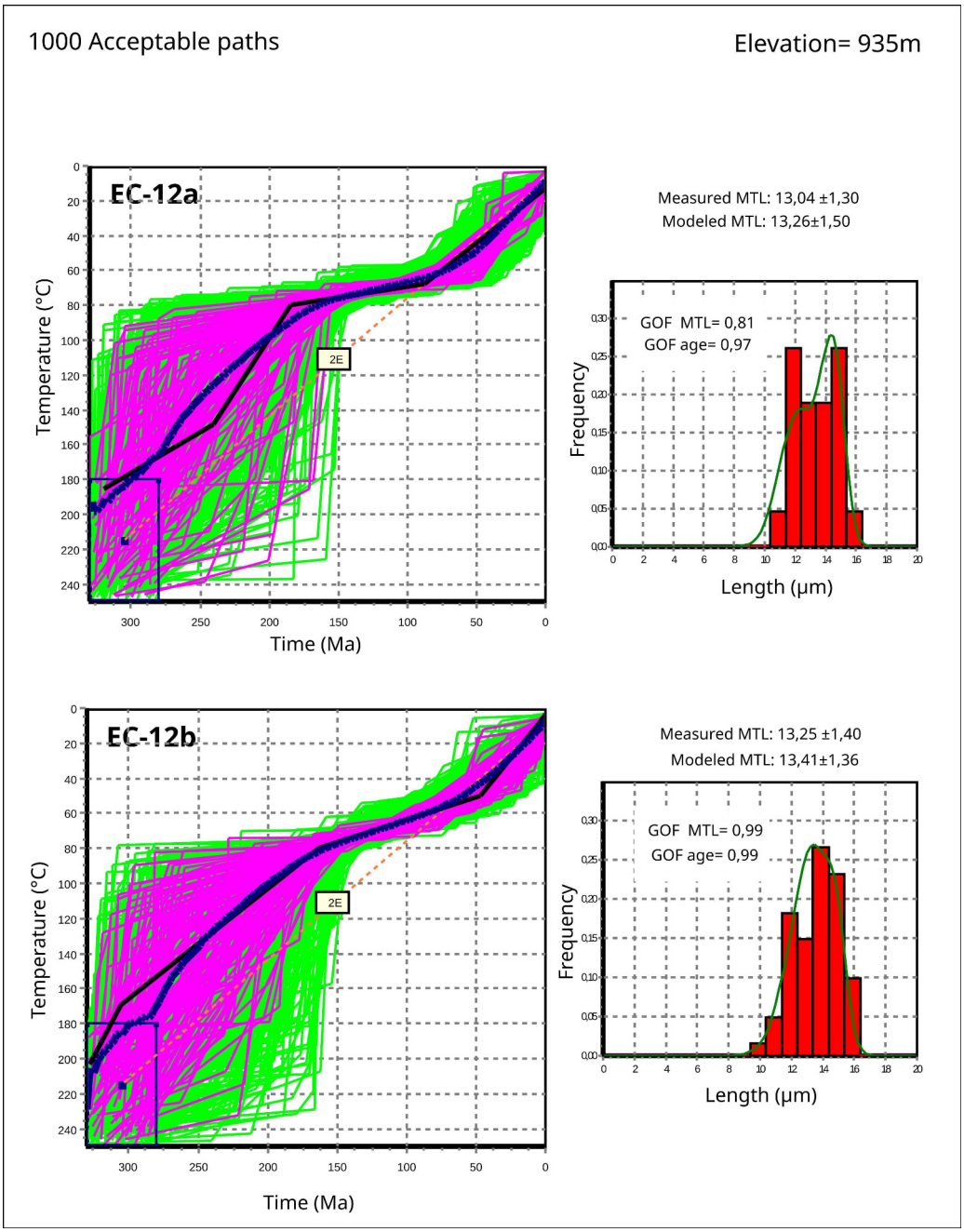

Fig. 10.2: Thermal models set up for the search of 1000 acceptable paths for the sample EC-12 ('a' and 'b'). The green lines represent the acceptable paths and the purple lines represent the good paths. The black line is the best fit path, and the blue line is the weighed mean curve. The goodness-of-fit (GOF) values are given in the figure together with the mean track lengths (MTL).

10.2.5 AS-23

Forty-six track length measurements were taken for AS-23 using a personal calibration file. The c-axis projected MTL for AS-23 is 12,81 ± 1,01 µm (Fig. 10.4), which corresponds to Fig 5.5. in Al-Samarray (2013). The track length distribution from Al-Samarray (2013) show a MTL around 12 µm in accordance with the histogram presented in the master thesis of the author. That value is very close to the results presented here. Al-Samarray reports a MTL of 12,43 ± 1,20 µm in his data table but a MTL of 10,70 ± 0,28 µm next to the histogram (Fig. 10.4). The latter is in

clear contradiction with the histogram of the track length distribution and is thus considered to be incorrect. The MTL of 12,43 ± 1,20 µm cited in the data table overlaps, within the uncertainties, with the MTL of 12,81 ± 1,01 µm presented here. For that reason, the thermal model included in the master thesis of Al-Samarray (2013) is used in the present study as a representative thermal model for the hanging wall of the Lærdal-Gjende fault. The results are extracted from a hand copy and do not match the current layout, however they are still suitable for comparison.

Al-Samarray (2013) results suggested a rapid cooling phase within the lower part of the PAZ from early Triassic to early Jurassic. A steady and slow cooling episode within the upper part of the PAZ can be observed from early Jurassic until Oligocene times (ca. 30 Ma ago). At the entrance to Neogene times. An accelerated cooling episode is identified concurrently with the exit from the PAZ (Fig. 10.4).

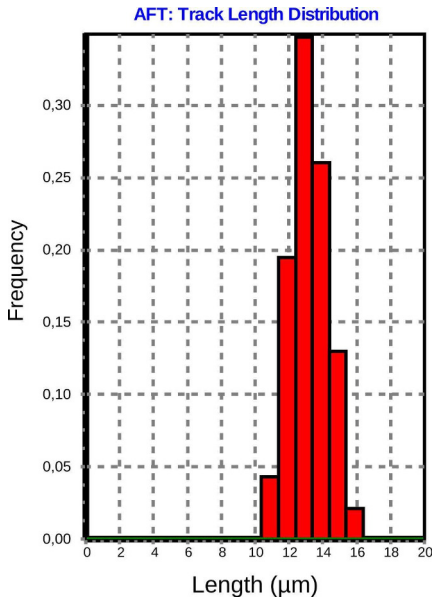

Fig. 10.3: Histogram of the c-axis projected length values for the sample AS-23 measured in the present study.

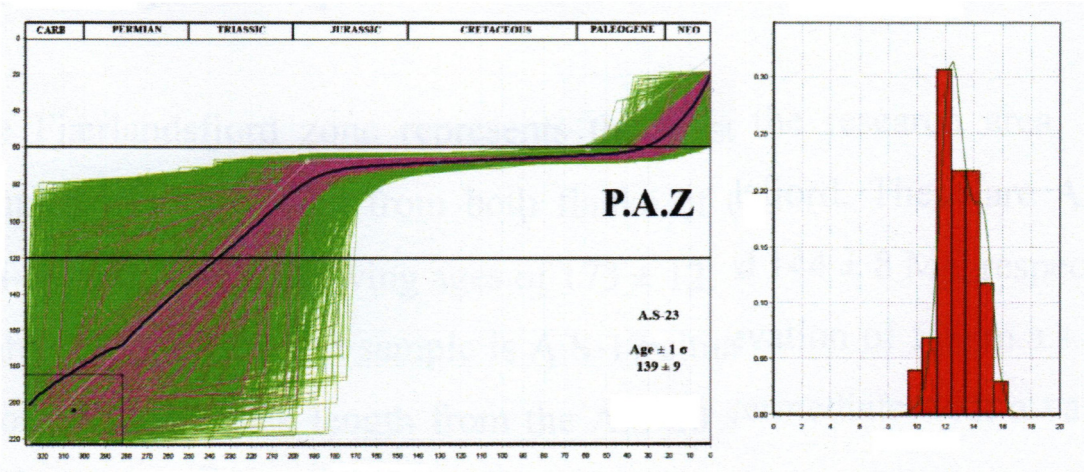

Fig. 10.4: Thermal model and MTL histogram of the samples AS-23, representative of the hanging wall of the Lærdal-Gjende fault. Fig. Extracted from Al-Samarray (2013).

10.2.6 Summary

The modeled cooling paths for the samples of the footwall present variations in their thermal histories. However all the samples recorded 3 phases of cooling: (1) initial rapid cooling before entering the PAZ (120 °C), (2) slow cooling within the upper side of the PAZ, and (3) Cenozoic accelerated cooling. Due to the proximity among the samples EC-05, EC-08 and EC-15, the interpretation of these will be made jointly through their comparison to avoid over-interpreting the data. EC-12 'a' and 'b' are the same sample divided in two, therefore the resulting thermal models will also be interpreted jointly. The thermal model of AS-23 was included in the Fig. 10.5 together with the rest, although the weighted mean curve is not compared with the rest (Fig. 10.6).

All the modeled samples mark an episode of rapid cooling that started before entering the PAZ (120 °C). This episode extends until the Early Jurassic to the end of Middle Jurassic times in most of the samples (Figs. 10.5 and 10.6). For most of the samples, this rapid cooling episode ends abruptly turning into a stable cooling period. The time-Temperature path from the sample EC-08 deviates from EC-05 and EC-15, suggesting that the end of this rapid cooling period occurred in the Late Triassic. EC-12 'a' and 'b' show a progressive change from initial rapid cooling into a slower exhumation around Middle Jurassic times. The representative sample of the hanging wall, AS-23 shows also an initial rapid cooling period that started before entering the PAZ, which ended in Early Jurassic times.

A long period of slow cooling is identified in the region close to the fault (EC-05, EC-08 and EC-15). A stable temperature between 70 to 65 °C (Fig. 10.6) is maintained throughout all the Cretaceous. EC-12 models 'a' and 'b' show a very slow cooling throughout Jurassic and Middle Cretaceous times within the upper side of the PAZ (Figs. 10.5 and 10.6). AS-23 records slow cooling from the Early Jurassic to the end of the Paleogene (Fig. 10.4).

EC-08 records the beginning a new exhumation event in Paleogene times (around the Eocene), whereas this new period of accelerated cooling is clearly recorded to start in Neogene times for the samples EC-05 and EC-15. Thus, it is feasible to assume that the youngest exhumation event occurred between the Paleogene to the Neogene for the region closest to the fault. On the other hand, EC-12 'a' and 'b' do not show a clear start of this exhumation period. They rather show an increasing progressive change in cooling rate. The representative sample of the hanging wall (AS-23), however, presents also a clear onset of accelerated cooling between Paleogene to Neogene times (Figs. 10.4 and 10.5).

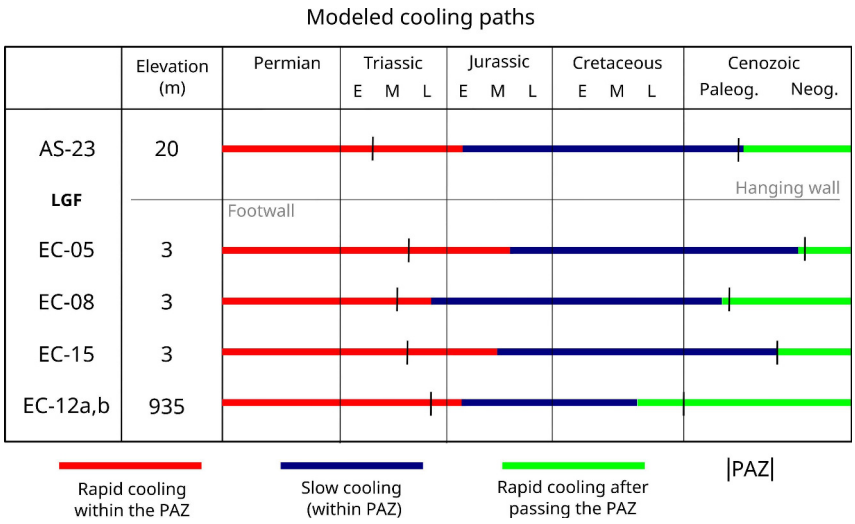

Fig. 10.5: Schematic summary of the cooling paths modeled.

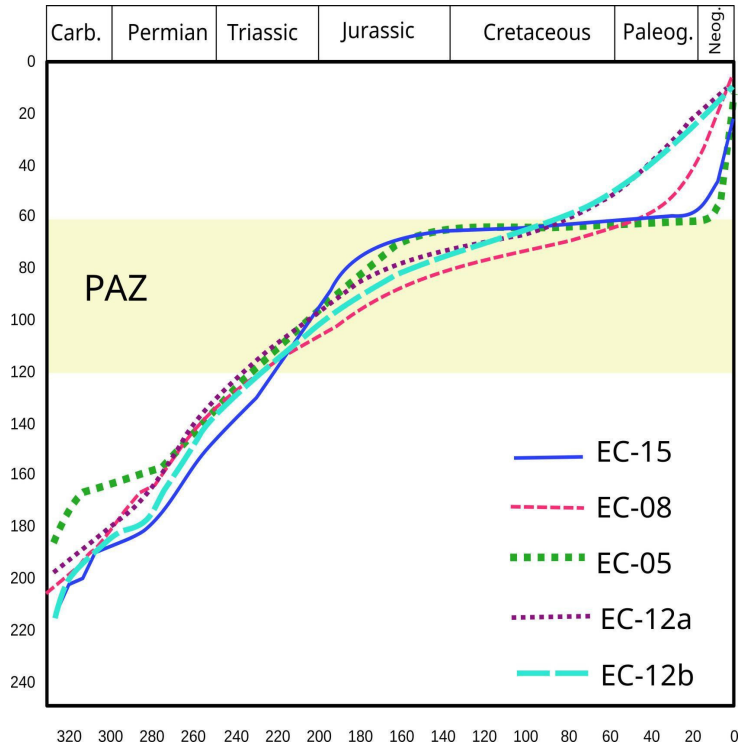

Fig. 10.6: Weighted mean curves for the samples from the footwall block displayed for comparison.

10.3 Thermal modeling considering peneplanation and reheating in Mesozoic and Cenozoic times.

The peneplanation of Norway is widely discussed by many authors (e.g. Rohrman et al., 1995, Chapter 9). Coastal sediments from the Jurassic were discovered in the region of Bergen (Fossen et al., 1997). Jurassic surface exposure and later re-burial is well established for coastal samples. Many authors suggest that peneplanation was an extended phenomenon that reached inland Norway (Gjessing, 1967). However, there is no direct proof that peneplanation reached far inland. Therefore, it is worth testing whether peneplanation affected the study area.

The time span set for peneplanation was adjusted from Jurassic times to Paleogene times. A reheating episode was added after peneplanation in order to obtain suitable thermal models. The tested samples were EC-05 and EC12 (b), at 3 meters and 935 meters above sea-level recpectively. The testing was made for a random search of 10000 paths under the same conditions as described and used previously. The constraints used to model peneplanation are seen as small boxes in Figs. 10.7 and 10.8. The boxes constrain peneplanation at 0 to 35 °C, from the Late Jurassic to the Neogene. The subsequent reheating scenario is depicted by the largest boxes in Figs. 10.7 and 10.8. The constraints were set for 80 to 70 °C to 0 °C, after peneplanation and up to present times. The box representing reheating is rather large in order to give less bias to the model.

For the closest region to the fault (EC-05), the constraint boxes for peneplanation were extended up to surface temperatures, although this sample could not have been at the surface when presumed peneplantion occurred. The models of peneplanation for a time span between late Middle Cretaceous and Late Jurassic times gave a larger number of good and acceptable paths. The mean weighted curve and the best fit path adjust quite well for all the cases. All the models show a considerable reburial after peneplanation (of around 1,5 km). In the models, the peneplanation event rarely achieve surface conditions. The models show rather a constant exhumation of the sample up to 20 °C (1 km deep).

EC-12 was collected from a distant region away from the fault (EC-12b) at an altitude of 935m, thus closer to the presumed peneplanation surface than the previous sample. The number of good and acceptable paths is larger when the peneplanation is assumed to happen between early Neogene times and Late Cretaceous age. The quality of the models decrease progressively in number of good and acceptable found paths and in terms of correlation between best fit and mean weighted curves. Based on the same terms, an improvement of the quality of the models is observed for peneplanation scenarios between Early Cretaceous to early Late Jurassic age. Therefore, EC-12 responds better to a peneplanation scenario set up for Cenozoic times and for an early peneplanation episode between Jurassic and Cretaceous ages (Figs. 10.7 and 10.8). The modeled reburial is larger for peneplanation scenarios before early Paleogene. The model assumes that the sample EC-12 reached near surface conditions (<20 °C) only for Paleogene peneplanation scenarios.

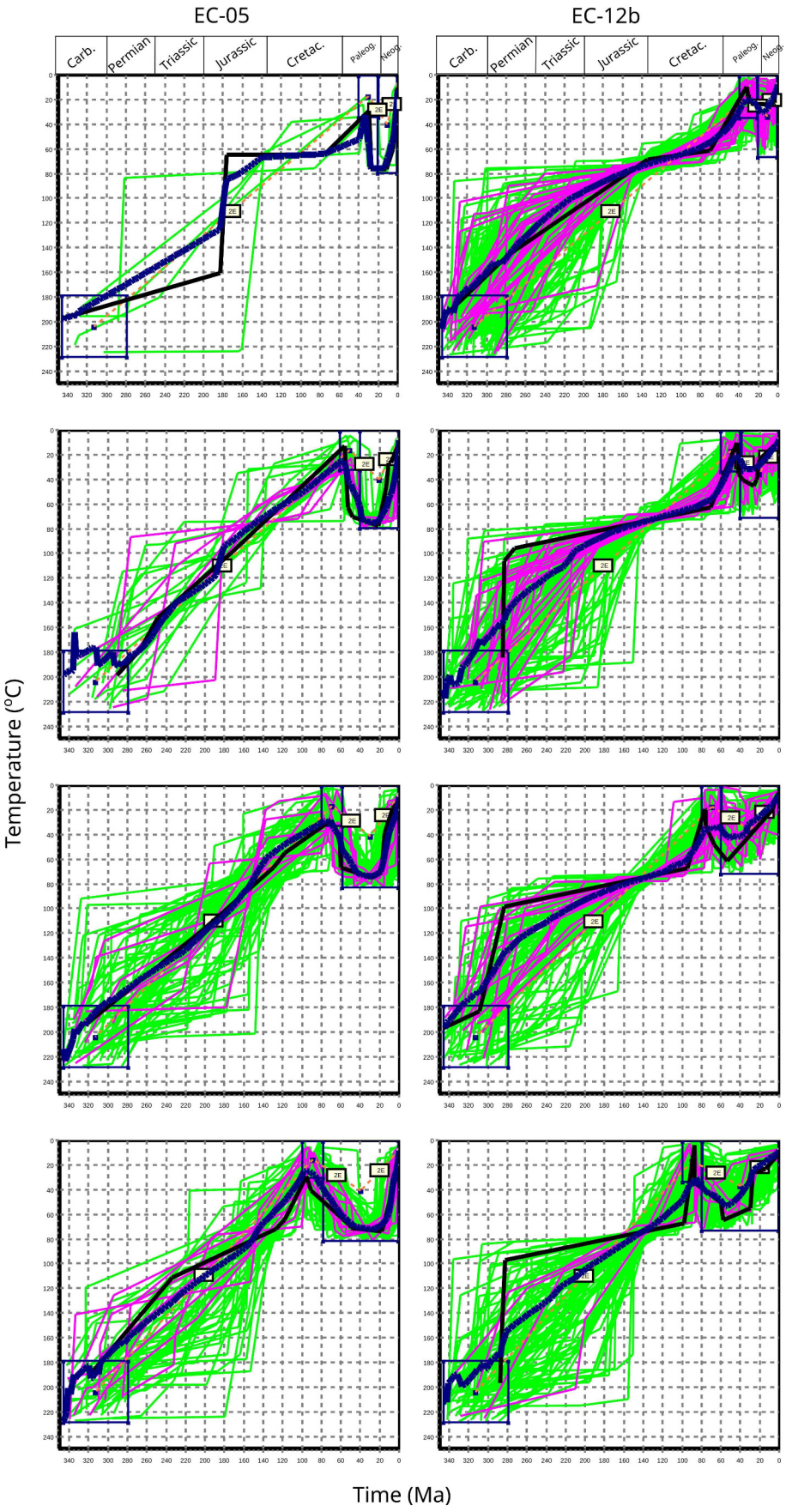

Fig. 10.7: Tested peneplanation and reheating scenarios from Neogene to Middle Cretaceous times in HeFTy software. The green paths are acceptable paths. The purple represent the good paths obtained. The blue and black curves are the weighted mean curve and the best fit path, respectively. The models presented in the figure correspond to runs for 10000 random paths.

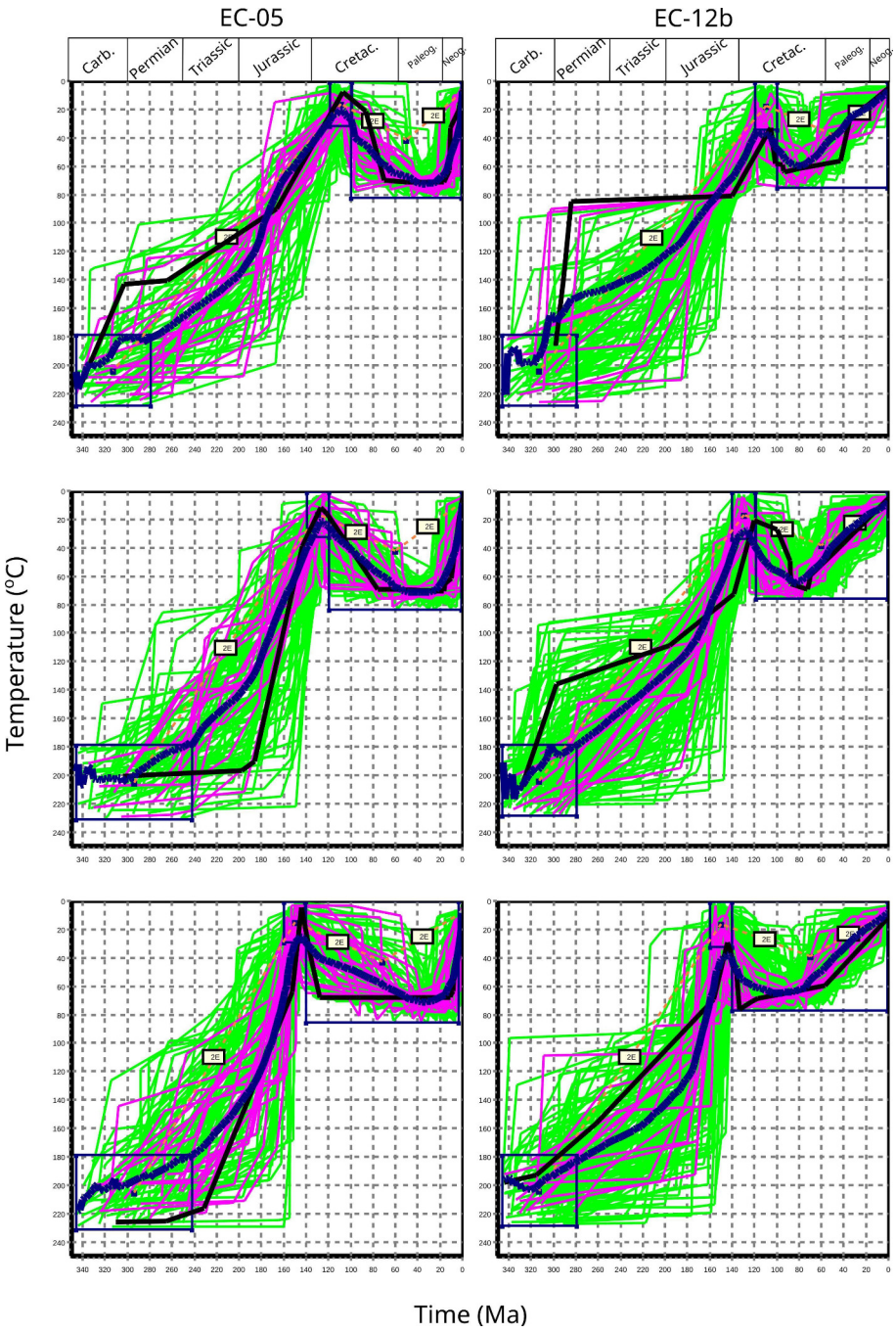

Fig. 10.8: Tested peneplanation and reheating scenarios from Middle Cretaceous to Late Jurassic times in HeFTy software. The green paths are acceptable paths. The purple represent the good paths obtained. The blue and black curves are the weighted mean curve and the best fit path, respectively. The models presented in the figure correspond to runs for 10000 random paths.

11 Interpretation and discussion

11.1 Interpretations of the thermochronological analysis

This section aims to provide an interpretation and discussion of the geological significance of the results obtained for the 10 samples analyzed by AFT dating methods. Additional samples from the Master Thesis presented by Al-Samarray (2013) are included into the discussion in order to compare the results and evaluate the relation that these may have. First, an assessment of the quality of the fission track results will be given. An interpretation of the AFT results will follow. The discussion of the thermal modeling will be left to the end of this section.

11.1.1 Assessment of data quality in Apatite Fission Track (AFT) analysis

The ages obtained by AFT analysis are subjected to a number of factors. The quality of the apatite crystals exert a critical influence in the results obtained from counting. A sample with low ^{238}U concentration makes the counting process more difficult, since it may cause a poor alignment between mica and grain mount. Fluctuations in the concentration of ^{238}U within the grains bias the resulting AFT age. This occurs because the counter would check the area of the grain that contain more fission tracks. For example, in a zoned grain, the counting would be made in the zoned part that contains more fission tracks. The counting in a zoned apatite grain, thus, could produce an over-estimation of the tracks density. It is also important to consider the own personal bias, especially of an inexperienced fission track counter. Inexperienced fission track counters may not distinguish easily between dislocations and real fission tracks, thus overestimating the density of tracks.

- **AFT ages**

Most of the samples of apatite collected for this thesis were zoned. Some zoned grains were unavoidably included in the counting due to the lack of good grains with homogeneous track density distributions. Most of the obtained AFT ages present a good margin of error (between 7 to 11 % compared to the age). The samples with large errors (14 to 23 %), EC-03 and EC-02, were extracted from the region of the hanging wall far away from the fault core. The chi-square test was not passed by all the samples (i.e EC-02, EC-03).

- **MTL distribution and Dpar values**

Track length measurements were taken from the samples EC-05, EC-08, EC-12 , EC-15 and AS-23 (Al-Samarray, 2013). A wide span of MTL lengths ranging from 12 to 9,9 µm was obtained. In general, it was difficult to measure 100 track lengths in all the samples due to the quality

of the confined tracks. Most of the confined tracks were tilted few degrees (not ideally horizontal), which leads to shorter length measurements. Many short confined tracks were found in the surface of the apatites. The confined tracks that are in the surface usually do not get fully etched, and therefore their measurement will trigger an unrealistic track length distribution. These kind of tracks were identified and avoided, although a significant amount of short confined tracks were also observed within the apatite crystals. Measurements of TINCLE or TINDEF tracks were considered, which may produce a certain level of inaccuracy in the measurements. The confined tracks usually agglomerate in areas of the grain with high ^{238}U concentration. The samples with higher ^{238}U concentrations whose grains were slightly zoned, exhibited a cluster of confined tracks that made the measurement of confined track more difficult.

The Dpar values were obtained with the support of a personal calibration file. No problems occurred during the measurement of Dpars. However, the Dpar measurements could be more accurate and easier to take if the led pointer used for measuring had smaller diameter, which was too large in comparison to Dpar lengths.

- **Thermal modeling**

The thermal modeling gives a good insight of the recent thermal history experienced by the rock according to the constraints introduced for modeling. The thermal models are approximations of the exhumation history and should not be considered as an absolute result. The thermal modeling is biased by the track length measurements and the Dpar measurements. Track length distributions are specially influencing the produced time-Temperature paths. Obviously, the spontaneous and induced track densities will determine in large measure the thermal model, and as previously mentioned, that depends on a number of factors. The thermal models are strongly dependent on relevant geological constraints.

The thermal modeling with just initial and end constraints was performed to acquire basic knowledge of the thermal history that the samples may have undergone. Two samples were tested to check the compatibility of the AFT data with one of the hypothesis of Norwegian landscape evolution: assuming peneplanation in Mesozoic or Cenozoic times. The models obtained by that experimental testing should be carefully assessed and should not be taken as real scenarios, but rather possible solutions as long as the models match in geological terms.

In conclusion, thermal modeling is used in order to test how well the obtained data fit different geological scenarios. The constraints introduced during modeling should be based on a previous idea or model and other geological sources.

11.1.2 Interpretation of apatite fission track data for the horizontal profile across the Lærdal-Gjende fault.

11.1.2.1 Relation between distance from the fault and AFT age

As seen in the results chapter, the footwall block samples show a positive correlation between AFT age and distance from the fault. Thus, the AFT ages are expected to decrease towards the fault. This trend has a moderate determination coefficient of $R^2 = 0,58$. Regarding the hanging wall block, the samples collected for this thesis and the samples from Al-Samarray (2013) show an increase in the AFT ages towards the fault. The adjustment of the data to the calculated regression line is relatively good, with a R^2 of $0,63$.

In the footwall block of the Lærdal-Gjende fault, a visual aging trend towards the SE can be discerned for the AFT age distribution on the map. If only samples from the Baltic basement are considered, the decreasing age trend towards the fault can be clearly discern. However, not all the samples from the footwall follow entirely this trend (i.e. EC-12 and EC-13).

EC-12 has a particular young age (Early Cretaceous) according the general trend outlined by the rest of the samples from the basement. In addition, the AFT age of EC-12 was expected to be older due to its higher elevation. On the contrary, the sample dates from Early Cretaceous time, same as the samples located closer to the fault. This may be caused by the effects of quick denudation. Recent quick denudation may have lead to the rapid exposure of the rock (sampled as EC-12) in a context where the isotherms were still adjusting to the new relief. In fact, EC-12 was collected from a depression caused by glacial erosion. Thus, despite its altitude, EC-12 may record young AFT ages due its location in a valley of the mountains of Jotunheimen. Assuming that a Paleogene or Neogene uplift has occurred as suggested by the thermal modelling, the young age of this sample is probably due to the Pliocene denudation by glaciar processes. The Pliocene erosion occurred a short period after the exhumation, leaving no time for the isotherms to readjust to the new relief, thus affecting the AFT ages (Fig. 11.1).

EC-13 dates from Middle Jurassic (173 ± 11 Ma) and is located in the Fillefjell erosional basement window. The sample is younger than EC-14, that dates of Early Jurassic (187 ± 18 Ma). EC-13 is farther away from the fault than EC-14. EC-13, is younger than expected and do not fulfill the age trend of the footwall. This unexpected relative young age may be due to the influence of the faults that passes across samples. Another possible explanation can be given is similar to the one given for EC-12, since EC-13 was collected from a depression.

The samples from the Lærdal basement window, are collected nearby the fault (EC-05, EC-06, EC-08, EC-15) and 12,7 km away from the fault at an altitude of <200 m (EC-14). For that difference in elevations, no great changes in AFT age are expected. Therefore, the samples nearby

the fault and EC-14 are treated together regardless of elevation as they are part of the same geological unit. This implies that rocks closer to the fault experienced exhumation later than rocks from farther away. Another hypothesis is that fission track ages may be recorded better in the region close to the fault if the exhumation was tectonically driven by faulting.

The samples from the hanging wall, EC-09, EC-02 and EC-03; exhibit a wide range of AFT ages. Within the hanging wall block, EC-09 is the most distant sample to the fault excluding the AFT data of Al-Samarray (2013). The samples EC-02 and EC-03 are closer to the fault, being EC-03 the one with most proximity of all. According to the AFT age distribution of these 3 samples in relation to their distance from the fault, an actual increasing age trend towards the LGF can be envisaged. In comparison with the sample set presented by Al-Samarray (2013), the tendency described previously seems rather biased by the samples EC-02 and EC-03. The latter two samples will be commented in further detail in the Section 11.1.3.2 of this chapter.

Summarizing, the AFT age distribution over the map suggest a decrease in age towards the fault in the case of the footwall block. On the contrary, the AFT on the hanging wall seem to be quite independent upon the distance from the fault. Although, two of the samples (EC-02 and EC-03) had Jurassic ages, which biased the AFT age trend of the hanging wall. The data set of the hanging wall (including EC-02 and EC-03) outlines an aging trend towards the fault. The moderate values of coefficient of determination for the footwall and the hanging wall blocks (R^2) do not give the certainty that there is an actual significant correlation between AFT age and distance from the fault. In order to test if the regression lines (or trendlines) described by plotting distance from the fault and AFT age are significant, a statistical analysis should be performed (next Section 11.1.2.2). Samples from the Lærdal basement window can be directly compared as a whole crustal block. The AFT age distribution in that region show that there is in fact a trend of decreasing AFT age towards the fault, regardless the elevation. The samples EC-13 and EC-12 belong to the mountainous part of the study area but were collected from the floor of old glacial valleys, which can create an interference in AFT age. Furthermore, EC-13 is collected from the Fillefjell erosional basement window, and it is separated across the map by Caledonian thrusts. Therefore, these samples cannot be considered as a geological analogous to the samples from the Lærdal basement window.

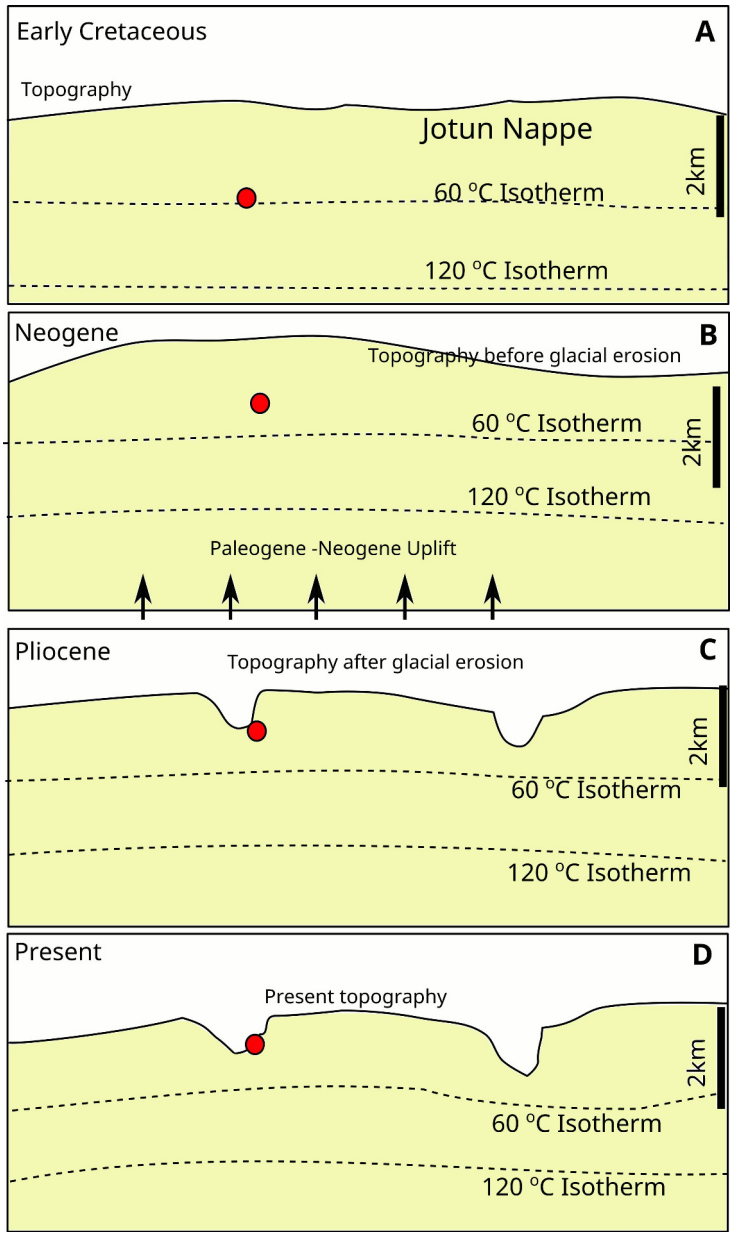

Fig. 11.1: Sketch of the situation before and after glacial erosion for the sample EC-12.

11.1.2.2 Fisher test of linear correlation between AFT ages of both crustal blocks of the LGF and the distance from the fault

The sample set used for AFT analysis encompasses 10 samples, seven of which belong to the footwall block. Despite of the reduced amount of samples available, their distribution throughout the study area make them suitable for the analysis of the exhumation pattern of the footwall block. The AFT age distribution on the map suggests a general decreasing age trend towards the Lærdal-Gjende fault (northwestwards) in the footwall. The Fisher-test can be applied for the study of a bivariate population of ages to test the significance of linear correlation. The number of samples of the hanging wall block presented in the present study (3) are not enough to run a statistical analysis. In order to test the age trend in the Lærdal Gjende fault's hanging wall, the ages presented in this thesis were combined together with other 9 samples from the master thesis

of Al-Samarray (2013). The samples used for the statistical analysis are presented in Tables 11.1 and 11.2.

Table 11.1: Footwall block ages for the corresponding samples.

Sample name	Crustal block	Elevation (m)	Distance from fault (m)	AFT Age (Ma)	
				Central age	1σ
EC-05	Footwall block	3	10	112	10
EC-06		3	100	117	9
EC-08		3	476	105	6
EC-12a		935	13400	137	7
EC-12b		935	13400	138	7
EC-13		495	15500	173	11
EC-14		169	12700	187	18
EC-15		3	1060	139	8
n=8					

Table 11.2: Hanging wall ages for samples from the present studies and from alsamarray2013thesis.

Sample name	Crustal block	Elevation (m)	Distance from fault (m)	AFT Age (Ma)	
				Central age	1σ
AS-1	Hanging wall block	5	8666,7	131	8
AS-3		7	6133,3	147	10
AS-4		800	10133,3	161	12
AS-5		3	12266,7	138	10
AS-6		210	12000	154	11
AS-7		325	9200	155	14
AS-8		525	9866,7	153	13
AS-9		160	10666,7	141	9
AS-23		20	6400	143	14
EC-02		6	1300	211	28
EC-03		6	533,3	289	67
EC-09		405	4266,7	187	18
n=12					

As mentioned previously, the age seems to decrease towards the fault at the northwest in the footwall block. The hanging-wall AFT age distribution suggest a increase in age towards the fault (southeastwards). However, the latter age distribution may be due to differences in chemical composition of the apatite in the samples. Establishing any possible linear correlation between age and distance from the fault is carried out by plotting the obtained AFT ages at the distinct locations (Fig. 11.1.A,.B), and if necessary by testing its correlation.

The plots presented in Fig. 9.7 show a positive and negative correlation between age and distance from the fault of the respective footwall and hanging wall blocks. This age distributions can be also observed over the map. The rxy values obtained from the goodness-of-fit (R^2) are not particularly high or low, therefore the Fisher-test was used to test the significance of linear correlation for both cases.

The footwall case shows a R^2 of $0,581$ and positive slope, which involves a decrease in age towards the fault. The calculated rxy was The t-value was calculate and compared with t_α, and H_0 was rejected with 97,5 % level of confidence. H_0 represents the hypothesis where there is a lack of correlation. This implies that the footwall age distribution corresponds to a positive linear relationship between age and distance away from the fault. Concluding, it is undeniable that, within the analyzed sample set, the ages decrease towards the fault in the footwall block.

The hanging wall case shows a R^2 of $0,634$ and negative slope, meaning a decrease in age away from the fault. The t-value was calculate and compared with t_α, and H_0 was rejected with 99,5 % level of confidence. For this case, it is undeniable that, within the analyzed sample set, there is an aging trend towards the fault in the hanging wall block. The procedures and calcultations are found in the Appendix E.

Concluding, according to the statistical analysis performed, the decreasing age trend towards the fault in the footwall block is proven to exist. The distance - AFT age correlation trend in the hanging wall is proven to be significant. Thus, the aging towards the fault in the hanging wall is factual.

11.1.3 Elevation vs. Age

In tectonically undisturbed regions, an age-elevation relationship is expected along vertical profiles and over large areas. In general, older ages are expected in elevated terrain. The maximum elevation in the study area is 935 m, whereas the minimum elevation is approximately 3 m above sea-level. Most of the samples, for exception of EC-12, are below 500 m above sea-level, which means that any elevation-related differences between them are likely smaller than the errors and thus undetectable, unless cooling was exceptionally fast.

The plot of elevation against AFT age show a lack of correlation between elevation and AFT age. Thus, it is demonstrated that the elevation do not play an important role on the age distribution of the samples. It is important to consider the geographical features where the samples were collected from. For instance, the sample EC-12 was collected from a glacial valley, thus in a depression. The hypothesis about the sample EC-12 has been explained already above (Section 11.1.2.1). EC-09, from the hanging wall, was collected in a mountain plateau. EC-13 was

collected from the floor of a glacial valley as well. The rest of the samples were picked very close to the sea level along the Lærdalsfjord.

It is worth to mention that, coincidentally, the relief increases to the SE within the area of study. Whether there is any relation between this geographic feature and the AFT age can be hardly proven due to the same reason previously given.

11.1.3.1 Mean track lengths and track length distributions

In general, a rock that had a long residency within the PAZ, will have a larger number of shorter tracks. A rock that has been quickly exhumed (a volcanic rock, for instance), will have a larger MTL and a narrower track length distribution. Therefore, shorter MTL depicts an scenario where the rock has been slowly exhumed or has had a complex exhumation history. In this study, the relation between measured MTL values and the obtained AFT ages show that there is a smooth positive correlation between the two parameters, although the overlap of error bars suggest that the significance of this correlation is questionable. Important information about the thermal histories of the rocks can be inferred from the MTL distributions (see Chapter 5. The MTL modeled distributions and MTL values obtained in this study will be discussed in this section.

EC-08 (a relatively young sample of 105 Ma) presents a long MTL similar to the measurements obtained for samples that gave ages round 140 Ma. The track length distribution of the sample EC-08 shows a wide span of lengths between 8 and 16 µm. The bell looks like the mixed unimodal type of distribution caused by a weak thermal disturbance or a complex thermal history. This broad distribution pattern matches with the neighbor samples; EC-05 and EC-15. The track length distributions of the three samples are slightly positively skewed. The frequency of tracks around 12,7 and 12,1 µm in EC-15 and EC-05 respectively, is higher than the recurrence of tracks with MTL of 12,7 µm in the sample EC-08. The modeled MTL round the 12,7 µm for EC-08 and EC-15, whereas EC-05 has a modeled MTL of 12 µm. The AFT ages of EC-15 and EC-05 are slightly older (from Early Cretaceous) than for EC-08 (Middle Cretaceous). Despite of these differences, the track length distributions look very similar and the measured and modeled MTL are also concordant. Thus, there are actually many similarities among these three samples from the same region. Some flaws are found between MTL values and AFT ages, although the significance of the MTL-AFT age correlation is questionable. These three samples should be interpreted as a single geological evidence. Thus, the conclusion drawn out of the analysis of track length distribution of these three samples is that this area have been probably subjected to a complex post-Caledonian history of exhumation, and may have involved repeated exhumation episodes and/or cooling close to the upper boundary of the PAZ.

The track length distributions shown in the histogram of the sample EC-12 (‘a’ and ‘b’) look different from the rest of the data set. The track length measurements for EC-12, ‘a’ and

'b', present two small peaks and produced track length distribution model with a wide weak double peak. That might suggest a complex history of entrances and exits very close to the upper boundary of the PAZ, which is difficult to predict in the thermal modeling. The modeled MTL curve is slightly to moderately negatively skewed, in contrast to EC-15, EC-08 and EC-05. The two small peaks and the wide bell may be due to a complex history of reheating and exhumation very close to the 60 °C isotherm. In addition, the negative skew of the distribution may reflect a slower cooling within the PAZ.

The representative sample from the hanging wall (Al-Samarray, 2013), has a MTL value around 12 µm that matches the AFT age of Early Cretaceous obtained from fission track analysis (Al-Samarray, 2013). The track length distribution depicted in the histogram is positively skewed, which suggest a relative quick exit from the PAZ. The modeled curve of track length distribution given by Al-Samarray show a weak double peak signal. This fact suggests, once again, a complex thermal history considering the scatter of track lengths.

11.1.3.2 Dpar values

As mentioned in the results, the significance of the Dpar values upon AFT age relates to the chemical composition of the apatites (e.g. Donelick et al., 2005; Green et al., 1987). Some apatites may be rich in F or Cl, which may lead to a resistance to the etching or the contrary. For the samples of the footwall there is no reason to believe that the apatite of the samples have different chemical compositions. Thus, bias is not expected in this end. On the other hand, the measured mean Dpar for the sample EC-02 of the hanging wall (2,05 µm) differ from the Dpars measured for the footwall (clustered around 1 to 1,40 µm). EC-09 and EC-03 match the Dpar values obtained for the footwall. Therefore, the only sample with distinct apatite chemistry is EC-02. A certain bias may be expected from EC-02, as for instance, the old AFT age obtained for this sample.

11.1.4 Interpretation of the inverse thermal models

- **Late Carboniferous and Permo-Triassic rapid exhumation of the North Sea rift flank**

All the thermal models included in this study show Late Carboniferous to Permo-Triassic rapid cooling. The end of this period of rapid cooling vary to some degree among samples, but it usually concludes in Early Jurassic times. Al-Samarray (2013) also reported early Triassic to early Jurassic accelerated cooling for the hanging wall block of the Lærdal-Gjende fault. Permo-Triassic rapid cooling is typically associated to rift flank uplift related to the the North Sea rifting (e.g. Dunlap & Fossen, 1998; Gabrielsen et al., 2010). The samples analyzed in this study have an average cooling rate of 1 °C/Ma. AFT ages.

- **Jurassic-Cretaceous thermal stability**

All the thermal models manifest a very well delimited period of slow cooling (0,1 °C/Ma) that begins before Early Jurassic times and that is maintained throughout the Cretaceous. The representative sample for the hanging wall block (AS-23) shows a period of slow cooling between Jurassic and Oligocene times (Al-Samarray, 2013). Thus, thermal stability during Jurassic times is implied in the study area. Some thermochronological studies conducted on cohesive breccias of central southern Norway and western Norway have shown a Jurassic component, subsequently linked to rifting in the northern North Sea ocean. There is a lack of Jurassic sediments in central southern Norway, whereas coastal sedimentary facies were found in the Bergen Arcs, the west coast of Norway (Fossen et al., 1997). The sediments show reburial of <1 km in Cretaceous times and quick exhumation thereafter. Thus, the influence of Jurassic northern North Sea rifting obviously affected western Norway (e.g. Gabrielsen et al., 2010; Ksienzyk et al., 2014; Torsvik et al., 1992). The Jurassic reactivation revealed through $^{K}/_{Ar}$ illite analysis for the LGF (Ksienzyk et al., 2014) implies certain tectonic activity of the LGF, however thermal models do not suggest reactivation in Jurassic time. It rather shows the end of a long rapid cooling period that started before the rock entered the PAZ in Early Carboniferous up to Early Jurassic times.

Based on the fission track data obtained in the present study, no manifested evidences of thermal disturbance due to northern North Sea rifting are observed in the study area. Nonetheless, a Jurassic magnetic component was detected for the cataclasites of the Lærdal-Gjende fault (Eide et al., 1997). Furthermore, illite dating of fault gouges of the LGF also suggest Jurassic fault activity.

- **Cenozoic accelerated exhumation**

Both the footwall and the hanging wall blocks of the Lærdal-Gjende fault have experienced Cenozoic uplift. Most of the samples manifest an onset of Cenozoic rapid cooling between Late Cretaceous age and Oligocene. The Cenozoic uplift has been linked to the break up of the northern North Sea Ocean in many apatite fission track studies (e.g. Andersen et al., 1999; Ksienzyk et al., 2014; Rohrman et al., 1995).

The thermal models for the samples collected in the Lærdalsfjord suggest Cenozoic rapid cooling up to present times. The cooling rates estimates range from ~2,2 °C/Ma up to 5 °C/Ma. The sample with the lowest estimates corresponds to EC-08, which had also slightly larger MTL values in comparison to the rest. These high cooling rates have to be critically questioned. The thermal models are, in fact, indicating a Cenozoic rapid cooling episode; although the exhumation rates associated to those cooling rates are not geologically justified. The fjords are relatively new geomorphologic features that occurred after Cenozoic uplift, as suggested by the thermal models. Thus, the young AFT ages of inland fjords are attributed to the Pliocene-Pleistocene glacial erosion, which exposed deep rocks to surface temperatures (Fig. 11.2). Hence, the thermal models from these samples will always display exaggerated cooling rates. Furthermore, the

apatite fission track system is not accurate nor precise for temperature below 60 °C, as pointed out by Redfield (2010).

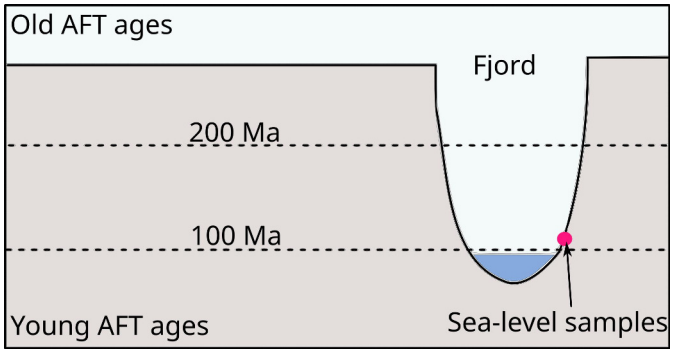

Fig. 11.2: Sketch of glacial incision related to AFT age distribution across the vertical profile.

All the MTL distributions of the samples nearby the fault (in the footwall block) were slightly positively skew. Furthermore, the distribution curve did not show a perfect peak, suggesting a complex thermal history that involves relatively rapid exhumation of the samples with a short stay within the PAZ. This observations match with what it is expected for samples collected at sea-level in inland fjords. The 'almost' double peak drawn by the MTL distribution curve may be caused by hydrothermal fluids of ~100 °C from con. The Lærdal-Gjende fault has undoubtedly experienced hydrothermal fluid alteration, as it is further discussed in Section 11.2. Thus, the influence of hydrothermal fluids may be causing an overprint on the AFT age of the samples, and thus affecting the modeled thermal paths for those samples.

The sample collected at a high elevation, EC-12, also records Cenozoic uplift. The cooling rate inferred for this sample is significantly lower than the predicted by the samples collected along the fjord. The cooling rate estimates for EC-12 are 0,7 °C/Ma. The sample was also collected from a glacial valley, and therefore glacial incision is also affecting the AFT age and modeled cooling rates. The MTL distribution curve is negatively skewed, contrary to the samples of the fjord. This implies a long period of slow cooling within the PAZ. It is unknown whether EC-12 is affected by hydrothermal fluids. Since no major faults are mapped near EC-12, it is feasible to assume that most likely it is not as influenced as samples collected next to the Lærdal-Gjende fault. Therefore, the cooling rate estimates are probably more realistic and can be considered as representative of the actual Cenozoic cooling.

For the hanging wall, Cenozoic uplift started in Neogene times (Al-Samarray, 2013). This is consistent with the models for the samples of the footwall that were picked from the fjord, close to the fault. EC-12, collected at high elevation, records an onset of rapid cooling between Late-Cretaceous and Paleocene times, significantly earlier than suggested in fjord samples.

Summarizing, the Cenozoic cooling rates inferred for samples near the fault are reflecting the fjord incision and are biased by hydrothermal fluids. The sample collected at higher altitude

(EC-12), despite of being picked from a depressed area, is less biased than the samples near the fault. Thus, the actual Cenozoic cooling rate of the footwall block of the Lærdal-Gjende fault should be approximate to the estimates from EC-12. The onset of rapid exhumation is similar for all the sample, between Paleogene to Neogene times. However, the sample from high altitude suggest that the onset of rapid exhumation occurred from Late Cretaceous.

- **Peneplanation and reheating models**

The peneplanation and uplift model (Rohrman et al., 1995) explains some of the geomorphological features seen in Norway. Although, there is not direct evidence that peneplanation occurred. Through inverse thermal modeling, different peneplanation scenarios were tested for the study area in order to reveal a potential peneplanation scenario. For both EC-05 and EC-12, the additional thermal models tested account for peneplanation to occur between Jurassic and Cenozoic times.

The models of peneplanation and reheating predicted for EC-05, and inland fjord sample, show the best peneplanation scenarios from Late Jurassic to Middle Cretaceous times. The sample could not have been at the surface during peneplanation, therefore the temperatures of peneplanation achived by the models should be >20 °C. Based on that observation, Paleogene and Middle Cretaceous exhumation can be totally discarded. However, from Early Cretaceous to Late Jurassic a peneplanation scenario might be feasible under the same terms. EC-05 dates from Early Cretaceous age (AFT age). The AFT age yields the time when rock rose through the 2 to 5 km depth window, which corresponds to ~60 to 120 °C. According to this definition, the rock was buried for at least 2 km during Early Cretaceous. Since the models for Early Cretaceous to Late Jurassic are adjusted to the lower boundary (higher temperature) of the constraint boxes depicting peneplanations, it is feasible to envisage that peneplanation occurred within that time span. Nevertheless, a significant reheating (2 to 1,5 km reburial) after peneplanation should had occurred to create a model with good GOF. Reburial for 1,5 km or 2 km is too large compared to coastal reburial of Jurassic sediments (Fossen et al., 1997). Therefore, despite a peneplanation could have occurred from Early Cretaceous to Late Jurassic, the reheating scenario did not suit the geological premises. In base to the previous reasons, no peneplanation and reheating scenario is suggested by the thermal models performed for EC-05.

EC-12 dates from Early Cretaceous and it is collected from an elevated area. The sample, as explained previously, displays a younger age than may be expected. Obeying to the same reasons as before, the models that involve ~1 km of reburial (reheating up to 30 °C) should be discarded. Thereafter, only Paleogene peneplanation models can be considered. The Paleogene exhumation up to surface conditions for EC-12, however, it is quite unlikely to have occurred. The sample EC-12 was collected from an surface generated after the presumed peneplanation by the incision of the glaciers, as well as occurred to EC-05. On the contrary, surface conditions

during peneplanation were reached according to the thermal models. A reburial after Paleogene times is geologically unjustified for the area of study.

Based on the arguments previously given, there is no reason to resolve that peneplanation has affected the study area. The analysis of the fault rocks of the Lærdal-Gjende fault, discussed further below, does not suggest any reheating scenario but rather a prolonged exhumation, contrary to what inverse thermal modeling for peneplanation requires.

11.1.5 Local exhumation pattern of the study area and role of the Lærdal-Gjende fault

- **Context**

The Lærdal-Gjende fault (LGF) is the brittle continuation to the northeast of the Hardangerfjord Shear Zone (HSZ) and runs through the central part of southern Norway. The HSZ represents kilometer-scale extensional ductile deformation from Devonian Mode II of extension or prior, and it is connected to the LGF by a hard-link. The Lærdal-Gjende fault was formed as consequence of rapid cooling and exhumation of the Caledonian basement during the end of the Mode II of Devonian extension. A Permo-Triassic and Jurassic component was found in fault-rocks of the Lærdal-Gjende fault (Andersen et al., 1999; Eide et al., 1997). The reactivation episodes experienced by the Lærdal-Gjende fault in mainland Norway have been linked to reactivation of the HSZ due to the rifting of the North Sea (Færseth, 1996). The Jurassic signature in the cataclasites of the Lærdal-Gjende fault is linked to fault reactivation triggered by the northern North Sea rifting (Andersen et al., 1999). Therefore, Permo-Triassic rifting of the North Sea and Jurassic rifting of the northern North Sea Ocean seem to have influenced inner regions of Norway, which is evidenced by fault reactivation. Rapid footwall uplift of reactivated extensional ductile shear zones had controlled the exhumation pattern of southern central Norway (Andersen et al., 1999). Fission track studies have traced a Cenozoic uplift which is discussed by several authors including Nielsen et al. (2009) and Rohrman et al. (1995). Cenozoic uplift is also suggested in the present analysis of the Lærdal-Gjende fault. The cooling rates associated to this episode point to an important exhumation in Cenozoic times that should associated to a reactivation of the Lærdal-Gjende fault and other structures. Recent reactivation (~60 Ma) along the Lærdal-Gjende fault is also demonstrated by $^{K}/_{Ar}$ illite data (Ksienzyk, 2012), probably linked to the North Atlantic opening in Paleogene-Eocene.

- **Proposal of the local exhumation model and role of the Lærdal-Gjende fault**

The exhumation pattern of the study area is believed to be influenced by the top-to-NW extensional reactivation of the Lærdal-Gjende fault (Andersen et al., 1999). The local exhumation pattern for areas affected by faults obeys to a particular AFT age layout caused by the effect of rapid exhumation and denudation of uplifted footwall blocks.

The AFT age distribution on the study area suggest a correlation between the AFT ages and the distance from the fault. The age trends for the footwall and the hanging wall blocks have been demonstrated to exist by statistical means in the previous sections. The decreasing age trend towards the fault seen for the footwall block can be explained by the differential uplift of the footwall, caused by the reactivation of the Lærdal-Gjende fault (Fig. 11.3). The pattern of AFT ages in the hanging wall resembles to an anticline structure. That can be easily explained by the rotation of the fault (dip reduction) provoked by the post-Caledonian extension rifting episodes (Fig. 11.4).

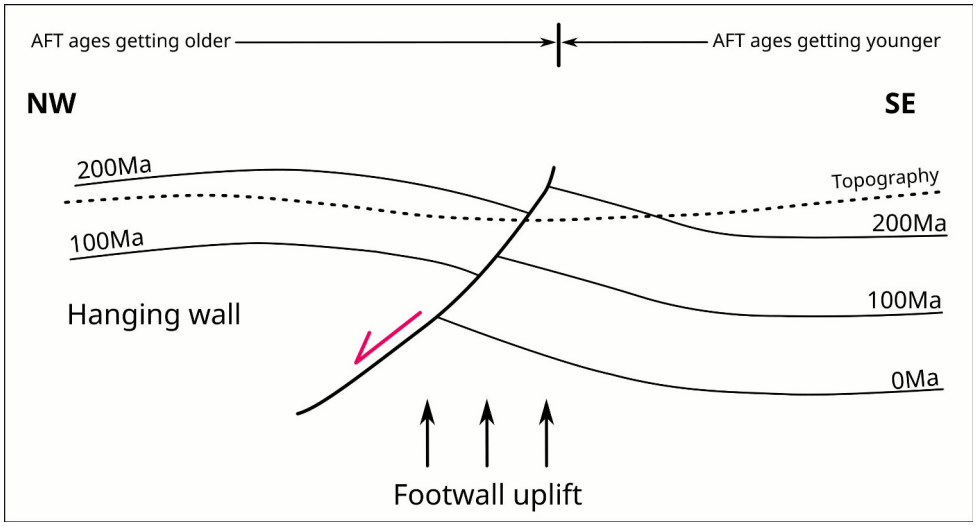

Fig. 11.3: proposal exhumation: Sketch of the model accounting for the current AFT ages distribution in footwall and hanging wall blocks. The footwall uplift only affects to the vicinity to the fault due to the morphology after extensional reactivation of the fault. Rotation of the hanging wall is similar to the listric fault development. The "AFT ages lines" in the sketch represent the pattern of predicted AFT ages after reactivation and footwall uplift.

The evolution of the AFT age pattern on the study area is explained in the Fig. 11.4. Rapid footwall uplift is the response to the denudation of the footwall block. Dip reduction and subsequent rotation of the hanging wall block is caused by continued stretching due to rifting.

The initial scenario in Fig. 11.4 depicts a total undisturbed terrain. Rocks at the same crustal level prior to extension are represented by red dots in the Fig. 11.4. At first, the fault dipped stepper than at present times. One could envisage that the fault dip was slightly rotated during Devonian continued extension, after the formation of the LGF. The uplift of the footwall block was triggered by the denudation of the abrupt topography after the faulting episode. North Sea rifting during the Mesozoic provoked the reactivation of the LGF via the HSZ. Significant reactivation along the HSZ has been detected in offshore (Færseth et al., 1995). Leighton (2007) estimated very different values of exhumation rate between crustal blocks of the LGF. For the footwall block the exhumation was 20 to 50 m/Ma quicker than for the hanging wall block. This fact reflects that the topographic development is highly controlled by faulting and footwall unroofing. The PAZ boundaries were probably Fig. 11.4. In conclusion, the AFT ages are showing

the effect of fault reactivation and unroofing. The Lærdal basement window is, thus, a consequence of continued denudation in the footwall of the LGF. The Filefjell basement window might be as well consequence of the strong influence of the nearest fault.

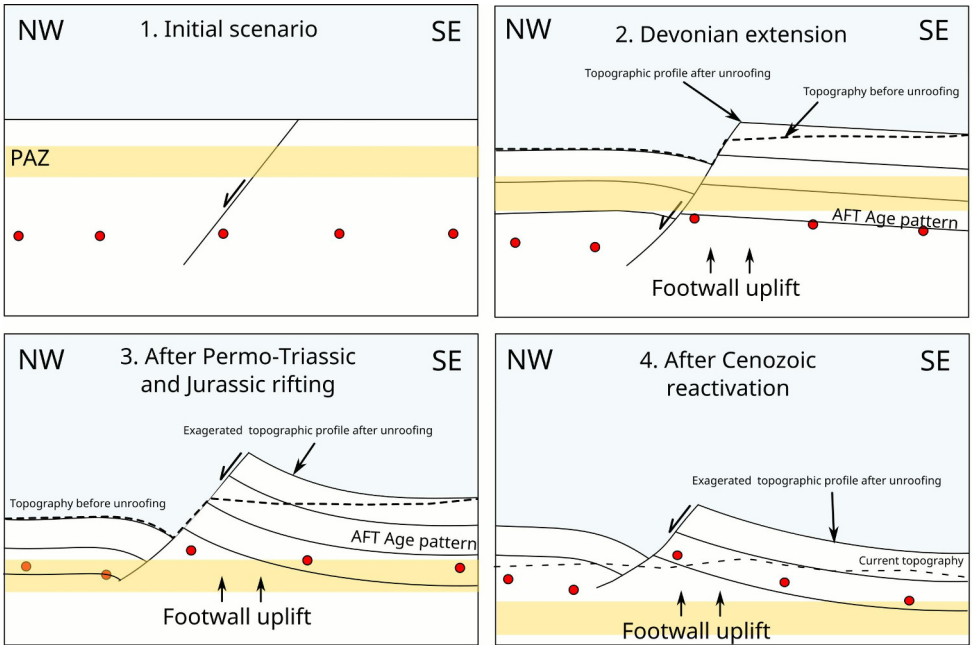

Fig. 11.4: proposal exhumation evolution: Sketch showing a simplistic model of the evolution of the exhumation pattern in the study area. 1) Initial scenario showing an undisturbed hypothetical setting where the red dots are rocks at the same crustal depth. 2) Scenario after Devonian extension. The rocks are moved differently according to the top-to-NW displacement of the fault and the effect of the footwall exhumation. 3) Great throw of the Lærdal-Gjende fault due to reactivation. The effect of footwall uplift is significant for this period (Leighton, 2007). 4) Footwall uplift after Cenozoic reactivation and current topography.

11.2 Interpretation and discussion of the structural results

11.2.1 Joints and lineations

Out of the three joint populations observed in the cataclasites, the first one shows an orientation parallel to the fault, dipping around 45° to NW. Its conjugate set of joints is also very prominent along the Raudbergerstunel. Some measurements of lineations taken from epidote slickenfibers indicate top-to-NW normal displacement. The presence of slickenfibers along these conjugate set of joints indicate fault displacement during the reactivation of the fault while hydrothermal fluids were present. It is difficult to constrain the slikenfiber formation to a single reactivation event. Slickenfibers may develop at a seismogenic depth (after greenschist metamorphic conditions), thus indicating reactivation of the Lærdal-Gjende fault at <10 km on the crust within brittle regime. A third population of joints perpendicular to the fault and very steep may be related to exhumation of the study area rather than faulting.

Two populations of planes were distinguished along the mylonitic package. The ENE-WSW trending population of planes are joints and foliations. The mylonitic foliation vary slightly in

orientation along the mylonite package, but it always dips to the NW. Joints with the same orientation than the mylonitic foliation are affecting pervasively along the mylonites. The foliation of the mylonites is a relict structure from Devonian extension. It may have accommodated brittle deformation, which clearly post-date the formation of the mylonitic foliation. Slickenfibers encountered along minor faults indicate down-to-WNW movement, corresponding to the stress field during Permo-Triassic North Sea rifting (E-W stretching). The slickenfibers from the migmatitic gneisses from the basement indicate normal sense of shear relative to minor faults.

11.2.2 Mylonites

Mylonites form under metamorphic conditions. If the mylonite form before the metamorphic peak, meaning that the deformation ends before this threshold, the deformation structures would be overprinted by recrystallization and grain growth (Passchier & Trouw, 2005). Mylonites record the last metamorphic condition in which they formed. The increase of temperatures will provoke the fading of the mylonitic foliation and structures.

Mylonites are affected by brittle deformation in the regions nearby the fault. Brittle deformation overprinting manifests in the first 20 m of the mylonitic package from the fault core outwards. Brittle deformation overprinting is believed to be the cause of fluid alteration. Euhedral epidote crystals are found in plagioclase porphyroclasts. Sericite and slightly less portion of saussurite are observed within the mylonitic rocks. Well crystallized chlorite in some of the mylonitic foliation planes indicate retrometamorphism to greenschist conditions.

The mylonites of the Lærdal-Gjende fault do not exhibit large porphyroclast, or winged structures on the field. Some areas of the mylonitic package have more ultramylonitic than mesomylonitic character. The observation scale is important in terms of classification. Since ultramylonites are defined as mylonites with 90 % of matrix, most of the mylonitic rocks on the field can be classified as ultramylonites. Whereas, under the microscope most of the thin sections range from meso to ultramylonites. Ultramylonites classified under the criterio given by Twiss and Moores (with <10 µm of clasts size), are found in the vicinity of fault, which indicates higher deformation strain.

The mylonite package show evidences of medium-grade conditions that had undergone retrometamorphism to low grade conditions of greenschist facies. Flame perthite structures are usually seen in rounded plagioclase porphyroclasts. Flame perthites in mylonites occur at high stress in greenschist facies, specially in ductile shear zones. Initial deformation under amphibolite metamorphic conditions is evidenced by a large number of features and textures within the mylonites. Partially recrystallized feldspar porphyroclasts by bulging mechanism and by nucleation and growth of new grains are very common in the thin sections. Subgrain rotation of quartz is very

prominent also in the thin sections 100 m away from the fault. Those recrystallization mechanisms in felspar and quartz occur at temperatures above 450 °C. An evidence of medium-grade conditions are the flattened old crystals, quartz ribbons and sigmoidal-shaped quartz bodies. Furthermore, deformation lamellae in feldspar is a clear indicator of crystal plasticity of feldspar. Mantled-and-core structures with sigma-type object development are as well usually found in this sections from mylonites 100 m away from the fault. The development of sigma objects indicates medium-grade conditions (450 to 600 °C). Signs of higher grade conditions (towards the 600 °C) are evidenced by incipient myrmekite growth along the edges of subrounded to subangulat porphyroclasts. Quartz ribbons On the other hand, bookshelf microfracturing in feldspar is common at low-grade conditions (400 to 500 °C). Thus, the mylonite package show signs of formation at a temperature around 500 °C, or probably more due to the incipient myrmekite growth.

The greenschist facies conditions are assumed to be related to exhumation of the footwall block of the Lærdal-Gjende fault. The brittle deformation in meso- and ultramylonites indicate reactivation temperatures below 300 °C. The shear bands observed in the field are interpreted to pre-date the microfaults seen at microscale. The microfault vastly affecting the ultramylonites nearby the fault are generally antithetic to the LGF. The microfault form micro-graben arrangements and planar normal fault arrays which indicate extensional reactivation of the fault.

Several kinematic indicators such as low and high angle fractures grains of feldspar, σ-objects and mineral fish indicate consistent top-to-NW sense of shear. The controversial meso-scaled kinematic indicators are probably complex winged objects ‘in development’. In the field, very often the observation plane is not parallel to the XZ plane of observation, some winged objects may have been misinterpreted.

Concluding, assuming a geothermal gradient of 30 °C/km, the mylonites were formed at 15 to 20 km depth associated to temperatures between 450 and 600 °C during top-to-NW shear displacement. Exhumation to greenschist facies conditions was accompanied by chloritization and the apparition of shear bands. Microfaulting occurred as a manifestation of late extensionl reactivation in the upper crust.

11.2.3 Cataclasites

Cataclastic rocks are very complex rocks that carry a handful of information about the deformation history of faults. Cataclasites can be good temperature indicators. At Lærdalsøyri outcrop the intensity of cataclastic deformation varies according to distance to the fault. The vicinity of the fault is densely veined and veins often display a sense of shear component. Therefore, it is feasible to assume that the influence of cataclasis increases progressively towards the fault.

Layers of cohesive breccias are found very close to the fault and date from Jurassic times (Eide et al., 1997). The cataclastic flow deformation is observed better under the microscope.

The signs of cataclasis are obvious under the microscope. Different episodes of cataclasis are inferred from microscopic analysis. The first cataclastic episode is interpreted to occur during the initial stages of formation of the LGF, during Mode II of Devonian extension. The cataclasites formed at low grade (<400 °C) are evidenced by transgranular fracturing that can be followed from grains separated between each other. Due to the top-to-NW displacement of the LGF, the temperatures increased and the signs of first cataclasis under 400 °C were partially erased by later dynamic recrystallization of quartz and felspar clasts of the cataclasitc matrix. This is interpreted as the second cataclastic deformation episode, although it is rather a progressive evolution of the cataclasistes to complex tectonites. Subgrain rotation (SGR) of quartz and bulging (BLG) of feldpar and quartz are dynamic recrystallization mechanisms that indicate medium-grade conditions (450 to 600 °C). Fractured feldspars are not so commonly observed under the microscopy, however some relict fractures are sometimes still present. Mechanical twinning in plagioclases indicate onset of crystal plasticity of feldspar, on amphibolite metamorphic conditions (~450 °C). Mechanical twinning is spotted locally in plagioclases but it is not a common structure within the rock. Growth (polysynthetic) twinning in plagioclase is often present as a relict structure from the parent rock. Mantles of fine-grained feldspar with a sharp boundary around cores of old grains are spotted very often in all the thin sections collected along the Raudbergerstunnel. That is consistent with medium-grade conditions. Winged objects of feldspar are not developed in the hanging wall cataclasites, which indicates temperatures below 500 to 600 °C. Lobate boundary contacts around feldspars indicate low-medium grade conditions. Boudinage of some hard clasts may indicate the extension axis during cataclasis, but it has not been used to indicate the sense of shear. Strain partitioning is seen very often in closer distance to the fault. Some portions of the thin sections present angular fragments and no signs of crystal plasticity, whereas in other portion of the thin section sigmoidal quartz ribbons are observed. An increase in crystal-plasticity can be observed from DS-7 to DS-11, suggested by the presence of sigmoidal-like shaped polycrystalline aggregates, quartz ribbons and onset of plagioclase kinking.

Cataclasis affects larger portions of rocks one or two meters away from the fault (DS-11 and DS-12). Transgranular fracturing affects clasts and matrix. Some of the fractures are refilled by quartz or healed. Interestingly, transgranular fractures are observed to cross-cut altered matrix, suggesting a post-deformation phase after dynamic recrystallization and fluid alteration. Since the transgranular fractures are healed and filled with quartz, it may be cause by a reactivation at upper greenschist metamorphic conditions. Veins cross cut previous ones and show shear movement. Cohesive breccia dating from Jurassic times might be originated during this deformation episode. The parent rock seem to have mylonitic origin since high crystal plasticity is suggested

by elongated polycrystalline quartz ribbons, fragments with total recrystallization and smaller clast cores of felspar. The structures found in EC-30d, such as winged objects, correspond to mylonites. On the other hand, comminution by cataclasis (angular grains) is observed in fractures. That interpreted as a consequence of cataclasis after ductile deformation. The mylonites may have been generated under amphibolite conditions in the hanging wall (Devonian) and are a structure from the parent rock (cataclasis affecting juxtaposed mylonites). Late cataclasis after the main episode in Devonian times is evidenced along the Raudbergerstunne by fractures within veins that die out towards its walls, or intragranular fractures in clasts that are joining each other.

Flame perthite exholution may occur in medium-grade conditions, although here the perthites are interpreted as exsolution symplectites caused by retromethamorphism to greenschist metamorphic conditions. Totally chloritized symplectites are identified and interpreted as a result of the retrometamorphism. The retrometamorphism to greenschist conditions is consequence of the exhumation after fault activity. Large radial crystals of Iron-rich chlorite are widespread on veins and mylonitic-cataclastic finer matrix. The radial growth of chlorite (Chl_2) is an obvious sign of stable greenschist conditions. Some chloritized bands show incipient radial growth generating polygonal arch textures. Complete chloritization of some minerals to iron-rich chlorite may be enhanced by the excess Fe_2^+ on the fluid due to the saussuritization process (Morad et al., 2010). Thus, the alteration to chlorite (Chl_1) occurs as a consequence to the introduction of hydrothermal fluids. The hydrothermal fluids provoked the alteration of alkali feldspar and plagioclase to sericite and saussurite, respectively. The saussuritization and albitization (exsolution perthites) of anorthite caused an excess of Ca_3^+ into the fluid, which explains the generation of epidote crystals. The parent rock had biotite, now totally replaced by chlorite (chlorite pseudomorphs). The saussuritization and sericitization are associated to release of magmatic fluids after crystallization of granitic rocks at a temperature of ca. 400 °C (Morad et al., 2010). Therefore, it seems feasible that hydrothermal fluid alteration along the fault was enhanced by the dynamic recrystallization of quartz and feldspar. Thus, fluid alteration is associated to cataclasis at upper amphibolite to greenschist metamorphic conditions.

Veins developed during extensional cataclasis are the main mechanism of fluid transportation. There are different types of veins; some veins with micrometric 'wall rock' fragments evidence cataclastic flow deformation. Other veins accommodate extensional deformation and recrystallize idiomorphic epidote crystals perpendicular to the walls, parallel to the σ3 axis during extension. The veining generally is refilled with saussurite. Smaller veins inject larger ones oriented practically horizontally. The presence of opaque minerals indicate oxidation due to weathering of Fe-rich mineral phases. The presence of euhedral opaques means that crystallization occurred after cataclasis, probably in later reactivations closer to the surface.

The cohesive breccias of the Lærdal-Gjende fault have a Permian and Jurassic component (Andersen et al., 1999; Eide et al., 1997; Torsvik et al., 1992), impliying reactivation took place

after formation. The epidote and altered alkali feldspar from the fault-rocks of the Lærdal-Gjende fault gave Middle Devonian ages through $^{Rb}/_{Sr}$ dating method (Larsen et al., 2003). Therefore, the hydrothermal fluids are confirmed to be active during first epiode of cataclasis and formation of Lærdal-Gjende fault.

11.2.4 Fault gouges and incohesive fault-related rocks

The fault core of the LGF exhibits fault gouges with different competences. The most competent fault gouges are interpreted to be pre-existent to the last reactivation of the fault core. The competent character thus is associated to the strain hardening of pre-exiting porous fault gouges within the fault core (Rutter, 1986). Therefore, the incohesive fault gouges (powder rock) and fault breccias along the upper fault boundary may represent the most recent reactivation of the fault core. Later reactivation with no significant displacement along the fault may have occurred later, although it has not been recognized through structural analysis.

The fault core consists on 1 m of brittle fault rocks. A total significant displacement during reactivation under the brittle regime is implied. The fault core of the LGF reveals an internal structure interpreted to be caused by extensional top-to-NW reactivation of the fault. It is difficult to evaluate whether the different fracture sets are associated to distinct reactivation episodes. However, at least two brittle reactivation episodes have been interpreted. This may demonstrate that both of interpreted brittle reactivation episodes were directed top-to-NW, since it is especially difficult to recognize overprinting structures that indicate the same sense of displacement.

The formation of the fault core is associated to brittle deformation of pre-existing mylonitic and cataclastic rocks, implied from the analysis of DS-12. The fault gouges under the microscope show microfaulting within plagioclase clasts, which is typical of low grade metamorphic conditions (<400 °C). The fine grained matrix and larger clasts accommodate brittle deformation. Microfaulting and fracturing without displacement affects differently to fine-grained mafic bands and quartzo-feldspatic bands. Quartzo-feldspatic bands look like microbreccias under the microscope. This is interpreted to be due to prior lithological heterogeneity of the parent rock.

Saussurite and sericite alteration is observed in hardened fault gouges. This indicates that hydrothermal fluid alteration occurred during or after the formation of these fault gouges. Euhedral epidote crystals are developed in competent fault gouges, which suggest stable conditions after deformation and alteration. The fault gouges of the Lærdal-Gjende fault are principally composed by smectite minerals (Ksienzyk, pers. comm.). The presence of smectite is an indicator of temperatures of less than 220 °C. Thus, the formation of the fault gouges should have occurred at a depth of <7 km accounting for a Permo-Triassic geothermal gradient of 30 °C/Ma. $^{K}/_{Ar}$ illite methods tested in fault gouges of the LGF revealed Paleogene, Early Jurassic, Permian and Early Carboniferous reactivation along the Lærdal-Gjende fault (Ksienzyk, 2012). The fault core, therefore should have been formed in more than two stages of exhumation.

11.2.5 Fault zone architecture and summary fault rocks generation history

The different fault related rocks generations in the Lærdal-Gjende fault and their arrangement within the fault zone is the result of Devonian extension and several reactivation events throughout the post-Caledonian history (present study; Andersen, 1998; Gathe & Andersen, 1996). A summary of the evolution of the fault is presented as

- **Fault rocks generation history**

The presence of complex tectonites (fault rocks with both ductile and brittle deformation) is consequence of a top-to-NW movement of the hanging wall. The initial and later cataclasis episodes form part of the same process of Mode II Devonian extension. The cataclasis at less than 400 °C (low-grade conditions) occurs simultaneously to the formation of the mylonites at deeper crust levels (amphibolite metamorphic conditions). The continued displacement of the fault top-to-NW provoked the juxtaposition of the cataclasites formed at relatively upper crustal levels onto the mylonites. The initially formed cataclasites reached the maximum metamorphic peak at amphibolite facies conditions. That is evidenced mainly by the overprinting of dynamic recrystallization textures and the onset of crystal-plasticity of feldspar clasts. The maximum metamorphic peak (amphibolite metamorphic conditions) was acquired by the cataclasites at 15 km depth assuming a geothermal gradient of 30 °C/km (Fig. 11.5). However, the cohesive cataclasites of the Lærdal-Gjende fault are reported to be formed at 10 km depth according to Fossen & Hurich (2005). The kinematic indicators are consistent with top-to-NW displacement.

Greenschist facies conditions were assumed during the exhumation of footwall and hanging wall blocks of the Lærdal-Gjende fault. Cataclasis during exhumation of the hanging wall is inferred by late cataclastic textures affecting first generation veins filled with hydrothermal fluid alteration minerals. Evidences of late cataclasis can be also observed nearby the fault core, where there are cohesive breccias and cataclastic fragments of mylonitic rocks. Flame perthite structures in plagioclases within mylonites may be caused by the change from amphibolite to greenschist consditions during exhumation of the footwall. The chlorite polygonal arch textures are good indicators of the retrometamorphism into greenschist conditions.

The hydrothermal fluid alteration in the mylonites is linked to the exhumation of the footwall block into greenschist facies conditions (Fig. 11.5). Considering the lack of initial porosity of mylonites, the hydrothermal fluids should have been introduced after a certain degree of extensional semi-brittle deformation. The mylonitic package presents less signs of hydrothermal alteration in comparison to the cataclasites, which supports the prior statement. Constraining the timing of brittle or semi-brittle deformation episodes in the mylonites is rather difficult through structural analysis. Overprint by brittle deformation is interpreted to be partly due to the entrance into greenschist metamorphic condition and partly triggered by brittle deformation occurred within the PAZ, at a depth closer to the surface (as will be explained in the next section).

Continued exhumation passed the greenschist facies conditions, at low to very low grade, is evidenced micro-faulting in mylonites and the formation of fault gouges. The microfaulting is associated to fault reactivation at brittle regime. A thick fault core consisting of incohesive fault rocks indicates a large total displacement produced probably by several reactivation episodes directed top-to-NW. The crystallization of idiomorphic crystals of epidote in fault gouges may signify that fluid alteration occurred late after Devonian times associated to reactivation of the LGF.

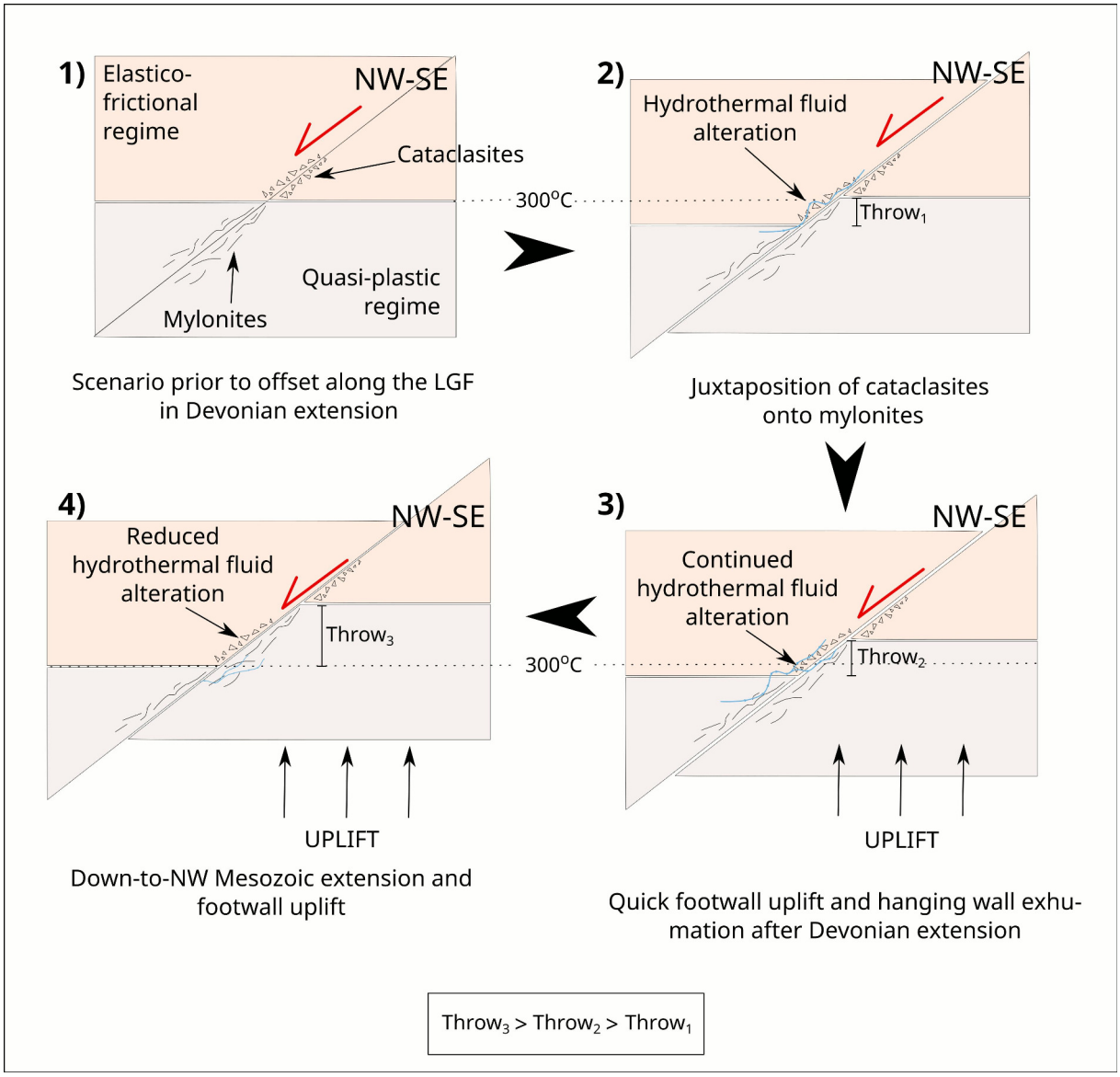

Fig. 11.5: Summary of the stages of development of fault rocks. 1) Scenario prior to faulting. The regimes and associated fault rocks are depicted. The fault rocks are drawn as a guidance. No fault rocks can be prior to faulting. 2) Lærdal-Gjende fault (LGF) formation. The cataclasites reach amphibolite metamorphic conditions. The regime boundaries are fossil regime boundaries, now used as a reference. 3) Unroofing and uplift of the footwall block as consequence of extension probably increment slightly the throw. The regime boundaries are fossil regime boundaries, now used as a reference. 4) After Mesozoic reactivation the rocks have been exhumed to low-grade conditions. Footwall uplift is also implied after Mesozoic reactivation.The regime boundaries are fossil regime boundaries, now used as a reference.

- **Fault zone architecture**

The fault architecture of the Lærdal-Gjende fault is directly related to Devonian extension. The juxtaposition of cataclastic rocks in the hanging wall onto mylonites from the footwall is a great kinematic indicator per se. Brittle fault rocks on top of footwall ductile deformed rocks indicate a normal-sense of shear of the fault zone (Snoke et al., 1998) (Fig. 11.5).

The fault gouges of the LGF are located between footwall and hanging wall blocks forming the fault core. Rutter et al. and co-workers (2001) suggested that fault reactivation usually occurs along the relict fault plane due to the contrast in competence between weakened fault rocks and wall rock. This model of reactivation is consistent with the type 2 fault zones proposed by Means (1984) and Mitra (1984). The loss of cohesion fault rocks (increased porosity) along the fault plane of the LGF caused by Devonian faulting, may have favored the reactivation along the relict fault plane. Simultaneously, the increasing porosity within the fault plane due to extensional displacement aided the circulation of hydrothermal fluids into the fault plane and the cataclasites of the hanging wall. The formation of low competence clay bands during shearing is common due to the high stress and chemical differentiation (Rutter et al., 2001). Therefore, the developement of the fault core may have started very early already in Devonian times.

The several brittle reactivation periods of LGF throughout Late Paleozoic and Mesozoic times may have increased the fault core composed by fault gouges. In order to increase the thickness of the fault core by reiterated movement, strain hardening should have occurred (Mitra, 1994). Strain hardening is observed in the lower part of the fault gouges within the fault core. Thus, the new generation of fault gouges without the hardened character are interpreted to be formed after hardened gouges (Fig. 11.6).

On the contrary, softened fault zones accommodate displacement without increasing the thickness of the fault zone (Mitra, 1994). The production of fault gouges is linked to changes in mineralogy, which could soften the fault zone (Mitra, 1984). In the fault core of the LGF, the thin brown layer of clay minerals separating hardened gouges from new generation gouges may have accommodated some deformation. The new fault gouges generation did not involve an increase in fault zone thickness (Fig. 11.6). If this clay layer has accommodated any displacement may be from recent reactivation periods, since its formation is interpreted to be synchronic to the new generation of fault gouges.

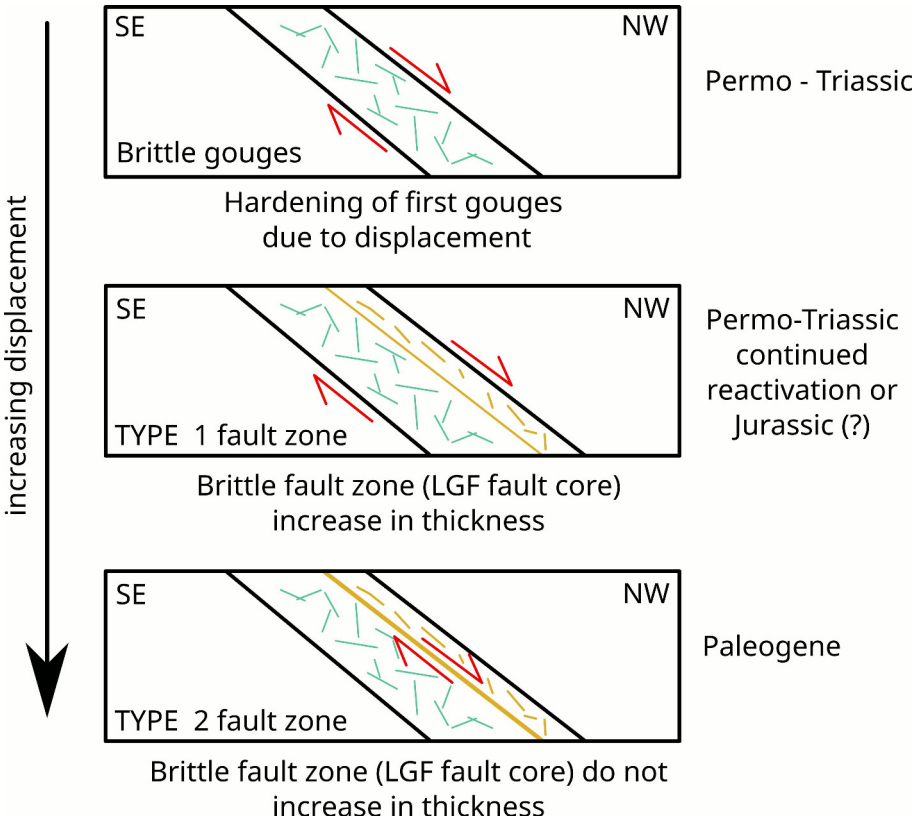

Fig. 11.6: Models of fault core development of the LGF during brittle deformation.

11.3 Comparative analysis

11.3.1 Fault rock formation linked to the thermal models

The apatite fission track data only reflects the brittle reactivation of the Lærdal-Gjende fault at low and very low grade conditions. According to the thermal modeling, only two episodes of accelerated cooling occurred since Carboniferous age to Early Jurassic age. The fault core is interpreted to record two different reactivation episodes under brittle regime, in accordance with the thermal models. Under a critical view, field observations may lead to misinterpretation. Furthermore, fault gouges from the fault were dated through $^{K}/_{Ar}$ illite methods and revealed reactivation in Early Carboniferous, Permian, Late Triassic to Early Jurassic and Late Cretaceous to Paleogene ages (Ksienzyk, 2012).

The MTL distribution curves suggest complex histories of exhumation. The thermal models probably only depict an average path rather than the distinct episodes of reactivation within the PAZ. The reactivation events occurred within the PAZ or close to the path and thus, the fission track lengths may not have well defined generations. Hence, all the reactivation episodes obtained from $^{K}/_{Ar}$ illite of the fault gouges are reflected in the thermal models as one single long episode of reactivation.

Based on $^{K}/_{Ar}$ illite data, four reactivation periods at very low and low grade conditions have been inferred (Fig. 11.7). The field observations of the fault core reflects at least two of the

episodes. The fault core might have been increasing in thickness according to the displacement of each reactivation episode prior or during the hardening of the gouges. If that has been the case, it would be difficult to evaluate through structural analysis. The hardened gouges should have occur within the first two reactivation episodes. The formation of fault breccia and new gouges (powder rock) is associated to the reactivation in Late Triassic to Early Jurassic times (Fig. 11.7). The last reactivation of the fault during Late Cretaceous - Paleogene times may have been along clay bands within the fault core, without involving the generation of new fault rocks (Fig. 11.7). The last brittle deformation overprint in the mylonites may be either from the reactivation episodes in Late Cretaceous to Paleogene times or from Late Triassic to Early Jurassic times.

The formation of the Lærdal-Gjende fault in Devonian times is not represented in the fission track data due to the low closure temperature of the apatite. Nonetheless, a summary with all the structural and AFT is available in Fig. 11.7. During the formation of the Lærdal-Gjende fault there the cataclasites that are today juxtaposing the footwall mylonites, were farther up. Therefore, to depict the Devonian throw of the LGF, the cataclasite box in gray (Fig. 11.7) is separated from the mylonite purple box. After the displacement, the cataclasite gray box is joined together with the mylonite box in purple (Fig. 11.7).

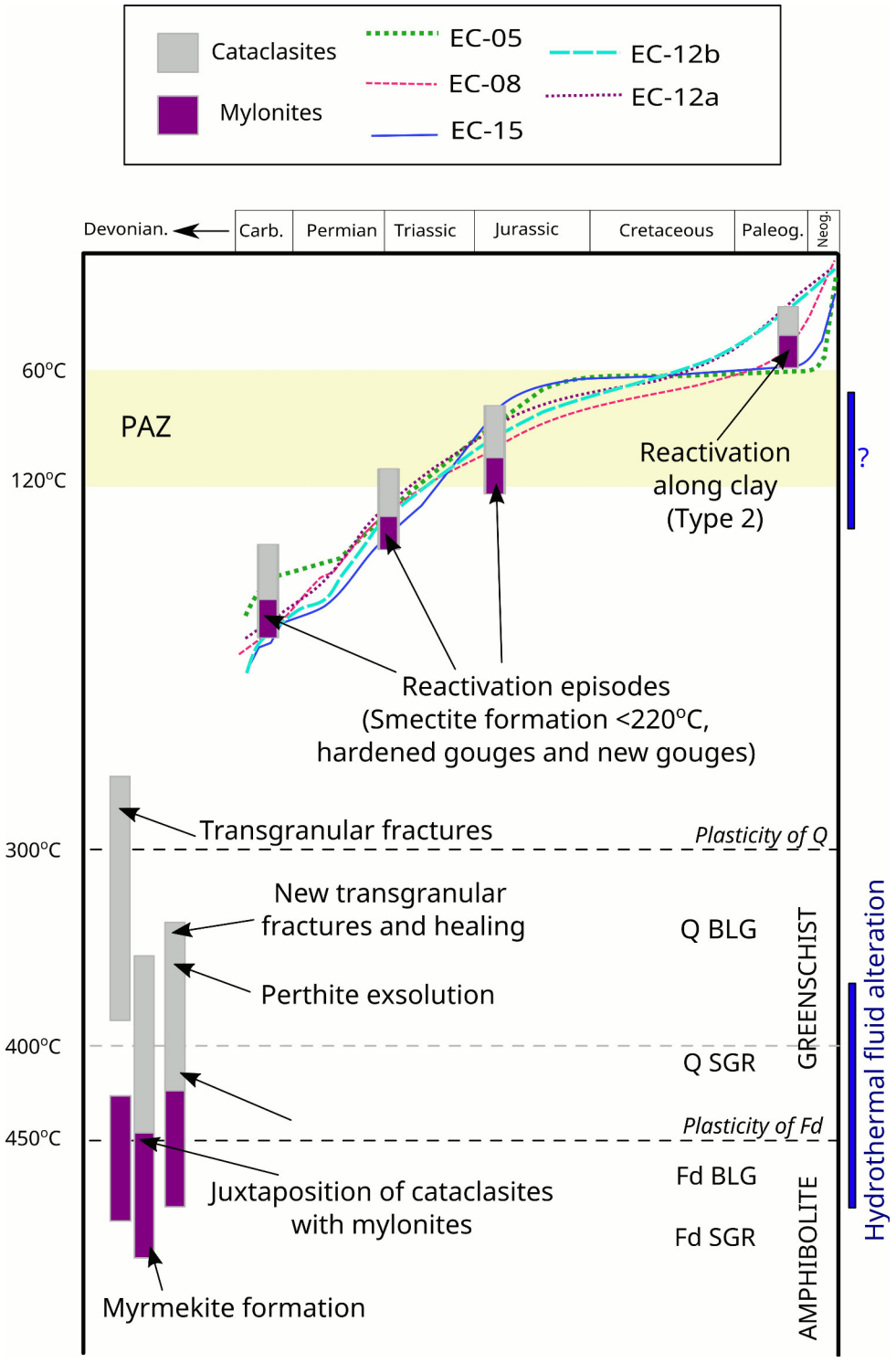

Fig. 11.7: AFT + Structural: Synthesizing figure merging together structural and AFT data. The boxes in gray and purple represent the cataclasites and mylonites exposed on the Lærdalsøyri outcrop. The size of the boxes represent the accuracy. No time scale is applied in Devonian events. At first, cataclasites were formed at low-grade conditions until their juxtaposition onto the mylonites.

11.3.2 Comparison with previous studies

The landscape evolution of southern central Norway has been regulated by the reactivation of the major Devonian lineaments crossing offshore and mainland Norway. The lack of information

on the exhumation pattern of southern central Norway represents a step down to fully understand the landscape evolution of Norway. Therefore, it is important to acknowledge the role of major fault reactivation in restricted areas influenced by faults in inland Norway. The case of study presented in this thesis covers the region that encompasses the Lærdal erosional window affected by the Lærdal-Gjende fault.

- **Relation between Mesozoic rifting and reactivation of the Lærdal-Gjende fault**

The evolution of the Norwegian continental margin was influenced very evidently by the reactivation of major detachments along the strongly faulted coastal region of Norway (e.g. Osmundsen et al., 1998; Redfield et al., 2004, 2005). The inland region is suspected to be affected by rifting of the North Sea and North Atlantic Ocean as well. Færseth et al. (1995) suggested that the offshore structural continuation of extensional detachments was responsible for fault reactivation in mainland. Osmundsen et al. (1998) concluded that the continuation of offshore shear detachments have played a very important role in basin geometry in the North Sea. The reactivation of the Lærdal-Gjende fault in onshore is linked to the different episodes of reactivation of the Hardangerfjord Shear Zone (HSZ) during North Sea rifting in Permo-Triassic and Jurassic times.

Rifting in central Pangea provoked the reactivation of Devonian fault zones of western and central Norway in Permo-Triassic times and in late Jurassic times. The Mesozoic brittle reactivation of the Lærdal-Gjende fault is linked to different rifting episodes of the North Sea and North Atlantic formation. An average cooling rate of 1 °C/Ma from Early Carboniferous up to Early Jurassic is suggested by the thermal models of the present study. An episode of reactivation of the Lærdal-Gjende fault in Early Carboniferous up to Triassic times has been revealed through thermochronological and structural data. Andersen et al. (1999) reported east directed slickenfibers, in correspondence to the fossil stress field (E-W) during Permian times. Cohesive cataclasites and breccias tested through paleomagnetic method gave also a Permian component (Eide et al., 1997; Torsvik et al., 1992). Illite dating of the Lærdal-Gjende fault gouges revealed an episode of within the same time span (Ksienzyk, 2012). Slickenfibers from cataclasites collected for the present study are in agreement with the structural results of Andersen et al. (1999). Rifting focused in the Horda platform, offshore southwestern Norway in the North Sea (Færseth et al., 1995), is linked to the onset in high cooling rates observed in the thermal models. Offshore brittle segments of the Hardangerfjord Shear Zone were active during this rifting episode, which triggered the reactivation of the Lærdal-Gjende fault in the onshore region. The Permo-Triassic rifting is associated with rift flank uplift. Ksienzyk et al. (2014) reported higher cooling rates in coastal samples than inland samples throughout Jurassic and Cretaceous times, which suggests rift flank uplift occurred within western Norway controlled mainly by fault activity. A Jurassic component was found in cohesive cataclasites and breccias (Eide et al., 1997; Torsvik et al., 1992). $^{K}/_{Ar}$ illite dating revealed Late Triassic-Early Jurassic reactivation. The onshore reactivation of southern Norway in Jurassic times have been linked to North Sea and North Atlantic

rifting (Fossen & Hurich, 2005). Jurassic immature sediments in the Bergen Arcs area supporting the hypothesis that a rapid cooling episode near shore occurred due to Jurassic fault activity (Eide et al., 1997; Gabrielsen et al., 2010; Ksienzyk, 2012; Torsvik et al., 1992). The Jurassic rifting episode had more localized mainly on the rift branches of the Viking Graben in the north and central graben and the Moray Firth Basin in the south (Doré et al., 1999). Late Cretaceous to Paleogene cooling episode is associated to the opening of the North Atlantic Ocean.

- **Comparison with landscape evolution models of Norway**

The post-Caledonian morphotectonic evolution of Norway is still poorly understood. Thermochronological studies from western Norway have revealed the strong tectonic influence in exhumation pattern by reactivation along brittle Devonian faults and shear zones (e.g. Redfield et al., 2004, 2005). The models of landscape evolution proposed for the evolution of the Norwegian landscape are "peneplanation and uplift" (Rohrman et al., 1995), the "ICE-hypothesis" (Nielsen et al., 2009) and the crustal taper related-to-topography model" (Osmundsen & Redfield, 2011).

Inland Norway exhumation pattern is rather unknown. Andersen et al. (1999) suggested that the topographic control of inland Norway was highly linked to footwall uplift of reactivated faults. As previously discussed, the reactivation along major lineaments is well established and it has been recognized as the principal reason for passive margin development. The reactivation along the HSZ has played an active role in passive margin developement, since it separates the strongly faulted Caledonian terrain from foreland undeformed basin. Hence, the topographic rejuvenation of inland Norway is linked to the development of the Norwegian passive margin, which is controlled by major onshore faults as the Lærdal-Gjende fault.

A model of landscape evolution based of fission track data at a regional level was suggested by Rohrman et al. (1995). Rohrman et al. (1995) proposed a domal exhumation pattern of southern Norway in order to explain the old AFT age in the coast and in the highlands. Ksienzyk et al. (2014) suggest rift flank uplift to a mean to explain the AFT age distribution of the coastal region of Norway in comparison with inland highlands. Leighton (2007) performed a regional study in southern Norway. The AFT ages presented by the latter author displayed large offsets across faults. Redfield et al. (2004, 2005) also found significant offset in AFT ages across the crustal blocks of the Møre-Trøndelag fault complex (MTFC). All the AFT studies distinguished two rapid cooling events; commonly starting in Permian times and in the Cenozoic.The present study concur with Leighton (2007) and other thermochronologists and distinguishes two different cooling events associated to North Sea rifting and Cenozoic uplift linked to the opening of the North Atlantic Ocean. Furthermore, offsets in AFT ages were found across the crustal blocks of the Lærdal Gjende fault. The AFT offsets were from Jurassic (hanging wall) to Cretaceous (footwall). Nonetheless, the AFT age distribution was related to the distance of the fault.

The cooling rates estimates for Permo-Triassic cooling were lower than for coastal samples. Ksienzyk et al. (2014) found 2 to 3 °C/Ma, in contrast to 1 °C/Ma suggested by thermal modeling in the present study, supporting that rift flank uplift may be the main cause for onshore exhumation during Permo-Triassic times.

To return to the different models of landscape evolution, a peneplanation scenario was considered. In order to test if the peneplanation during Mesozoic times matched the AFT data, some thermal models were performed for peneplanation set for Jurassic times up to Paleogene. The peneplanation ages were based on the discovery of Jurassic sediments near the Bergen coast (Fossen et al., 1997). The peneplanation models were not favorable for the study area. All of the modeled paths required a reburial of ~2 km, which is much larger than the reburial for the coast. The peneplanation and uplift model do not fit the thermal models since reburial (instead of uplift) is required. Therefore, there is no evidence that peneplation has affected to the study area.

The steep cooling rate for the last episode of accelerated cooling cannot be explained only as to an isostatic response to unloading. Furthermore, thermal modeling suggest that the accelerated cooling starts before Pliocene-Pleistocene denudation. The crustal taper hypothesis may explain the persistent fault activity after rifting up to Cretaceous times. Osmundsen & Redfield (2011) proposed that rejuvenation of the passive margins depends on the taper break location (the first highly thinned crust in the distal margin). They suggested that basin development controls the fault reactivation even after rifting. Hordalan basin and Møre basin were points of concentrated deformation during rifting and important basins that influenced passive margin development. Hordalan basin is in the southwest of offshore Norway, thus related to the rifting of the North Sea which affects directly to the offshore segments of the HSZ. The post-rift fault activity is justified by isostatically driven vertical adjustments. That may also correlate with the several reactivation episodes experienced by the Lærdal-Gjende fault.

Both the ICE hypothesis and the ‘peneplanation an uplift’ model fail to explain the different time-Temperature paths obtained for the present study. The ‘crustal taper related-to-topography model’ may partly explain the frequency in reactivation along the LGF during and after rifting of the North Sea. The present study, however, do not cover enough area to make a sensitive approach of a regional exhumation pattern. On the other hand, the treatment of the AFT data have been enough to demonstrate that local exhumation patterns are strongly related to fault activity.

This page is intentionally left blank

12 Conclusion

Low-temperature thermochronological analysis has provided new insights in local reactivation patterns of inland areas under the influence of faults. A detailed analysis of the fault rocks exposed in Lærdalsøyri has provided understanding of the fault rock generations of the Lærdal-Gjende fault. The following conclusions can be drawn from the present study:

1. The AFT ages range from Permian age to Middle Cretaceous age. Most of the ages date from Early Cretaceous for the region close to the fault. The scatter of the ages is due to the local exhumation pattern.
2. A positive AFT age - elevation is expected for tectonically undisturbed terrains. Within the study area there is no significant elevation - AFT age correlation, which implies a strong tectonic influence. The AFT age distribution on both footwall and hanging wall blocks show an exhumation pattern influenced by tectonic and topographic controls. Denudation after extensional fault reactivation causes the uplift of the footwall block, affecting the AFT age distribution (younger ages nearby the fault and older ages farther away). The opposite trend is observed for the hanging wall block. The ages tend to increase towards the fault due to the anticline structure formed similarly as to a roll-over in listric faults. Some local variations in the age trend are caused by fault interaction. Samples collected from depression show some bias.
3. MTL distribution show slighly positive and negative skewness. Most significantly, the incipient double peak in the MTL distribution curve suggest a complex thermal history of reactivation episodes within the PAZ. The MTL - AFT age relation show questionable smooth positive correlation, supporting the previous statement.
4. The thermal history modeling suggest two episodes of accelerated cooling events and one slow cooling episode. The first rapid cooling event extended from Late Carboniferous age to Early Jurassic with cooling rates of 1 °C/Ma, concomiant to Permo-Triassic rifting. The difference in cooling rates between coastal samples and the current samples support that rift flank uplift may be the main process responsable for onshore exhumation in lower Mesozoic. Paleogene cooling rates estimates range widely between 2,2 to 5 °C/Ma. Paleogene cooling rates are interpreted to reflect fjord incision and thermal disturbance due to the North Atlantic opening. The extended fault activity post-dating the rifting episodes has been interpreted as to be related to the crustal taper hypothesis.
5. The current fault-rock arrangement in Lærdalsøyri is inherited from Devonian times. The juxtaposition of cohesive cataclasites from the hanging wall block onto the footwall mylonites indicates extensional top-to-NW displacement for several kilometers.
6. The mylonitic package is formed by medium to low grade meso and ultramylonites. The maximum temperature that the mylonites reached is ~500 °C evidenced by incipient generation of myrmekite. Mylonites indicate top-to-NW normal shear sense.

7. An early episode of cataclasis at low to very low grade conditions is overprited by textures from amphibolite to greeschist conditions. The overprint is caused by top-to-NW dipping of the hanging wall block into deeper crustal levels. The subsequent exhumation provoked the switch from upper amphibolite metamorphic conditions into greenschist facies. Cataclastic flow was enhanced by hydrothermal fluid circulation. The dense veining nearby the fault indicates successive deformation with different hydrothermal fluid pulses. Late cataclasis occurs at low grade conditions. In general, the cohesive cataclasites show signs of strain partition, typical from complex tectonites formed between 400 to 300 °C.
8. Mesozoic deformation is produced at low to very low grade conditions. According to $^{K}/_{Ar}$ illite data from other studies, the Lærdal-Gjende fault was reactivated four times under the brittle regime. Thermal models do not show such time-Temperature path, which is interpreted to be due to successive reactivation within the PAZ. Brittle deformation is observed in the mylonites along 20 m from the fault outwards. Shear bands and minor faults are interpreted to occur from low grade conditions up to very low grade.
9. Different generations of fault gouges can be discerned within the fault core of the Lærdal-Gjende fault. Hardened fault gouges are interpreted to be caused by reactivation in Permo-Triassic times. The formation of fault breccias and fault gouge powder is interpreted to date from Jurassic times. The Paleogene reactivation may have not represented a thickness increase of the fault core. PYR foliations within fault gouges indicate top-to-NW displacement.

This page is intentionally left blank

13 Outlook

This thesis is contributing to the research of landscape development of central southern Norway by adding up more thermochronological data and some new insights in the exhumation pattern of the Lærdal-Gjende fault. In the same line of investigation, a handful of additional work can be carried out following this thesis.

The AFT age distribution presented by regional studies lead to an inaccurate approximation or an oversimplification of the exhumation pattern of southern Norway. Over the last years, more studies are focusing in reduced geographic areas along the coast (such as Møre-Trondelag fault zone). These studies have proven the importance of the influence of major faults in the exhumation pattern. As it turns out, not only the western coast of Norway is influenced by fault reactivation. The Lærdal-Gjende fault and associated structures are of considerable relevance in the exhumation pattern of central southern Norway. Thus, a realistic exhumation pattern of central southern Norway may be achieved if thermochronological studies are applied for a relatively reduced geographic area. The Filefjell erosional basement window can be tested as the Lærdal-Gjende fault has been analysed in the present study.

Within the sample set of this study, the footwall samples show a general decreasing age trend towards the fault. The sample EC-12a, b show consistent Early Cretaceous age where older ages (Jurassic probably) are expected. That should be studied in detail through AFT analysis in order to describe exhaustively the exhumation pattern along the LGFS, concretely at that locality. The sample EC-13 from the Fillefjell window also displays a younger age that what was expected. However, this age is attributed to the proximity of the décollement zone separating the Jotun nappe from para-autochthonous migmatitic gneisses. Despite of the resolution given in this thesis, more data from this area up to the Ølestol fault should be collected to confirm this hypothesis or to obtain new insights. The Øvre cataclatives (showing in the maps from the present study) can be also studied as in this thesis. A comparative study of the structural characteristics between the Lærdalsøyri and the Øvre outcrops may be of interest to link crustal processes along the Lærdal-Gjende fault. In the same line, the Lærdal-Gjende fault can be studied in detail from south (Aurdalen) up to the northern part of the fault in Rondane. The comparative studies may reveal different features of the fault rocks constrained to different T, P conditions.

AFT analysis is suited for constraining latter post-Caledonian movements of the upper crust due to its reliability to date relatively recent history. The AFT method can be reproduced by diverse investigators due to the non-destructible nature of the method, meaning that the present results can be reproduced by many other. On the other hand, the sampling strategy for AFT analysis should be elaborated according the geological problem that needs to be addressed. Vertical

profiles are the main tool to establish the exhumation rate, and may unveil different exhumation trajectories for different crustal blocks. Horizontal profiles, as the one presented in the present study, can be also of great importance to determine age trends across crustal blocks. The sampling strategy for this particular case should be limited to a range of elevations. The structural setting of the study area should always be well known prior to the sampling. The sampling should also be done according to the geological and statistical problem to be treated. Statistical analysis, if used correctly, can help in large measure to discern between valid results or hypothesis, and should be therefore always considered.

This page is intentionally left blank

Appendices

Table A.1: Field Data.

Sample name	Area code	UTM		Elevation (m)	Lithology	Crustal block	Outcrop type	Comments
		Northing	Easting					
EC-01	32V	6777606	410636	ca. 6	Gabbroic protolith with garnets	HW	Road-cut (Aurland-Lærdal old road)	2km away from the fault to NW
EC-02	32V	6775454	415903	ca. 6	Veined rock of gabbroic composition	HW	Road-cut (Aurland-Lærdal old road)	600-800 m away from the fault to NW
EC-03	32V	6763789	415721	ca. 6	Veined rock of gabbroic composition	HW	Road-cut (Aurland-Lærdal old road)	300 m away from the fault to NW
EC-04	32V	6775515	416638	ca. 5	Cataclasite	HW	Road-cut (Aurland-Lærdal old road)	150 m away from the fault to SE
EC-05	32V	6775309	416763	ca. 3	Cataclastic and mylonitic rocks	FW	Road-cut (Aurland-Lærdal old road)	10 away from the fault to SE
EC-06	32V	6775262	416,785	ca. 3	Migmatitic gneiss with granitic protolith	FW	Road-cut (Aurland-Lærdal old road)	100 m away from the fault to SE
EC-07	32V	6775112	416870	ca. 3	Fault gouges	FC	Road-cut (Aurland-Lærdal old road)	Fault outcrop at Lærdalsøyri
EC-08	32V	6774970	417204	ca. 3	Migmatitic gneiss with granitic protolith	FW	Road-cut (Aurland-Lærdal old road)	In front of the abandoned Revnes ferry quay
EC-09	32V	6797591	437706	405	Gabbroic compositional rock	HW	Road-cut in the mountainside	at Ovre Årdal
EC-10	32V	6795342	442475	757	Metarkose	FW	Road-cut in the mountainside	-
EC-11	32V	6788891	458670	1086	Metarkose	FW	Road-cut in the mountainside	Close to the hotel in Tyin
EC-12	32V	6781997	448734	935	Augen gneiss	FW	Road-cut in the mountainside	-
EC-13	32V	6771476	443258	495	Monzogranit ortogneiss with pegmatitic veins	FW	Road-cut in the mountainside	-
EC-14	32V	6769445	429110	169	Ortogneiss	FW	Road-cut in the mountainside	next to the interest point (Arkeologiskefunn Bjørkum)
EC-15	32V	6774681	417567	3	Migmatitic gneiss with granitic protolith	FW	Road-cut (Aurland-Lærdal old road)	ca. 1 km away from fault to SE (close to EC-08)

Where:

FW = Footwall

HW = Hanging wall

FC = Fault Core

This page is intentionally left blank

B Dosimeter: Track density calculation

Table B.1: Dosimeter table

Position	NoB-025	HeFTy RhoD (N/cm^2)	TrackKey RhoD ($10^5 N/cm^2$)	
1	**IRMM 2-2**	**1947169,467**	**19,47169467**	**106,627**
2	NTW-15-13	1942366,691	19,42366691	
3	NTW-21-13	1937563,915	19,37563915	
4	NTW-40-13	1932761,14	19,3276114	
5	CH-01	1927958,364	19,27958364	
6	CH-02	1923155,588	19,23155588	
7	CH-03	1918352,812	19,18352812	
8	CH-04	1913550,037	19,13550037	
9	CH-05	1908747,261	19,08747261	
10	CH-06	1903944,485	19,03944485	
11	CH-07	1899141,709	18,99141709	
12	CH-08	1894338,934	18,94338934	
13	CH-09	1889536,158	18,89536158	
14	CH-10	1884733,382	18,84733382	
15	**DUR**	**1879930,606**	**18,79930606**	
16	**FCT**	**1875127,831**	**18,75127831**	
17	**IRMM 2-3**	**1870325,055**	**18,70325055**	**102,419**
18	BG-179	1865522,279	18,65522279	
19	BG-180	1860719,503	18,60719503	
20	BG-187	1855916,728	18,55916728	
21	BG-189	1851113,952	18,51113952	
22	EC-02	1846311,176	18,46311176	
23	EC-03	1841508,4	18,415084	
24	EC-05	1836705,625	18,36705625	
25	EC-06	1831902,849	18,31902849	
26	EC-08	1827100,073	18,27100073	
27	EC-09	1822297,297	18,22297297	
28	EC-12	1817494,522	18,17494522	
29	EC-12	1812691,746	18,12691746	
30	EC-13	1807888,97	18,0788897	
31	EC-14	1803086,194	18,03086194	
32	EC-15	1798283,419	17,98283419	
33	**IRMM 2-4**	**1793480,643**	**17,93480643**	**98,211**

C Radial Plots

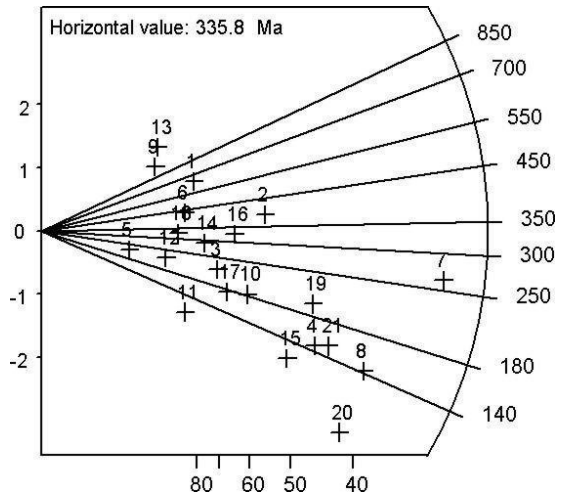

Fig. C.1: EC-02

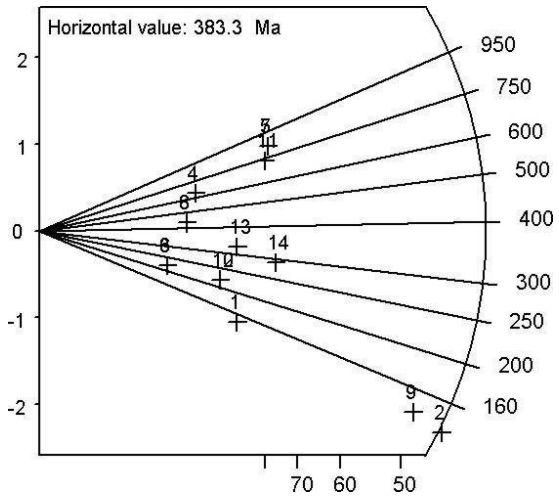

Fig. C.2: EC-03

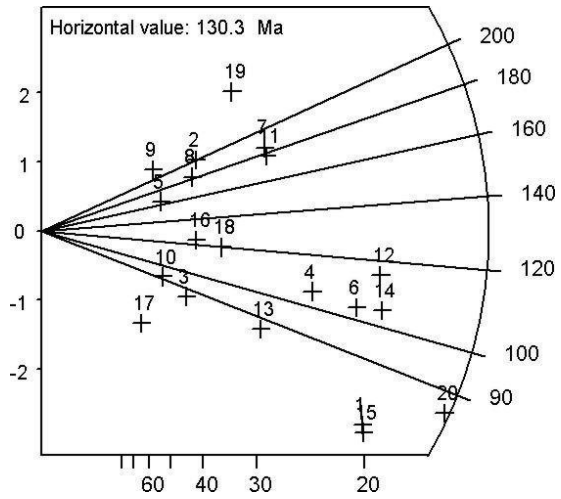

Fig. C.3: EC-05

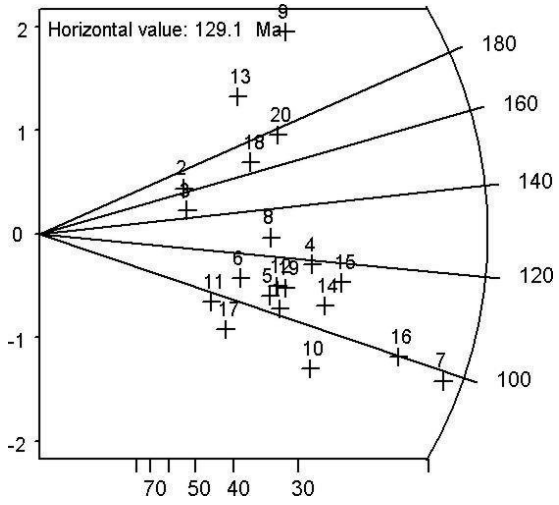

Fig. C.4: EC-06

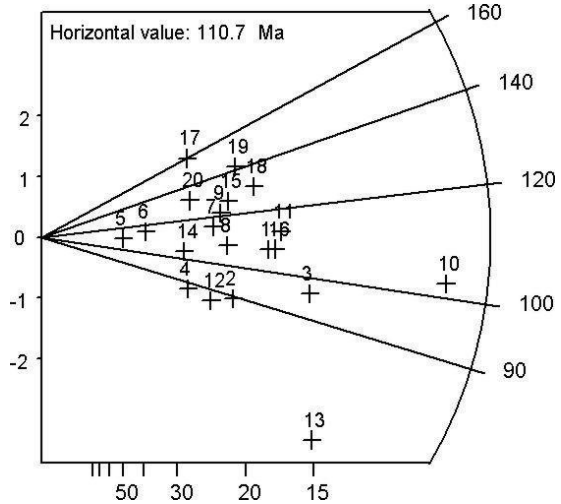

Fig. C.5: EC-08

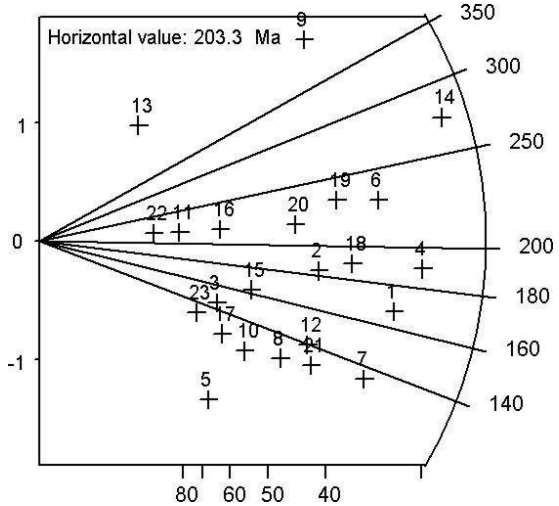

Fig. C.6: EC-09

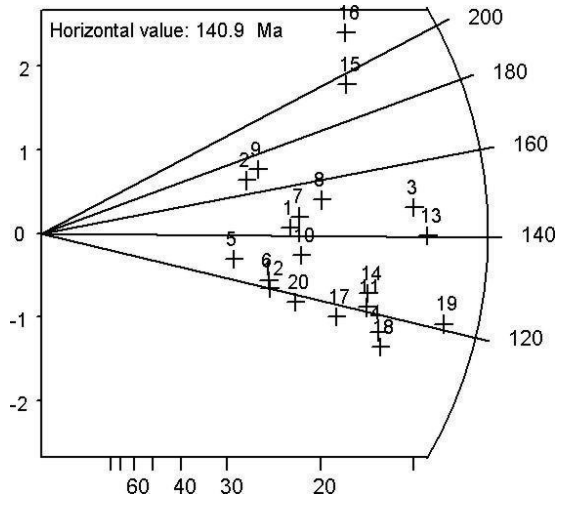

Fig. C.7: EC-12

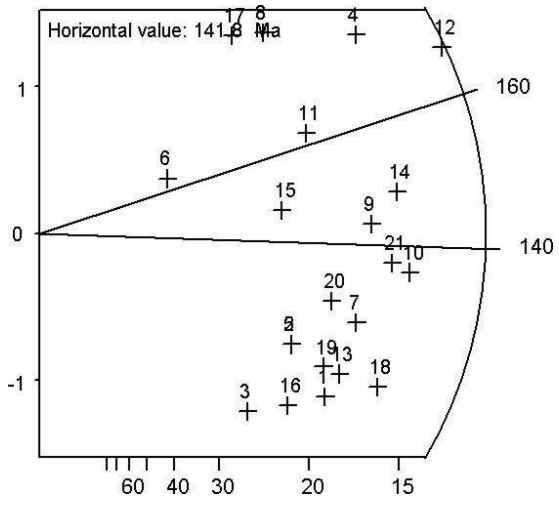

Fig. C.8: EC-12

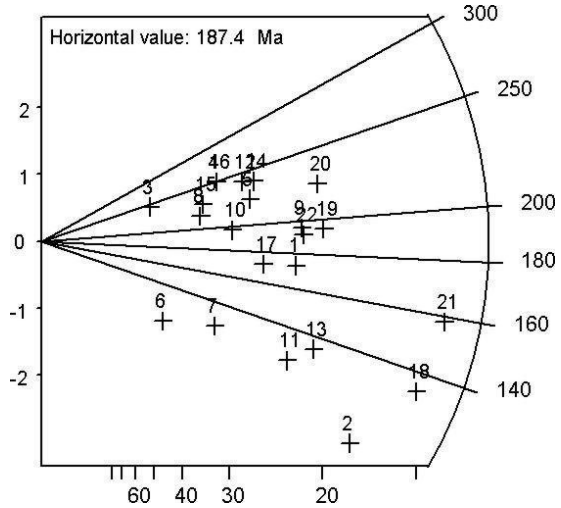

Fig. C.9: EC-13

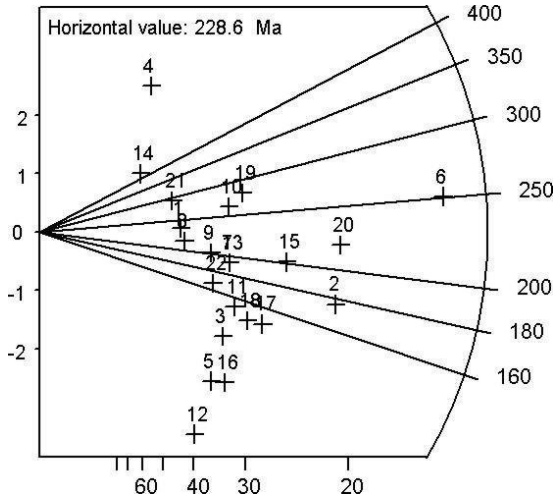

Fig. C.10: EC-14

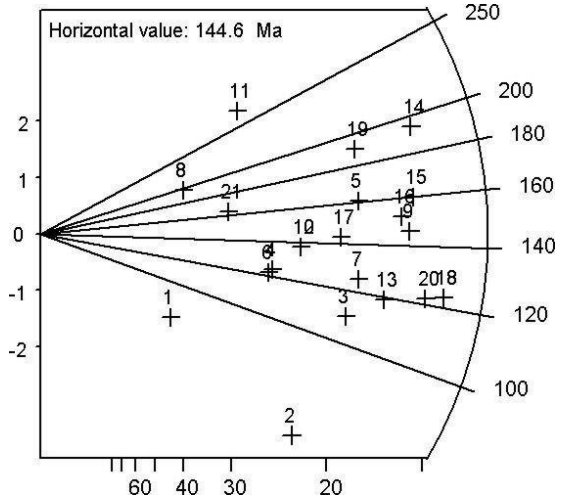

Fig. C.11: EC-15

D Joints and lineaments

Table D.1: 15 Meters Away

Max Strike	Dip
278	48
236	33
233	15
50	39
51	38
53	38
182	68
157	63
248	42
280	54
247	40
252	52
270	40
265	45
258	45
266	45
261	45
38	62
53	70
52	70
313	84
322	70
327	64
158	31
8	60
247	29
205	18
320	78
54	67
298	16
235	44
48	64
50	66
326	86
322	84
325	83

Table D.2: Fault Cataclasite

Max Strike	Dip
85	78
322	86
55	64
53	64
53	69
320	86
324	86
56	68
222	24

Table D.3: Fault Joints

Dip Azimuth	Dip
312	30
309	30
207	86
348	53
353	54
282	82
125	75
300	75
300	88
301	84
190	35

Table D.4: Fault Lineations

Dip Azimuth	Dip
44	340

Table D.5: Hangingwall Joints

Dip Azimuth	Dip
40	33
38	71
90	69
285	30
236	60
230	60
106	88

Table D.6: Hangingwall Lineations

Dip Azimuth	Dip
42	352
296	28
51	297

Table D.7: Migmatite Joints

Max Strike	Dip
176	86
251	43
205	50
77	84
296	58
52	83
100	80
256	77
58	71
345	75
58	71
50	80
210	35
180	60
180	64
53	18
200	74
198	52
205	40
210	58

Table D.8: Migmatite Lineations

Max Strike	Dip
73	98
52	70
51	77
83	133

Table D.9: Mylonite Foliation

Dip Azimuth	Dip
343	40
340	36
53	60
350	42
3	40

Table D.10: Mylonite Joints

Dip Azimuth	Dip
347	30
328	32
237	52
237	52
340	38
354	44
347	48
350	38
284	80
266	40
306	41
84	87
172	57
269	81
58	44
263	50
265	40
340	35
359	25
274	71
277	72
274	76
276	77
297	72
10	30
303	78
299	72
358	30
288	86
5	30
121	80
52	82

Table D.11: Mylonite Lineations

Max Strike	Dip
30	310
18	291
23	294
21	295
20	300

Table D.12: Sample Sites Joints

Name	Max Strike	Dip
EC-01	340	52
	317	68
	342	48
EC-02	20	28
	220	34
EC-03	254	34
EC-04	320	88
	234	32
EC-06	180	89
	267	45
EC-10	4	79
	238	25
EC-11	75	78
	200	80
	243	32
EC-12	40	68
	58	41
	98	38
EC-13	345	52
	66	68
EC-14	154	54
	33	80
EC-15	348	82

Table D.13: Tunnel Joints

Name	Max Strike	Dip
DS-1	94	85
	335	28
	330	39
	322	40
	337	28
	330	25
DS-2	330	28
	180	83
	330	28
	280	80
DS-3	190	24
	135	83
DS-4	301	70
	296	40
	248	18
	238	20
DS-5	74	76
	248	40
	240	40
	74	76
	310	20
	220	24
DS-6	109	72
	116	84
	185	66
	20	79
	328	35

Table D.14: Tunnel Joints

Name	Max Strike	Dip
DS-7	227	44
	310	86
	310	86
DS-8	308	78
	312	85
	310	74
	198	78
	287	23
	42	67
	15	68
DS-9	320	76
	357	40
	150	9
	23	80
	152	33
DS-10	318	82
	50	80
DS-11	35	49
	250	38
	245	29
	35	49
	255	44
	260	36
	230	26
	52	68
	301	74
	360	72
DS-12	307	58
	282	60
	307	62
	245	49
	165	58
	250	38
	170	54
	190	50
	180	60
	173	60
	170	60

Table D.15: Tunnel Lineations

Name	Max Strike	Dip
DS-5	22	93

E Fisher test for significance of linear correlation

R^2 footwall : 0,581 for a positive slope
R^2 hanging wall : 0,624 for a negative slope

- Pearson's correlation coefficient $r_{xy} : -1 < r_{xy} \leqslant 1$

$$r_{xy} \text{ footwall } = \sqrt{R^2} = 0,7622$$
$$r_{xy} \text{ hanging wall } = \sqrt{R^2} = 0,7899$$

T-value : $|r_{xy}| \cdot \sqrt{\frac{n-2}{1-r_{xy}^2}}$

Where:

N footwall : $8 - 2 = 6$
N hanging wall : $12 - 2 = 10$
T-value footwall : 2,884
T-value hanging wall : 4,0735

- Approaching the hypothesis:

Once the t-function values are obtained, the following step is to approach the hypothesis:

For the footwall:

$$H_0 = \rho_{xy} \leqslant 0 \text{ (lacking linear correlation)}$$
$$H_1 = \rho_{xy} > 0$$

For the hanging wall:

$$H_0 = \rho_{xy} \geqslant 0 \text{ (lacking linear correlation)}$$
$$H_1 = \rho_{xy} < 0$$

If $t \geqslant t_\alpha$, H_0 can be rejected with $(1 - \alpha)100\,\%$ confidence. T_α is found in a table of the Student's t-function according to the degrees of freedom for each case and for a certain level of confidence. The degrees of freedom (DF) are defined as $n-2$. The level of confidence in science should be always at least 90 %, therefore the α needed goes from 0,1 to 0,0005 (90 to 99,5 % confidence).

For the footwall, the H_0 is rejected because $t \geqslant t_\alpha$ $(2,884 > 2,447)$. This implies that there is an actual linear correlation between age and distance from the fault that indicates a decrease in age towards the fault.

For the hanging wall, the H_0 is rejected because $t \geqslant t_\alpha$ $(4,0735 > 3,169)$. This implies that there is an actual linear correlation between age and distance from the fault that indicates an increase in age towards the fault.

Table E.1: Critical values for the Student's t-function values (t_α)

DF/α	**0,1**	**0,05**	**0,025**	**0,005**
6	1,44	1,943	2,447	3,707
10	1,372	1,812	2,228	3,169

DF footwall : $8-2=6$
DF hanging wall : $12-2=10$

List of Tables

This page is intentionally left blank

List of Figures

This page is intentionally left blank

References

Andersen, T. B. 1998. "Extensional tectonics in the Caledonides of southern Norway, an overview". *Tectonophysics* 285 (3), 333–351.

Andersen, T. B., Torsvik, T. H., Eide, E. A., Osmundsen, P. T., Faleide, J. I. 1999. "Permian and Mesozoic extensional faulting within the Caledonides of central south Norway". *Journal of the Geological Society* 156 (6), 1073–1080.

Andriessen, P. A., Bos, A. 1986. "Post-Caledonian thermal evolution and crustal uplift in the Eidfjord area, western Norway". *Norsk geologisk tidsskrift* 66 (3), 243–250.

Barbarand, J, Pagel, M, Blanc, P., Braun, J.-J., Chaussidon, M, Vetil, C, Walgenwitz, F 1996. "Combined Cathodoluminescence spectra, fission-track age and chemistry of detrital apatite grains: Towards a better understanding of fission track annealing". In: *International conference on cathodoluminescence and related techniques in geosciences and geomaterials*, 19–20.

Bard, J. P. 1986. *Microtextures of igneous and metamorphic rocks*. Vol. 1. Springer Science & Business Media.

Battey, M. H., McRitchie, W. D. 1973. "A geological traverse across the pyroxene-granulites of Jotunheimen in the Norwegian Caledonides". *Norsk Geologisk Tidsskrift* 53, 237–265.

Baumhauer, H. A. 1894. *Die resultate der aetzmethode: in der krystallographischen forschung, an einer reihe von krystallisirten körpern dargestellt*. Vol. 12. W. Engelmann.

Beck, R. A. et al. 1995. "Stratigraphic evidence for an early collision between northwest India and Asia". *Nature* 373 (6509), 55–58.

Bell, T., Etheridge, M. 1973. "Microstructure of mylonites and their descriptive terminology". *Lithos* 6 (4), 337–348.

Bhandari, N., Bhat S.G.; Lal, D., Rajagopalan, G., Tamhane, A., Venkatavaradan, V. 1971. "Fission fragment tracks in apatite: recordable track lengths". *Earth and Planetary Science Letters* 13 (1), 191–199.

Blenkinsop, T. G. 2000. *Deformation microstructures and mechanisms in minerals and rocks*. Springer Science & Business Media.

Bruhn, D, Groebner, N, Kohlstedt, D. 2000. "An interconnected network of core-forming melts produced by shear deformation". *Nature* 403 (6772), 883–886.

Buck, W. R. 1986. "Small-scale convection induced by passive rifting: the cause for uplift of rift shoulders". *Earth and Planetary Science Letters* 77 (3), 362–372.

Burke, K., Fox, P., Şengör, A. 1978. "Buoyant ocean floor and the evolution of the Caribbean". *Journal of Geophysical Research: Solid Earth (1978–2012)* 83 (B8), 3949–3954.

Butler, R., Coward, M. 1984. "Geological constraints, structural evolution, and deep geology of the Northwest Scottish Caledonides". *Tectonics* 3 (3), 347–365.

Caine, J. S., Evans, J. P., Forster, C. B. 1996. "Fault zone architecture and permeability structure". *Geology* 24 (11), 1025–1028.

Carlson, W. D. 1990. "Mechanisms and kinetics of apatite fission-track annealing". *American Mineralogist;(United States)* 75.

Chauvet, A, Dallmeyer, R. 1992. "40 Ar/39 Ar mineral dates related to Devonian extension in the southwestern Scandinavian Caledonides". *Tectonophysics* 210 (1), 155–177.

Chauvet, A., Séranne, M. 1994. "Extension-parallel folding in the Scandinavian Caledonides: implications for late-orogenic processes". *Tectonophysics* 238 (1), 31–54.

Chester, F., Friedman, M, Logan, J. M. 1985. "Foliated cataclasites". *Tectonophysics* 111 (1), 139–146.

Dahl, S. O., Nesje, A. 1994. "Holocene glacier fluctuations at Hardangerjøkulen, central-southern Norway: a high-resolution composite chronology from lacustrine and terrestrial deposits". *The Holocene* 4 (3), 269–277.

Davids, C., Wemmer, K., Zwingmann, H., Kohlmann, F., Jacobs, J., Bergh, S. G. 2013. "K–Ar illite and apatite fission track constraints on brittle faulting and the evolution of the northern Norwegian passive margin". *Tectonophysics* 608, 196–211.

Dewey, J. F., Bird, J. M. 1970. "Mountain belts and the new global tectonics". *Journal of Geophysical Research* 75 (14), 2625–2647.

Donelick, R. A., O'Sullivan, P. B., Ketcham, R. A. 2005. "Apatite fission-track analysis". *Reviews in Mineralogy and Geochemistry* 58 (1), 49–94.

Doré, A. 1992. "Basins on the Atlantic Seaboard: Petroleum Geology, Sedimentology and Basin Evolution".

Doré, A., Lundin, E., Jensen, L., Birkeland, Ø, Eliassen, P., Fichler, C 1999. "Principal tectonic events in the evolution of the northwest European Atlantic margin". In: *Geological Society, London, Petroleum Geology Conference series*. Vol. 5. Geological Society of London, 41–61.

Dumitru, T. A. 1993. “A new computer-automated microscope stage system for fission-track analysis”. *Nuclear Tracks and Radiation Measurements* 21 (4), 575–580.

Dunlap, W., Fossen, H 1998. “Early Paleozoic orogenic collapse, tectonic stability, and late Paleozoic continental rifting revealed through thermochronology of K-feldspars, southern Norway”. *Tectonics* 17 (4), 604–620.

Durrani, S., Bull, R. 1987. *Solid state nuclear detection*.

Eide, E., Torsvik, T., Andersen, T., Arnaud, N. 1999. “Early Carboniferous unroofing in western Norway: A tale of alkali feldspar thermochronology”. *The Journal of geology* 107 (3), 353–374.

Eide, E. A., Torsvik, T. H., Andersen, T. B. 1997. “Absolute dating of brittle fault movements: Late Permian and late Jurassic extensional fault breccias in western Norway”. *Terra Nova* 9 (3), 135–139.

Færseth, R. 1996. “Interaction of Permo-Triassic and Jurassic extensional fault-blocks during the development of the northern North Sea”. *Journal of the Geological Society* 153 (6), 931–944.

Færseth, R., Sjøblom, T., Steel, R., Liljedahl, T, Sauar, B., Tjelland, T 1995. “Sequence Stratigraphy on the Northwest European Margin”.

Fenner, D. P. 1988. “Some leeward reefs and corals of Cozumel, Mexico”. *Bulletin of Marine Science* 42 (1), 133–144.

Fleischer, R., Hart, H. 1972. “Fission track dating: techniques and problems”. *Proc. Burg Wartenstain Conf. on Calibration of Hominoid Evolution*, 135–170.

Fleischer, R., Price, P. 1964. “Fission track evidence for the simultaneous origin of tektites and other natural glasses”. *Geochimica et Cosmochimica Acta* 28 (6), 755–760.

Fleischer, R., Price, P., Walker, R. 1965. “Ion explosion spike mechanism for formation of charged-particle tracks in solids”. *Journal of applied Physics* 36 (11), 3645–3652.

Fleischer, R. L., Price, P. B., Walker, R. M. 1975. *Nuclear tracks in solids: principles and applications*. Univ of California Press.

Fleitout, L., Yuen, D. A. 1984. “Steady state, secondary convection beneath lithospheric plates with temperature- and pressure-dependent viscosity”. *Journal of Geophysical Research: Solid Earth (1978–2012)* 89 (B11), 9227–9244.

Fossen, H, Mangerud, G, Hesthammer, J, Bugge, T, Gabrielsen, R. 1997. “The Bjoroy Formation: a newly discovered occurrence of Jurassic sediments in the Bergen Arc System”. *Norsk Geologisk Tidsskrift* 77 (4), 269–287.

Fossen, H. 1992. “The role of extensional tectonics in the Caledonides of south Norway”. *Journal of structural geology* 14 (8), 1033–1046.

Fossen, H. 1993. “Structural evolution of the Bergsdalen Nappes, southwest Norway”. *Norges geologiske undersøkelse Bulletin* 424, 23–50.

Fossen, H. 2010. *Structural geology*. Cambridge University Press.

Fossen, H., Dallmeyer, R. 1998. “40 Ar/39 Ar muscovite dates from the nappe region of southwestern Norway: dating extensional deformation in the Scandinavian Caledonides”. *Tectonophysics* 285 (1), 119–133.

Fossen, H., Dunlap, W. J. 1998. “Timing and kinematics of Caledonian thrusting and extensional collapse, southern Norway: evidence from 40 Ar/39 Ar thermochronology”. *Journal of structural geology* 20 (6), 765–781.

Fossen, H., Dunlap, W. J. 1999. “On the age and tectonic significance of Permo-Triassic dikes in the Bergen-Sunnhordland region, southwestern Norway”. *Norsk Geologisk Tidsskrift* 79 (3), 169–178.

Fossen, H., Holst, T. B. 1995. “Northwest-verging folds and the northwestward movement of the Caledonian Jotun Nappe, Norway”. *Journal of Structural Geology* 17 (1), 3–15.

Fossen, H., Hurich, C. A. 2005. “The Hardangerfjord Shear Zone in SW Norway and the North Sea: a large-scale low-angle shear zone in the Caledonian crust”. *Journal of the Geological Society* 162 (4), 675–687.

Fossen, H., Rykkelid, E. 1992. “Postcollisional extension of the Caledonide orogen in Scandinavia: Structural expressions and tectonic significance”. *Geology* 20 (8), 737–740.

Fossen, H., Tikoff, B., Teyssier, C. 1994a. “Strain modeling of transpressional and transtensional deformation”. *Norsk Geologisk Tidsskrift* 74 (3), 134–145.

Fossen, H., Tikoff, B., Teyssier, C. 1994b. “Strain modeling of transpressional and transtensional deformation”. *Norsk Geologisk Tidsskrift* 74 (3), 134–145.

Gabrielsen, R., Færseth, R., Steel, R., Idil, S, Kløvjan, O. 1990. “Architectural styles of basin fill in the northern Viking Graben”. *Tectonic evolution of the North Sea rifts* 181, 158–179.

Gabrielsen, R. H., Faleide, J. I., Pascal, C., Braathen, A., Nystuen, J. P., Etzelmuller, B., O’Donnell, S. 2010. “Latest Caledonian to Present tectonomorphological development of southern Norway”. *Marine and Petroleum Geology* 27 (3), 709–723.

Galbraith, R. 1981. “On statistical models for fission track counts”. *Journal of the International Association for Mathematical Geology* 13 (6), 471–478.

Galbraith, R. 1984. “On statistical estimation in fission track dating”. *Journal of the International Association for Mathematical Geology* 16 (7), 653–669.
Galbraith, R. 1988. “Graphical display of estimates having differing standard errors”. *Technometrics* 30 (3), 271–281.
Galbraith, R. 1990. “The radial plot: graphical assessment of spread in ages”. *International Journal of Radiation Applications and Instrumentation. Part D. Nuclear Tracks and Radiation Measurements* 17 (3), 207–214.
Galbraith, R., Laslett, G. 1985. “Some remarks on statistical estimation in fission-track dating”. *Nuclear Tracks and Radiation Measurements (1982)* 10 (3), 361–363.
Gallagher K.; Brown, R., Johnson, C. 1998. “Fission track analysis and its applications to geological problems”. *Annual Review of Earth and Planetary Sciences* 26 (1), 519–572.
Gathe, R, Andersen, T. B. 1996. “Extensional structures below the Jotun Nappe in Central south Norway; an example from the Lærdal area”. *Nordisk Geologisk Vintermöte, Åbo (1996) Abstract Volume*.
Gaál, G., Gorbatschev, R. 1987. “An outline of the Precambrian evolution of the Baltic Shield”. *Precambrian Research* 35, 15–52.
Gjessing, J. 1967. “Norway’s paleic surface”.
Gleadow, A., Duddy, I. 1981. “A natural long-term track annealing experiment for apatite”. *Nuclear Tracks* 5 (1), 169–174.
Gleadow, A., Lovering, J. 1977. “Geometry factor for external detectors in fission track dating”. *Nuclear Track Detection* 1 (2), 99–106.
Gleadow, A., Duddy I.R.and Green, P. F., Lovering, J. 1986. “Confined fission track lengths in apatite: a diagnostic tool for thermal history analysis”. *Contributions to Mineralogy and Petrology* 94 (4), 405–415.
Goldschmidt, V. M. 1912. *Die kaledonische Deformation der südnorwegischen Urgebirgstafel*. Dybwad in Komm.
Green, P., Durrani, S. 1977. “Annealing studies of tracks in crystals”. *Nuclear Track Detection* 1 (1), 33–39.
Green, P., Duddy, I., Gleadow, A., Tingate, P., Laslett, G. 1986. “Thermal annealing of fission tracks in apatite: 1. A qualitative description”. *Chemical Geology: Isotope Geoscience section* 59, 237–253.
Griffin, W., Austrheim, H, Brastad, K, Bryhni, I, Krill, A., Krogh, E., Mørk, M., Qvale, H, Tørudbakken, B 1985. “High-pressure metamorphism in the Scandinavian Caledonides”. In: *The Caledonide Orogen—Scandinavia and Related Areas*. Wiley Chichester, 783–801.
Hanmer, S., McEachern, S. 1992. “Kinematical and rheological evolution of a crustal-scale ductile thrust zone, Central Metasedimentary Belt, Grenville orogen, Ontario”. *Canadian Journal of Earth Sciences* 29 (8), 1779–1790.
Hasebe, N., Barbarand, J., Jarvis, K., Carter, A., Hurford, A. J. 2004. “Apatite fission-track chronometry using laser ablation ICP-MS”. *Chemical Geology* 207 (3), 135–145.
Helle, S. K., Rye, N., Stabell, B., Prösch-Danielsen, L., Hoel, C. 2007. “Neotectonic faulting and the Late Weichselian shoreline gradients in SW Norway”. *Journal of Geodynamics* 44 (3), 96–128.
Hendriks, B., Andriessen, P., Huigen, Y., Leighton, C., Redfield, T., Murrell, G., Gallagher, K., Nielsen, S. B. 2007. “A fission track data compilation for Fennoscandia”. *Norsk Geologisk Tidsskrift* 87 (1/2), 143.
Hicks, E. C., Bungum, H., Lindholm, C. D. 2000. “Stress inversion of earthquake focal mechanism solutions from onshore and offshore Norway”. *Norsk Geologisk Tidsskrift* 80 (4), 235–250.
Hobbs, B. E., Means, W. D., Williams, P. F. 1976. *An outline of structural geology*. John Wiley & Sons.
Hurford, A. J., Green, P. F. 1983. “The zeta age calibration of fission-track dating”. *Chemical Geology* 41, 285–317.
Hurford, A., Carter, A. 1991. “The role of fission track dating in discrimination of provenance”. *Geological Society, London, Special Publications* 57 (1), 67–78.
Hurford, A. J., Hammerschmidt, K. 1985. “40Ar39Ar and K/Ar dating of the Bishop and Fish Canyon Tuffs: Calibration ages for fission-track dating standards”. *Chemical Geology: Isotope Geoscience section* 58 (1), 23–32.
Jackson, J., McKenzie, D. 1983. “The geometrical evolution of normal fault systems”. *Journal of Structural Geology* 5 (5), 471–482.
Ketcham, R. A., Carter, A., Donelick, R. A., Barbarand, J., Hurford, A. J. 2007. “Improved measurement of fission-track annealing in apatite using c-axis projection”. *American Mineralogist* 92 (5-6), 789–798.
Ketcham, R. 2005. “Forward and inverse modeling of low-temperature thermochronometry data”. *Reviews in mineralogy and geochemistry* 58 (1), 275–314.
Killick, A. 2003. “Fault rock classification: an aid to structural interpretation in mine and exploration geology”. *South African Journal of Geology* 106 (4), 395–402.
Ksienzyk, A. K. 2012. “From mountains to basins: geochronological case studies from southwestern Norway, Western Australia and East Antarctica”.
Ksienzyk, A. K., Dunkl, I., Jacobs, J., Fossen, H., Kohlmann, F. 2014. “From orogen to passive margin: constraints from fission track and (U–Th)/He analyses on Mesozoic uplift and fault reactivation in SW Norway”. *Geological Society, London, Special Publications* 390, SP390–27.

Kvale, A. 1960. *The nappe area of the Caledonides in western Norway*. Norwegian Government's Organizing Committee.

Larsen, O, Fossen, H., Langeland, K., Pedersen, R.-B. 2003. "Kinematics and timing of polyphase post-Caledonian deformation in the Bergen area, SW Norway". *Norsk Geologisk Tidsskrift* 83 (3), 149–166.

Laslett, G., Green, P. F., Duddy, I., Gleadow, A. 1987. "Thermal annealing of fission tracks in apatite 2. A quantitative analysis". *Chemical Geology: Isotope Geoscience Section* 65 (1), 1–13.

Leighton, C. A. 2007. "The thermotectonic development of southern Norway: constraints from low-temperature thermochronology". PhD thesis. Imperial College London (University of London).

Lister, G. S., Davis, G. A. 1989. "The origin of metamorphic core complexes and detachment faults formed during Tertiary continental extension in the northern Colorado River region, USA". *Journal of Structural Geology* 11 (1), 65–94.

Lister, G., Snoke, A. 1984. "SC mylonites". *Journal of Structural Geology* 6 (6), 617–638.

Lutro, O, Tveten, E 1996. "Geological map of Norway, Berggrunskart Årdal M 1: 250'000". *Geological Survey of Norway, Trondheim*.

Maddock, R. 1983. "Melt origin of fault-generated pseudotachylytes demonstrated by textures". *Geology* 11 (2), 105–108.

McDowell, F. W., McIntosh, W. C., Farley, K. A. 2005. "A precise 40 Ar–39 Ar reference age for the Durango apatite (U–Th)/He and fission-track dating standard". *Chemical Geology* 214 (3), 249–263.

Means, W. 1984. "Shear zones of types I and II and their significance for reconstruction of rock history". *Geol. Soc. Am. Bull., Abstract Programs* 16, 50.

Milnes, A., Koestler, A. 1985. "Geological structure of Jotunheimen, southern Norway (Sognefjell-Valdres cross-section)". *The Caledonide Orogen—Scandinavia and Related Areas* 1, 457–474.

Milnes, A., Wennberg, O., Skår, Ø, Koestler, A. 1997. "Contraction, extension and timing in the South Norwegian Caledonides: the Sognefjord transect". *Geological Society, London, Special Publications* 121 (1), 123–148.

Mitra, G. 1984. "Brittle to ductile transition due to large strains along the White Rock thrust, Wind River Mountains, Wyoming". *Journal of Structural Geology* 6 (1), 51–61.

Mitra, G. 1994. "Strain variation in thrust sheets across the Sevier fold-and-thrust belt (Idaho-Utah-Wyoming): Implications for section restoration and wedge taper evolution". *Journal of Structural Geology* 16 (4), 585–602.

Mitra, G., Ismat, Z. 2001. "Microfracturing associated with reactivated fault zones and shear zones: what can it tell us about deformation history?" *Geological Society of London Special Publications* 186, 113–140.

Naeser, C. 1967. "The use of apatite and sphene for fission track age determinations". *Geological Society of America Bulletin* 78 (12), 1523–1526.

Naeser, C., Forbes, R. 1976. "Variation of fission track ages with depth in two deep drill holes". *EOS, Trans., Am. Geophys. Union;(United States)* 57 (4).

Nielsen, S. B. et al. 2009. "The evolution of western Scandinavian topography: a review of Neogene uplift versus the ICE (isostasy–climate–erosion) hypothesis". *Journal of Geodynamics* 47 (2), 72–95.

Norton, M. 1986. "Late Caledonide extension in western Norway: A response to extreme crustal thickening". *Tectonics* 5 (2), 195–204.

Osmundsen, P. T., Redfield, T. 2011. "Crustal taper and topography at passive continental margins". *Terra Nova* 23 (6), 349–361.

Osmundsen, P., Andersen, T., Markussen, S 1998. "Tectonics and sedimentation in the hangingwall of a major extensional detachment: the Devonian Kvamshesten Basin, western Norway". *Basin Research* 10 (2), 213–234.

Passchier, C., Trouw, R. 2005. "Microtectonics", 366.

Passchier, C., Ten Brink, C., Bons, P., Sokoutis, D 1993. "δ objects as a gauge for stress sensitivity of strain rate in mylonites". *Earth and Planetary Science Letters* 120 (3), 239–245.

Press, F, Siever, R 1986. *Earth (4th edn)*.

Price, P., Walker, R. 1962. "Observations of Charged-Particle Tracks in Solids". *Journal of Applied Physics* 33 (12), 3400–3406.

Priem, H., Boelrijk, N., Verschure, R., Hebeda, E., Verdurmen, E. 1968. "Th.(1968): Second progress-report on the isotopic dating project in Norway". *ZWO Laboratory for Isotope Geology, Amsterdam*.

Reber, J. E., Dabrowski, M., Galland, O., Schmid, D. W. 2013. "Sheath fold morphology in simple shear". *Journal of Structural Geology* 53, 15–26.

Redfield, T. 2010. "On apatite fission track dating and the Tertiary evolution of West Greenland topography". *Journal of the Geological Society* 167 (2), 261–271.

Redfield, T., Torsvik, T., Andriessen, P., Gabrielsen, R. 2004. "Mesozoic and Cenozoic tectonics of the Møre Trøndelag Fault Complex, central Norway: constraints from new apatite fission track data". *Physics and Chemistry of the Earth, Parts A/B/C* 29 (10), 673–682.

Redfield, T., Braathen, A, Gabrielsen, R., Osmundsen, P., Torsvik, T., Andriessen, P. 2005. "Late Mesozoic to Early Cenozoic components of vertical separation across the Møre–Trøndelag fault complex, Norway". *Tectonophysics* 395 (3), 233–249.

Reimold, W. 1995. "Pseudotachylite in impact structures—generation by friction melting and shock brecciation?: A review and discussion". *Earth-Science Reviews* 39 (3), 247–265.

Riis, F, Fjeldskaar, W 1992. "On the magnitude of the Late Tertiary and Quaternary erosion and its significance for the uplift of Scandinavia and the Barents Sea". In: *Structural and tectonic modelling and its application to petroleum geology*. Vol. 1. Elsevier Amsterdam, 163–185.

Riis, F. 1996. "Quantification of Cenozoic vertical movements of Scandinavia by correlation of morphological surfaces with offshore data". *Global and Planetary Change* 12 (1), 331–357.

Rohrman, M., Beek, P., Andriessen, P., Cloetingh, S. 1995. "Meso-Cenozoic morphotectonic evolution of southern Norway: Neogene domal uplift inferred from apatite fission track thermochronology". *Tectonics* 14 (3), 704–718.

Rutter, E. 1986. "On the nomenclature of mode of failure transitions in rocks". *Tectonophysics* 122 (3), 381–387.

Rutter, E., Holdsworth, R., Knipe, R. 2001. "The nature and tectonic significance of fault-zone weakening: an introduction". *Geological Society, London, Special Publications* 186 (1), 1–11.

Schärer, U. 1980. "U-Pb and Rb-Sr dating of a polymetamorphic nappe terrain: the Caledonian Jotun Nappe, southern Norway". *Earth and Planetary Science Letters* 49 (2), 205–218.

Schmid, S., Handy, M. 1991. "Towards a genetic classification of fault rocks: Geological usage and tectonophysical implications. In: Controversies in Modern Geology (DW Müller, JA McKenzie & H. Weissert, editors), Academic Press London, 339-361".

Scholz, C. H. 1990. "The mechanics of earthquakes and faulting".

Shand, S. J. 1916. "The pseudotachylyte of Parijs (Orange free State), and its relation to 'Trap-Shotten Gneiss' and 'Flinty Crush-rock'". *Quarterly Journal of the Geological Society* 72 (1-4), 198–221.

Sibson, R. 1977. "Fault rocks and fault mechanisms". *Journal of the Geological Society* 133 (3), 191–213.

Sibson, R. H. 1994. "An assessment of field evidence for 'Byerlee'friction". *Pure and Applied Geophysics* 142 (3-4), 645–662.

Silk, E., Barnes, R. 1959. "Examination of fission fragment tracks with an electron microscope". *Philosophical Magazine* 4 (44), 970–972.

Smethurst, M. A., Khramov, A. N., Torsvik, T. H. 1998. "The Neoproterozoic and Palaeozoic palaeomagnetic data for the Siberian Platform: from Rodinia to Pangea". *Earth-Science Reviews* 43 (1), 1–24.

Snoke, A. W., Tullis, J., Todd, V. R. 1998. *Fault-related Rocks: A Photographic Atlas*. Princeton University Press.

Spry, A 1969. *Metamorphic textures, 350 pp*.

Steer, P., Huismans, R. S., Valla, P. G., Gac, S., Herman, F. 2012. "Bimodal Plio-Quaternary glacial erosion of fjords and low-relief surfaces in Scandinavia". *Nature Geoscience* 5 (9), 635–639.

Steiger, R., Jäger, E. 1977. "Subcommission on geochronology: convention on the use of decay constants in geo-and cosmochronology". *Earth and Planetary Science Letters* 36 (3), 359–362.

Tagami, T., Lal, N., Sorkhabi, R., Ito, H., Nishimura, S. 1988. "Fission track dating using external detector method".

Ter Voorde, M, Ravnås, R, Faerseth, R, Cloetingh, S. 1997. "Tectonic modelling of the Middle Jurassic synrift stratigraphy in the Oseberg–Brage area, northern Viking Graben". *Basin Research* 9 (2), 133–150.

Torske, T 1972. "Tertiary oblique uplift of Western Fennoscandia; crustal warping in connection with rifting and break-up of the Laurasian continent". *Norges Geologiske Undersøkelse* 273, 43–48.

Torsvik, T., Sturt, B., Swensson, E, Andersen, T., Dewey, J. 1992. "Palaeomagnetic dating of fault rocks: evidence for Permian and Mesozoic movements and brittle deformation along the extensional Dalsfjord Fault, western Norway". *Geophysical Journal International* 109 (3), 565–580.

Torsvik, T. H. 2003. "The Rodinia jigsaw puzzle". *Science* 300 (5624), 1379–1381.

Torsvik, T. H., Cocks, L. R. M. 2014. "Gondwana (Africa) from top to base in space and time". In: *EGU General Assembly Conference Abstracts*. Vol. 16, 2913.

Torsvik, T. H., andersen, T. B., Eide, E. A., Walderhaug, H. J. 1997. "The age and tectonic significance of dolerite dykes in western Norway". *Journal of the Geological Society* 154 (6), 961–973.

Trouw, R. A., Passchier, C. W., Wiersma, D. 2010. *Atlas of Shear Zone Microstructures*. Springer.

Tullis, J., Yund, R. A. 1977. "Experimental deformation of dry Westerly granite". *Journal of Geophysical Research* 82 (36), 5705–5718.

Twiss, R. J., Moores, E. 1992. *Structural Geology, 532 pp*.

Wagner, G., Wuthrich, K. 1979. "Truncated driven nuclear overhauser effect (TOE). A new technique for studies of selective 1 H 1 H overhauser effects in the presence of spin diffusion". *Journal of Magnetic Resonance (1969)* 33 (3), 675–680.

Wagner, G., Haute, P. Van den 1992. *Fission track dating*. Kluwer Academic Publishers.

Wise, D., Dunn, D., Engelder, J., Geiser, P., Hatcher, R., Kish, S., Odom, A., Schamel, S 1984. “Fault-related rocks: suggestions for terminology”. *Geology* 12 (7), 391–394.

Yonkee, W. A. 1992. “Basement-cover relations, Sevier orogenic belt, northern Utah”. *Geological Society of America Bulletin* 104 (3), 280–302.

Young, D. 1958. “Etching of radiation damage in lithium fluoride”. *Nature* 182.

Young, E., Myers, A., Munson, E., Conklin, N. M. 1969. “Mineralogy and geochemistry of fluorapatite from Cerro de Mercado, Durango, Mexico”. *US Geological Survey Professional Paper* 650 (D), D84–D93.